Development of Bioactive Carbon-Based Nanomaterials for Healthcare Applications

Anjana Sharma

A thesis submitted for the partial fulfilment of
the degree of Doctor of Philosophy

Institute of Nano Science and Technology, Sector-81, Knowledge City, Sahibzada Ajit Singh Nagar, Punjab, Pin-140306

Indian Institute of Science Education and Research, Mohali, Knowledge city, Sector 81, SAS Nagar, Manauli Pin-140306

July, 2022

Dedicated to my family

Declaration

The work presented in this thesis has been carried out by me under the guidance of Prof. Deepa Ghosh at the Institute of Nano Science and Technology, Mohali. This work has not been submitted in part or in full for a degree, a diploma, or a fellowship to any other university or institute. Whenever contributions of others are involved, every effort is made to indicate this clearly, with due acknowledgement of collaborative research and discussions. This thesis is a bona fide record of original work done by me and all sources listed within have been detailed in the bibliography.

Anjana Sharma

In my capacity as the supervisor of the candidate's thesis work, I certify that the above statements by the candidate are true to the best of my knowledge.

Prof. Deepa Ghosh

Acknowledgements

At the end of my PhD tenure at INST Mohali, I came to realize that my research journey would not have completed without support and guidance of many people who have provided me with invaluable assistance. Whether it be valuable guidance or access to materials and services that helped me a lot in my research work, it is greatly appreciated. I would like to take this opportunity for expressing my sincere thankfulness to following people.

First of all, I would like to express my profound gratitude to my mentor ***Dr. Deepa Ghosh,*** *Professor INST Mohali, for her priceless advices, remarks, suggestions and guidance for the past five years. I have been extremely fortunate to have a mentor like her who paid so much attention to my research work and always responded promptly to all my doubts and queries. She was always there to lend a hand of support whenever I face difficulty in my lab projects. She always inspired and motivated me to work hard which allowed to me to explore those areas which were newer to me. She has provided me a liberal lab environment which helped me to work freely and establish myself as an independent researcher. Her patience and insightful suggestions directed me to the right track even in some hard times during this journey. She never lost faith in me and continued to motivate me during this period. I thank her from the bottom of my heart for helping me in the successful completion of my PhD journey.*

I am extremely grateful to my doctoral committee members ***Dr Sangita Roy*** *and* ***Dr Debaprata Patra*** *who were always equipped with kind words of encouragement and advice as I maneuvered my way through the process.*

*I would extend my sincere gratitude to **Prof. A.K Ganguli** (Founding Director of INST) **Prof. H.N. Ghosh** (former Director (INST)), and **Prof. Amitava Patra, Director (INST)** for providing an excellent research environment under the roof of INST.*

I would like to extend my sincere thanks to all the faculty members and administration staff for their help and suggestions.

*I want to pay my reverence to **INST Mohali** and for providing financial assistance in the form of fellowship to carry out my research.*

I owe a very important debt to animals for sacrificing their lives for the sake of my project.

*I thank my lab mates **Dr Vineeta Panwar, Dr Swati Kaushik, Jijo, Vianni, Himadri, Navita**, **Preethi** and **Mallika** for their support in some or another way throughout my research tenure.*

*I cannot thank enough to **Dr Vineeta Panwar** as she was my second research guide. Her knowledge and wisdom helped me a lot in the successful completion of my PhD thesis. Inspite of her numberless commitments and tasks, she was always there to lend her support and guidance and help me in every possible way.*

*Special thanks to **Sanchita Shah** urf **Chinti** (roommate) who is one of the purest souls I have ever met in my life. We shared so many good memories be it outings, relishing good food, watching movies or gossiping at night while drinking coffee.*

*I would be remiss in not mentioning my **Chai Peelo Group** members, **Dr Pranjali Yadav**, **Dr Vineeta Panwar** and **Mimansa.** Our endless discussions, gossips and laughter during chai sessions are one of my favourite memories of INST. I also thank my friends (too many to list here but you know who you are!) for providing support and friendship*

*I could not have undertaken this journey without the support of my husband **Mr. Sahil Kumar** who supported me endlessly throughout this tenure by taking me for outings whenever I was stressed, feeding me delicious food to cheer me up and has constantly encouraged me when the tasks seemed difficult and overwhelming.*

*My special thanks go to my family especially my mother **Mrs Vijay Sharma** and sisters **Dr. Ranjana Sharma** & **Vandana Sharma** for their incomparable love, care, support, sacrifice and patience. I am what I am because of their infinite love and confidence in me. I would also express my heartfelt thanks to **Dr Dixit Prasher** and **Mr. Munish Sharma** for being a pillar of emotional as well as moral support. I also thank my **mother-in-law (Mrs.Shatakshi) and father-in-law (Mr.Vijay Kumar)** for supporting me throughout this journey and for standing by me in all my moments of happiness and sadness. I am also thankful to my little cute nephews **Prishu** and **Madhav** for being a stress buster for me as by seeing their faces I forgot my all worries and feel so relax.*

I would like to thank all those who have contributed to my work in some or the other way.

Last but not the least, I place a deep sense of gratitude to God, the Almighty for every blessing he has showered on me and giving me the patience and courage for this journey.

Anjana Sharma

Abbreviations

3D	*Three dimensional*
BSA	*Bovine serum albumin*
CBN	*Carbon nanomaterials*
CDs	*Carbon dots*
CEA	*Chick embryo assay*
CNTs	*Carbon nanotubes*
CurCD	*Curcumin carbon dot*
DMEM	*Dulbecco's modified eagle medium*
DMF	*Dimethyl formamide*
DMSO	*Dimethyl sulphoxide*
DNA	*Deoxy ribo nucleic acid*
DPBS	*Dulbecco's phosphate buffered saline*
DWNTS	*Double walled nanotubes*
EC	*Endothelial cells*
FACS	*Fluorescence-activated cell sorting*
FBS	*Foetal bovine serum*
FDA	*Fluorescein diacetate*
FESEM	*Field emission scanning electron microscopy*
FGF	*Fibroblast growth factor*
FTIR	*Fourier Transform Infrared Spectroscopy*

GBM	*Glioblastoma multiforme*
GO	*Graphene oxide*
GQDs	*Graphene quantum dots*
HDF	*Human dermal fibroblasts*
MMP-2	*Matrix metallopeptidase 2*
MTT -	*(4,5-dimethylthiazol-2-yl)-2,5-diphenyl-2H-tetrazolium bromide*
MWNTS	*Multi walled nanotubes*
PBS	*Phosphate buffered saline*
PDGF	*Platelet derived growth factor*
PENG	*Piezoelectric nanogenerator*
PI	*Propidium iodide*
PL	*Photoluminescence*
PVDF	*Polyvinylidene fluoride*
ROS	*Reactive oxygen species*
SEM	*Scanning electron microscopy*
SWNTs	*Single walled nanotubes*
TENG	*Triboelectric nanogenerator*
TGF-β	*Transforming growth factor-β*

Table of Contents

LIST OF FIGURES

Abstract

In the present era where scientific technology is growing and developing at an enormous pace, nanoscience provides innumerable opportunities in material engineering. Nanomaterial science involves the study of structures in which atleast one of the dimensions is in the nano size range. Carbon nanomaterial (CBN) is an important member in the field of material sciences and continues to be an area of interest for the scientists in the field of electronics, optical and biomedical sciences. The exceptionally good physicochemical properties, durability and sensitivity of CBN has been explored in various healthcare applications.

Because of novel optical and electronic properties and their ease of functionalization, carbon nanostructures are expected to be used in several biomedical applications such as nanoelectronics, live cell imaging, drug delivery, theranostics, tissue engineering and drug delivery. Realizing the enormous potential of carbon-based nanomaterials nanomaterials for their applications in the field of medicine, I synthesized different carbon nanomaterials and established their activity in cancer theanostics and wound healing dressings.

In the present study, my focus will be on the development of two types of carbon nanomaterials i.e carbon dots and graphene nanohybrid composites and exhibiting its application in healthcare. The first part of the thesis focuses on the synthesis, characterization and biomedical application of carbon dots. In the first study, I explored the possibility of overcoming some of the limitations of natural compounds in bio-medical applications. I had used curcumin as a model, as the molecule, despite its well-known therapeutic activity, has limited clinical application in view of poor solubility and low bioavailability. The curcumin derived carbon dots (CurCD) were synthesized with curcumin, with ethylenediamine, as a nitrogen source. The CurCD was superior to curcumin in terms of improved solubility, photostability and fluorescent properties, while the anti-cancer activity of CurCD was comparable to curcumin.

The strategy of converting phytopigments into carbon dots in order to improve their physicochemical properties can be used for the compounds whose usage is limited otherwise.

In another study, we established the wound healing activity of CurCD. To enable its sustained release at the wound site, it was incorporated as a cross-linker in a protease responsive hydrogel dressing. The hydrogel had shown excellent antibacterial efficiency and the rate of wound was faster than curcumin alone.

Carbon dots are being explored extensively for drug delivery applications. However, there is limited information available about their interaction with different systems of the body. In most applications, the carbon dots are administered into the biological system by an intravenous route where they interact with endothelial cells. To evaluate the effect of carbon dots on endothelial system, we used carbon dots synthesised from the commonly used precursors (citric acid/urea). The as-synthesised carbon dots exhibited pro-angiogenic activity both in the *in-vitro* and *ex-vivo* angiogenesis model. As the endothelial cells are the first line of contact for intravenously administered carbon dots, its pro-angiogenic activity might be detrimental to anti-cancer therapies. Our studies suggest the importance of evaluating the response of multiple cells that might come in contact with the carbon nano materials.

The second part of the thesis focuses on one of the most important and less explored applications of carbon nanomaterials which is its conductivity. As carbon nanomaterials have excellent electrical conductivity, I utilized this feature to develop a self-powered, user-friendly and wearable device using carbonised nanomaterials for the healing of chronic wounds. In this application, carbonised polydopamine (CPDA) was used to assign conductivity to the hydrogel. As the structure of CPDA was similar to graphitic sheets, it was used as a conductive material in the hydrogel. The hydrogel was fabricated in close proximity to PVDF membrane to serve as a piezo-responsive triboelectric nanogenerator (PTENG) for providing electrical

stimulation to the underlying wound bed. The fabricated wound dressing was evaluated for its ability to support various phases of wound healing using in vitro and in vivo wound model.

To summarise, I have been able to synthesize and explore the bioactivity of carbon-based nanomaterials for healthcare applications. Provided the easy method of synthesis, biocompatibility and non-toxic nature of these synthesised materials, I propose that these nanostructures hold great promise in the field of medicine. Based on the above studies it was inferred that the developed different carbon-based smart nanomaterials hold a bright future for healthcare applications, further studies are needed to be carried out with higher animal models.

Chapter 1A: Introduction

1.1 Carbon Nanomaterials

Nanoscience is defined as the study of materials at the nanoscale and nanotechnology involves the development of technologies using such materials [1]. Among the crucial domains in this field is the carbon nanomaterials as they possess some exceptionally unique features, such as attractive photo-physical properties, conductive nature, high mechanical strength and ease of functionalization [2-4]. These unique features offer an added advantage for the use of these materials in a myriad of applications and cover most of the scientific fields, including engineering, chemistry and medicine [5-7]. Apart from the existing extensive literature on carbon nanomaterials, it continues to be a topic of interest for research. These nanomaterials are synthesized chiefly via two approaches, i.e., top down and bottom up [8]. Top-down approaches are simple and mainly comprise the removal/breakage of bulk materials to fabricate the desired structure with optimum features. The biggest problem with this approach is the imperfect surface structure [9]. On the contrary, bottom-up approach refers to the synthesis of nanomaterial from scratch, assembling it atom by atom, molecule by molecule or cluster by cluster. Bottom-up approaches result in materials with desired size and structure, but many of these processes are expensive and still in the developmental stage [10].

The utilization of carbon nanomaterials in biological applications is tremendously affecting the field of biotechnology. Carbon nanomaterials are being used for the development of highly sensitive biosensors with high selectivity and a versatile detection range [11]. To exploit the carbon nanomaterials effectively for biological applications, it is crucial to optimize their size, shape, morphology and surface modifications [12]. Such optimized carbon nanomaterials can be highly stable, biocompatible and selective in nature. Our present understanding suggests that carbon nanomaterials are potential candidates for biological applications [13-16].

1.2 Classification of carbon nanomaterials

Carbon is one of the few elements in the periodic table that possess the ability to polymerize and leads to the formation of carbon allotropes [17]. This property of carbon atoms can be attributed to its special electronic configuration and smaller size as compared with other elements in the same group [18]. The phenomenon of allotropy is responsible for the formation of different carbon-based nanomaterials, like graphene, carbon nanotubes, carbon dots, graphene quantum dots, conductive polymers and metal oxides [19], as shown in Figure. 1.1. Among all the different carbon-based nanomaterials, in this thesis I will be focussing primarily on carbon dots and conducting carbon nanomaterial-based nanocomposites.

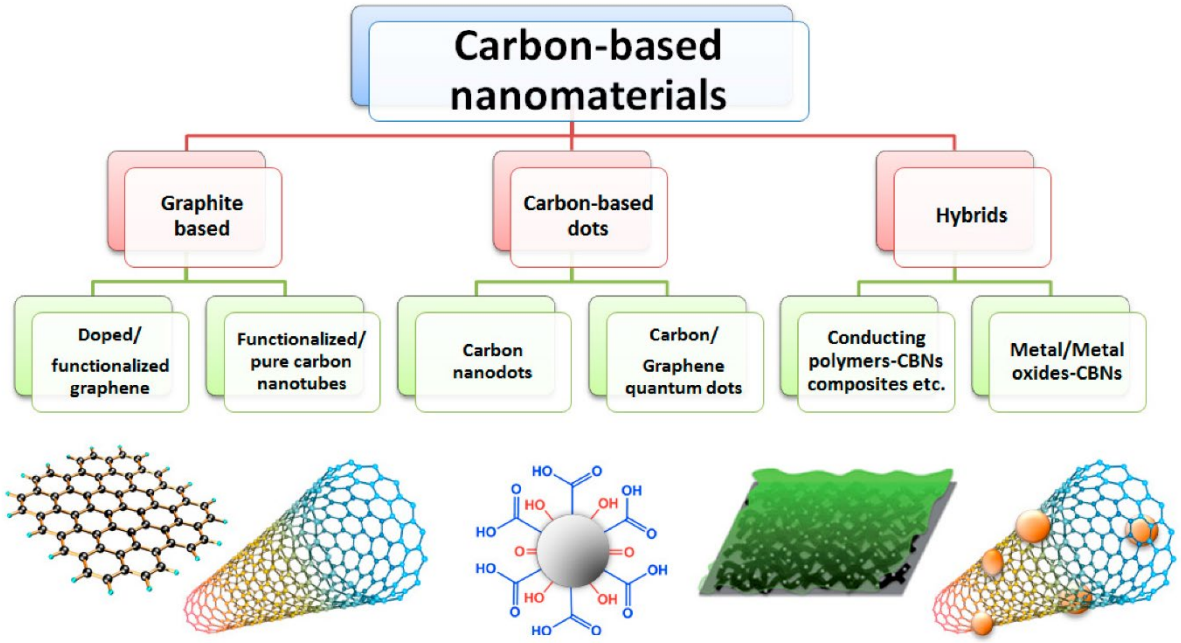

Figure 1.1: Classification of carbon nanomaterials

1.2.1 Carbon nanodots

Carbon nanodots or carbon dots belong to a novel class of carbon nanomaterials with a size range of <10 nm [20]. Originally, carbon is black in colour (non-fluorescent) and has very low

water solubility [21]. However, carbon dots are highly fluorescent in nature and have excellent water solubility; hence, they are termed as fluorescent carbon [22]. Carbon dots were discovered during the purification of carbon nanotubes using electrophoresis in 2004 [23]. Since then, they have received significant attention in the field of biological and chemical applications because of their economical and simple synthetic approaches, highly tunable photoluminescence, excellent water solubility and biocompatible nature [24]. The favourable features of carbon dots that are conducive for their usage in the biomedical field are shown in Figure. 1.2.

Figure 1.2: Characteristic features of carbon nanodots

Carbon dots can be synthesised from various precursors of chemical and biological origin, such as citric acid [25], glucose [26], plant-derived molecules [27], urine [28], nails [29] and glycerol etc. [30]. Processes used for the synthesis of fluorescent carbon dots include solvothermal [31], hydrothermal [32], carbonization [33], ultrasonication [34] and laser

ablation methods [35]. The synthesis of carbon dots with a uniform size distribution is quite challenging. However, it is crucial to control the dimensions of the carbon dots during the synthesis to attain desirable properties. The fluorescent property and toxicity profile of the carbon dots are highly dependent on their size, which plays a pivotal role in their biological applications, especially *in vivo* [36-38]. Carbon dots are being used in different scientific fields, such as photocatalytic reactions [39], theranostics [40], drug delivery systems [41], bioimaging [42], biosensing [43] and photodynamic therapy for cancer [44]. In the past few decades, there has been massive research interest in carbon nanodots because of their unique and exceptional properties, which continue to be explored.

1.2.2 Conductive carbon nanomaterial composites

Conducting polymers have attracted great interest among the global scientific community as a novel class of electronic materials [45]. Conductive polymers are being exploited for the development and fabrication of several electronic devices [46], artificial muscles or skin [47], sensors [48], solar energy conversion devices [49], etc. Most of the polymers are fundamentally electronic insulators in nature, except a few which are able to conduct electricity in their native state [50]. For the past few decades, scientists have been trying to improve the conduction of polymers by imparting electronic properties with the aid of conductive materials, such as carbon nanotubes [51], metal nanoparticles [52] and carbon fibres [53]. Owing to the advent of nanotechnology in the field of materials science and engineering, nanocluster-based nanocomposites came into existence. Nanocomposites are special materials that are derived from the amalgamation of nano range particles under optimized experimental conditions [54]. These nanocomposites possess reinforced properties and are being utilized in different scientific fields across the globe as shown in Figure 1.3.

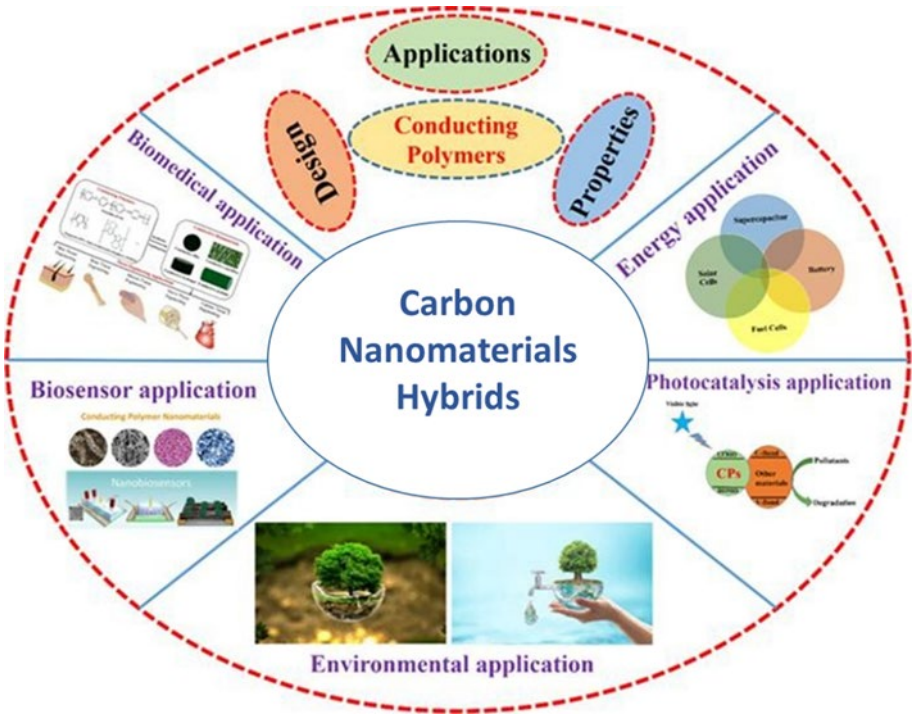

Figure 1.3: Overview of carbon nanomaterials hybrids

1.3 Synthesis of carbon nanomaterials

For the synthesis of carbon nanomaterials, two types of approaches are used name as top down and bottom-up approach [55]. In top-down method, bulk carbon source is broken down into nano dimensional particles by the means of external source of energy. On the other hand, bottom-up approach involves the self-assembling of small molecules to form a nano range particle by means of physical or chemical interactions [56]. Nowadays, as carbon nanomaterials are gaining significant amount of attention in the biomedical field, the need of facile and economic synthesis methods has aroused. The type of process used for the synthesis of nanomaterial defines the size and physicochemical properties of these materials. The growth of carbon nanomaterials usually influenced by the type of precursor and temperature used for the synthesis [57]. An elaborative summary on the synthesis methods of all types of carbon nanomaterials is considered to be out of scope of the introductory chapter of this thesis. Therefore, for the sake of better understanding, I will mainly focus on the synthesis methods of carbon dots. However, the synthesis strategies of all carbon nanomaterials share almost

similar approaches like pyrolysis, laser ablation, chemical vapour deposition, microwave synthesis, hydrothermal/solvothermal and arc discharge methods.

1.3.1 Carbon dot synthesis

In the past decade, numerous strategies have been applied to synthesize carbon dots with desirable features required for targeted application [58]. Like for synthesis of other nanomaterials, synthesis approaches for carbon dots are also classified into two broad categories, top down and bottom-up approach. Methods like laser ablation, arc discharge, chemical exfoliation falls under the category of top-down synthetic methods. On the contrary, bottom-up synthesis involves the self-assembling of smaller molecules into the desired carbon nanostructures. This approach includes four phases in the carbon dot formation, namely condensation, polymerization, carbonization and passivation. In the further sections, I will be discussing these methods in detail.

(a) Arc discharge method: The fabrication of CDs by arc discharge method was discovered in 2004 [23]. Xu *et al.* while making single walled carbon nanotubes via arc discharge method accidently found three kinds of carbon-based nanoparticles with different fluorescence properties. In this method, bulk carbon electrodes are vaporised with the help of arc discharge at a very high temperature, which leads to the production of high energy plasma. Carbon soot formed on the opposite electrode contains carbon dots [59]. The yield of carbon dots obtained via this method is very low and often results in the production of other impurities which are difficult to remove.

(b) Laser ablation method: In this method, high energy nanosecond laser impulses are used to illuminate the surface of a bulk carbon material, which leads to a thermodynamic phase in which extremely high temperature and pressure are produced [60]. As a result, the bulk carbon material gets evaporated to state of plasma and slowly cools down to form carbon dots. Li *et al.* demonstrated a simple strategy for the synthesis of CDs with tunable fluorescence via

laser ablation of carbon source dispersed in different organic solvents [61]. Carbon dots obtained by this approach are uniform in size, aqueous soluble and highly fluorescent in nature. However, the only drawback associated with this method which limits its application is complicated process and high cost.

(c) Hydrothermal/solvothermal synthesis: The most common and inexpensive method for the fabrication of carbon dots is the hydrothermal synthesis. Organic polymers or small molecules are dissolved in a solvent (aqueous/organic) to constitute a reaction mixture, which is then shifted to an autoclave. At a high temperature, these carbon molecules merge to form seeding carbon cores and slowly grow into carbon dots having a size of <10 nm [62]. Sharma *et al*. has shown that inner structure of CDs obtained by hydrothermal condensation can be tailored by using biomolecules enriched in carbon and nitrogen source [63]. Ease of synthesis and controllable doping with heteroatoms make this approach popular and reliable for the fabrication of carbon dots.

(d) Microwave synthesis: Among all the available bottom-up approaches, microwave synthesis is the one that has been employed commercially. In this method, carbon dots are produced by irradiating the reaction mixture containing precursor molecules with the aid of electromagnetic radiations. It is an easy, cheap and eco-friendly method for the synthesis of carbon dots rich in oxygen-containing functionalities [64]. Zhu *et al* synthesised a carbon dot by heating a solution containing polyethylene glycol and a sugar moiety in a microwave oven. The as synthesized CDs has shown an excitation-dependent fluorescence properties due to the presence of multiple emissive sites [65].

(e) Carbonization synthesis: The process of carbonization involves the prolonged pyrolysis of organic precursor molecules to form solid residual mixtures with a high carbon content. It is one of the superior, inexpensive, straightforward and ultra-fast methods to synthesise carbon dots of a uniform size [66].

(f) Acidic oxidation: Acid oxidation involves the exfoliation and decomposition of bulk carbon precursor into carbon dots with hydroxyl and carboxyl groups as functional moieties on the surface. Introduction of hydrophilic functional moieties on the surface of as synthesises carbon dots improvise its water solubility and fluorescence properties [67]. Yang *et al.* has demonstrated a scale up method for the synthesis of doped CDs by acidic oxidation which followed by hydrothermal reaction to reduce the size of the carbon dots [68].

1.4 Biomedical applications of carbon nanomaterials

Carbon nanomaterials have gained acclaim as a critical member in the field of nanomaterial-based technology. Different allotropes of carbon exhibit versatile features and have been used in several biological applications, including drug delivery, theranostics, cancer therapy, tissue regeneration and bioimaging.

1.4.1 Bioimaging

In the field of fluorescence and multimodal bioimaging, carbon nanomaterials have gained extensive attention due to their unique properties like tunable photoluminescence, water soluble nature, excellent biocompatibility and resistance to photo bleaching. Application of carbon nanomaterials in respective bioimaging is tabulated below:

Sr.No	Carbon nanomaterial	Bioimaging agent	Application	Ref
1.	SWCNTs	Labelled recombinant thermo-stable *Luciola cruciata* luciferase (LcL)	*In vivo* imaging	[70]
2.	Carbon dots	Pyrolysis of sucrose and oleic acid shows strong fluorescence and quantum yield.	*In vitro* cell imaging	[71]
3.	Fullerenes	Fluorescent fullerene-coated mesoporous silica nanoparticles.	*In vitro* bioimaging and pH-responsive drug release.	[72]

Sr.No	Carbon nanomaterial	Bioimaging agent	Application	Ref
4.	SWCNTs	Radical polymer grafted SWCNT shown brighter emission	Bio-imaging and biosensing in vivo in near-infrared region.	[73]
5.	Graphene oxide	GO nanosheets implanted with aptamer-labelled CdSe@ZnS QDs	Bio-imaging and cell-targeted drug delivery.	[74]
6.	MWCNTs	Conjugated MWCNTs with polyelectrolytes	In vitro & in vivo bioimaging	[75]
7.	Carbon dots	Folic acid modified carbon dots	Selective detection of cancer cells from normal one	[76]
8.	Carbon dots	Carboxylic acid functionalised CD	DNA detection for disease diagnosis	[77]
9.	Graphene oxide	GO@Ag nanocomposite	MRI contrast agent	[78]
10.	GQDs	Hyaluronic acid conjugated GQD	CD 44 targeted imaging	[79]

Table 1: Carbon nanomaterials as bioimaging agents

1.4.2 Drug delivery and cancer therapy

The efficacy of a drug highly depends upon its biodistribution, pharmacokinetics and excretion from the body. As the dimensions of carbon nanomaterials are very much similar to biological structures, they have become an attractive choice for drug delivery devices. Carbon nanostructures are easy to functionalize, they can be conjugated with anticancer drugs, antibodies or other kind of therapeutic agents, some them are summarized in table below.

Sr.No	Carbon nanomaterial	Therapeutic agent	Targeted disease	Ref
1.	Fullerenes	Tamoxifen	Breast cancer	[80]
2.	Carbon nanotubes	Metformin	Diabetes	[81]
3.	Graphene oxide	Paclitaxel	Lung cancer	[82]

Sr.No	Carbon nanomaterial	Therapeutic agent	Targeted disease	Ref
3.	Graphene oxide	Paclitaxel	Lung cancer	[82]
4.	Diamonds	Doxorubicin	Breast cancer	[83]
5.	Multiwall carbon nanotubes	Diltiazem hydrochloride	Angina pectoris	[84]
6.	Nano graphene oxide (NGO)	NGO conjugated with ICG	Enhanced antiviral activity against *E. faecalis*	[85]
7.	Single walled carbon nanotubes (SWCNTs)	SWCNTs coated with Fe3O4 and Dox loaded CQDs	Multifunctional delivery system for cancer treatment	[86]
8.	Carbon silica nanoparticles (CSN)	CSN as immunoadjuvant and PDT agent	Photothermal &photodynamic agent for tumor therapy	[87]
9.	Carbon dots	Dox conjugated CDs	Selected killing of liver cancer cells	[88]
10.	Fullerenes	Dox conjugated fullerenes	On-off drug delivery system for anticancer therapy	[89]

Table 2: Carbon nanomaterials as therapeutic agents

1.4.3 Biosensing applications

Carbon nanomaterials are being used substantially for the fabrication of biosensors because of the low cost, small background signal and capability of surface regeneration. These carbon-based nanomaterials allow direct coupling of biomolecules on their surface and exhibits highly reproducible electrochemical behaviour. Applications of carbon nanomaterials are tabulated below

Sr.No	Carbon nanomaterial	Biosensors	Targeted analyst	Ref
1.	Single walled carbon nanotubes	Conjugated aptamer-anchor polynucleotide sequence	Estimation of real time protein efflux from single cell organism	[90]
2.	Multi walled carbon nanotubes	CNT resistors.	Detection of Arginase 1	[91]
3.	Ag-Pt carbon nanofibres	Modified carbon electrode for dopamine detection.	Dopamine	[92]
4.	Carboxyl functionalised graphene oxide	HRP labelled carboxyl functionalised graphene oxide with glassy carbon electrode	Highly sensitive DNA detection with ranges between 1×10^{-6} and 1×10^{-14}.	[93]
5.	Graphene	Graphene-bismuth nanocomposite with immobilised glucose oxidase	Detection of glucose	[94]
6.	Graphene quantum dots	aptamers/DNAzyme-GQDs-carbon fiber composite	Lysozyme detection	[95]
7.	Multi walled carbon nanotubes	Modified MWCNTs with cholesterol esterase, oxidase and peroxidase	Cholesterol detection in blood	[96]
8.	Carbon dots	Tyrosinase conjugated CDs	Levodopa detection	[97]
9.	Reduced graphene oxide QDs	rGO/QDs ZnO nanofibres	Hydrogen peroxide detection	[98]
10.	Graphene quantum dots	GQD modified ceramic electrode	Detection of blood glucose.	[99]

Table 3: Carbon nanomaterials as biosensors

1.4.4 Tissue engineering applications

Carbon nanomaterials have shown great potential in the field of tissue engineering to develop biomimetic scaffolds for the replacement of whole or a part of tissue [100]. A good scaffold should have a physical structure and chemical composition similar to inherent extracellular matrix. Carbon nanomaterials serves as a reinforcing material in the fabrication of tissue

scaffolds because of their excellent mechanical properties. In addition to mechanical strength, carbon nanomaterials can also provide electric stimulation to the scaffolds which aids in tissue regeneration [101]. Several carbon nanomaterials based artificial scaffolds are developed for tissue regeneration therapy, some of them are summarised below.

Sr.No	Carbon nanomaterial	Artificial Scaffold	Application	Ref
1.	Carbon nanotubes	Hydrazide functionalised carbon nanotubes	Improved cardiac tissue engineering	[102]
2.	Nanodiamond	Poly lactic acid and octadecylamine functionalised nanodiamond	Serves as a component for bone scaffolds and surgical tool in regenerative therapy	[103]
3.	Carbon dots	CD-nanofiber nanocomposite	Guided cell growth and enhanced cellular activity	[104]
4.	Graphene nanosheets	Gelatin and bioactive glass scaffold	Enhanced biocompatibility and mechanical strength	[105]
5.	Carbon nanotubes	Chitosan/CNTs mesh	Supports cell recolonization	[106]
6.	Graphene oxide (GO)	Nano hydroxyapatite/GO composites	Improved viability and proliferation of MG-63 cells for 14 days	[107]
7.	Multi walled carbon nanotubes (MWCNTs)	Amine functionalised MWCNTs	Enhanced neuronal differentiation	[108]
8.	Carbon quantum dots (CQD)	P-phenylenediamine functionalised CQDs	Enhanced viability and metabolic activity of cardiac myocytes	[109]

9.	Reduced graphene oxide (rGO)	3D scaffold containing rGO	Bone tissue engineering	[110]
10.	Single walled carbon nanotubes (SWCNTs)	Amine functionalised SWCNTs	Enhanced proliferation and differentiation of rat BMSCs	[111]

Table 4: Applications of carbon nanomaterials in tissue regeneration

Chapter 1B: Thesis motivation

Motivation: With the advent of nanotechnology, it is now possible to design versatile materials for biomedical applications. Example of one such inimitable material is carbon dots. Ever since the serendipitous invention of carbon dots, it has gained considerable amount of attention. Some of its unique characteristics like smaller size, excellent fluorescence properties and water solubility makes it a unique material for healthcare applications like bioimaging, tissue regeneration, biosensing and drug delivery systems.

Since most of the carbon dots are reported for their excellent physical or optical properties, very few reports have been present in the literature about the therapeutic potential of carbon dots. It has been observed that selection of precursor molecule plays an important role in deciding the biological properties of carbon dots. Carbon dots synthesised from natural precursors especially plant-based, possess some inherent therapeutic properties [112]. Gopinath *et al* synthesised a highly specific carbon dots from *Catharanthus roseus* with inherent potential to bind to microtubules of cancer cells and destroy them [113].

Curcumin ((1,7-bis(4-hydroxy-3-methoxyphenyl)–1, 6-heptadiene3,5-dione), a phytopigment is derived from the rhizomes of *Curcuma longa* (Turmeric) [114]. Turmeric has a long history of being used in the Ayurveda for the treatment of several diseases. Research has demonstrated that curcumin is beneficial in the treatment of health disorders like impaired wound healing, cancer, alzheimer, arthritis etc., and most of these therapeutic effects are due to the anti-inflammatory, chemopreventive, antioxidant and chemotherapeutic activities. Despite of its numerous health benefits, the usage of curcumin in clinical scenario is limited because of some the drawbacks like poor solubility profile, rapid metabolism and low bioavailability. Multiple strategies are being tested to overcome these limitations which comprises of developing curcumin nanoformulations [115], synthesising curcumin analogs [116] and functionalisation of curcumin [117] with different moieties. Recently, Lin, Chin-Jung et al has demonstrated the amplified anti-viral activity of curcumin carbon dots obtained by the calcination of curcumin

molecule at very high temperature [118]. On the basis of above-mentioned studies, I hypothesised that the carbon dots of curcumin may be able to exhibit desirable biological activities, while overcoming some of the limitations exhibited by curcumin.

Objective of thesis: In the present thesis, the advancement of nanotechnology in the field of medicine was explored by targeting the bioactive molecules obtained from natural sources like plants. The limitation of such molecules may be overcome by converting them into carbonised materials for example carbon dots while they retain their inherent therapeutic activity.

1. Synthesis and characterization of curcumin derived carbon dots (CurCD) for anticancer appplications.
2. Development of CurCD crosslinked and protease responsive hydrogels for wound healing applications.
3. Evaluating the interaction of endothelial cells with carbon dot derived from citric acid and urea.
4. Fabrication of a piezo responsive bioelectronics device using PVDF and graphitic sheets for the treatment of chronic wounds like diabetic foot ulcers.

First Chapter focus on the introduction of carbon nanomaterials, their synthesis methods and biomedical applications.

Second chapter of the thesis deals with the exploration of biological response of carbon dots synthesised by solvothermal process from the well-known phytopigment curcumin. The clinical potential of curcumin is being hindered by some of the drawbacks like low aqueous solubility, high photosensitivity and low bioavailability. Carbon dots derived from curcumin were synthesized and its physical, chemical and anti-cancer activity was compared to the parent molecule, curcumin.

Third chapter focuses on the wound healing activity of the curcumin-derived carbon dots. As the carbon dots are very small (4 nm), the carbon dots may be excreted from the in vivo system at a very fast rate. To overcome this limitation, I had developed a protease responsive delivery system. Curcumin carbon dots loaded hydrogels were fabricated and wound healing response was evaluated using *in vitro* and *in vivo* models.

Fourth chapter of the thesis deals with the investigation of interactions between the carbon dots and endothelial system by exploring the most commonly reported carbon dot (synthesised from citric acid and urea). Using both in vitro and in vivo studies, I had evaluated the angiogenic response.

Fifth chapter comprises of fabrication of piezo driven nanogenerator and conductive hydrogel nanocomposite wound dressing. Whereas carbon nanomaterials are explored in bioimaging and drug delivery applications, its application on the basis of its conductive properties has not been evaluated in health care applications. In recent years, the development of portable, human-friendly, wearable electronic devices such as triboelectric and piezoelectric nanogenerators (TENG and PENG) is attracting tremendous attention due to their self-powered functionality. In this chapter I developed a hydrogel containing carbonised polydopamine. On the basis of the favourable conductivity, the hydrogel was used in conjunction with a piezo responsive PVDF membrane. The composite device provided electrical stimulation to the underlying wound, through a piezo-responsive triboelectric nanogenerator. The composite dressing was evaluated for its physical, mechanical, electrical and wound healing properties using appropriate models.

Bibliography

1. Bayda, S., Adeel, M., Tuccinardi, T., Cordani, M. and Rizzolio, F., 2019. The history of nanoscience and nanotechnology: from chemical–physical applications to nanomedicine. Molecules, 25(1), p.112.

2. Speranza, G., 2021. Carbon nanomaterials: Synthesis, functionalization and sensing applications. Nanomaterials, 11(4), p.967.

3. Papageorgiou, D.G., Kinloch, I.A. and Young, R.J., 2017. Mechanical properties of graphene and graphene-based nanocomposites. Progress in Materials Science, 90, pp.75-127.

4. Baig, N., Kammakakam, I. and Falath, W., 2021. Nanomaterials: A review of synthesis methods, properties, recent progress, and challenges. Materials Advances, 2(6), pp.1821-1871.

5. Sarkar, P., Ghosal, K., Chakraborty, D. and Sarkar, K., 2021. Biocompatibility and biomedical applications of various carbon-based materials. In Handbook of Carbon-Based Nanomaterials (pp. 829-875). Elsevier.

6. Tambe, P., Mane, S., Chaudhari, B.P. and Kulabhusan, P.K., 2022. Carbon nanomaterials for therapeutic applications. In Fundamentals of Bionanomaterials (pp. 293-325). Elsevier.

7. Power, A.C., Gorey, B., Chandra, S. and Chapman, J., 2018. Carbon nanomaterials and their application to electrochemical sensors: a review. Nanotechnology Reviews, 7(1), pp.19-41.

8. Baig, N., Kammakakam, I. and Falath, W., 2021. Nanomaterials: A review of synthesis methods, properties, recent progress, and challenges. Materials Advances, 2(6), pp.1821-1871.

9. Ramanathan, S., Gopinath, S.C., Arshad, M.M., Poopalan, P. and Perumal, V., 2021. Nanoparticle synthetic methods: strength and limitations. In Nanoparticles in Analytical and Medical Devices (pp. 31-43). Elsevier.

10. Patil, S. and Chandrasekaran, R., 2020. Biogenic nanoparticles: A comprehensive perspective in synthesis, characterization, application and its challenges. Journal of Genetic Engineering and Biotechnology, 18(1), pp.1-23.

11. Hwang, H.S., Jeong, J.W., Kim, Y.A. and Chang, M., 2020. Carbon nanomaterials as versatile platforms for biosensing applications. Micromachines, 11(9), p.814.

12. Khan, I., Saeed, K. and Khan, I., 2019. Nanoparticles: Properties, applications and toxicities. Arabian journal of chemistry, 12(7), pp.908-931.

13. Rauti, R., Musto, M., Bosi, S., Prato, M. and Ballerini, L., 2019. Properties and behavior of carbon nanomaterials when interfacing neuronal cells: How far have we come? Carbon, 143, pp.430-446.

14. Bhong, S.Y., More, N., Choppadandi, M. and Kapusetti, G., 2019. Review on carbon nanomaterials as typical candidates for orthopaedic coatings. SN Applied Sciences, 1(1), pp.1-16

15. Liu, W. and Speranza, G., 2019. Functionalization of carbon nanomaterials for biomedical applications. C, 5(4), p.72.

16. Liu, J., Li, R. and Yang, B., 2020. Carbon dots: A new type of carbon-based nanomaterial with wide applications. ACS Central Science, 6(12), pp.2179-2195.

17. Tiwari, S.K., Kumar, V., Huczko, A., Oraon, R., Adhikari, A.D. and Nayak, G.C., 2016. Magical allotropes of carbon: prospects and applications. Critical Reviews in Solid State and Materials Sciences, 41(4), pp.257-317.

18. More, R.B., Haubold, A.D. and Bokros, J.C., 2004. Pyrolytic carbon for long-term medical implants, in "Biomaterials science: an introduction to materials in medicine" BD Ratner, AS Hoffmann, FJ. Schoen, Editors.

19. Georgakilas, V., Perman, J.A., Tucek, J. and Zboril, R., 2015. Broad family of carbon nanoallotropes: classification, chemistry, and applications of fullerenes, carbon dots, nanotubes, graphene, nanodiamonds, and combined superstructures. Chemical reviews, 115(11), pp.4744-4822.

20. Sharma, A., Panwar, V., Chopra, V., Thomas, J., Kaushik, S. and Ghosh, D., 2019. Interaction of carbon dots with endothelial cells: implications for biomedical applications. ACS Applied Nano Materials, 2(9), pp.5483-5491.

21. Ray, S.C., Saha, A., Jana, N.R. and Sarkar, R., 2009. Fluorescent carbon nanoparticles: synthesis, characterization, and bioimaging application. The Journal of Physical Chemistry C, 113(43), pp.18546-18551.

22. Zuo, J., Jiang, T., Zhao, X., Xiong, X., Xiao, S. and Zhu, Z., 2015. Preparation and application of fluorescent carbon dots. Journal of Nanomaterials, 2015.

23. Xu, X., Ray, R., Gu, Y., Ploehn, H.J., Gearheart, L., Raker, K. and Scrivens, W.A., 2004. Electrophoretic analysis and purification of fluorescent single-walled carbon nanotube fragments. Journal of the American Chemical Society, 126(40), pp.12736-12737.

24. Sharma, A., Panwar, V., Thomas, J., Chopra, V., Roy, H.S. and Ghosh, D., 2021. Actin-binding carbon dots selectively target glioblastoma cells while sparing normal cells. Colloids and Surfaces B: Biointerfaces, 200, p.111572.

25. Chahal, S., Yousefi, N. and Tufenkji, N., 2020. Green synthesis of high quantum yield carbon dots from phenylalanine and citric acid: Role of stoichiometry and nitrogen doping. ACS Sustainable Chemistry & Engineering, 8(14), pp.5566-5575.

26. Javed, M., Saqib, A.N.S., Ali, B., Faizan, M., Anang, D.A., Iqbal, Z. and Abbas, S.M., 2019. Carbon quantum dots from glucose oxidation as a highly competent anode material for lithium and sodium-ion batteries. Electrochimica Acta, 297, pp.250-257.

27. Naik, G.G., Alam, M.B., Pandey, V., Dubey, P.K., Parmar, A.S. and Sahu, A.N., 2020. Pink fluorescent carbon dots derived from the phytomedicine for breast cancer cell imaging. ChemistrySelect, 5(23), pp.6954-6960.

28. Essner, J.B., Laber, C.H., Ravula, S., Polo-Parada, L. and Baker, G.A., 2016. Pee-dots: biocompatible fluorescent carbon dots derived from the upcycling of urine. Green Chemistry, 18(1), pp.243-250.

29. Chatzimitakos, T., Kasouni, A., Sygellou, L., Leonardos, I., Troganis, A. and Stalikas, C., 2018. Human fingernails as an intriguing precursor for the synthesis of nitrogen and sulfur-doped carbon dots with strong fluorescent properties: analytical and bioimaging applications. Sensors and Actuators B: Chemical, 267, pp.494-501.

30. Lai, C.W., Hsiao, Y.H., Peng, Y.K. and Chou, P.T., 2012. Facile synthesis of highly emissive carbon dots from pyrolysis of glycerol; gram scale production of carbon dots/mSiO 2 for cell imaging and drug release. Journal of Materials Chemistry, 22(29), pp.14403-14409.

31. Zhao, D., Liu, X., Wei, C., Qu, Y., Xiao, X. and Cheng, H., 2019. One-step synthesis of red-emitting carbon dots via a solvothermal method and its application in the detection of methylene blue. RSC advances, 9(51), pp.29533-29540.

32. Wang, C., Xu, Z., Cheng, H., Lin, H., Humphrey, M.G. and Zhang, C., 2015. A hydrothermal route to water-stable luminescent carbon dots as nanosensors for pH and temperature. Carbon, 82, pp.87-95.

33. Xia, C., Zhu, S., Feng, T., Yang, M. and Yang, B., 2019. Evolution and synthesis of carbon dots: from carbon dots to carbonized polymer dots. Advanced Science, 6(23), p.1901316.

34. Preethi, M., Viswanathan, C. and Ponpandian, N., 2022. A metal-free, dual catalyst for the removal of Rhodamine B using novel carbon quantum dots from muskmelon peel under sunlight and ultrasonication: A green way to clean the environment. Journal of Photochemistry and Photobiology A: Chemistry, 426, p.113765.

35. Gonçalves, H., Jorge, P.A., Fernandes, J.R.A. and da Silva, J.C.E., 2010. Hg (II) sensing based on functionalized carbon dots obtained by direct laser ablation. Sensors and Actuators B: Chemical, 145(2), pp.702-707.

36. Esfandiari, N., Bagheri, Z., Ehtesabi, H., Fatahi, Z., Tavana, H. and Latifi, H., 2019. Effect of carbonization degree of carbon dots on cytotoxicity and photo-induced toxicity to cells. Heliyon, 5(12), p.e02940.

37. Fan, J., Claudel, M., Ronzani, C., Arezki, Y., Lebeau, L. and Pons, F., 2019. Physicochemical characteristics that affect carbon dot safety: Lessons from a comprehensive study on a nanoparticle library. International Journal of Pharmaceutics, 569, p.118521.

38. Havrdova, M., Hola, K., Skopalik, J., Tomankova, K., Petr, M., Cepe, K., Polakova, K., Tucek, J., Bourlinos, A.B. and Zboril, R., 2016. Toxicity of carbon dots–Effect of surface functionalization on the cell viability, reactive oxygen species generation and cell cycle. Carbon, 99, pp.238-248.

39. Zhou, Y., Zahran, E.M., Quiroga, B.A., Perez, J., Mintz, K.J., Peng, Z., Liyanage, P.Y., Pandey, R.R., Chusuei, C.C. and Leblanc, R.M., 2019. Size-dependent photocatalytic activity of carbon dots with surface-state determined photoluminescence. Applied Catalysis B: Environmental, 248, pp.157-166.

40. Du, J., Xu, N., Fan, J., Sun, W. and Peng, X., 2019. Carbon dots for in vivo bioimaging and theranostics. Small, 15(32), p.1805087.

41. Kong, T., Hao, L., Wei, Y., Cai, X. and Zhu, B., 2018. Doxorubicin conjugated carbon dots as a drug delivery system for human breast cancer therapy. Cell proliferation, 51(5), p.e12488.

42. Li, H., Yan, X., Kong, D., Jin, R., Sun, C., Du, D., Lin, Y. and Lu, G., 2020. Recent advances in carbon dots for bioimaging applications. Nanoscale Horizons, 5(2), pp.218-234.

43. Ji, C., Zhou, Y., Leblanc, R.M. and Peng, Z., 2020. Recent developments of carbon dots in biosensing: A review. ACS sensors, 5(9), pp.2724-2741.

44. Pang, W., Jiang, P., Ding, S., Bao, Z., Wang, N., Wang, H., Qu, J., Wang, D., Gu, B. and Wei, X., 2020. Nucleolus-Targeted Photodynamic Anticancer Therapy Using Renal-Clearable Carbon Dots. Advanced healthcare materials, 9(16), p.2000607.

45. Ates, M., Karazehir, T. and Sezai Sarac, A.J.C.P.C., 2012. Conducting polymers and their applications. Current Physical Chemistry, 2(3), pp.224-240.

46. Angelopoulos, M., 2001. Conducting polymers in microelectronics. IBM Journal of Research and Development, 45(1), pp.57-75.

47. Smela, E., Inganas, O. and Lundstrom, I., 1993. Conducting polymers as artificial muscles: challenges and possibilities. Journal of Micromechanics and Microengineering, 3(4), p.203.

48. Sukeerthi, S. and Contractor, A.Q., 1994. Applications of conducting polymers as sensors.

49. Ameen, S., Akhtar, M.S., Song, M. and Shin, H.S., 2013. Metal oxide nanomaterials, conducting polymers and their nanocomposites for solar energy. Solar Cells-Research and Application Perspectives, pp.203-259.

50. Bakhshi, A.K., 1995. Electrically conducting polymers: from fundamental to applied research. Bulletin of Materials Science, 18(5), pp.469-495.

51. De Lannoy, C.F., Jassby, D., Davis, D.D. and Wiesner, M.R., 2012. A highly electrically conductive polymer–multiwalled carbon nanotube nanocomposite membrane. Journal of membrane science, 415, pp.718-724.

52. Zare, Y. and Shabani, I., 2016. Polymer/metal nanocomposites for biomedical applications. Materials Science and Engineering: C, 60, pp.195-203.

53. Feller, J.F., Linossier, I. and Grohens, Y., 2002. Conductive polymer composites: comparative study of poly (ester)-short carbon fibres and poly (epoxy)-short carbon fibres mechanical and electrical properties. Materials Letters, 57(1), pp.64-71.

54. de Oliveira, A.D. and Beatrice, C.A.G., 2018. Polymer nanocomposites with different types of nanofiller. Nanocomposites-Recent Evolutions, pp.103-104.

55. Paramasivam, G., Palem, V.V., Sundaram, T., Sundaram, V., Kishore, S.C. and Bellucci, S., 2021. Nanomaterials: Synthesis and applications in theranostics. Nanomaterials, 11(12), p.3228.

56. Biswas, A., Bayer, I.S., Biris, A.S., Wang, T., Dervishi, E. and Faupel, F., 2012. Advances in top–down and bottom–up surface nanofabrication: Techniques, applications & future prospects. Advances in colloid and interface science, 170(1-2), pp.2-27.

57. Xia, C., Zhu, S., Feng, T., Yang, M. and Yang, B., 2019. Evolution and synthesis of carbon dots: from carbon dots to carbonized polymer dots. Advanced Science, 6(23), p.1901316.

58. Khayal, A., Dawane, V., Amin, M.A., Tirth, V., Yadav, V.K., Algahtani, A., Khan, S.H., Islam, S., Yadav, K.K. and Jeon, B.H., 2021. Advances in the methods for the synthesis of carbon dots and their emerging applications. Polymers, 13(18), p.3190.

59. Chao-Mujica, F.J., Garcia-Hernández, L., Camacho-López, S., Camacho-López, M., Camacho-López, M.A., Reyes Contreras, D., Pérez-Rodríguez, A., Peña-Caravaca, J.P., Páez-Rodríguez, A., Darias-Gonzalez, J.G. and Hernandez-Tabares, L., 2021. Carbon quantum dots by submerged arc discharge in water: Synthesis, characterization, and mechanism of formation. Journal of Applied Physics, 129(16), p.163301.

60. Calabro, R.L., Yang, D.S. and Kim, D.Y., 2019. Controlled nitrogen doping of graphene quantum dots through laser ablation in aqueous solutions for photoluminescence and electrocatalytic applications. ACS Applied Nano Materials, 2(11), pp.6948-6959.

61. Li, X., Wang, H., Shimizu, Y., Pyatenko, A., Kawaguchi, K. and Koshizaki, N., 2010. Preparation of carbon quantum dots with tunable photoluminescence by rapid laser passivation in ordinary organic solvents. Chemical Communications, 47(3), pp.932-934.

62. Ye, Z., Li, G., Lei, J., Liu, M., Jin, Y. and Li, B., 2020. One-step and one-precursor hydrothermal synthesis of carbon dots with superior antibacterial activity. ACS Applied Bio Materials, 3(10), pp.7095-7102.

63. Sharma, A. and Das, J., 2019. Small molecules derived carbon dots: synthesis and applications in sensing, catalysis, imaging, and biomedicine. Journal of nanobiotechnology, 17(1), pp.1-24.

64. Jiang, K., Sun, S., Zhang, L., Lu, Y., Wu, A., Cai, C. and Lin, H., 2015. Red, green, and blue luminescence by carbon dots: full-color emission tuning and multicolor cellular imaging. Angewandte Chemie International Edition, 54(18), pp.5360-5363.

65. Stefanakis, D., Philippidis, A., Sygellou, L., Filippidis, G., Ghanotakis, D. and Anglos, D., 2014. Synthesis of fluorescent carbon dots by a microwave heating process: structural characterization and cell imaging applications. Journal of nanoparticle research, 16(10), pp.1-10.

66. Liu, X., Pang, J., Xu, F. and Zhang, X., 2016. Simple approach to synthesize amino-functionalized carbon dots by carbonization of chitosan. Scientific reports, 6(1), pp.1-8.

67. Shen, P. and Xia, Y., 2014. Synthesis-modification integration: one-step fabrication of boronic acid functionalized carbon dots for fluorescent blood sugar sensing. Analytical chemistry, 86(11), pp.5323-5329.

68. Yang, S., Sun, J., Li, X., Zhou, W., Wang, Z., He, P., Ding, G., Xie, X., Kang, Z. and Jiang, M., 2014. Large-scale fabrication of heavy doped carbon quantum dots with tunable-photoluminescence and sensitive fluorescence detection. Journal of Materials Chemistry A, 2(23), pp.8660-8667.

69. El-Sayed, R., Eita, M., Barrefelt, Å., Ye, F., Jain, H., Fares, M., Lundin, A., Crona, M., Abu-Salah, K., Muhammed, M. and Hassan, M., 2013. Thermostable luciferase from Luciola cruciate for imaging of carbon nanotubes and carbon nanotubes carrying doxorubicin using in vivo imaging system. Nano letters, 13(4), pp.1393-1398.

70. El-Sayed, R., Eita, M., Barrefelt, Å., Ye, F., Jain, H., Fares, M., Lundin, A., Crona, M., Abu-Salah, K., Muhammed, M. and Hassan, M., 2013. Thermostable luciferase from Luciola cruciate for imaging of carbon nanotubes and carbon nanotubes carrying doxorubicin using in vivo imaging system. Nano letters, 13(4), pp.1393-1398.

71. Zhang, J. and Yu, S.H., 2016. Carbon dots: large-scale synthesis, sensing and bioimaging. Materials Today, 19(7), pp.382-393.

72. Tan, L., Wu, T., Tang, Z.W., Xiao, J.Y., Zhuo, R.X., Shi, B. and Liu, C.J., 2016. Water-soluble photoluminescent fullerene capped mesoporous silica for pH-responsive drug delivery and bioimaging. Nanotechnology, 27(31), p.315104.

73. Nagai, Y., Nakamura, K., Yudasaka, M., Shiraki, T. and Fujigaya, T., 2020. Radical Polymer Grafting on the Surface of Single-Walled Carbon Nanotubes Enhances Photoluminescence in the Near-Infrared Region: Implications for Bioimaging and Biosensing. ACS Applied Nano Materials, 3(9), pp.8840-8847.

74. Wang, Y., Yao, H.B., Wang, X.H. and Yu, S.H., 2011. One-pot facile decoration of CdSe quantum dots on graphene nanosheets: novel graphene-CdSe nanocomposites with tunable fluorescent properties. Journal of Materials Chemistry, 21(2), pp.562-566.

75. Feng, G., Ding, D. and Liu, B., 2012. Fluorescence bioimaging with conjugated polyelectrolytes. Nanoscale, 4(20), pp.6150-6165.

76. Zhang, J., Zhao, X., Xian, M., Dong, C. and Shuang, S., 2018. Folic acid-conjugated green luminescent carbon dots as a nanoprobe for identifying folate receptor-positive cancer cells. Talanta, 183, pp.39-47.

77. Loo, A.H., Sofer, Z., Bouša, D., Ulbrich, P., Bonanni, A. and Pumera, M., 2016. Carboxylic carbon quantum dots as a fluorescent sensing platform for DNA detection. ACS applied materials & interfaces, 8(3), pp.1951-1957.

78. Shi, J., Wang, L., Zhang, J., Ma, R., Gao, J., Liu, Y., Zhang, C. and Zhang, Z., 2014. A tumor-targeting near-infrared laser-triggered drug delivery system based on GO@ Ag nanoparticles for chemo-photothermal therapy and X-ray imaging. Biomaterials, 35(22), pp.5847-5861.

79. Nahain, A.A., Lee, J.E., In, I., Lee, H., Lee, K.D., Jeong, J.H. and Park, S.Y., 2013. Target delivery and cell imaging using hyaluronic acid-functionalized graphene quantum dots. Molecular pharmaceutics, 10(10), pp.3736-3744.

80. Day, C.M., Hickey, S.M., Song, Y., Plush, S.E. and Garg, S., 2020. Novel tamoxifen nanoformulations for improving breast cancer treatment: old wine in new bottles. Molecules, 25(5), p.1182.

81. Lotfi, H., Abadi, R.J.K. and Vadi, M., 2015. Adsorption of Metformin as Anti-Diabetic Drug on Carbon Nanotube and Activated Carbon. RESEARCH JOURNAL OF PHARMACEUTICAL BIOLOGICAL AND CHEMICAL SCIENCES, 6(3), pp.1422-1427.

82. Lin, S., Ruan, J. and Wang, S., 2019. Biosynthesized of reduced graphene oxide nanosheets and its loading with paclitaxel for their anti-cancer effect for treatment of lung cancer. Journal of Photochemistry and Photobiology B: Biology, 191, pp.13-17.

83. Xiao, J., Duan, X., Yin, Q., Zhang, Z., Yu, H. and Li, Y., 2013. Nanodiamonds-mediated doxorubicin nuclear delivery to inhibit lung metastasis of breast cancer. Biomaterials, 34(37), pp.9648-9656.

84. Gaur, M., Misra, C., Yadav, A.B., Swaroop, S., Maolmhuaidh, F.Ó., Bechelany, M. and Barhoum, A., 2021. Biomedical applications of carbon nanomaterials: fullerenes, quantum dots, nanotubes, nanofibers, and graphene. Materials, 14(20), p.5978.

85. Ye, S., Shao, K., Li, Z., Guo, N., Zuo, Y., Li, Q., Lu, Z., Chen, L., He, Q. and Han, H., 2015. Antiviral activity of graphene oxide: how sharp-edged structure and charge matter. ACS applied materials & interfaces, 7(38), pp.21571-21579.

86. Zhang, M., Wang, W., Cui, Y., Chu, X., Sun, B., Zhou, N. and Shen, J., 2018. Magnetofluorescent Fe3O4/carbon quantum dots coated single-walled carbon nanotubes as dual-modal targeted imaging and chemo/photodynamic/photothermal triple-modal therapeutic agents. Chemical Engineering Journal, 338, pp.526-538.

87. Wang, H., Pan, X., Wang, X., Wang, W., Huang, Z., Gu, K., Liu, S., Zhang, F., Shen, H., Yuan, Q. and Ma, J., 2020. Degradable carbon–silica nanocomposite with immunoadjuvant property for dual-modality photothermal/photodynamic therapy. ACS nano, 14(3), pp.2847-2859.

88. Wang, S., Chen, L., Wang, J., Du, J., Li, Q., Gao, Y., Yu, S. and Yang, Y., 2020. Enhanced-fluorescent imaging and targeted therapy of liver cancer using highly luminescent carbon dots-conjugated foliate. Materials Science and Engineering: C, 116, p.111233.

89. Gaur, M., Misra, C., Yadav, A.B., Swaroop, S., Maolmhuaidh, F.Ó., Bechelany, M. and Barhoum, A., 2021. Biomedical applications of carbon nanomaterials: fullerenes, quantum dots, nanotubes, nanofibers, and graphene. Materials, 14(20), p.5978

90. Landry, M.P., Ando, H., Chen, A.Y., Cao, J., Kottadiel, V.I., Chio, L., Yang, D., Dong, J., Lu, T.K. and Strano, M.S., 2017. Single-molecule detection of protein efflux from microorganisms using fluorescent single-walled carbon nanotube sensor arrays. Nature nanotechnology, 12(4), pp.368-377.

91. Baldo, S., Buccheri, S., Ballo, A., Camarda, M., La Magna, A., Castagna, M.E., Romano, A., Iannazzo, D., Di Raimondo, F., Neri, G. and Scalese, S., 2016. Carbon nanotube-based sensing devices for human Arginase-1 detection. Sensing and bio-sensing research, 7, pp.168-173.

92. Huang, Y., Miao, Y.E., Ji, S., Tjiu, W.W. and Liu, T., 2014. Electrospun carbon nanofibers decorated with Ag–Pt bimetallic nanoparticles for selective detection of dopamine. ACS applied materials & interfaces, 6(15), pp.12449-12456.

93. Zhou, M., Zhai, Y. and Dong, S., 2009. Electrochemical sensing and biosensing platform based on chemically reduced graphene oxide. Analytical chemistry, 81(14), pp.5603-5613.

94. Mani, V., Devasenathipathy, R., Chen, S.M., Subramani, B. and Govindasamy, M., 2015. A novel glucose biosensor at glucose oxidase immobilized graphene and bismuth nanocomposite film modified electrode. Int. J. Electrochem. Sci, 10, pp.691-700.

95. Sun, Y., Lin, Y., Han, R., Wang, X. and Luo, C., 2019. A chemiluminescence biosensor for lysozyme detection based on aptamers and hemin/G-quadruplex DNAzyme modified sandwich-rod carbon fiber composite. Talanta, 200, pp.57-66.

96. Saxena, U., Das, M., Ahmad, S., Barbora, L., Borthakur, M., Verma, A., Bora, U. and Goswami, P., 2011. Multiwalled carbon nanotube-based bi-enzyme electrode for total cholesterol estimation in human serum. Journal of Experimental Nanoscience, 6(1), pp.84-95.

97. Tang, Z., Jiang, K., Sun, S., Qian, S., Wang, Y. and Lin, H., 2019. A conjugated carbon-dot–tyrosinase bioprobe for highly selective and sensitive detection of dopamine. Analyst, 144(2), pp.468-473.

98. Yang, C., Hu, L.W., Zhu, H.Y., Ling, Y., Tao, J.H. and Xu, C.X., 2015. rGO quantum dots/ZnO hybrid nanofibers fabricated using electrospun polymer templates and applications in drug screening involving an intracellular H 2 O 2 sensor. Journal of Materials Chemistry B, 3(13), pp.2651-2659.

99. Shehab, M., Ebrahim, S. and Soliman, M., 2017. Graphene quantum dots prepared from glucose as optical sensor for glucose. Journal of Luminescence, 184, pp.110-116.

100. Eivazzadeh-Keihan, R., Maleki, A., De La Guardia, M., Bani, M.S., Chenab, K.K., Pashazadeh-Panahi, P., Baradaran, B., Mokhtarzadeh, A. and Hamblin, M.R., 2019. Carbon based nanomaterials for tissue engineering of bone: Building new bone on small black scaffolds: A review. Journal of advanced research, 18, pp.185-201.

101. Veetil, J.V. and Ye, K., 2009. Tailored carbon nanotubes for tissue engineering applications. Biotechnology progress, 25(3), pp.709-721.

102. Roshanbinfar, K., Mohammadi, Z., Mesgar, A.S.M., Dehghan, M.M., Oommen, O.P., Hilborn, J. and Engel, F.B., 2019. Carbon nanotube doped pericardial matrix derived electroconductive biohybrid hydrogel for cardiac tissue engineering. Biomaterials science, 7(9), pp.3906-3917.

103. Zhang, Q., Mochalin, V.N., Neitzel, I., Knoke, I.Y., Han, J., Klug, C.A., Zhou, J.G., Lelkes, P.I. and Gogotsi, Y., 2011. Fluorescent PLLA-nanodiamond composites for bone tissue engineering. Biomaterials, 32(1), pp.87-94.

104. Shahriar, S.S., Mondal, J., Hasan, M.N., Revuri, V., Lee, D.Y. and Lee, Y.K., 2019. Electrospinning nanofibers for therapeutics delivery. Nanomaterials, 9(4), p.532.

105. Zeimaran, E., Pourshahrestani, S., Nam, H.Y., bin Abd Razak, N.A., Kalantari, K., Kamarul, T., Salamatinia, B. and Kadri, N.A., 2020. Engineering stiffness in highly porous biomimetic gelatin/tertiary bioactive glass hybrid scaffolds using graphene nanosheets. Reactive and Functional Polymers, 154, p.104668.

106. Cirillo, G., Vittorio, O., Kunhardt, D., Valli, E., Voli, F., Farfalla, A., Curcio, M., Spizzirri, U.G. and Hampel, S., 2019. Combining carbon nanotubes and chitosan for the vectorization of methotrexate to lung cancer cells. Materials, 12(18), p.2889.

107. Mahmoodi, M., Hydari, M.H., Mahmoodi, L., Gazanfari, L. and Mirhaj, M., 2021. Electrophoretic deposition of graphene oxide reinforced hydroxyapatite on the tantalum substrate for bone implant applications: In vitro corrosion and bio-tribological behavior. Surface and Coatings Technology, 424, p.127642.

108. Lee, S.J., Zhu, W., Nowicki, M., Lee, G., Heo, D.N., Kim, J., Zuo, Y.Y. and Zhang, L.G., 2018. 3D printing nano conductive multi-walled carbon nanotube scaffolds for nerve regeneration. Journal of neural engineering, 15(1), p.016018.

109. Yan, C., Ren, Y., Sun, X., Jin, L., Liu, X., Chen, H., Wang, K., Yu, M. and Zhao, Y., 2020. Photoluminescent functionalized carbon quantum dots loaded electroactive Silk fibroin/PLA nanofibrous bioactive scaffolds for cardiac tissue engineering. Journal of Photochemistry and Photobiology B: Biology, 202, p.111680.

110. Cabral, C.S., Miguel, S.P., de Melo-Diogo, D., Louro, R.O. and Correia, I.J., 2019. Green reduced graphene oxide functionalized 3D printed scaffolds for bone tissue regeneration. Carbon, 146, pp.513-523.

111. Tohidlou, M.H., Shafiei, S.S. and Shiralipoor, F., 2020. Preparation and evaluation of polycaprolactone/amine functionalized carbon nanotube electrospun nanocomposite scaffold containing mesenchymal stem cells for use in hard tissue engineering. Journal of Advanced Materials and Technologies, 8(4), pp.19-30.

112. Luo, W.K., Zhang, L.L., Yang, Z.Y., Guo, X.H., Wu, Y., Zhang, W., Luo, J.K., Tang, T. and Wang, Y., 2021. Herbal medicine derived carbon dots: synthesis and applications in therapeutics, bioimaging and sensing. Journal of Nanobiotechnology, 19(1), pp.1-30.

113. Kumar, S.U., Bhushan, B. and Gopinath, P., 2017. Bioactive carbon dots lights up microtubules and destabilises cell cytoskeletal framework–A robust imaging agent with therapeutic activity. Colloids and Surfaces B: Biointerfaces, 159, pp.662-672.

114. Sharifi-Rad, J., Rayess, Y.E., Rizk, A.A., Sadaka, C., Zgheib, R., Zam, W., Sestito, S., Rapposelli, S., Neffe-Skocińska, K., Zielińska, D. and Salehi, B., 2020. Turmeric and its major compound curcumin on health: bioactive effects and safety profiles for food, pharmaceutical, biotechnological and medicinal applications. Frontiers in pharmacology, 11, p.01021.

115. Gera, M., Sharma, N., Ghosh, M., Lee, S.J., Min, T., Kwon, T. and Jeong, D.K., 2017. Nanoformulations of curcumin: An emerging paradigm for improved remedial application. Oncotarget, 8(39), p.66680.

116. Vyas, A., Dandawate, P., Padhye, S., Ahmad, A. and Sarkar, F., 2013. Perspectives on new synthetic curcumin analogs and their potential anticancer properties. Current pharmaceutical design, 19(11), pp.2047-2069.

117. Bhandari, R., Gupta, P., Dziubla, T. and Hilt, J.Z., 2016. Single step synthesis, characterization and applications of curcumin functionalized iron oxide magnetic nanoparticles. Materials Science and Engineering: C, 67, pp.59-64.

118. Lin, C.J., Chang, L., Chu, H.W., Lin, H.J., Chang, P.C., Wang, R.Y., Unnikrishnan, B., Mao, J.Y., Chen, S.Y. and Huang, C.C., 2019. High amplification of the antiviral activity of curcumin through transformation into carbon quantum dots. Small, 15(41), p.1902641.

Chapter 2: Anti-cancer activity of curcumin-derived carbon dots

2.1 Introduction: Curcumin ((1,7-bis(4-hydroxy-3-methoxyphenyl)–1, 6-heptadiene-3,5-dione), a polyphenolic phytochemical is a component of turmeric and is obtained from the rhizomes of Curcuma longa. Turmeric has been used as a spice and a food colouring agent in Asian cuisine and is widely used in Indian Ayurvedic medicine for treating multiple health disorders [1]. The therapeutic benefits of curcumin in treating several chronic diseases like cancer, arthritis etc., is mostly attributed to its antioxidant and anti-inflammatory properties [2]. Numerous studies have confirmed that curcumin acts as an anti-proliferative agent and induces apoptosis in cancer cell lines [3]. Additionally, curcumin inhibits the initiation, progression, invasion and metastasis [4,5]. Despite curcumin's well-substantiated anti-cancer activity, its poor aqueous solubility (≤0.125 mg/l), low absorption, rapid metabolism and clearance serve as hurdles for its clinical development [5,8]. Several approaches that are being pursued to overcome such limitations include, the use of micro/nano formulations like solid lipid nanoparticles (SLN), micelles, liposomes, nanoparticles etc., in which curcumin is entrapped in the formulation; with the other approach being, the use of curcumin-analogs [6]. Ever since the accidental discovery of carbon-dots (C-dots) in 2004[7], it has been of interest to scientists. Its small size (<10 nm), good water solubility and photoluminescence[8] make it an attractive material for biological applications like biosensing[9], bioimaging and drug delivery[10,14]. Most of the reported biological applications of carbon dots are mainly in the area of cell imaging[11,16], drug and gene delivery[12,13], sensing, [13,19], photo-dynamic therapy (PDT)[14],photo-thermal (PTT)[15] and in photocatalytic reactions[16]. Only few studies have demonstrated the therapeutic use of carbon dots [17,24].

Glioblastoma multiform (GBM) is the most malignant human brain tumour with a median survival of one year [18]. The present treatment strategies which include surgical removal of tumor, radiotherapy and chemotherapy, or its combinations are unable to stop the progression of GBM. The benefits of curcumin in the treatment of GBM is established [19]. To improve

the outcome, several strategies including curcumin-loaded lipid-core nanocapsules [20], nanoparticles –loaded curcumin [21], and nano micelles of curcumin [22] were developed. The methodologies nevertheless, are chemically elaborate.

Recently a few studies reported the bioactivity of carbon dots [23,31]. On the basis of these studies, we hypothesized that curcumin-derived carbon dots might retain some of its therapeutic potential. To test this, we prepared curcumin derived C-dots (henceforth referred to as CurCD) using a simple single-step process and compared its activity with curcumin. Even though curcumin is known to follow multiple pathways to inhibit glioblastoma [24], our focus in this study was to compare the activity on widely reported characteristics like proliferation, migration, apoptosis etc using a glioblastoma cell line. We observed that CurCD was photostable and showed improved solubility as compared to curcumin. While the response of glioblastoma cells to the treatment was similar to curcumin, the response of normal cells to the respective treatments was however different. Our findings draw attention to the possibility of developing a new therapeutic strategy with compounds that are otherwise challenged with limited bioavailability, by developing their carbon dots.

2.2 Material and methods:

(I) Materials: Curcumin and ethylenediamine, were purchased from Sigma Aldrich, India. Ethanol was purchased from MERCK, USA. DMEM, Trypsin, FBS, Penicillin-streptomycin-Amphotericin B, MTT, Hoechst, Rhodamine TRITC, tubulin polyclonal antibody and secondary antibody alexa flour568 were procured from Thermo Fisher, USA. All plasticware for tissue culture were procured from Invitrogen. Dyes like FDA and PI were obtained from Sigma Aldrich and Himedia laboratories respectively. Annexin apoptosis kit was from BD life sciences.

(II) Experimental

2.2.1 Preparation of CurCD: Curcumin and ethylene diamine were taken in 1:2 ratio and dissolved in ethanol (20ml). To this, 50ml of water was added and the resulting solution was heated for half an hour at 60 ºC. Finally, the reaction mixture was transferred to a hydrothermal reactor and heated at 200 ºC for 12 h. The resulting dark brown solution was cooled and filtered using a filter paper and centrifuged at 20000 rpm for 20 min to separate the heavy particles. The supernatant containing the carbon dots was lyophilized using 3.5k Da dialysis membrane and lyophilized to obtain the carbon dots referred to as CurCD.

2.2.2 Characterization of CurCD

(a) UV absorption and Fluorescence spectroscopy: UV-Visible absorption spectra was recorded in the range from 200 to 800 nm with a Shimadzu UV-Vis 2600 spectrophotometer. Fluorescence spectra were recorded with an Edinburg FS 5 spectrofluorometer. All absorbance and fluorescence spectra were measured at room temperature using quartz cuvettes having a volume of 1 ml. All the measurements were repeated 3 times. The fluorescence lifetimes were checked by F900 fluorescence spectrometer (Edinburgh, UK) using a time-correlated single photon counting (TCSPC) technique. Both CurCD/curcumin were excited using a 405nm laser source and the fluorescence emission intensity at respective emission wavelengths were collected to obtain the fluorescence intensity decay profile.

(b) X-ray diffraction studies (XRD): X-ray diffraction pattern (XRD) was determined using Bruker Eco D8 setup consisting of Cu Kα radiation (λ = 0.154056 nm). Copper anode was taken as the target material with fine focus filament as the cathode. The freeze-dried

samples were dissolved in a mixture of water and ethanol and drop casted on the coverslips to take the measurements.

(c) Transmission electron Microscopy (TEM): The particle size of the synthesized carbon dots was measured with the help of TEM instrument (JEOL) JEM 2100) at an accelerating voltage of 200 kV. The diluted samples were probe sonicated and drop casted on copper coated carbon grids. The grids were dried at room temperature. To avoid any cross contamination with dust particles, TEM grids were kept in desiccator till use.

(d) AFM: The height profiling of synthesised CurCD was performed using atomic force microscopy (AFM, Nanoscope IIIa, Digital Instrument, USA) in tapping mode. Sample for the measurement was prepared by drop casting the dispersion of CurCD on the silicon wafer.

(e) Fourier Transform Infrared Spectroscopy (FTIR): FTIR spectra of curcumin, and CurCD were measured using a Bruker FTIR spectrophotometer equipped with a horizontal attenuated total reflectance (ATR) accessory containing a zinc selenide crystal.

(f) Photostability Studies: Photostability of fluorescent CurCD and curcumin was determined by Edinburg FS 5 spectrofluorometer equipped with a xenon lamp at an emission wavelength of 530 nm for CurCD and 550 nm for curcumin for 60 minutes at an interval of 5 minutes. The excitation and emission slit width were kept at 5 nm.

2.2.3 Isolation of Human Dermal Fibroblasts: Effect of CurCD on human dermal fibroblasts was studied using the cells derived from neonatal foreskin after taking the consent as per the protocol approved by the Institutional Ethics Committee of PGIMER (IEC-08/2017-658), Chandigarh, India. The primary fibroblasts were isolated as previously reported [25].

2.2.4 MTT Assay: Cells were seeded in 96-well plates at a cell density of 5000 cells/well and were incubated for 24 h. For treatment with curcumin /CurCD, the indicated concentrations

were added and the plates were incubated for 24 h at 37°C in a 5% CO2 incubator. Culture medium was removed and MTT was added. The resulting formazan crystals were solubilized in DMSO and the absorbance was measured at 570 nm using a microplate reader (Tecan multimode reader) [26].

2.2.5 Cell migration assay: Effect of CurCD and curcumin on the migration of tumor cells investigated through scratch assay as per reported protocol [35]. In brief, C6 cells were seeded in 12 well tissue culture plates (Nunc) in DMEM media and allowed to form a monolayer. In order to avoid the effect FBS on cell proliferation, cells were serum starved overnight and after that DMEM media containing 2% FBS was used to carry out rest of the experiment. To make the wound sterile 20ul tip was used. After that cells were washed with DPBS in order to remove the cell debris. Further, creating the scratch media containing different concentrations of CurCD and curcumin was added. On completion of 24h incubation period cells were washed with PBS and fixed with 4% paraformaldehyde solution. After fixation, Hoechst was added to stain the nucleus and images were taken with the help of confocal microscope.

2.2.6 Apoptosis assay: Rat C6 cells were seeded in a 6 well tissue culture plate six-well culture plate and treated with above mentioned treatments for 24h. Untreated cells were taken as Control group. Normal, apoptotic and necrotic cells were differentiated FITC Annexin V apoptosis detection kit (BD lifesciences) according to the manufacturer's instructions. Briefly, after the 24h of treatment period, the cells were harvested, washed and resuspended in 1X annexin binding buffer. After the addition of annexin and PI cells were incubated for 30 min in dark at room temperature. Analysis was done using FACS flow cytometer [27].

2.2.7 Soft Agar spheroid formation Assay: 3D spheroids were prepared using previously reported method [28]. Briefly, 10gm of agar was suspended in 10ml of water to

prepare 1.0% (w/v) solution. As prepared agar solution was poured into 96 well plate and allowed to solidify. After that cells were seeded at a density of 2.4×10^3 cells/well in complete medium and allowed to form compact 3D spheroids. 48h after the seeding and spheroids formation, treatments with curcumin as well as CurCD were given. To check the viability of cancer cells in the spheroid culture live/dead staining was performed with FDA and PI. Images were taken with the help of confocal microscope with an objective 5x.

2.2.8 Determination of reactive oxygen species: C6 cells were cultured in six well plates at a cell density of 25000 cells/well and treated with different concentrations of CurCD and curcumin in DMEM media. Untreated cells were taken as control to calculate the basal ROS level of cancer cells. After an incubation period of 24h, cells were incubated with 25µM of DCFDA (2', 7' –dichlorofluorescein diacetate) dye for 30 minutes at 37^0C. Upon cellular uptake, the nonfluorescent DCFDA is oxidized by ROS into 2', 7' –dichlorofluorescein (DCF) which is a fluorescent compound. After that cells were washed several times with DPBS and finally the fluorescence images of treated as well as untreated were captured using Zeiss LSM880 confocal microscope (Carl Zeiss,) confocal microscope. For the quantification of data, fluorescence was measured (Ex/Em = 485/535 nm) in a microplate reader.

2.2.9 Cytoskeletal Analysis: The effect of synthesised CurCD and curcumin on cytoskeleton of C6 cells was determined and compared using confocal microscopy. For analysis, cells were seeded in confocal dishes and incubated with CurCD as well as curcumin for 24h at 37^0C. After incubation with the treatment, cells were washed twice with DPBS and fixed with 4% paraformaldehyde. Cells were then incubated with 10 µg/mL of Hoescht-33342 for 5 min followed by cytoskeletal staining with rhodamine TRITC (Invitrogen) for 20 min. The cells were washed twice with PBS and cytoskeleton was analysed using confocal microscope with an objective of 63X.

2.2.10 Tubulin Antibody staining: Immunofluorescence analysis of microtubule staining was performed both on C6 as well as HDF cells. Briefly, both the cells were seeded on a confocal glass dish at a cell density of 10000cells/dish. After 24 h, the cells were incubated with CurCD and curcumin and kept for 24 h incubation period. After 24 h cells were fixed with paraformaldehyde. In order to permeabilize the cells for antibody incubation, the cells were treated with 0.1% Triton X-100 for 15 minutes and blocking was done with BSA (1%) for 1 h at room temperature. To check the microtubule staining, the cells were labelled with tubulin polyclonal antibody (Invitrogen) at 1:500 dilution overnight at 4^0C and subsequently stained with Alexa Fluor® 568 conjugated Superclonal™ Secondary Antibody, (Invitrogen) Hoechst (Invitrogen) was used as nuclear stain.

2.2.11 Scanning electron microscopy: Cell morphology of untreated and treated rat C6 cells were checked using scanning electron microscopy using JSM-IT300 scanning electron microscope (Jeol Ltd., Japan). As per previously reported protocol, cells were seeded on coverslips at a cell density of $5x10^3$ cells in 6- well tissue culture plates. After 24h treatment with CurCD as well as curcumin was given. Cells were fixed with 2.5% glutaraldehyde and were dehydrated through graded ethanol solutions (25%, 50%, 75% and 100%). The coverslips were air dried completely and then sputter coated with gold palladium before SEM analysis [29].

2.2.12 Zebrafish embryo toxicity assay: The zebrafish (*Danio rerio*) were raised in an aquarium at 28°C under controlled conditions. Ten fertilized eggs in each group were treated individually with Curcumin/CurCD. The developmental status of zebrafish embryos and larvae were analyzed at 24 h post fertilization (hpf), by use of an Olympus stereomicroscope equipped with a digital camera. The number of surviving embryos was determined at the end of each

time point. Each group contained 10 embryos per condition, and all experiments were performed twice in duplicate.

2.2.13 Statistics: The significance level in all statistical observations was set at a probability of $p < 0.05$. All the data is presented as mean ± SD. ANOVA and Bonferroni test were used to analyse the data and to calculate the level of significance.

2.3 Results and discussion

2.3.1 Physical characterization of CurCD: CurCD was synthesized using solvothermal process with 1:2 molar mixture of curcumin and ethylenediamine (EDA) at 200°C for 12 h using water and ethanol as solvents. EDA was used for surface passivation to improve the QY of CurCD. A significant improvement in water solubility was observed in CurCD (1mg ml^{-1}) as compared to curcumin (7.8 µg ml^{-1}). CurCD examined by transmission electron microscopy (TEM) revealed small spherical particles of CurCD with size ranging from 3-5 ± 2 nm as shown in (Figure 2.1a). The image further confirmed that there was no agglomeration of the particles. HRTEM studies were conducted to determine the interplanar spacing and the results depicted 0.21 nm d-spacing value corresponding to 100 plane of graphene [30]. The real-space image and its fast fourier transform (FFT) pattern (inset in Figure 2.1b) further revealed that CurCD are layered graphene with a spacing of 0.21 nm [31]. Selected area electron diffraction pattern revealed the semi-crystalline nature of the material which may be due to change in the molecular packing of curcumin by heat-driven dehydration/condensation reactions [32,41] (Figure 2.1c). The height analysis as shown in (Figure 2.1d) of CurCD by atomic force microscopy (AFM) displayed an average thickness of 5.8 ± 1.5 nm which corresponds to ≈17 layers of graphene [33]. Furthermore, the AFM image of CurCD reveals their topographic heights in the range 4 to 8 nm (inset in Figure 2.1d)

indicating that the CurCD primarily consisted of eleven to twenty-three layers of graphene-like sheets.

The X-ray Photoelectron Spectroscopy (XPS) measurements were carried out to identify the composition of the CurCD and the full scan spectrum is shown in (Figure.2.1 (e-g)). The de-convoluted XPS spectra of C1s, and O1s followed with fitting peaks show the presence of C=C, C-O, C–OH and C=O groups indicating that the CurCD retained some functional groups even after hydrothermal treatment. As ethylene diamine is used as a precursor, N1s was also deconvoluted into three components with peaks at 398.70, 399.24 and 400.44 eV indicating the existence of nitrogen mostly in the form of C-N-C, C-N and C-N-H/N-H [34, 44]. The peaks at 283.02 eV and 285.01 eV are due to C=C and aliphatic C-C from the precursors[35] and the peaks at 286.74 eV and 287.29 eV due to C–N–C and C=O provide evidence for the existence of a amide linkage [34]. Similarly, the peaks of O1s can be deconvolved into three components with binding energies of 530.01 eV, 531.65 eV and 534.02 eV which correspond to C-O, C=O and C–OH/C-O-C groups and indicate the presence of oxygen in CurCD. To know the exact effect of hydrothermal treatment, we had compared the XPS spectra of pure curcumin with the as-synthesized CurCD. Curcumin displayed the presence of sp^2 and sp^3 carbon along with oxygen with peaks located at 282.18, 283.74, 285.10, 285.71 and 530.17 eV, 531.72 eV and 533.59 eV respectively as reported in literature. In comparison to curcumin, the deconvoluted X-ray photoelectron spectroscopy (XPS) spectra of CurCD revealed an increase in the ratio of sp^2/sp^3 upon hydrothermal treatment, indicating a higher degree of carbonization [23]. Furthermore, Elemental analysis (EA) was performed to understand the elemental composition and the data revealed the presence of C, N and O element in CurCD having atomic ratio 55.04%, 7.49% and 37.47% respectively (Figure 2.1h) while in pure curcumin the ratio of C and O was found to be 82.49% and 17.51% respectively as per reported in literature. The percentage composition of oxygen in CurCD was higher than that of

curcumin, indicating the oxidation of some carbons to form oxygen-containing functional groups.

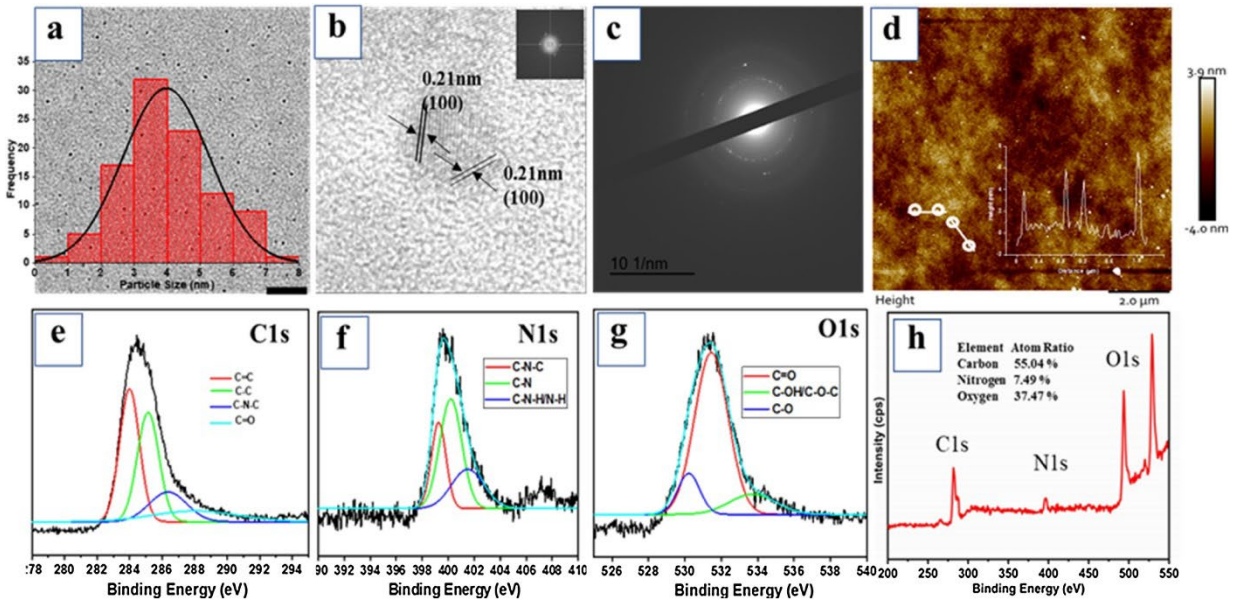

Figure 2.1: Characterization of CurCD (a) TEM image of CurCD (scale bar =20 nm, Inset in (a) shows size distribution of the particles (n = 100); (b) HR-TEM image (scale bar =5 nm), Inset in (b) shows the FFT pattern of CurCD; (c) SAED pattern of CurCD; (d) AFM image of CurCD; (e-g) XPS high-resolution survey scans of C1s, N1s, and O1s region and (h) XPS full scan spectrum of CurCD.

The Uv–Vis absorption and photoluminescence (PL) spectroscopy was used to determine the optical properties of curcumin and CurCD. As shown in Figure. 2.2a, CurCD exhibited the first absorption band at 265 nm due to π–π* transition of conjugated C=C indicating the formation of graphitic carbon cores [35]. The second absorption band at 345 nm–420 nm is due to n–π* transition of C=O, confirming the presence of oxygen functionalities on CurCD. In pure curcumin, a sharp absorption peak is detected at around 420 nm due to π–π* transition, implying that curcumin like structure is indeed present on the surface of CurCD [36].

In the fluorescence study, while curcumin exhibited an excitation -independent fluorescence emission behaviour (Figure. 2.2b) [37], CurCD revealed a typical excitation dependent emission behaviour. The maximum and minimum emission intensity at 450 nm and 530 nm of

CurCD was observed due to excitation at 350 nm and 460 nm as shown in (Figure. 2.2c). Such shifts in the emission peaks are suggestive of the presence of different emissive sites on the surface of CurCD [38]. It is likely that the self-passivated oxygen and nitrogen-containing functional groups on the surface of CurCD are responsible for the efficient PL with an enhanced quantum efficiency of ~20 % as compared to pure curcumin which is regarded as almost non-fluorescent due to its negligible quantum yield [39]. The carbon dots prepared with curcumin alone is reported to have very low to no excitation-dependent emission properties [23]. This could be due to the absence of nitrogen doping. The photostability studies revealed a drop in the fluorescence intensity of curcumin while no change was observed in the fluorescence of CurCD, indicating the superior photostability of CurCD in comparison to curcumin. The FTIR spectra is shown Figure. 2.2d & 2.2e. The peaks observed in curcumin in the region from 1100−1300 cm^{-1}, 1620 cm^{-1} and 2930 cm^{-1} are due to C-O-C bending, C=O stretching and C-H stretching vibration along with other peaks at 3500 cm^{-1}, 960 cm^{-1}, 852 cm^{-1} and 808 cm^{-1} which were due to OH stretch, C-O stretch, C-H bending and C=C bending vibration [40]. The FTIR spectra of CurCD showed a difference in stretching vibration between keto/enol and the hydroxyl group of phenols in the molecular packing of curcumin indicating the destruction of hydrogen bonding due to carbonization and polymerization of curcumin at a higher temperature. In the fingerprint region (1300–400 cm^{-1}), a noticeable change is observed, indicating that the pyrolysed products of curcumin still remained on CurCD surface even after hydrothermal treatment [41, 52]. Additional peaks in CurCD at 1620 cm^{-1}, 1517 cm^{-1}, 1100−1300 cm^{-1}, 833 cm^{-1} and 701 cm^{-1} were due to C=O (Amide I), C-N stretching (Amide II), C-N-C/C-O-C stretching, NH2 bending and N-H wagging vibration because of the presence of ethylenediamine that was used as a precursor in the synthesis of CurCD (Figure. 2e). Figure. 2f shows the XRD pattern of pure curcumin. Multiple peaks in the range of 10°–30°, is due to the high crystal polymorphism [42]. In contrast, CurCD displayed a broad peak at $2\theta \approx 25°$

which is due to 002 plane corresponding to the spacing of 0.33 nm of the graphitic interlayer [31].

The PL decay curve for curcumin and CurCD was measured with an excitation wavelength of 430 nm and monitored in the respective emission maxima as shown in Figure. 2.2g. The data indicated that the decay curves were mono-exponential with an average lifetime of 2.34 ns for CurCD and 0.25 ns for pure curcumin indicating the increased stability of CurCD [43,48]. The average lifetime values, obtained by fitting these decay plots with the biexponential decay model, are tabulated in the table provided in Figure.2

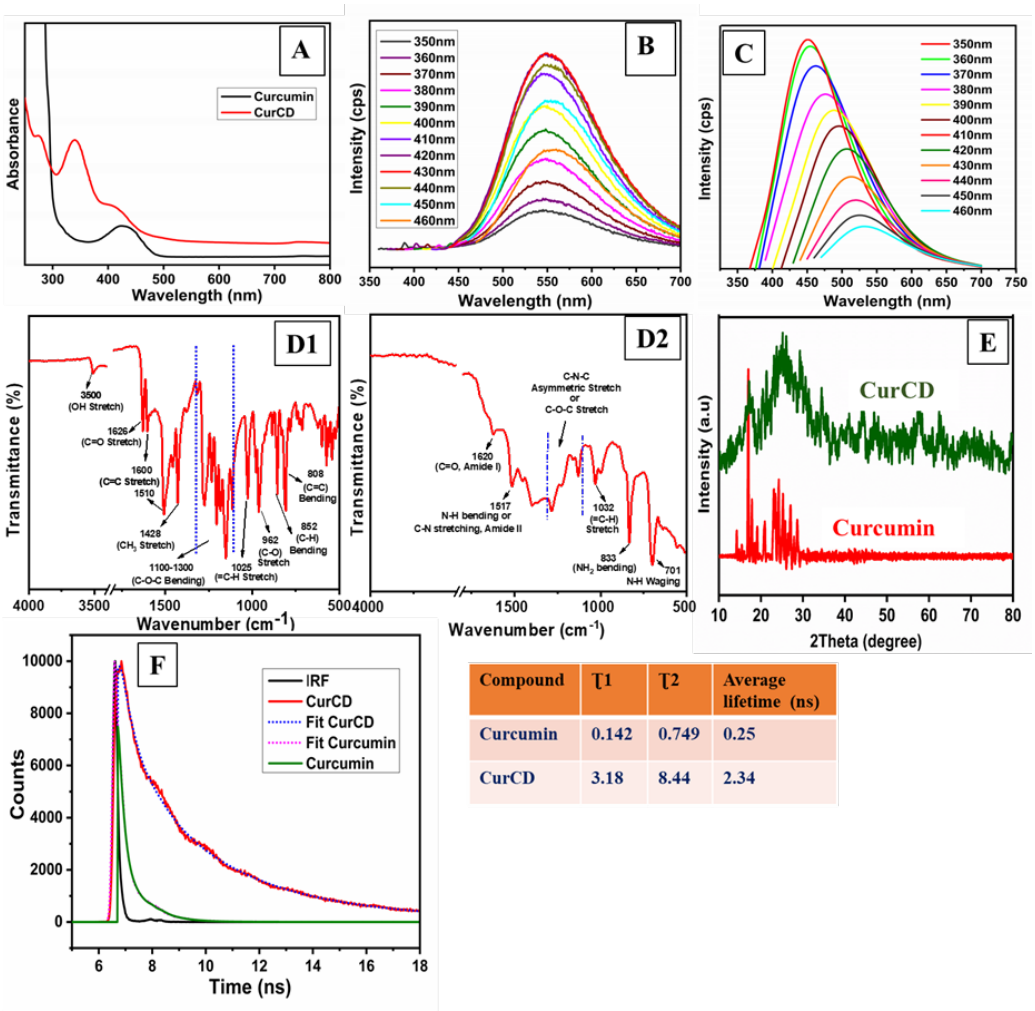

Compound	τ1	τ2	Average lifetime (ns)
Curcumin	0.142	0.749	0.25
CurCD	3.18	8.44	2.34

Figure 2.2: Photophysical properties of CurCD (a) UV-Vis absorbance spectra of Curcumin and CurCD; (b) Excitation-dependent fluorescence emission of Curcumin with excitation from 350 to 460 nm (c) Excitation-dependent fluorescence emission of CurCD with excitation from 350 to 460 nm; (d)

& (e) FTIR spectra of pure curcumin and CurCD respectively; (f) XRD Diffractogram of curcumin and CurCD and (g) Time-resolved fluorescence decay spectra of Curcumin and CurCD. Table shows the average fluorescence lifetime decay**.**

2.3.2 Effect on cell proliferation: The effect of CurCD /curcumin on C6 proliferation was evaluated using MTT assay after 24 h of treatment [44]. Treatment of C6 cells with curcumin (0.3–11.04 μg ml^{-1}) which corresponds to 1−30 μM reported in literature [22, 57] demonstrated a dose dependent inhibition in cell viability. While lower concentrations of up to 3.68 μg ml^{-1} had no effect, a significant inhibition in cell viability was observed with 7.36 μg ml^{-1} and 11.04 μg ml^{-1} respectively (Figure. 2.3a). A similar dose dependent inhibition in cell viability was reported in other studies [45]. Treatment with CurCD (0−500 μg ml^{-1}), likewise showed a dose dependent inhibition in cell viability, with a significant inhibition observed with 250 μg ml^{-1} and 500 μg ml^{-1} respectively (Figure. 2.3b). The inhibition in cell viability observed with CurCD was almost similar to curcumin indicating its anti-proliferative effect. A major challenge in anticancer therapy is to increase the selectivity towards cancer cells and spare normal cells [46]. We compared the effect of curcumin and CurCD on the proliferation of human dermal fibroblasts (HDF). The cultured cells were similarly treated with curcumin/CurCD as mentioned above and the viability of the cells was assessed after 24 h using MTT assay. On curcumin treatment, HDF cells revealed no change in cell viability up to 0.368 μg ml^{-1} but a significant inhibition was observed from 1.84 μg ml^{-1}. It is worth noting that curcumin was cytotoxic to the fibroblasts at a dose that was ineffective on C6 cells (Figure. 2.3c). This observation indicated that in comparison to C6 cells, curcumin was more cytotoxic to fibroblasts, an observation similarly reported by others [47,59]. No significant change in viability was observed in HDF cells treated with CurCD (0−500 μg ml^{-1}) (Figure. 2.3d). The results indicate that in comparison to curcumin, CurCD is cytocompatible with normal cells.

Nonetheless, both curcumin and CurCD were cytotoxic to C6 cells.

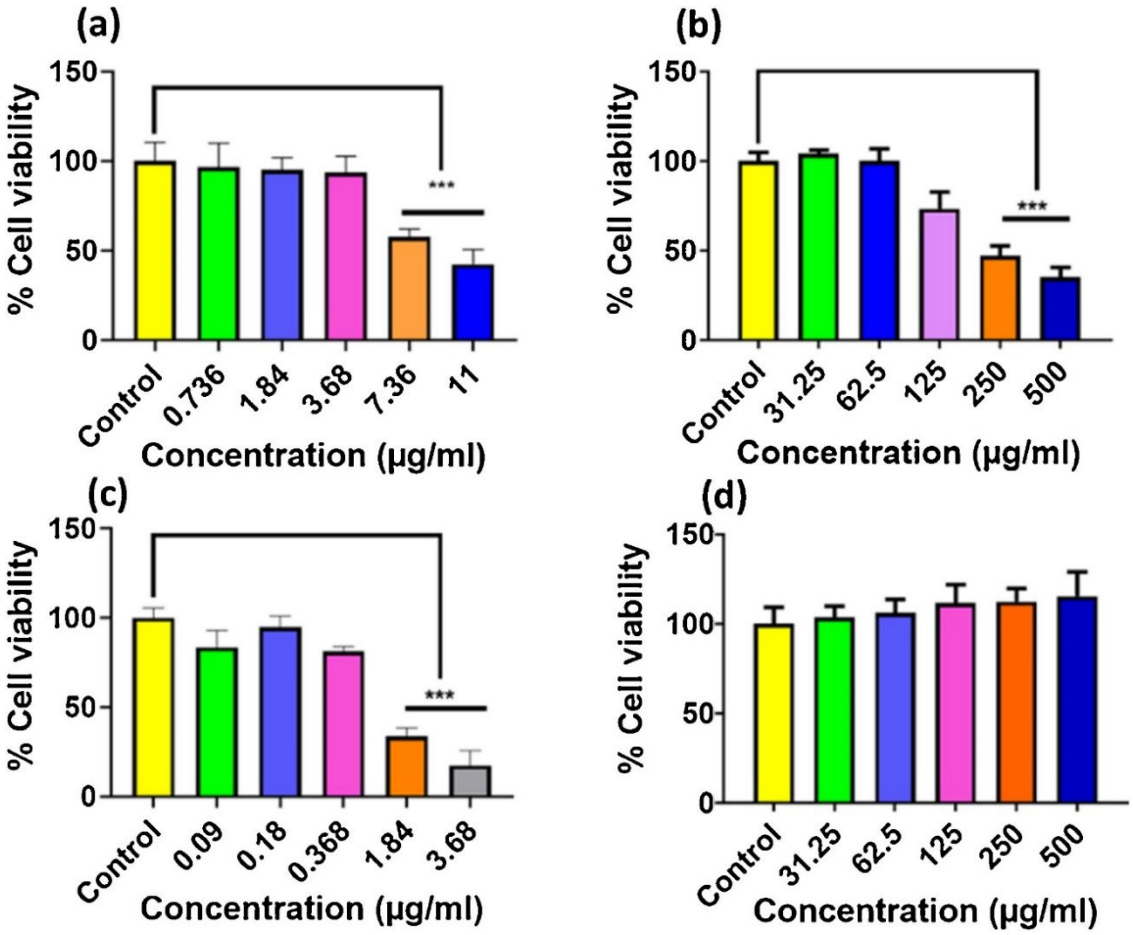

Figure 2.3: Effect on cell viability. Viability of C-6 cells treated with (a) curcumin and (b) CurCD. Viability of human dermal fibroblasts treated with (c) curcumin and (d) CurCD respectively. Data represents average values obtained from 3 experiments conducted in duplicate. The data is presented as the mean ± standard deviation. *** represents P value ≤0.001.

2.3.3 Effect on cell migration: Glioma cells are reported to be highly invasive and hence drugs that inhibit the cancer cell mobility are highly sought after [48]. As curcumin is known to inhibit glioblastoma cell migration [49], a wound healing assay was performed. Figure 2.4 depicts representative images of the migrated cells 24 h post scratch wound creation. As compared to untreated control cells (Figure. 2.4a), the presence of very few cells in the scratch area of CurCD (Figure. 2.4b and c) and curcumin (Figure. 2.4d and e) treated cells indicated that the migration of the cells was blocked. It is worth to note that the same concentration of

CurCD and curcumin had demonstrated anti-proliferative effect (Figure. 2.3c and d). Fig. 2.4f represents the migrated cells quantified with the help of image J software. The data represents the percentage of migrated cells following the respective treatment. While several pathways have been implicated in the suppression of glioblastoma cell migration [49], it is encouraging to note that CurCD, like curcumin significantly inhibited the glioblastoma cell migration.

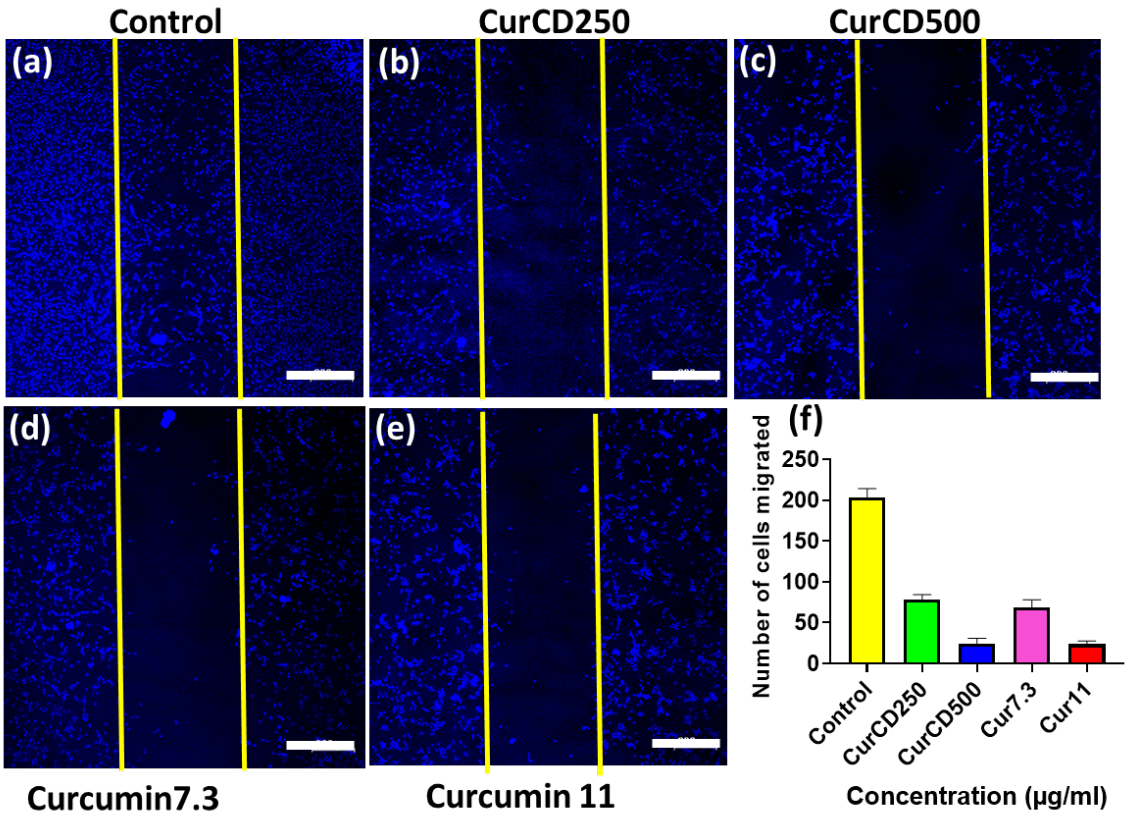

Figure 2.4: Migratory response of C6 cells. Confocal microscopic images of the scratch wound area in C6 cells stained with Hoechst after 24 h treatment. (a) Control cells, (b) CurCD 250 µg ml^{-1}, (c) CurCD 500 µg ml^{-1}, (d) Curcumin 7.3 µg ml^{-1} and (e) Curcumin 11 µg ml^{-1}. (f) Graph depicts the average number of migrated cells captured from 10 random areas. Data expressed represents the average of three experiments performed in triplicate. Scale bar represents 200 µm.

2.3.4 Effect on apoptosis: Curcumin is widely reported to induce apoptosis in various cancer cells [50,63]. In a glioblastoma cell line, curcumin is known to induce apoptosis either

through activation of p53 and caspase 3 or inhibition of anti-apoptotic genes like AP-1, NF-κB and Bcl2 [6]. To identify the type of cell death that was observed with CurCD, the C6 treated cells were evaluated with annexin-V/PI staining using FACS analysis. Figure. 2.5 depicts the data obtained following the flow cytometric analysis of treated and untreated cells. Our study showed that the treatment of C6 cells with CurCD (250−500 μg ml^{-1}) and curcumin (7.3−11 μg ml^{-1}) resulted in a large number of apoptotic cells. This data was consistent with the results of the cytotoxicity assay (Figure. 2.3a and b) and confirmed that the inhibition of viability observed with CurCD in the MTT studies was through apoptosis and not necrosis.

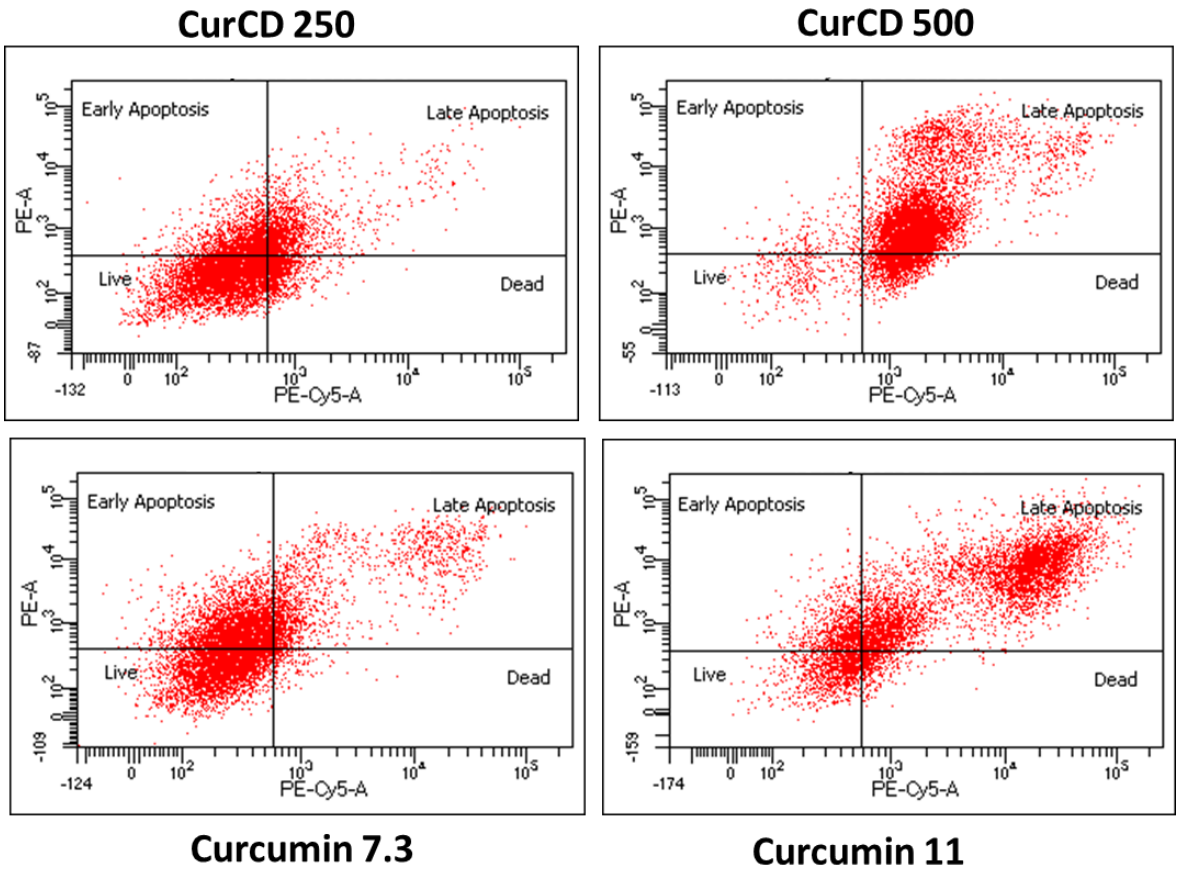

Figure 2.5: Apoptotic response of C6 cells following 24 h treatment with CurCD /curcumin

2.3.5 Response of 3D tumour model to CurCD: The microenvironment associated with culture conditions is known to influence the behaviour of tumour cells, including their

drug-responsiveness [51]. To confirm the anti-tumour efficacy in a 3D model, a comparative evaluation of the viability of the cells after 24 h treatment was conducted on spheroids that were developed in soft agar [52,66]. Representative confocal images of the spheroids following treatment are displayed in Figure. 2.6. Live and dead cells were differentiated on the basis of green [Fluorescein diacetate treatment (FDA) staining] and red [Propidium iodide (PI)] fluorescence respectively. The higher propensity of dead cells in CurCD-treated spheroids as compared to curcumin, might be due to its better penetration into the spheroid, facilitated by its small size. The results suggest that the anti-tumour activity of CurCD in a 3D environment was more pronounced than curcumin.

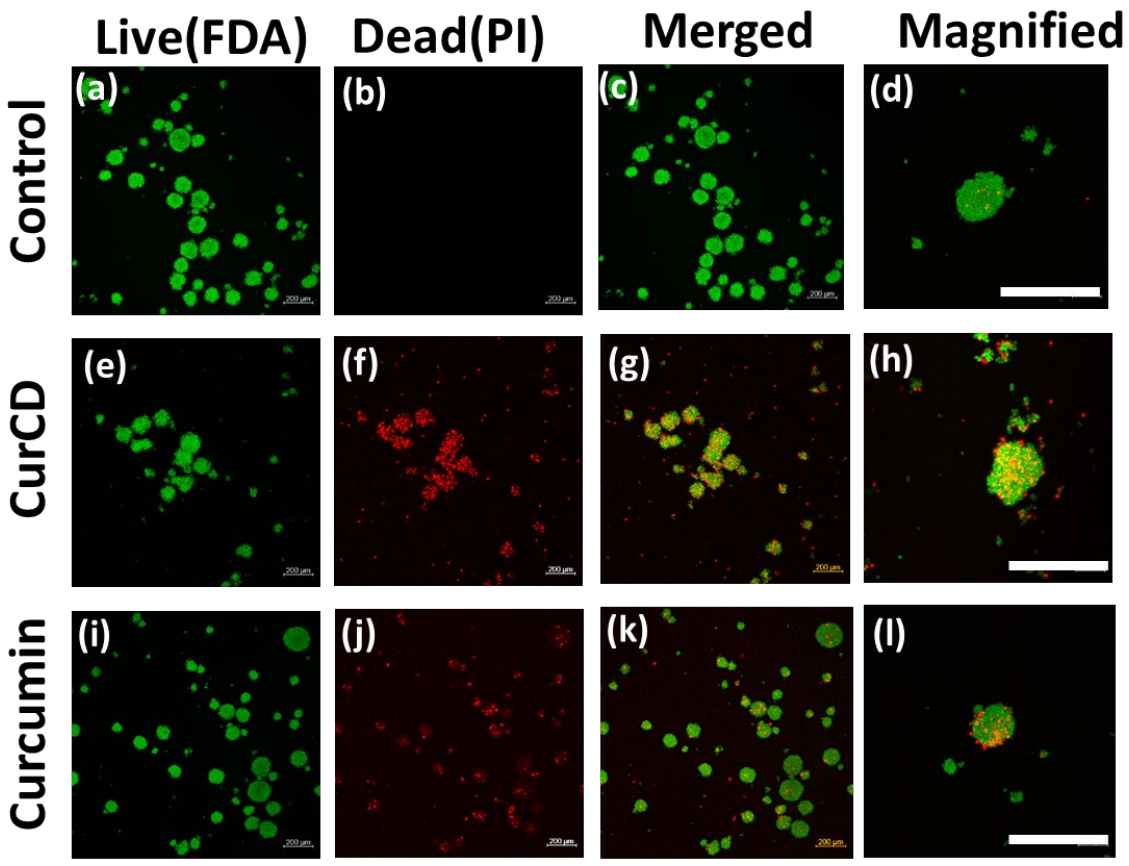

Figure 2.6: Effect of CurCD/Curcumin on 3D spheroids. Spheroids were prepared with C6 cells and treated with curcumin/CurCD for 24 h. Live (green)/dead (red) cells in the spheroids were identified

using FDA/PI staining. (a-d) Untreated spheroids, (e-h) CurCD treated spheroids and (i-l) Curcumin treated spheroids. Scale bar represents 200 μm,

2.3.6 ROS activity: Although cells are known to undergo apoptosis through different pathways, it is apparent that increased reactive oxygen species (ROS) expression causes cell death [53]. ROS plays an essential role in normal cell signalling and its dysregulation has been implicated in many diseases including cancer. ROS plays a dichotomist role in cancer with low levels promoting stimulation of cancer cell proliferation, increased cell survival etc., whereas high levels induce anti-cancer effects by affecting cell cycle arrest and apoptosis [54]. Curcumin is reported to induce ROS in various cancer cell lines [55] and is known to induce apoptotsis [56]. To investigate the ROS activity in presence of CurCD, C6 and human dermal fibroblasts were exposed to curcumin/ CurCD for 24 h and the ROS levels were assessed using H2DCFDA, a general oxidative stress indicator. In comparison to untreated control, C6 cells treated with both curcumin/CurCD showed intense green fluorescence, an indicator of ROS generation (Figure. 2.7a). A semi-quantitative analysis of the fluorescence intensity is displayed in (Figure. 2.7b). No change in ROS activity was visualized in fibroblasts even on treatment with high concentrations of CurCD (500 μg ml^{-1}). The data indicated that unlike normal cells, the selective cytotoxic response of cancer cells to CurCD might be related to its induction of ROS.

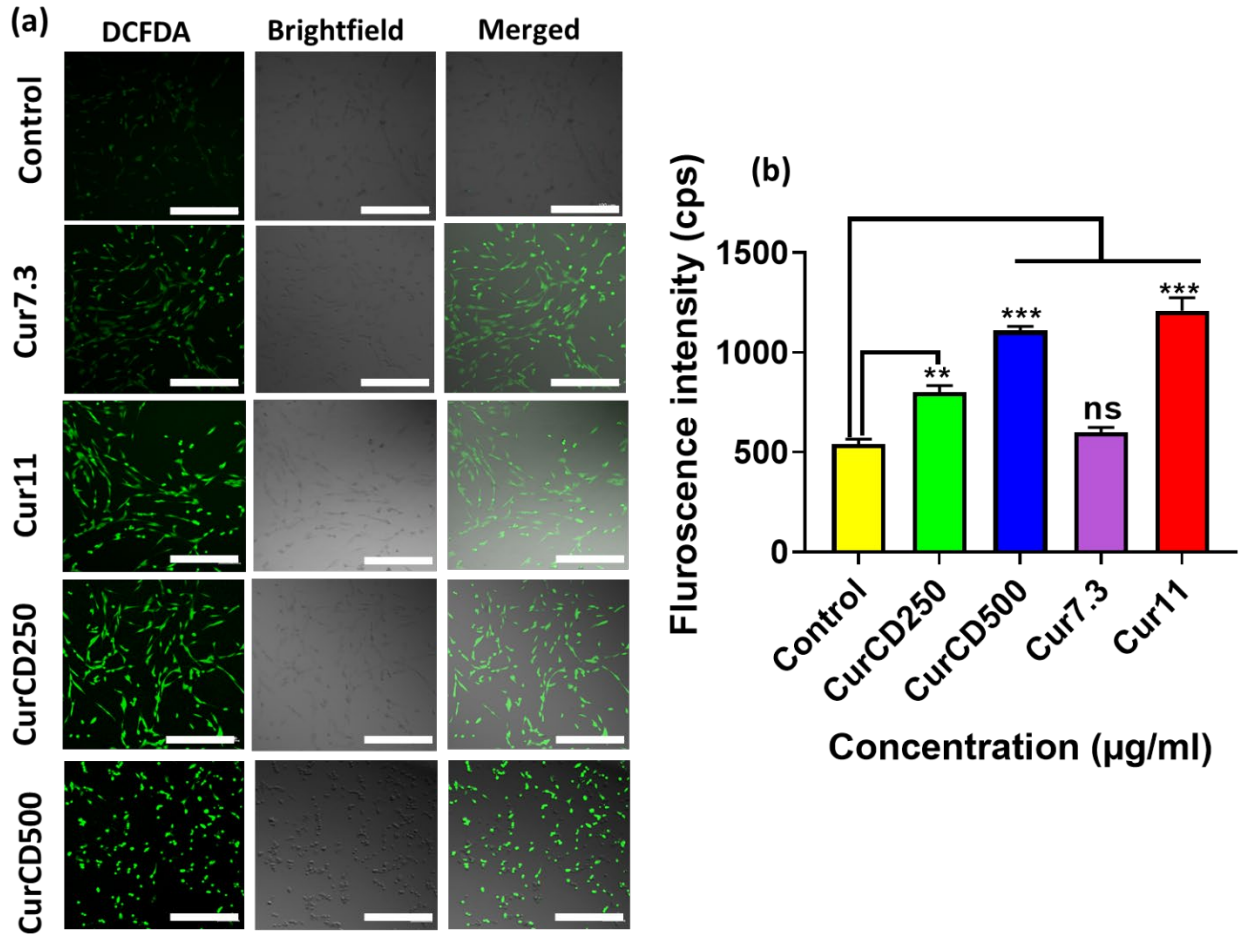

Figure 2.7: Effect of CurCD and curcumin on reactive oxygen species in C6 cells; (a) confocal microscopic images of untreated and treated cells, scale bar represents 200 µm (b) Quantification of DCFDA fluorescence data. The data is presented as the mean ± standard deviation. Data represents average values obtained from 3 experiments conducted in duplicate. *** Represents P value ≤0.001

2.3.7 Effect on cytoskeleton: Curcumin is reported to inhibit cancer cell proliferation through binding and destabilization of the cytoskeleton resulting in apoptosis in a wide range of cancer cell types including glioblastoma cells [57,30]. In normal cells, actin serves as an important contractile protein that is involved in maintaining the integrity of cell shape, cell growth and motility [58], while in tumour cells, it is known to regulate tumour relevant processes like cell cycle, morphogenesis or migration in cancer cells [59]. Curcumin is weakly fluorescent in aqueous solution, and on binding to actin, its fluorescence is enhanced several

folds due to a large blue shift in the emission maximum [60], enabling its visualization. To identify the influence of CurCD/curcumin on actin filament network, the treated cells (24 h) were additionally counterstained with rhodamine-conjugated phalloidin, a marker that specifically binds to F-actin filaments. Representative images of human fibroblasts treated with curcumin (0.18 μg ml^{-1}) / CurCD (500 μg ml^{-1}) is shown in Figure. 8I. The untreated fibroblasts served as control (Figure. 2.8I a–c). Phalloidin binding to actin filaments was confirmed by the red fluorescence and the nucleus was identified by blue Hoechst staining. CurCD and curcumin were observed to bind to the cytoskeleton. (Figure. 2.8I d and g) Since the binding patterns of CurCD (Figure. 2.8I d) and curcumin (Figure. 2.8I g) were similar to the respective phalloidin binding (Figure. 2.8I e and h), it can be concluded that both bind to actin filaments. An interesting observation noted with curcumin-treated cells was the presence of disrupted actin filaments (indicated with arrows). The results show that despite the use of non-toxic concentration of curcumin (interpreted from the proliferation data displayed in Figure. 2.4c), the presence of disrupted actin filaments would eventually result in cell death, confirming curcumin's cytotoxic effect on normal cells. Visualization of CurCD binding to the intact actin filaments, reaffirmed that it was non-cytotoxic (Figure. 2.8I d–f). A similar study was conducted with C6 cells. The cells were visualized following treatment with curcumin (11 μg ml^{-1}) or CurCD (250 μg ml^{-1}) respectively for 24 h. Figure. 8II displays the confocal images of the respective treated cells. In the untreated control cells like the fibroblasts, F-actin network was observed throughout the cell (Figure. 2.8II b and c). CurCD (Figure. 2.8II d) and curcumin (Figure. 2.8II g) binding to actin in the cells could be confirmed by a similar pattern of staining as that seen with Phalloidin (Figure. 2.8II e and h). Except for the presence of bright fluorescent actin fibres localized mainly at the outside edge of the cell, majority of the actin network in these cells were disrupted following treatment with CurCD/curcumin (Figure. 2.8II f and i). The distinct morphological changes observed in the treated cells could be the consequence of

the destabilisation of the actin filaments [61]. A similar observation was reported in curcumin-treated prostate cancer cells and lung carcinoma cells [62]. The inhibition in cell proliferation and migration observed in C6 cells treated with CurCD/Curcumin can be directly co-related with actin destabilization. In a recent study, F-actin was fluorescently labelled with cabon-dots conjugated to phalloidin [63]. Unlike this study, we demonstrate the direct ability of CurCD to fluorescently label F-actin.

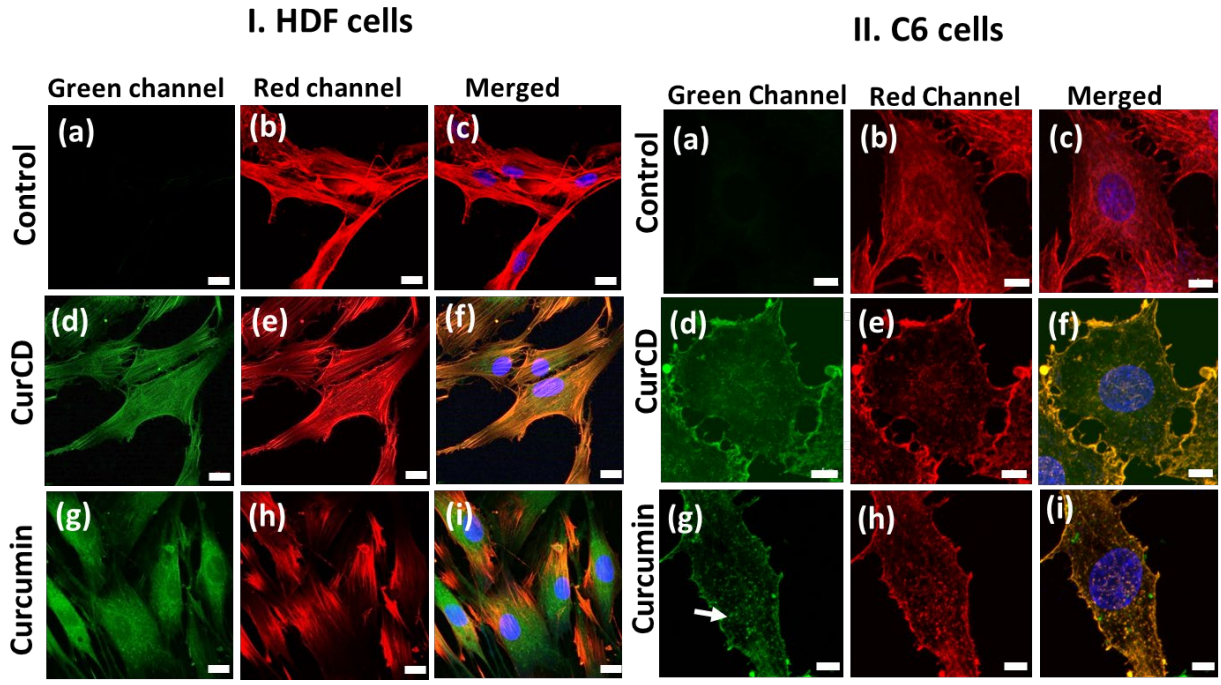

Figure 2.8: I. HDF cells treated with curcumin/CurCD. (a-c) Untreated control cells. (d-f) CurCD (250 µg ml^{-1}) treated cells and (g-i) Curcumin (0.368 µg ml^{-1}) –treated cells. II: C6 cells treated with curcumin/CurCD (a-c) Untreated control cells, (d-f) CurCD (250 µg ml^{-1}) treated and (g-i) Curcumin (11 µg ml^{-1}) treated cells. Green channel shows CurCD/curcumin attachment to actin filaments, Red channel shows actin filaments stained with Phalloidin. Scale bar represents 5 µM.

In addition, curcumin is reported to bind and disrupt the microtubule assembly in cancer cells [50]. To evaluate its effect on microtubules, the respective treated cells were further incubated with α-tubulin antibody. Curcumin was observed to bind to the microtubules, whereas CurCD

did not bind to tubulin. No significant change in tubulin structure was observed in HDF cells treated with CurCD/curcumin (Figure. 2.9I d–i) as compared to untreated control (Figure. 2.9I a–c). In contrast, C6 cells treated with CurCD displayed a drastic disruption in tubulin (Figure. 9II d–f), which was similarly evident in curcumin-treated cells (Figure. 2.9II g–i), although the effect was less dramatic than CurCD. The role of ROS in modifying the cytoskeleton and regulating the activity of proteins that are associated with cytoskeleton dynamics such as Rho GTPases is well recognized [64]. Recent studies have revealed that the unique structure of curcumin facilitated its binding directly close to the cytochalasin site in the cytoskelton and caused its perturbations [50]. While our results reveal the binding of CurCD to actin, the exact mechanism of binding is however not clear and warrants further investigation. Perhaps the carbonized curcumin, retains some of the structures that facilitated such binding. The cytoskeletal disturbances observed in C6 cells following treatment with CurCD can be however attributed to the increased ROS expression. Nevertheless, the ability of CurCD to directly bind to actin can serve as a powerful tool for cell imaging and to identify the status of cellular actin.

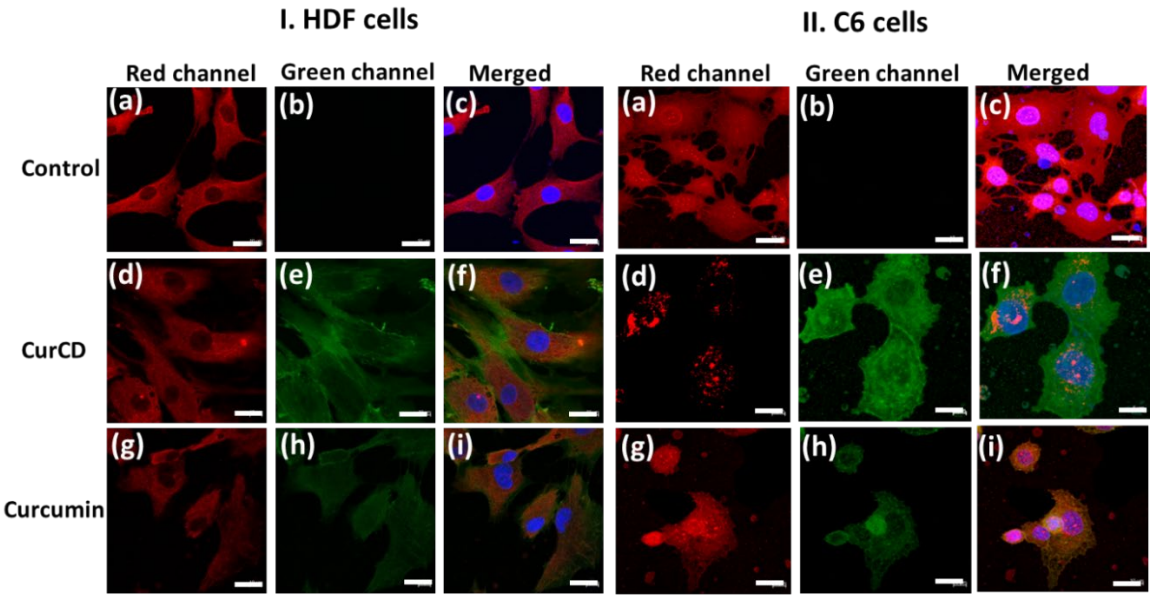

Figure 2.9: I. HDF cells treated with curcumin/CurCD. (a-c) Untreated control cells (d-f) CurCD (250 μg ml^{-1}) treated cells and (g-i) Curcumin (0.368 μg ml^{-1}) –treated cells. II: C6 cells treated with curcumin/CurCD (a-c) Untreated control cells, (d-f) CurCD (250 μg ml^{-1}) treated and (g-i) Curcumin (11 μg ml^{-1}) treated cells. Green channel shows CurCD /curcumin binding, red channel shows microtubules stained with tubulin polyclonal antibody. Scale bar represents 10 μM.

2.3.8 SEM analysis of C6 cells: SEM studies were conducted on C6 cells treated with either curcumin/CurCD for 24 h. As shown in (Figure. 2.10a), the surface of untreated control cells was smooth. In contrast, the cells treated with CurCD (Figure. 2.10b and c) and curcumin (Figure. 2.10d and e) showed a distorted morphology with membrane deformations that appeared as 'blebs' which are the typical signs of apoptotic cells [65]. This data further confirmed that cytoskeletal distortion induced by CurCD/curcumin treatment resulted in apoptosis.

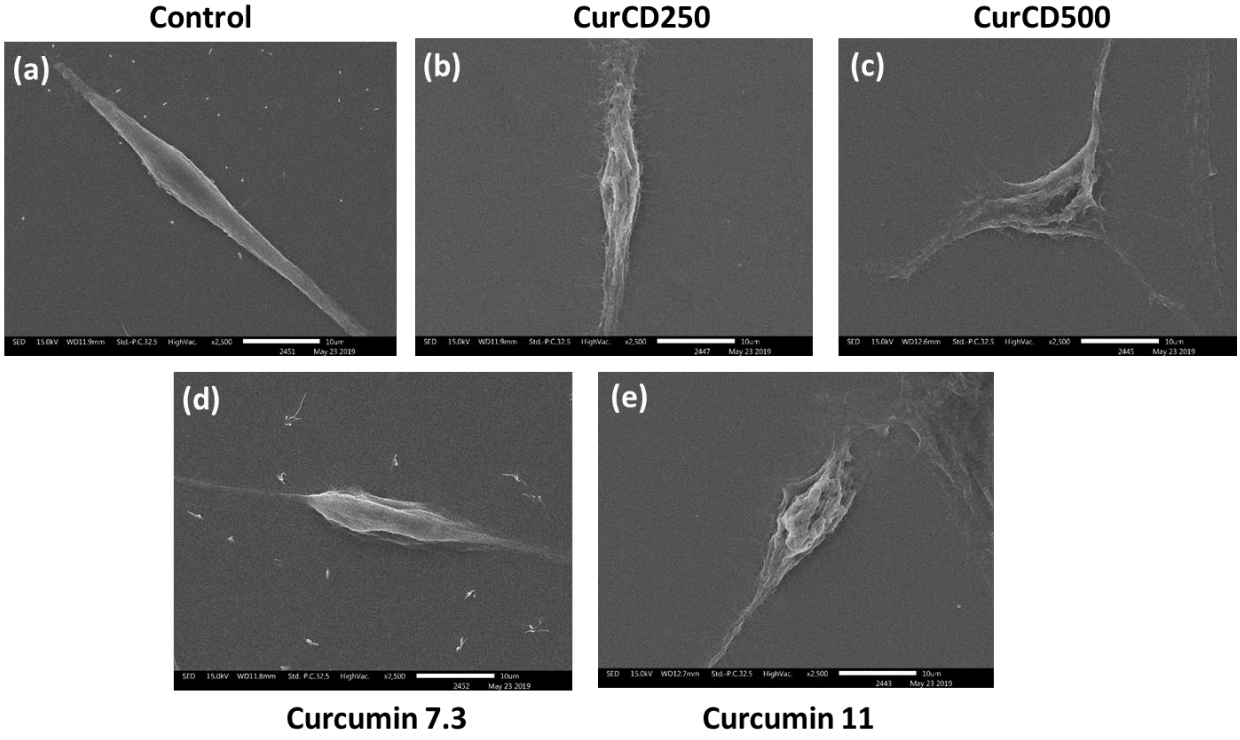

Figure 2.10: Change in cell morphology observed through Scanning electron microscopy; (a) control cells (no treatment), (b) CurCD 250 µg/ml, (c) CurCD 500 µg/ml, (d) Curcumin 7.3 µg/ml and (e) Curcumin 11 µg/ml. Scale bar represents 10 µM.

2.3.9 In vivo studies: The compatibility of CurCD/curcumin was checked using Zebrafish embryos as a bridge model between in vitro and in vivo studies [66]. Zebra fish embryos were exposed to CurCD (250/500 µg ml^{-1}) and curcumin (7.3/11 µg ml^{-1}) for 24 h post-fertilisation (hpf) to assess its effect on development. Untreated embryos served as control. At 24 hpf, the embryos were evaluated for mortality using a stereomicroscope. Respective images of the embryos at 24 hpf is displayed in (Figure. 2.11). As illustrated, the development of the embryos exposed to CurCD appeared to be similar to the untreated control. In contrast, the development of the embryos treated with curcumin (7.3 µg ml^{-1}) was delayed, while embryos treated with curcumin 11 µg ml^{-1} were dead. The toxic effect of curcumin on embryonic development of mouse blastocyst was also confirmed by Chia-Chi Chen et al. [67] and this effect was attributed to ROS generation. The results confirmed the biocompatibility of CurCD. Future studies to evaluate the pharmacokinetic behaviour of CurCD and efficacy in relevant in vivo models would help to compare its potential with curcumin for further clinical development.

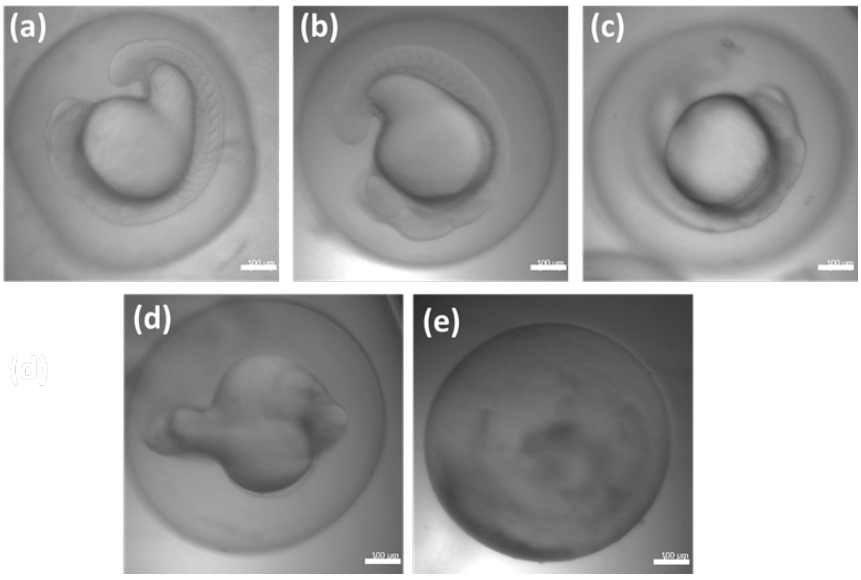

Figure 2.11: Effect of curcumin/CurCD on zebrafish embryo; (a) control cells (no treatment), (b) CurCD 250 µg ml^{-1}, (c) CurCD 500 µg ml^{-1}, (d) Curcumin 7.3 µg ml^{-1} and (e) Curcumin 11 µg ml^{-1}. Scale bar represents 10 µM.

2.4 Conclusion: In summary, we present carbon dots (CurCD) prepared with curcumin as a carbon source. CurCD was extensively characterized and found to be highly photo stable. The fluorescent CurCD had a higher quantum efficiency as compared to curcumin. In contrast to curcumin, the as synthesized carbon dots had better solubility, stability and biocompatibility. The anti-cancer properties of CurCD were comparable to curcumin, as evidenced by its anti-proliferative, apoptotic and anti-migratory activities in GBM cells. While the exact mechanism responsible for the biological activities of CurCD is not clear, the role of ROS in influencing the anti-cancer activity is nevertheless evident. In contrast to curcumin, CurCD did not affect normal cells, indicating the latter's safety profile. In addition, the unique ability of CurCD to selectively bind to the actin filaments of cells make it ideal for assessing the status of the cell cytoskeleton, apart from live cell imaging.

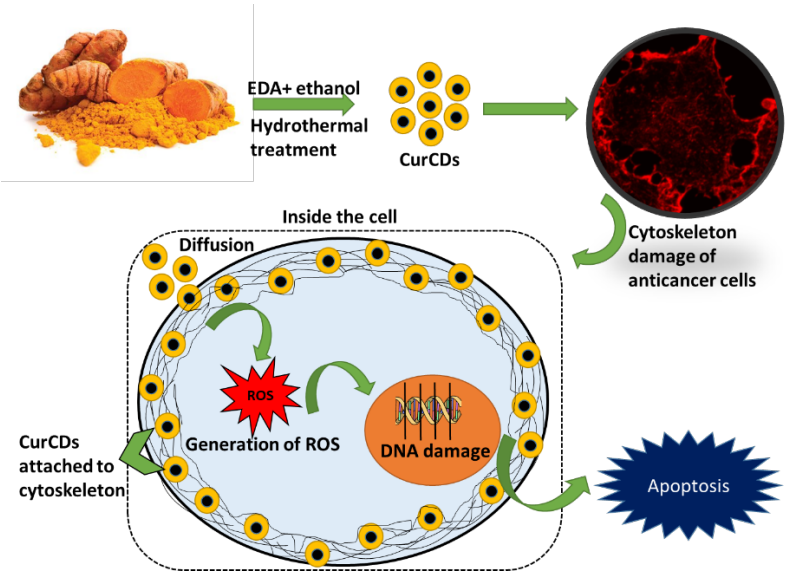

Effect of CurCD on glioblastoma cells

Bibliography

1. B.B. Aggarwal, C. Sundaram, N. Malani, H. Ichikawa, Curcumin: The Indian Solid Gold, the Molecular Targets and Therapeutic Uses of Curcumin in Health and Disease, Springer (2007), pp. 1-75.
2. A. Giordano, G. Tommonaro, Curcumin and cancer, Nutrients, 11 (2019), p. 2376.
3. B.L. Tan, M.E. Norhaizan, Curcumin combination chemotherapy: the implication and efficacy in cancer, Molecules, 24 (2019), p. 2527.
4. J. Zhao, J. Zhu, X. Lv, J. Xing, S. Liu, C. Chen, Y. Xu, Curcumin potentiates the potent antitumor activity of ACNU against glioblastoma by suppressing the PI3K/AKT and NF-κB/COX-2 signaling pathways, Onco. Ther. , 10 (2017), p. 5471.
5. K.M. Nelson, J.L. Dahlin, J. Bisson, J. Graham, G.F. Pauli, M.A. Walters, The essential medicinal chemistry of curcumin: mini perspective, J. Med. Chem., 60 (2017), pp. 1620-1637.
6. Z. Shabaninejad, M.H. Pourhanifeh, A. Movahedpour, R. Mottaghi, A. Nickdasti, E. Mortezapour, A. Shafiee, S. Hajighadimi, S. Moradizarmehri, M. Sadeghian, Therapeutic potentials of curcumin in the treatment of glioblstoma, Eur. J. Med. Chem., 188 (2020), p. 112040.
7. M. Bottini, C. Balasubramanian, M.I. Dawson, A. Bergamaschi, S. Bellucci, T. Mustelin, Isolation and characterization of fluorescent nanoparticles from pristine and oxidized electric arc-produced single-walled carbon nanotubes, J. Phys. Chem. B, 110 (2006), pp. 831-836.
8. Y. Su, Z. Xie, M. Zheng, Carbon dots with concentration-modulated fluorescence: aggregation-induced multicolor emission, J. Colloid Interface Sci. (2020).
9. Y. Zhou, K.J. Mintz, L. Cheng, J. Chen, B.C. Ferreira, S.D. Hettiarachchi, P.Y. Liyanage, E.S. Seven, N. Miloserdov, R.R. Pandey, Direct conjugation of distinct carbon dots as Lego-like building blocks for the assembly of versatile drug nanocarriers, J. Colloid Interface Sci. (2020).
10. J. Wang, J. Qiu, A review of carbon dots in biological applications, J. Mater. Sci., 51 (2016), pp. 4728-4738.
11. J. Wang, J. Qiu, A review of carbon dots in biological applications, J. Mater. Sci., 51 (2016), pp. 4728-4738.

12. X. He, Q. Luo, J. Zhang, P. Chen, H.-J. Wang, K. Luo, X.-Q. Yu, Gadolinium-doped carbon dots as nano-theranostic agents for MR/FL diagnosis and gene delivery, Nanoscale, 11 (2019), pp. 12973-12982.
13. N. Wang, A.-Q. Zheng, X. Liu, J.-J. Chen, T. Yang, M.-L. Chen, J.-H. Wang, Deep eutectic solvent-assisted preparation of nitrogen/chloride-doped carbon dots for intracellular biological sensing and live cell imaging, ACS Appl. Mater. Interfaces, 10 (2018), pp. 7901-7909.
14. M. Xue, J. Zhao, Z. Zhan, S. Zhao, C. Lan, F. Ye, H. Liang, Dual functionalized natural biomass carbon dots from lychee exocarp for cancer cell targetable near-infrared fluorescence imaging and photodynamic therapy, Nanoscale, 10 (2018), pp. 18124-1813.
15. X. Peng, R. Wang, T. Wang, W. Yang, H. Wang, W. Gu, L. Ye, Carbon dots/Prussian blue satellite/core nanocomposites for optical imaging and photothermal therapy, ACS Appl. Mater. Interfaces, 10 (2018), pp. 1084-1092.
16. Z. Kang, S.-T. Lee, Carbon dots: advances in nanocarbon applications, Nanoscale, 11 (2019), pp. 19214-19224.
17. N. Vasimalai, V. Vilas-Boas, J. Gallo, M. de Fátima Cerqueira, M. Menéndez-Miranda, J.M. Costa-Fernández, L. Diéguez, B. Espiña, M.T. Fernández-Argüelles, Green synthesis of fluorescent carbon dots from spices for in vitro imaging and tumour cell growth inhibition, Beilstein J. Nanotechnol., 9 (2018), pp. 530-544.
18. L.M. DeAngelis, Global consequences of malignant CNS tumours: a call to action. Lancet Neurol., 18 (2019), pp. 324-325.
19. L.A. Sordillo, P.P. Sordillo, L. Helson, Curcumin for the treatment of glioblastoma, Anticancer Res., 35 (2015), pp. 6373-6378.
20. A. Zanotto-Filho, K. Coradini, E. Braganhol, R. Schröder, C.M. De Oliveira, A. Simões-Pires, A.M.O. Battastini, A.R. Pohlmann, S.S. Guterres, C.M. Forcelini, Curcumin-loaded lipid-core nanocapsules as a strategy to improve pharmacological efficacy of curcumin in glioma treatment, Eur. J. Pharm. Biopharm., 83 (2013), pp. 156-167.
21. K.J. Lim, S. Bisht, E.E. Bar, A. Maitra, C.G. Eberhart, A polymeric nanoparticle formulation of curcumin inhibits growth, clonogenicity and stem-like fraction in malignant brain tumors, Cancer Biol. Ther., 11 (2011), pp. 464-473.

22. A. Hesari, M. Rezaei, M. Rezaei, M. Dashtiahangar, M. Fathi, J.G. Rad, F. Momeni, A. Avan, F. Ghasemi, Effect of curcumin on glioblastoma cells, J. Cell. Physiol., 234 (2019), pp. 10281-10288.
23. C.J. Lin, L. Chang, H.W. Chu, H.J. Lin, P.C. Chang, R.Y. Wang, B. Unnikrishnan, J.Y. Mao, S.Y. Chen, C.C. Huang, High amplification of the antiviral activity of curcumin through transformation into carbon quantum dots, Small, 15 (2019), p. 1902641.
24. A.B. Kunnumakkara, D. Bordoloi, G. Padmavathi, J. Monisha, N.K. Roy, S. Prasad, B.B. Aggarwal, Curcumin, the golden nutraceutical: multitargeting for multiple chronic diseases, Br. J. Pharmacol., 174 (2017), pp. 1325-1348.
25. A. Sharma, V. Panwar, V. Chopra, J. Thomas, S. Kaushik, D. Ghosh, Interaction of carbon dots with endothelial cells: implications for biomedical applications, Acs Appl. Nano Mater., 2 (2019), pp. 5483-5491.
26. M.H. Khosropanah, A. Dinarvand, A. Nezhadhosseini, A. Haghighi, S. Hashemi, F. Nirouzad, S. Khatamsaz, M. Entezari, M. Hashemi, H. Dehghani, Analysis of the antiproliferative effects of curcumin and nanocurcumin in MDA-MB231 as a breast cancer cell line, Iran. J. Pharm. Res.: IJPR, 15 (2016), p. 231
27. C. Zhang, Y. Hao, L. Wu, X. Dong, N. Jiang, B. Cong, J. Liu, W. Zhang, D. Tang, M. De Perrot, Curcumin induces apoptosis and inhibits angiogenesis in murine malignant mesothelioma, Int. J. Oncol., 53 (2018), pp. 2531-2541.
28. N. Abe-Fukasawa, K. Otsuka, A. Aihara, N. Itasaki, T. Nishino, Novel 3D liquid cell culture method for anchorage-independent cell growth, cell imaging and automated drug screening, Sci. Rep., 8 (2018), pp. 1-12.
29. V. Janson, P. Behnam-Motlagh, R. Henriksson, P. Hörstedt, K.G. Engström, K. Grankvist, Phase-contrast microscopy studies of early cisplatin-induced morphological changes of malignant mesothelioma cells and the correspondence to induced apoptosis, Exp. Lung Res., 34 (2008), pp. 49-67.
30. S. Khan, A. Sharma, S. Ghoshal, S. Jain, M.K. Hazra, C.K. Nandi, Small molecular organic nanocrystals resemble carbon nanodots in terms of their properties, Chem. Sci., 9 (2018), pp. 175-180.
31. L. Wang, Y. Wang, T. Xu, H. Liao, C. Yao, Y. Liu, Z. Li, Z. Chen, D. Pan, L. Sun, Gram-scale synthesis of single-crystalline graphene quantum dots with superior optical properties, Nat. Commun., 5 (2014), pp. 1-9.
32. J. Yang, G. Gao, X. Zhang, Y.-H. Ma, X. Chen, F.-G. Wu, One-step synthesis of carbon dots with bacterial contact-enhanced fluorescence emission: fast Gram-type

identification and selective Gram-positive bacterial inactivation, Carbon, 146 (2019), pp. 827-839.

33. C.J. Shearer, A.D. Slattery, A.J. Stapleton, J.G. Shapter, C.T. Gibson, Accurate thickness measurement of graphene, Nanotechnology, 27 (2016), p. 125704.
34. Z. Yang, M. Xu, Y. Liu, F. He, F. Gao, Y. Su, H. Wei, Y. Zhang, Nitrogen-doped, carbon-rich, highly photoluminescent carbon dots from ammonium citrate, Nanoscale, 6 (2014), pp. 1890-1895.
35. F. Ehrat, S. Bhattacharyya, J. Schneider, A. Löf, R. Wyrwich, A.L. Rogach, J.K. Stolarczyk, A.S. Urban, J. Feldmann, Tracking the source of carbon dot photoluminescence: aromatic domains versus molecular fluorophores, Nano Lett., 17 (2017), pp. 7710-7716.
36. H. Nie, M. Li, Q. Li, S. Liang, Y. Tan, L. Sheng, W. Shi, S.X.-A. Zhang, Carbon dots with continuously tunable full-color emission and their application in ratiometric pH sensing, Chem. Mater., 26 (2014), pp. 3104-3112.
37. S. Panja, S. Behera, S.C. Kundu, M. Halder, Optical spectroscopic and morphological characterizations of curcuminized silk biomaterials: a perspective from drug stabilization, ACS Omega, 2 (2017), pp. 6755-6767.
38. P. Khandelwal, A. Alam, A. Choksi, S. Chattopadhyay, P. Poddar, Retention of anticancer activity of curcumin after conjugation with fluorescent gold quantum clusters: an in vitro and in vivo xenograft study, ACS Omega, 3 (2018), pp. 4776-4785.
39. Y. Dong, H. Pang, H.B. Yang, C. Guo, J. Shao, Y. Chi, C.M. Li, T. Yu, Carbon-based dots co-doped with nitrogen and sulfur for high quantum yield and excitation-independent emission, Angew. Chemie Int. Ed., 52 (2013), pp. 7800-7804.
40. P. Sanphui, N.R. Goud, U.R. Khandavilli, S. Bhanoth, A. Nangia, New polymorphs of curcumin, Chem. Commun., 47 (2011), pp. 5013-5015.
41. L. Vallan, E.P. Urriolabeitia, F. Ruipérez, J.M. Matxain, R. Canton-Vitoria, N. Tagmatarchis, A.M. Benito, W.K. Maser, Supramolecular-enhanced charge transfer within entangled polyamide chains as the origin of the universal blue fluorescence of polymer carbon dots, J. Am. Chem. Soc., 140 (2018), pp. 12862-12869.
42. P. Sanphui, G. Bolla, Curcumin, a biological wonder molecule: a crystal engineering point of view, Cryst. Growth Des., 18 (2018), pp. 5690-5711.
43. S. Qu, D. Zhou, D. Li, W. Ji, P. Jing, D. Han, L. Liu, H. Zeng, D. Shen, Toward efficient orange emissive carbon nanodots through conjugated sp2-domain controlling and surface charges engineering, Adv. Mater., 28 (2016), pp. 3516-3521.

44. Y. Wang, X. Ying, H. Xu, H. Yan, X. Li, H. Tang, The functional curcumin liposomes induce apoptosis in C6 glioblastoma cells and C6 glioblastoma stem cells in vitro and in animals, Int. J. Nanomed., 12 (2017), p. 1369.
45. Z.C. Gersey, G.A. Rodriguez, E. Barbarite, A. Sanchez, W.M. Walters, K.C. Ohaeto, R.J. Komotar, R.M. Graham, Curcumin decreases malignant characteristics of glioblastoma stem cells via induction of reactive oxygen species, BMC Cancer, 17 (2017), pp. 1-11.
46. A. Muscella, C. Vetrugno, F. Fanizzi, C. Manca, S. De Pascali, S. Marsigliante, A new platinum (II) compound anticancer drug candidate with selective cytotoxicity for breast cancer cells, Cell Death Dis., 4 (2013), e796-e796.
47. N. Kianvash, A. Bahador, M. Pourhajibagher, H. Ghafari, V. Nikoui, S.M. Rezayat, A.R. Dehpour, A. Partoazar, Evaluation of propylene glycol nanoliposomes containing curcumin on burn wound model in rat: biocompatibility, wound healing, and anti-bacterial effects, Drug Deliv. Transl. Res., 7 (2017), pp. 654-663.
48. K.P. Lee, J.E. Kim, W.H. Park, H. Hong, Regulation of C6 glioma cell migration by thymol, Oncol. Lett., 11 (2016), pp. 2619-2624.
49. C. Senft, M. Polacin, M. Priester, V. Seifert, D. Kögel, J. Weissenberger, The nontoxic natural compound Curcumin exerts anti-proliferative, anti-migratory, and anti-invasive properties against malignant gliomas, BMC Cancer, 10 (2010), pp. 1-8.
50. S. Chakraborti, L. Das, N. Kapoor, A. Das, V. Dwivedi, A. Poddar, G. Chakraborti, M. Janik, G. Basu, D. Panda, Curcumin recognizes a unique binding site of tubulin, J. Med. Chem., 54 (2011), pp. 6183-6196.
51. K. Shin, H. Shin, H.J. Cho, H. Kang, J.-K. Lee, Y.J. Seo, Y.J. Shin, D. Kim, H. Koo, D.-S. Kong, Sphere-forming culture for expanding genetically distinct patient-derived glioma stem cells by cellular growth rate screening, Cancers, 12 (2020), p. 549.
52. C. Sarisozen, S. Dhokai, E.G. Tsikudo, E. Luther, I.M. Rachman, V.P. Torchilin, Nanomedicine based curcumin and doxorubicin combination treatment of glioblastoma with scFv-targeted micelles: In vitro evaluation on 2D and 3D tumor models, Eur. J. Pharm. Biopharm., 108 (2016), pp. 54-67.
53. H. Kinugasa, K.A. Whelan, K. Tanaka, M. Natsuizaka, A. Long, A. Guo, S. Chang, S. Kagawa, S. Srinivasan, M. Guha, Mitochondrial SOD2 regulates epithelial–mesenchymal transition and cell populations defined by differential CD44 expression, Oncogene, 34 (2015), pp. 5229-5239.

54. C.-Z. Qin, X. Zhang, L.-X. Wu, C.-J. Wen, L. Hu, Q.-L. Lv, D.-Y. Shen, H.-H. Zhou, Advances in molecular signaling mechanisms of β-phenethyl isothiocyanate antitumor effects, J. Agric. Food Chem., 63 (2015), pp. 3311-3322.
55. C. Rana, H. Piplani, V. Vaish, B. Nehru, S. Sanyal, Downregulation of PI3-K/Akt/PTEN pathway and activation of mitochondrial intrinsic apoptosis by Diclofenac and Curcumin in colon cancer, Mol. Cell. Biochem., 402 (2015), pp. 225-241.
56. S. Guerrero, M. Inostroza-Riquelme, P. Contreras-Orellana, V. Diaz-Garcia, P. Lara, A. Vivanco-Palma, A. Cárdenas, V. Miranda, P. Robert, L. Leyton, Curcumin-loaded nanoemulsion: a new safe and effective formulation to prevent tumor reincidence and metastasis, Nanoscale, 10 (2018), pp. 22612-22622.
57. J. Holy, Curcumin inhibits cell motility and alters microfilament organization and function in prostate cancer cells, Cell Motil. Cytoskeleton, 58 (2004), pp. 253-268.
58. D.A. Fletcher, R.D. Mullins, Cell mechanics and the cytoskeleton, Nature, 463 (2010), pp. 485-492.
59. A. Hall, The cytoskeleton and cancer, Cancer Metastasis Rev., 28 (2009), pp. 5-14.
60. G. Dhar, D. Chakravarty, J. Hazra, J. Dhar, A. Poddar, M. Pal, P. Chakrabarti, A. Surolia, B. Bhattacharyya, Actin–curcumin interaction: Insights into the mechanism of actin polymerization inhibition, Biochemistry, 54 (2015), pp. 1132-1143.
61. M. Izdebska, W. Zielińska, D. Grzanka, M. Gagat, The role of actin dynamics and actin-binding proteins expression in epithelial-to-mesenchymal transition and its association with cancer progression and evaluation of possible therapeutic targets, Biomed Res. Int., 2018 (2018).
62. P.H. Killian, E. Kronski, K.M. Michalik, O. Barbieri, S. Astigiano, C.P. Sommerhoff, U. Pfeffer, A.G. Nerlich, B.E. Bachmeier, Curcumin inhibits prostate cancer metastasis in vivo by targeting the inflammatory cytokines CXCL1 and-2, Carcinogenesis, 33 (2012), pp. 2507-2519.
63. E. Butkevich, N.C. Verma, N. Oleksiievets, I. Gregor, C.F. Schmidt, C.K. Nandi Enderlein Jr., A.I. Chizhik, Carbon dots for studying muscle architecture, ACS Appl. Nano Mater., 2 (2019), pp. 7466-7472.
64. A. Stanley, K. Thompson, A. Hynes, C. Brakebusch, F. Quondamatteo, NADPH oxidase complex-derived reactive oxygen species, the actin cytoskeleton, and Rho GTPases in cell migration, Antioxid. Redox Signal., 20 (2014), pp. 2026-2042.

65. P. Acedo, J. Stockert, M. Cañete, A. Villanueva, Two combined photosensitizers: a goal for more effective photodynamic therapy of cancer, Cell Death Dis., 5 (2014), e1122-e1122.
66. C. Dias, N. Vasimalai, M.P. Sárria, I. Pinheiro, V. Vilas-Boas, J. Peixoto, B. Espiña, Biocompatibility and bioimaging potential of fruit-based carbon dotsNanomaterials, 9 (2019), p. 199.
67. C.-C. Chen, W.-H. Chan, Injurious effects of curcumin on maturation of mouse oocytes, fertilization and fetal development via apoptosis, Int. J. Mol. Sci., 13 (2012), pp. 4655-4672.

Chapter 3: Wound healing activity of curcumin-derived carbon dots

3.1 Introduction: The skin is a crucial and largest organ of human body and serves as a shield to prevent direct contact with the external environment [1]. Continuous exposure to external stimuli, makes the skin highly vulnerable to injuries [2]. The healing of skin wounds is majorly divided into four well-orchestrated and continuous processes namely haemostasis, inflammation, proliferation, and remodelling [3]. However, wound healing can be delayed at any stage by multiple factors such as oxidative stress, diabetes, excessive bacterial load etc. [4].

Curcumin is a low molecular weight polyphenolic compound found in the Indian spice turmeric (*Curcuma longa*) [5]. Curcumin has shown its therapeutic potential in multiple diseases like cancer [6], diabetes [7], arthritis [8], Alzheimer [9], wound healing etc [10]. The wound healing potential of curcumin is mainly attributed to its antioxidant, anti-inflammatory and antimicrobial properties [11]. Curcumin has been characterized as a hormetic compound as it exhibits a dose-dependent biphasic effect .Several *in vitro* studies have established the biphasic property of curcumin [12-14]. Rattan *et al* have shown that curcumin encouraged wound healing at low doses (1-5 μM) while an opposite effect was observed at higher doses (above 10 μM) [15].

Despite the established therapeutic potential of curcumin, its application is being limited by its poor water solubility, susceptibility to degradation in the physiological environment, high rate of metabolism, and prompt systemic elimination [16] [17]. With the advent of nanoscience, it is possible to overcome the limitations of therapeutic molecules derived from natural sources [18]. Carbon dot, a relatively newest member of carbon nanomaterials family are being currently favoured because of their unique characteristics like water solubility, highly fluorescent nature and excellent biocompatibility [19]. Till date very few reports show carbon dots derived from natural sources to possess biological properties of the parent compound [20-22]. Previously, we had synthesised carbon dots (CurCD) from curcumin and ethylene diamine

which was superior to curcumin in terms of solubility, stability and fluorescence properties. In addition, the CurCD at higher concentrations was found to exhibit anticancer activity in glioblastoma cells which was comparable to curcumin [21].

As a hormetic compound, curcumin at lower concentrations induce a stimulatory effect on cells. To evaluate if CurCD had a similar hormetic effect like curcumin, we chose to compare the wound healing activity of curcumin in this study. Curcumin is known to modulate wound healing by encouraging fibroblasts migration and angiogenesis [23]. The effect of CurCD on fibroblasts and endothelial cells was evaluated using appropriate *in vitro* studies. To enable sustained delivery of CurCD at the wound site, a protease responsive hydrogel (GHCD) was developed using gelatin and CurCD served as a cross-linker. During the healing process, proteases secreted by the cells facilitate the removal of dead tissue facilitating tissue debridement, cell migration, tissue remodelling etc. We selected gelatin due to its susceptibility to protease [24]. On application of the GHCD hydrogel on the wound, we proposed that the proteases present at the wound site would degrade the hydrogel thus releasing the CurCD. The effect of the hydrogel on wound healing was confirmed using *in vivo* studies.

3.2 Material and methods

I Materials: Curcumin, ethylenediamine, bovine gelatin (Type B), DMSO, ethanol were procured from Sigma Aldrich, USA. DMEM, Medium 200, trypsin, phosphate buffered saline (PBS) (pH 7, 0.01 M), foetal bovine serum, (3-(4,5-dimethylthiazol-2-yl)-2,5-diphenyltetrazolium bromide (MTT), fluorescein diacetate (FDA) and propidium iodide (PI) solutions were purchased from Thermo Fisher Scientific, USA. Matrigel was procured from Corning, USA. Primers used in the QPCR study were supplied by Invitrogen, USA. All plastic-ware for tissue culture were procured from Invitrogen, USA. CD31, cytokeratin and Alexa flour 568 secondary antibodies were purchased from Invitrogen, USA.

II Experimental

3.2.1 Synthesis and characterization of CurCD: Curcumin derived carbon dots were synthesised as previously reported [21] and further characterized. UV–vis absorption spectra was recorded from 200 to 800 nm with a Shimadzu UV–vis 2600 spectrophotometer. Fluorescence spectra were recorded with an Edinburg FS 5 spectrofluorometer. The particle size of CurCD was measured with the help of TEM (JEOL JEM 2100). FTIR spectra was measured using a Bruker FTIR spectrophotometer.

3.2.2 Cell proliferation assay: The effect of CurCD on cell proliferation was checked using the 3-[4,5-Dimethylthiazol-2-yl]-2,5-diphenyltetrazolium bromide (MTT) assay as reported [25]. Human umbilical vein endothelial cells (HUVEC) and human dermal fibroblasts (HDF) were seeded in 96 well plate at a cell density of 2500 cells/well and incubated for 24 h at 37 °C in a 5 % CO_2 incubator. The cells were treated with different concentrations of curcumin and CurCD respectively in triplicates. After 24 h of treatment, MTT was added to each well and incubated for additional 3 h. Thereafter, 100 µl DMSO was added in each well and the optical density was recorded at 570 nm wavelength on a plate reader (Infinite M Plex (Tecan) multimode plate reader).

3.2.3 Cell uptake assay: To compare the cellular uptake and distribution of CurCD and curcumin, HUVEC/HDF were seeded in confocal dishes at a cell density of 1×10^5 cells/dish and incubated for 24 h. Thereafter, the cells were treated with either CurCD (100 µg/ml) or curcumin (0.18 µg/ml) for further 24 h. At the end of treatment, the cells were washed with PBS and subsequently fixed with 4 % paraformaldehyde solution for 5 min at room temperature. The fixed cells were then stained with Hoechst & Phalloidin and observed under a confocal microscope (LSM 880 confocal microscope, Zeiss) [25].

3.2.4 Cell migration assay: The migratory response of fibroblasts to CurCD (100 μg ml^{-1})/curcumin (0.18 μg ml^{-1}) was checked using a scratch assay. To investigate the migratory response human dermal fibroblasts were seeded in 12 well plate to form a monolayer. To avoid cell proliferation, the cells were serum starved and maintained in 2 % FBS during the entire experiment. Scratch was created with the help of sterile 20 μl pipette tip. After PBS rinse, media containing either CurCD or curcumin was added to the respective wells and incubated at 37 °C. Cells in the scratch area were counted at 0, 8 and 24 h. The scratch area was photographed at 4 × magnification using a digital camera mounted on a microscope. Covered scratch area was quantified using image J software.

3.2.5 *In vitro* angiogenesis assay: *In vitro* angiogenesis assay was performed using Matrigel as per our earlier reported protocol [25]. In short, 50 μl/well of matrigel was added in a 96-well plate. The HUVEC cells were harvested and labelled with a cell tracker (Dil, Cell Vibrant Invitrogen) dye as per the protocol specified by the company. After labelling, the cells were seeded at a cell density of 25 × 10^3 cells/well and curcumin (0.18 μg ml^{-1})/CurCD (100 μg ml^{-1}) was added and incubated in dark for 24 h at 37 °C in a CO_2 incubator. The cell images were captured by confocal microscope using red channel (Carl Zeiss) and quantified using ImageJ software.

3.2.6 ROS Assay: 2′,7′-Dichlorofluorescin diacetate (DCFDA) dye-based assay was used to measure intracellular ROS levels [21]. On uptake, DCFDA is oxidised in the presence of ROS to generate a fluorescent compound 2′,7′-dichlorofluorescein (DCF), which can be detected by fluorescence spectroscopy. For estimating the antioxidant potential, the cells were seeded in a 24-well plate at a cell density of 1 × 10^4 cells/well and stimulated with 1 % H_2O_2 and then treated with CurCD (100 μg ml^{-1}) / curcumin (0.18 μg ml^{-1}) for 24 h. The cells treated with only H_2O_2 served as positive control. At the end of 24 h, the cells were washed

with PBS and incubated with DCFH-DA dye for 30 min at 37 °C. Images were captured using confocal microscope and quantified by measuring the fluorescence intensity in a microplate reader.

3.2.7 NF-κB p65 translocation: NF-κB p65 translocation into the nucleus was checked through immunofluorescence assay as reported [25]. Briefly, the cells were seeded in confocal dishes and stimulated with 1 % H_2O_2 followed by treatment with CurCD (100 μg ml^{-1}) and curcumin (0.18 μg ml^{-1}) respectively. After 24 h, the cells were fixed with paraformaldehyde and the translocation of p65 unit into the nucleus was assessed using NFκB p65 antibody overnight at 4 °C. Alexa Fluor® 568 conjugated Superclonal™ was used as secondary antibody and Hoechst was used to stain the nucleus. Images were captured using confocal microscopy at a magnification of 63×.

3.2.8 Gene expression analysis: **A**ngiogenic gene profiling was performed by creating multiple scratches in the monolayer of HUVEC cells followed by treatment with curcumin (0.18 μg ml^{-1}) and CurCD (100 μg ml^{-1}) [26]. Untreated cells were taken as control. The angiogenic primers used were FGF2 (Hs00266645_m1), and VEGFA (Hs00900055_m1), PDGF: (Hs00966522_m1), GAPDH (Hs02786624-g1) (Applied Biosystems). In short, total RNA was harvested from the cells using RNA isolation kit. Obtained RNA was, was reverse transcribed to form cDNA using RNA to cDNA kit. After that to the mixture of qPCR mastermix, respective primers and Dnase free water, 1 μl of as prepared cDNA (equivalent amounts) was added. The amplification conditions were used for the gene analysis as per manufacturer's instructions. ΔCt value was calculated w.r.t to housekeeping gene *i.e.* GAPDH. Fold changes between various groups are represented using ΔΔCt values.

3.2.9 Antimicrobial activity: The antimicrobial activity of CurCD released from the hydrogels was determined using *E. coli* (IMTECH, Chandigarh, India). Briefly, the bacteria were cultured for 18 h at 37 °C in Luria Bertani broth and inoculated to get an initial loading of 2×10^5 CFU/ml. The bacterial cultures were treated with curcumin (0.18 μg ml^{-1}) and CurCD (100 μg ml^{-1}) for 24 h and the OD was measured at 600 nm. After 24 h, 100 μl of the supernatant was plated on an agar plate. The number of colony-forming units (CFUs) were counted after incubation for 16 h at 37 °C. Each test was carried out in triplicate. To differentiate between live and dead bacteria, Fluorescein diacetate (FDA) and propidium iodide (PI) were used respectively. CurCD/curcumin treated bacterial cultures were incubated with 100 μl of the dye-containing solution at room temperature in dark conditions for 30 min. To assess the viability of bacterial cells, samples were observed under a laser scanning confocal microscope (Zeiss, LSM 880) using red and green channel [27].

3.2.10 Preparation of GHCD hydrogels: Gelatin hydrogels were prepared using CurCD as cross-linking agent. Briefly, gelatin (5 g) was dissolved in 50 ml of phosphate buffered saline (PBS) and heated at 40 °C until a clear solution was obtained. To this, either 500 μg ml^{-1} (GHCD1) or 1000 μg ml^{-1} of CurCD (GHCD2) was added and stirred at 40 °C stirred overnight. The above solutions were cast in moulds and allowed to form hydrogels at room temperature. The hydrogels prepared without CurCD was denoted as blank hydrogel (GH).

3.2.11 Morphology, swelling ratio, and *in vitro* degradation of hydrogels: The morphological analysis of the GHCD hydrogels was done using FESEM. After freeze drying, the hydrogels were sputter coated and visualized under the FESEM (Jeol Ltd., Japan). Swelling properties of the hydrogels were checked using PBS at an ambient temperature condition [28]. Briefly, the hydrogels of definite weight were immersed in PBS and at every time point, PBS

was removed, the hydrogels were blotted with filter paper and weighed. The swelling ratio was calculated using the equation.

Swelling ratio= w_2-w_1/w_1 x100 (Equation 1)

Where w_1 and w_2 were the initial and swollen weight of the hydrogel

The degradation of the GHCD hydrogel was assessed in the absence/presence of proteases for 72 h. Briefly, pre-weighed GHCD hydrogels were incubated in a test tube and kept in PBS containing with or without proteases at 37 ^{0}C for 72 h. At the end of each time point, the PBS was removed, the hydrogel was dried and weighed. The above experiment was conducted in triplicate using same conditions. The degradation rate at different incubation times was evaluated using the given equation.

Degradation rate= w_t-w_o/w_o x100 (Equation 2)

Where w_t is the weight at that time point and w_0 is the initial weight of the hydrogel.

3.2.12 Rheological studies

The rheological behaviour of the respective hydrogels was checked using a modular Rheometer, MCR302 (AntonPaar, Austria) as reported [29]. Stress sweeps were performed at a constant frequency of 1 Hz in oscillatory rotational mode to find out the crossover point of storage (G') and loss (G'') moduli and the linear viscoelastic region (LVE) was determined. Frequency sweeps were performed to determine the storage (G') and loss (G'') modulus.

3.2.13 Cell attachment and proliferation in the hydrogels

To evaluate the ability of the hydrogel to support cell proliferation, human dermal fibroblasts were used [29]. Hydrogels were sterilised by immersing them in 70% alcohol and then washed twice with Dulbecco's buffered saline (DPBS). After sterilisation the hydrogels were incubated in DMEM media for 24 h. Human dermal fibroblasts (HDF) cells were seeded on the hydrogels at a cell density of 1X 10^4 cells. At various intervals, the cell viability was assessed using

FDA/PI using confocal laser scanning microscope (Zeiss LSM880 confocal microscope, Carl Zeiss). To quantify cell proliferation, alamar blue was added to each well and optical density of the media was determined at 570 nm using a plate reader (Infinite M Plex, Tecan) multimode plate reader.

3.2.14 *In vivo* studies

To compare the efficacy of CurCD2 hydrogel and curcumin on wound healing, an excision wound healing model was used. Male Sprague− Dawley (SD) rats weighing ~ 200-220 g were used in the study. The studies were performed with the permission of the Institutional Animal Ethics Committee of Maharishi Markandeshwar University, Mullana (Ambala), India. The wounds created on the dorsal side of the rats were treated with either curcumin / CurCD hydrogel respectively. Wounds covered with standard wound dressing (Tegaderm film-dressing, 3M-dressing) served as control group. Each group containing 6 animals were anesthetized using ketamine (100 mg/kg) and xylazine (10 mg/kg). A full-thickness wound was excised with the help of 10 mm biopsy punch and the wounds covered with respective treatments. The wounds were assessed on day 1, 3, 7 and 14. At the end of 14 days, all animals were sacrificed and the skin tissue were harvested for immunohistological and histological studies. Cryosections were stained with haemotoxylin and eosin as per standard protocol. For immunological staining, the sections were blocked with 5% bovine serum albumin for 2h followed by cytokeratin and CD31 antibodies respectively overnight at 4 ^{0}C. The secondary goat anti-rabbit antibody was used at 1: 200 at 37 ^{0}C for 1 h. The images were captured with confocal laser microscope (LSM 880, Zeiss).

3.2.15 Statistical analysis

The significance level in all statistical observations was set at a probability of $p < 0.05$. All the data is presented as mean ± SD. ANOVA was used to analyse the data and to calculate the significance level.

3.3 Results and discussion

3.3.1 CurCD characterization: The particle size of the synthesized CurCD was characterized using TEM. Quasispherical shape of the CurCD with an average size of 4 nm was observed as shown in Figure 3.1 (a&b). The UV–Vis absorption spectra of CurCD exhibited two absorption bands, one at 265 nm which corresponds to π–π* transition of conjugated C=C confirming the formation of graphitic carbon cores and the other at 345 nm–420 nm due to n–π* transition of C– O, indicating the existence of oxygen functionalities on CurCD (Figure 3.1 c) [37]. In the fluorescence study, CurCD revealed a typical excitation dependent emission behaviour. The maximum and minimum emission intensity at 450 nm and 530 nm of CurCD was observed due to excitation at 350 nm and 460 nm as shown in (Figure 3.1d). Such shifts in the emission peaks are suggestive of the presence of different emissive sites on the surface of CurCD [21] .

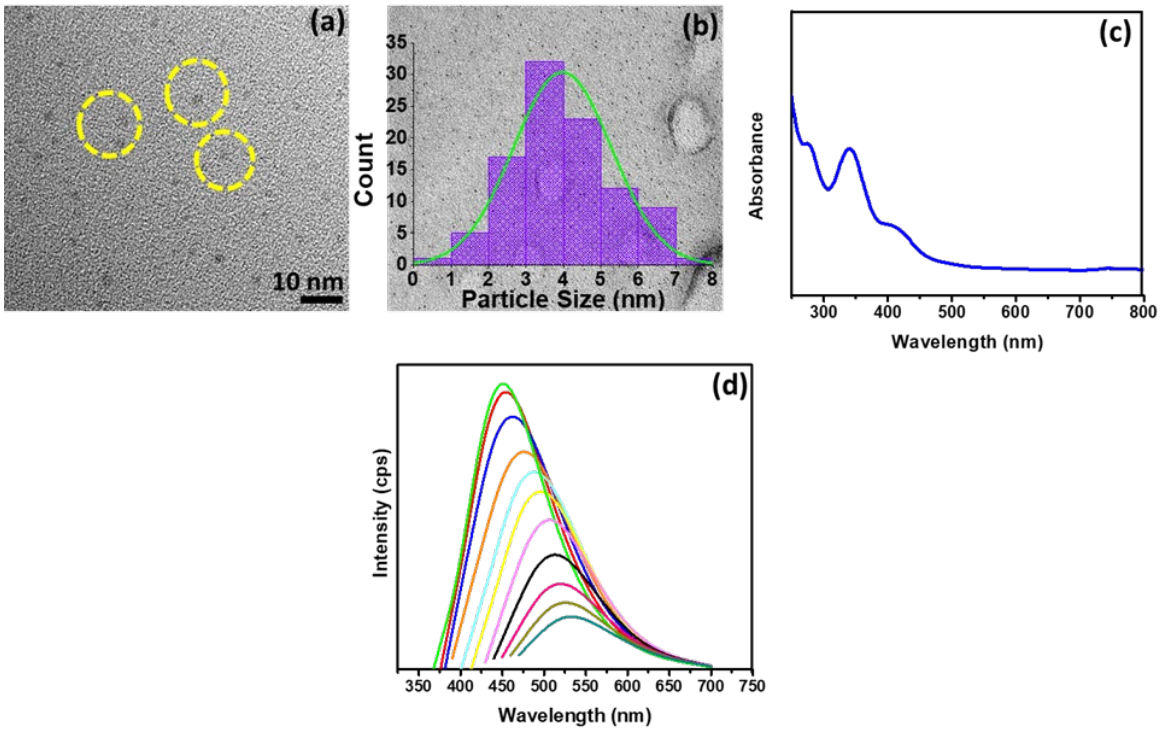

Figure 3.1: Physical characteristics of CurCD; (a) TEM (b) Size distribution of CurCD, (c) Uv-visible spectrum, (d) Photoluminescence emission spectrum.

3.3.2 Proliferative response of cells to CurCD: Multiple *in vitro* studies have shown the biphasic effect of curcumin in human skin cells [12]. In our previous study, we had established that CurCD retained the bioactivity of the parent compound curcumin with an additional improvement in solubility and stability [21]. Given the challenges facing in the use of curcumin in biological applications, we determined if CurCD possessed hormetic activity like curcumin. To explore if CurCD, like curcumin possess hormetic activity, we studied its effect on human umbilical vein endothelial cells (HUVEC) and human dermal fibroblasts (HDF). Angiogenesis is the formation of new blood vessels and has an important role both in wound healing as well as in cancers. Since the pro-angiogenic and anti-angiogenic activity of curcumin is dose-dependent [30], [31], we compared the angiogenic activity of CurCD with curcumin using endothelial cells. Curcumin treatment resulted in a biphasic response with the cellular proliferation being inhibited at higher concentrations, whereas an increase was observed at lower concentrations (Figure 3.2A i). Similar response was observed with CurCD on endothelial, suggesting that CurCD, like curcumin possess hermetic property (Figure 3.2A ii). The fluorescence of curcumin is reported to be enhanced several fold on binding to cytoskeleton in the cells [32]. Previously we had noted that on treatment of HDF cells with CurCD (250 μg ml^{-1}) and curcumin (0.368 μg ml^{-1}), the cytoskeleton of the cells could be visualized by fluorescence microscopy [21]. In contrast we observed that on treatment of HUVEC with curcumin (0.368 μg ml^{-1}) the cytoskeleton is not clearly visualized (Figure 3.2B). However due to the high fluorescence intensity of the CurCD, the cytoskeleton of CurCD treated cells could be clearly visualized even when treated at such low concentration (100 μg ml^{-1}). The higher fluorescence intensity of the CurCD confirms the superior photo physical properties of CurCD as compared to curcumin.

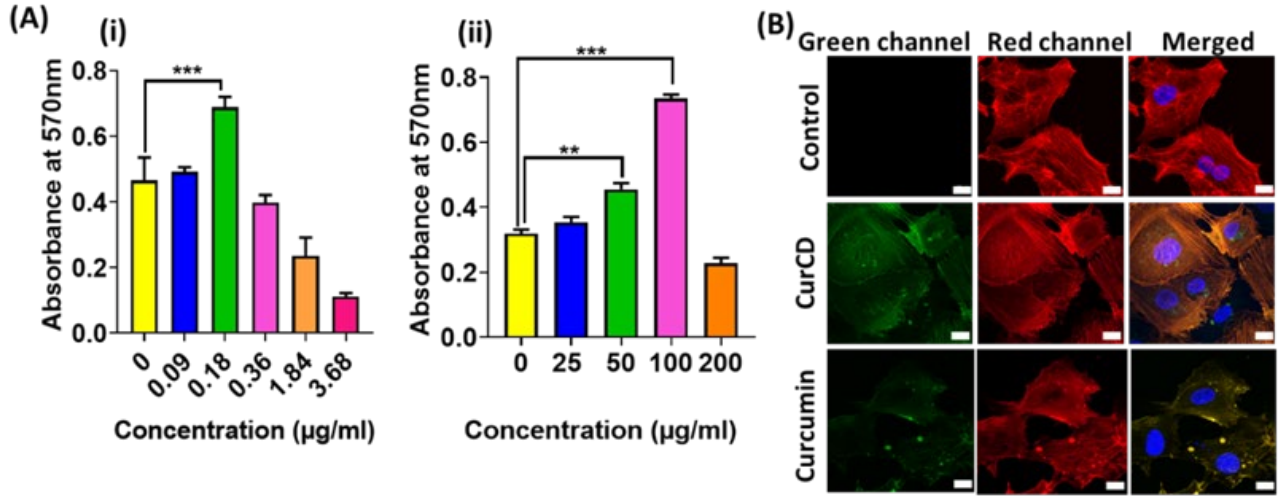

Figure 3.2: Proliferative response and cytoskeleton binding; (A) Effect of curcumin (i) and CurCD (ii) on the proliferation of HUVEC cells; (B) Cytoskeleton binding of curcumin and CurCD in HUVEC. Scale bar represents 10 µm. Data is represented as mean ± SD (n = 3). **P < 0.01, and ***P < 0.001.

3.3.3 Cell migration: Cellular migration is a dynamic biological event that occurs during the various phases of wound healing [3]. Curcumin is reported to increase fibroblast migration at lower concentrations [15]. Using a scratch model, we evaluated the migratory response of fibroblasts to curcumin (0.18 µg ml^{-1}) and CurCD (100 µg ml^{-1}) respectively for a period of 24 h. The concentration selected in this study was on the basis of the stimulatory response observed with the cells (Figure 3.2 A). Cell migration in the scratch area was monitored at 8 h and 24 h post-wound creation (Figure 3.3A). In comparison to untreated control and curcumin treated cells, the migration was initiated early and completed by 24 h in CurCD treated cells suggesting that it had a greater potential to induce cell migration. Figure 3.3B represents the percentage of the wound area filled with the fibroblasts at a given time point, indicating the significant improvement in fibroblasts migration treated with CurCD as compared to curcumin.

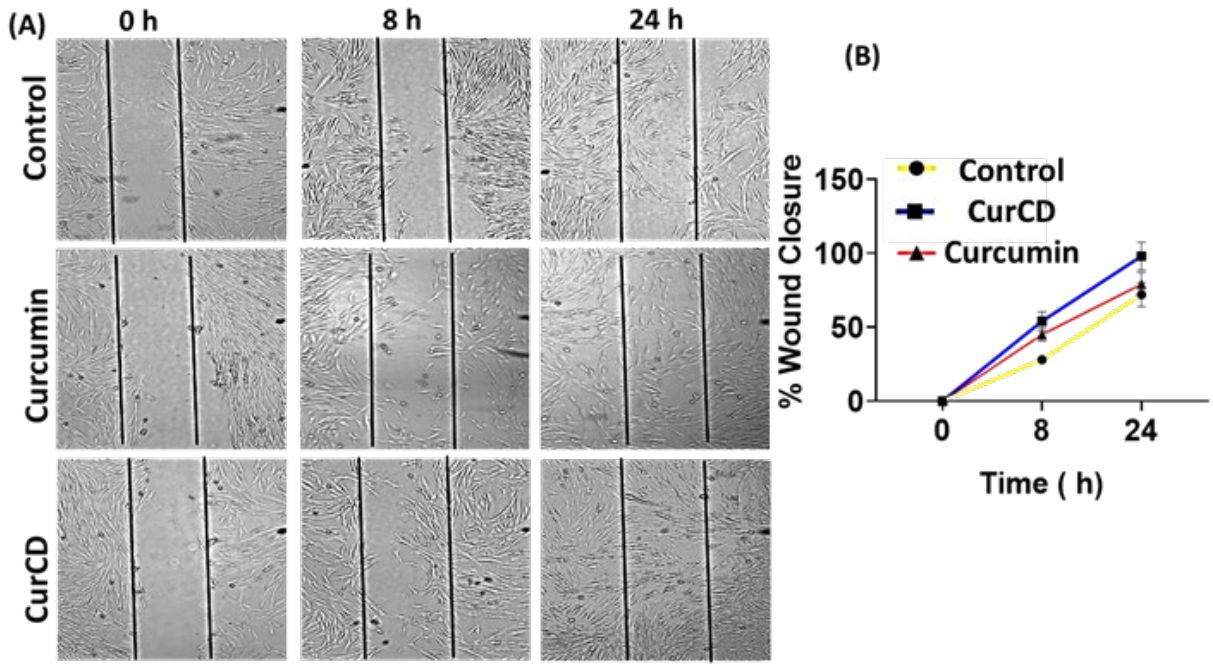

Figure 3.3: Cell migration. (A) Migratory response of fibroblasts treated with CurCD and curcumin at 0, 8 and 24 h respectively; untreated cells served as control. (B) Percentage wound closure at various time points. Data expressed represents the average of three experiments performed in triplicate. Scale bar represents 250 µm.

3.3.4 *In vitro* angiogenesis assay: Angiogenesis, an important aspect in wound healing is mediated by the release of various pro-angiogenic factors such as bFGF (basic fibroblast derived growth factor, VEGF (vascular endothelial growth factor) and PDGF (platelet derived growth factor). Kant *et al.* had observed that curcumin accelerated wound healing in diabetic rats by influencing the expression of VEGF, which leads to the formation of new blood vessels and promoted angiogenesis [30]. To explore the angiogenic response of CurCD, we used an *in vitro* matrigel model and compared the effect of CurCD with curcumin on the network formation by the HUVEC cells. Figure 3.4A represents the fluorescent images of network formation after 24 h of treatment with curcumin (0.18 µg/ml) and CurCD (100 µg/ml) respectively. Upon treatment with CurCD, extensive network formation was observed as compared to untreated and curcumin treated cells. Quantitative analysis of the network formation revealed that the number of branches (Figure 3.3B), number of rings (Figure 3.4C)

and length of the tubules (Figure 3.4D) formed on the surface of matrigel was significantly higher than the curcumin treatment. From the data, it can be inferred that CurCD induced a higher proangiogenic response than the curcumin.

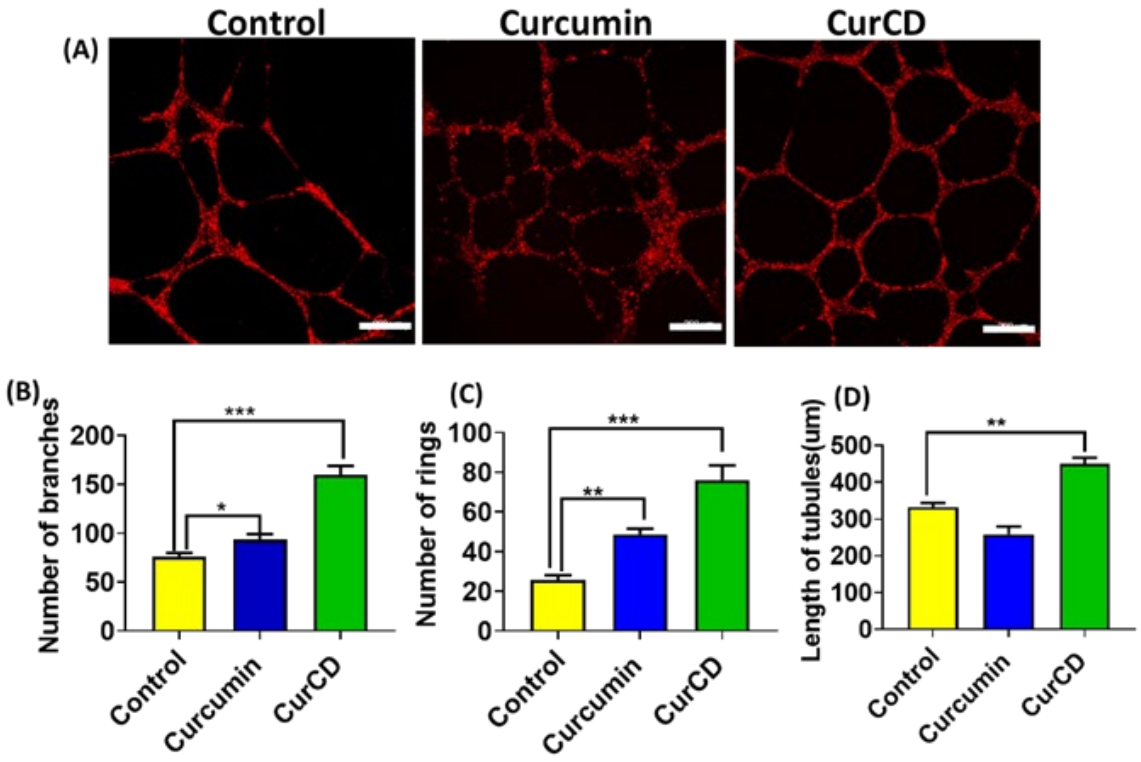

Figure 3.4: In vitro angiogenesis assay. (A) Confocal images of the network formation after 24 h of treatment. Scale bar represents 200 µm. Quantification of the network formation (n=6), (B) number of branches, (C) number of rings and (D) length of the tubules. *** represents P value ≤0.001, ** represents P value ≤0.01.

3.3.5 Intracellular ROS determination: Whereas optimal ROS is necessary during the inflammatory phase of wound healing, prolonged exposure of the cells to high level of ROS may lead to oxidative stress leading to delayed wound healing [33]. To check the ROS scavenging activity of CurCD, oxidative stress was induced in the cells with 0.001M H_2O_2 followed by treatment with curcumin/ CurCD respectively. As shown in Figure 3.5A, in H_2O_2 treated cells, the high fluorescence intensity of DCFDA indicates increased ROS activity. In comparison, the low fluorescent signals observed in both CurCD and curcumin treated cells

suggests efficient quenching of ROS. In comparison to curcumin, the fluorescence intensity was much lower in CurCD treated cells. Quantitative analysis of the fluorescence intensity indicated significant reduction in the ROS activity by CurCD as compared to curcumin (Figure 3.5B). This may be attributed to the improved uptake of CurCD in the cells as compared to curcumin. Several groups have attributed the antioxidant property of curcumin to its suppression of the NF-κB pathway [34]. NF-κB plays a pivotal role in activating the secretion of inflammatory mediators like interleukins and cytokines, which can delay wound healing. To compare the influence of CurCD treatment on NF-κB activation, the cells were activated with H_2O_2 followed by treatment with curcumin and CurCD respectively. As revealed in Figure 3.5C, p65 was identified in the nucleus of the H_2O_2 treated cells, suggesting activation of the NF-κB pathway. In contrast, p65 was observed in the cytoplasm of cells treated with both CurCD and curcumin. The ability to block oxidative responses by curcumin and CurCD would be beneficial for the wound healing process.

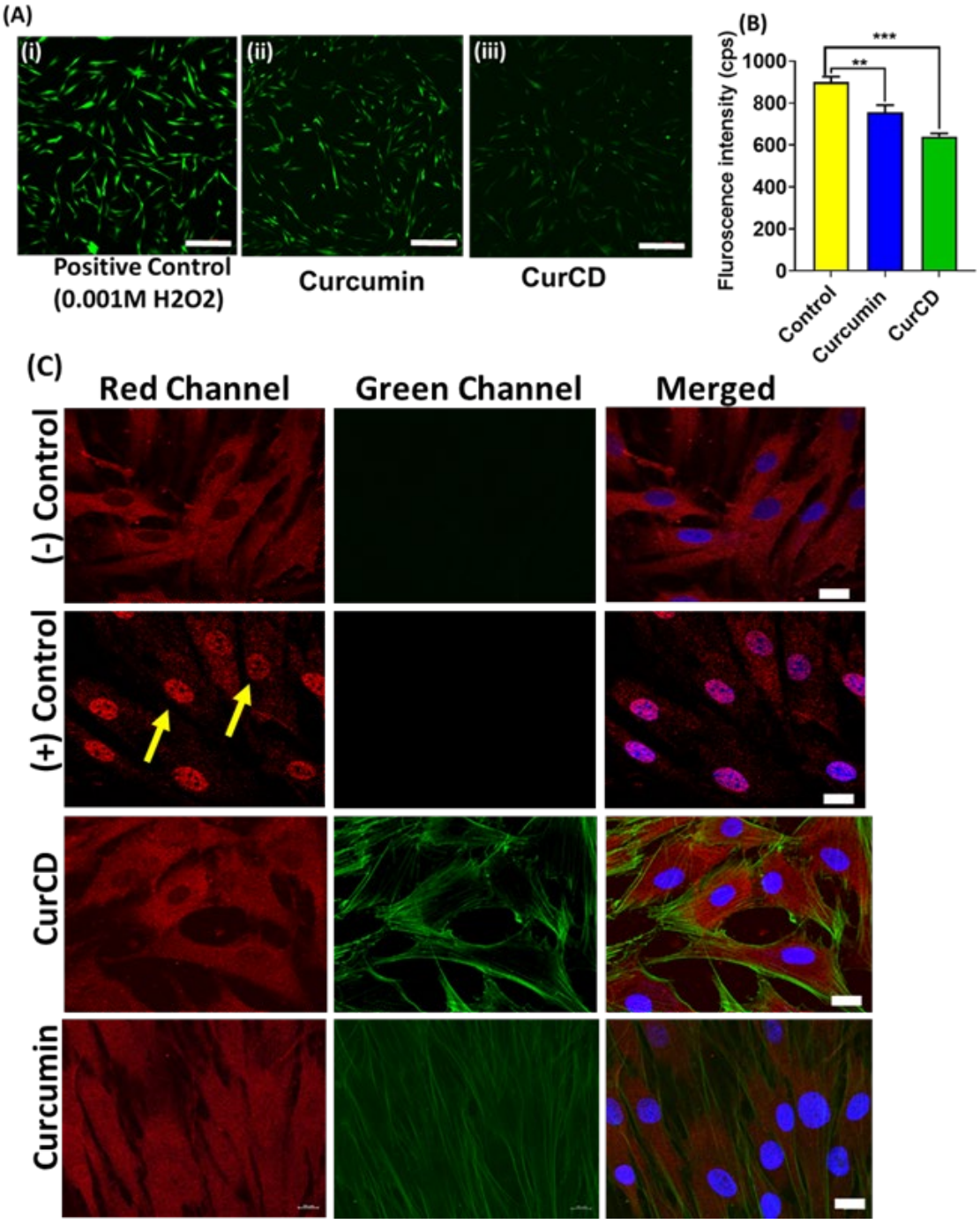

Figure 3.5: Antioxidant activity of CurCD: (A) ROS expression in activated and CurCD/curcumin cells. Scale bar represents 200 µm. (B) Quantitative analysis of ROS quenching activity after 24 h treatment, *** represents P value ≤0.001, ** represents P value ≤0.01 (C) Detection of p65 unit. Cells stimulated with H_2O_2, followed by CurCD/curcumin treatment. Unstimulated cells served as negative control. Yellow arrows indicate the translocation of p65 unit into the nucleus of stimulated cells. Scale bar represents 10 µm.

3.3.6 Mechanical stress induced angiogenic gene expression: In order to simulate the wound conditions during injury, we had subjected the endothelial cells to mechanical stress by creating multiple scratch wounds in the monolayer of HUVEC cells [26]. Post 24 h treatment, RNA was isolated from the cells for gene expression studies. HUVEC is known to express genes like VEGF, PDGF and FGF under stress conditions [26] [35]. QPCR studies revealed that CurCD significantly increased the expression of growth factors like PDGF VEGF and FGF in comparison to control and curcumin treated cells (Figure 3.6). A comparative increase in the expression of these genes in CurCD treated cells as compared to curcumin may be due to its better uptake in cells. As these growth factors are mainly responsible for migration and proliferation of cells during healing process, it can be assumed that CurCD could be efficient in inducing wound healing.

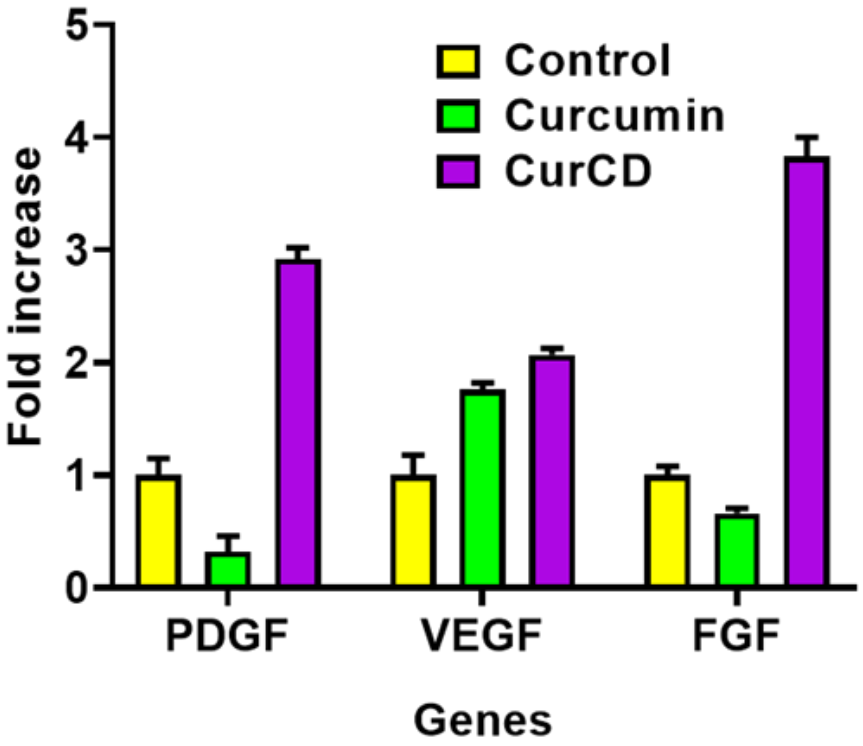

Figure 3.6: Gene expression in mechanically injured HUVEC. Relative expression (fold increase) of the respective genes analysed by qPCR in HUVEC treated with curcumin/CurCD. Data represents average values obtained from 2 experiments conducted in duplicate.

3.3.7 Antibacterial Activity: Active wounds serve as a favourable environment for bacteria to breed. Persistent infection can delay wound healing. Despite the antibacterial activity of curcumin being well established [36], the MIC (maximum inhibitory concentration) required for antibacterial activity is however very high (7.82-250 μg ml^{-1}) depending upon the bacterial strain [37]. Hence the proposed antibacterial dose may not be optimal for wound healing applications. To compare antibacterial activity at concentrations that favour wound healing, *E.coli* was treated with either CurCD (100 μg ml^{-1}) or curcumin (0.18 μg ml^{-1}) respectively. A significant decrease in bacterial growth assessed by optical density was observed in CurCD treated cultures. In comparison, the cultures treated with curcumin were not affected suggesting that curcumin was ineffective at this concentration (Figure 3.7B). This was confirmed by streaking of the above cultures on bacterial plates (Figure 3.7A (i-iii)). To differentiate between live and dead bacteria, FDA (fluorescein diacetate) and PI (propidium iodide) staining was performed. The significant number of dead bacteria (identified red) in CurCD treated cultures in contrast to curcumin treatment confirmed its antibacterial efficacy at lower concentrations (Figure 3.7A (iv-vi). This indicated the superior antibacterial efficiency of the synthesised CurCD in preventing the bacterial infection in wounds. Recently, the improved antibacterial efficiency observed with nano formulations of curcumin have attributed it to its smaller size and better penetration as compared to native curcumin particle (2350 nm), confirming the importance of size for better cellular uptake [38] [37].

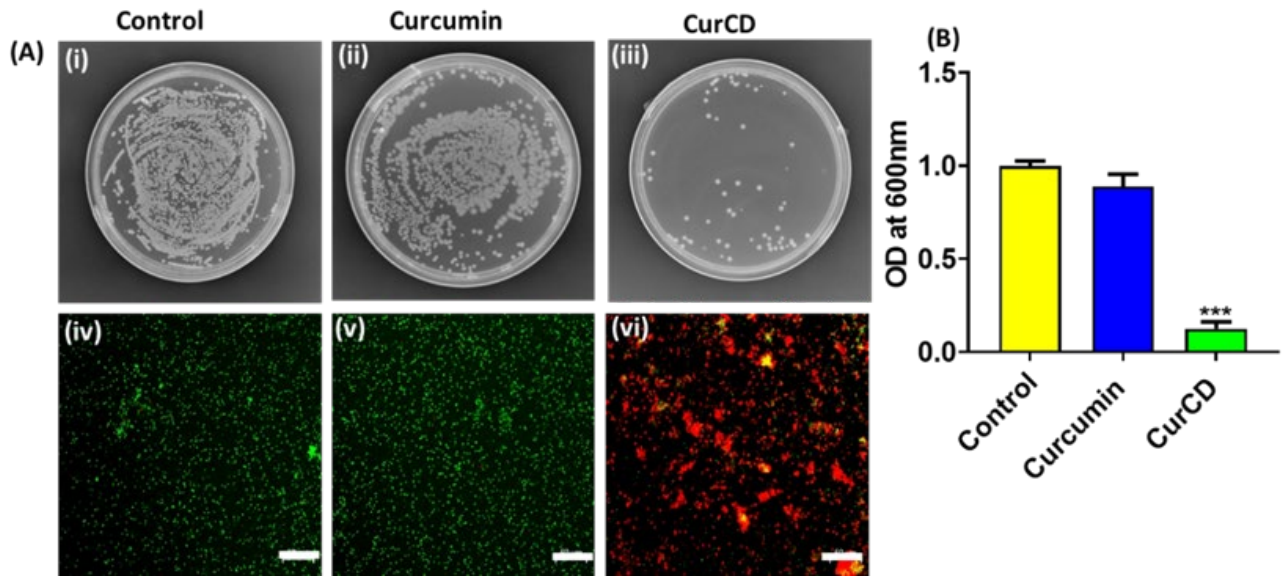

Figure 3.7: Antibacterial property of CurCD/curcumin; (A) Bacterial colony formation post Curcumin/CurCD treatment (i-iii). Untreated cultures served as control. Corresponding cultures tested using Live/dead analysis using FDA and PI. Green cells reflects live cells and red cells reflects dead cells (iv-vi). Scale bar represents 50 µm. (B) Optical density at 600 nm. Data is represented as mean ± SD (n = 3). ***P < 0.001.

3.3.8 Physical characteristics of GHCD hydrogels: The aforesaid biological activity of CurCD indicated that it could favour wound healing. To enable sustained delivery of CurCD at the wound site, we chose gelatin as a protease responsive polymer. As per earlier reports, gelatin's backbone consists of various functional sites which facilitates the process of crosslinking [39] . In our previous study, we have reported that curcumin derived carbon dots were rich in functional moieties like hydroxyl and carboxylic groups [21]. Hence when CurCD reacts with the gelatin polymer, the carbonyl groups present on the CurCD and NH_2 groups on gelatin would interact to cross-link the polymer. The synthesised hydrogels, henceforth referred to as GHCD1 and GHCD2 were prepared using 0.5 mg ml^{-1} and 1 mg ml^{-1} of CurCD respectively. Representative images of the hydrogels are displayed in Figure 3.8A. The surface morphology of the hydrogels was determined using FESEM (Figure 3.8B). In comparison to the plain gelatin hydrogel, the morphology of CurCD crosslinked hydrogel appear dense. The formation of dense structures in hydrogels prepared with higher concentration of carbon dots,

suggested increased crosslinking. The FTIR spectrum (Figure 3.8C) demonstrated the functional moieties present on CurCD and GHCD respectively. In CurCD two strong absorption peaks were observed at 1620 cm^{-1} and 1510 cm^{-1} due to the asymmetric and symmetric stretching of COO^- groups. The peaks ranging from 1000-1200 cm^{-1} is due to C-O, C-O-C stretching vibrations of -OCH3 groups present on the surface of CurCD. From FTIR spectra it can be concluded that CurCD surface mostly contain -OH, -COOH and OCH_3 functional moieties [21]. In case of GHCD and gelatin hydrogel, the absorption peak appeared in the range from 3300-3500 cm^{-1} corresponding to O-H and N-H vibration. The peaks of symmetrical stretching vibration of $–CH_3$ groups were observed at 2930 cm^{-1}. In plain gelatin hydrogel, three characteristics peaks of amide I (C=O), amide II (N− H), and amide III (C−N) groups were shown at 1640 cm^{-1}, 1533 cm^{-1} and 1236 cm^{-1} respectively. [27]. On addition of CurCD in the hydrogels (GHCD), peaks corresponding to amide I and amide II merge and became a single broad peak suggesting the formation of amide linkage which further confirms the crosslinking in the hydrogel is due to CurCD [39]. As the swelling performance of the hydrogel is directly proportional to crosslinking, we studied swelling this property of the GHCD hydrogels. Data displayed in Figure 3.8D indicates that the swelling of the hydrogel is comparatively lower in the hydrogels crosslinked with higher concentration of CurCD, confirming increased crosslinking. During wound healing, the extracellular matrix (ECM) undergoes significant changes. In wounds, the degradation and remodelling of the ECM is regulated by proteases [40]. In presence of proteases, gelatin hydrogels undergo hydrolytic degradation due to solvation and depolymerization of the polymeric chains [41]. The presence of proteases, is expected to accelerate the digestion of the gelatin hydrogels leading to the release of CurCD [42]. This was confirmed by incubating the GHCD hydrogels in the presence of proteases like collagenase. The data displayed in Figure 3.8E suggests that proteases increased the rate of degradation of the GHCD hydrogels in comparison to PBS alone. To

determine the influence of CurCD concentration on the mechanical properties of the hydrogels, rheological studies were carried out. From the modulus graph (Figure 3.8 F&G), it was evidenced that there was a concentration dependent increase in the strength of the hydrogels on addition of CurCD. The formation of strong amide linkage may be responsible for the improved elasticity as compared to blank gelatin hydrogel. A constant rise was observed both in case of storage as well as loss modulus of CurCD loaded hydrogels. The obtained rheology data is in accordance with the previously reported literature [43]. The release of CurCD from the hydrogels incubated in PBS containing proteases (collagenase 1.4 µg/ml) confirmed the protease responsive release of CurCD with time. During wound healing, the proteases available at the wound site is expected to digest the gelatin and release CurCD (Figure 3.8H). GHCD2 has shown a more sustained release in the presence of proteases as compared to GHCD1 because of the more stable mechanical properties of the former hydrogel. On the basis of above physical properties, GHCD2 hydrogel was selected for further biological studies.

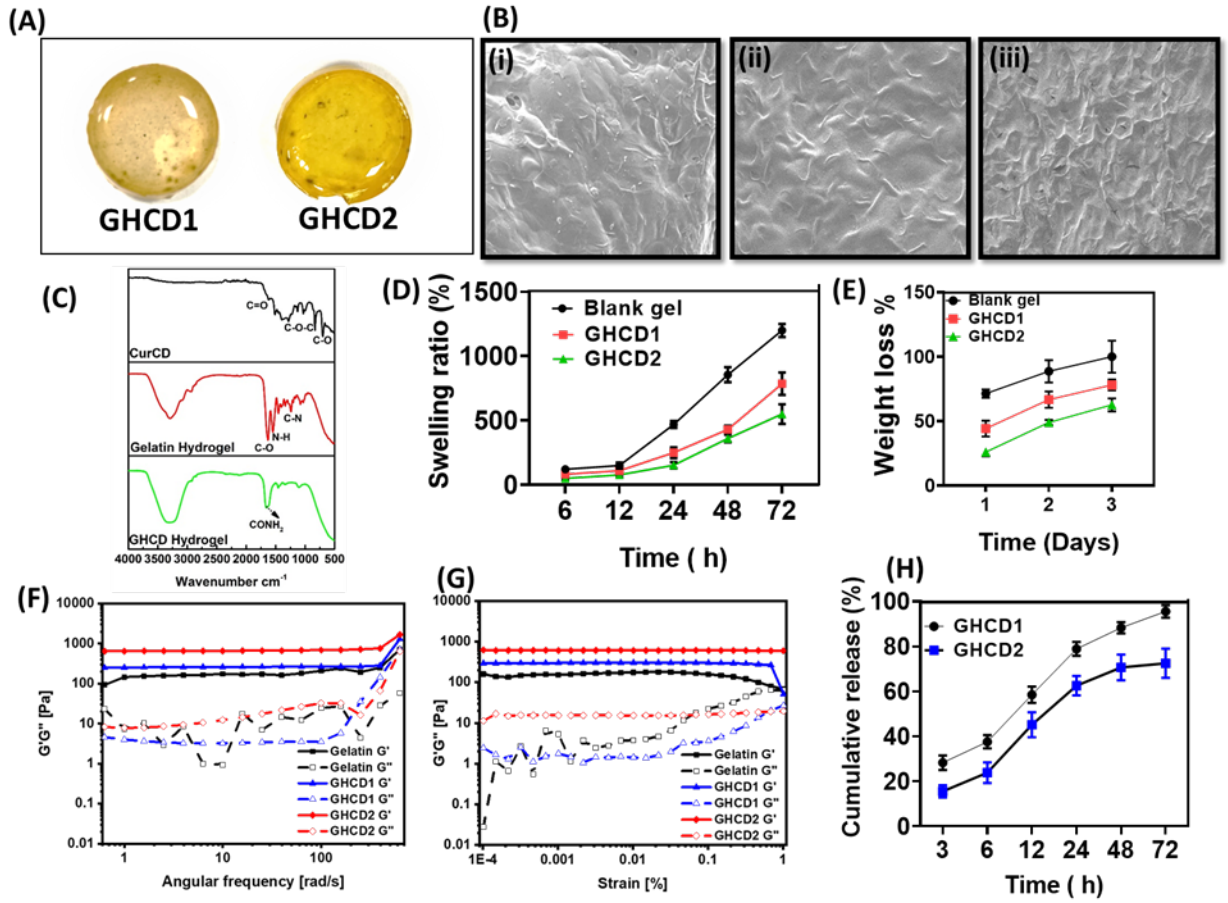

Figure 3.8: Physical properties of CurCD crosslinked hydrogels. (A) Representative images of the GHCD1 (0.5 mg/ml) and GHCD2 (1mg/ml); (B) FESEM images of hydrogels (i) Gelatin hydrogel (ii) GHCD1 (iii) GHCD2; (C) FTIR spectrum of CurCD, gelatin hydrogel and GHCD hydrogel (D) Swelling characteristics (E) Degradation of hydrogels in the presence of collagenase (1.4 µg/ml) ; (F) Amplitude sweep, showing the elastic modulus (solid lines) and viscous modulus (dotted lines) at different shear strain (G) Frequency sweep measurements. Solid lines show the elastic modulus and dotted lines show the viscous modulus of the respective gels; (H) Cumulative release of CurCD from GHCD1 and GHCD2 hydrogel in the presence of collagenase.

3.3.9 Biocompatibility studies: To evaluate the cellular compatibility, Human dermal fibroblasts cells were seeded on the top of the GHCD2 hydrogel and incubated for 5 days with media. For evaluating the growth of cells at each time point, the hydrogels were stained with FDA/PI in order to differentiate between live (stained green) and dead (stained red) cells. The increase in cell numbers suggested that the hydrogel supported cell proliferation (Figure 3.9A). Figure 3.9B shows the metabolic activity of the cells in the hydrogel at different time points

suggesting increased cell proliferation. The increase in cell number confirms the cellular compatibility of GHCD2 hydrogels.

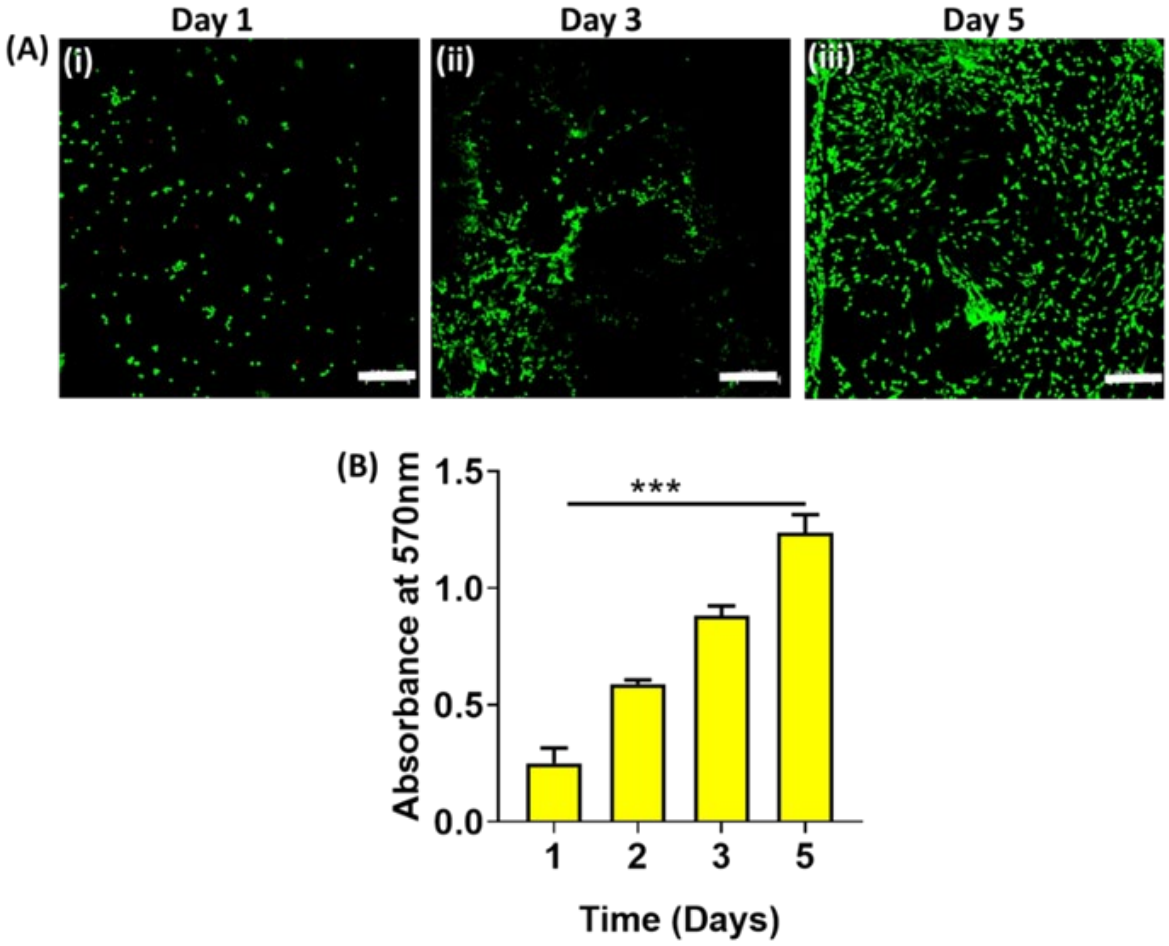

Figure 3.9: Cell proliferation in GHCD2 hydrogel. (A) Representative merged images of Live/dead staining of cells seeded on the GHCD2 hydrogels at day 1, 3 and 5. Scale bar represents 200 μm. (B) Quantification of cellular metabolic activity using alamar blue. Data represented as mean of 3 independent experiments. *** P value = 0.001.

3.3.10 *In vivo* studies: Fabrication of new, smart and efficient wound dressings is highly desirable for the treatment of chronic wounds [44], [45]. Among the reported dressings till now, hydrogel-based dressings have gained interest because of their favourable features like ability to provide a moist wound environment, mimicking native skin characteristics and patient compliance [46]. Curcumin's ability to improve wound healing can be attributed to its anti-oxidative activity, increased proliferation and migration of fibroblasts, improved

angiogenesis and faster epithelialization. [47] [48]. Due to its low bioavailability through oral route, topical application of curcumin has been found to be more efficient [49].To evaluate the potential of GHCD2 hydrogel to hasten the healing of wounds, GHCD2 hydrogel was tested in excisional wounds created on the dorsal side of the rats. The rat wounds (10mm) were treated with either ethanolic solution of free curcumin or GHCD2 hydrogel respectively. Wounds covered with standard wound dressing (Tegaderm) served as control. The photographs of the wounds taken on day 1, 3, 7 and 14 revealed time dependent wound closure in all cases (Figure 3.10A). Quantitative estimation of the wound area at various time points showed significant improvement in wound closure with GHCD2 hydrogel treatment as compared to control (Figure 3.10B). Evaluation of the tissue sections collected on day 14 and stained with H&E showed incomplete epithelialization in the control wounds whereas the wounds treated with both curcumin and GHCD 2 hydrogel revealed complete epithelialization. In comparison to curcumin treatment, the dermis was well organized in the GHCD2 hydrogel treated wounds, suggesting improved remodelling. The presence of numerous hair follicles in the dermis of GHCD 2 hydrogel treated wounds further confirmed wound regeneration [50].

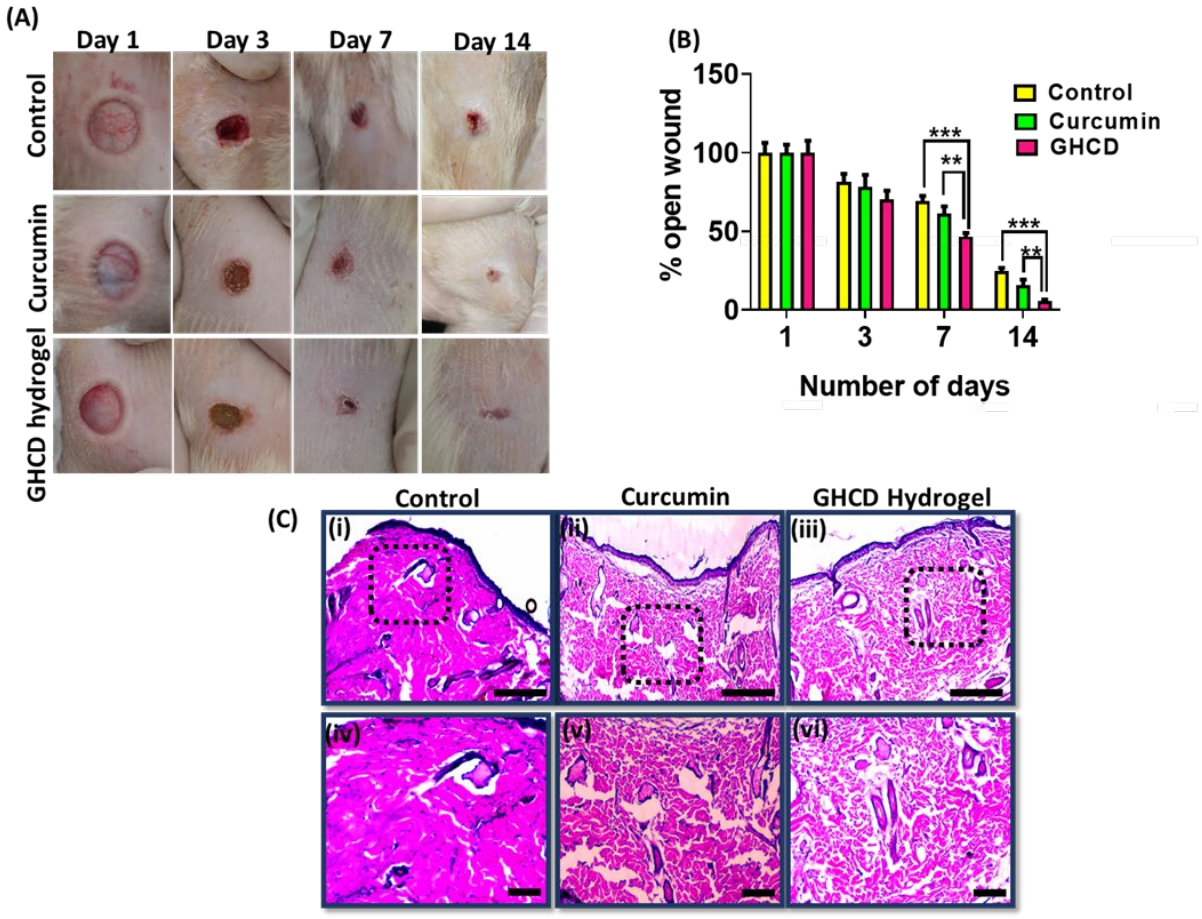

Figure 3.10: Wound response to treatment. (A) Photographs of the wounds at 1, 3, 7 and 14 days after the injury. (B) Quantification of wound closure area (C) H&E staining of the tissue sections harvested on 14th day, (i) control, (ii) Curcumin and (iii) GHCD2 hydrogel. Scale bar = 400 µm; (iv-vi) magnified images of the above images respectively. Scale bar = 200 µm.

In cutaneous wound healing, re-epithelialization is pivotal for the restoration of skin integrity to protect the underlying tissues from infection and dehydration [51]. To investigate the epithelialization, the tissue sections were stained with cytokeratin primary antibody and visualised using Alexa flour 488 conjugated secondary antibody. Cytokeratin, a marker expressed by the epithelial cells was highly expressed in GHCD2 hydrogel as compared to both curcumin or control wounds (Figure 3.11 upper panel). The presence of multilayer epidermis in the sections indicated differentiation of the epithelium [52]. While curcumin induced

complete restoration of the lost epidermal tissue, the effect was less significant in comparison to GHCD2 hydrogel treated wounds, suggested delay in the healing process.

Angiogenesis in the wounds was confirmed by evaluating CD31, a marker expressed by the endothelial cells [53]. In the GHCD2 hydrogel treated wounds, the CD31 expression pattern denoted the presence of multiple large capillaries, in comparison to control wounds. Whereas the curcumin treated wounds revealed higher expression of CD31 than control, the expression was remarkably lower than the GHCD2 hydrogel treated wounds (Figure 3.11 lower panel). The results further confirmed the pro-angiogenic potential of CurCD. The increase in the healing rate observed in wounds treated with GHCD2 as compared to curcumin may be facilitated by the sustained release of CurCD in response to the protease activity in wound bed. The limited response in wounds observed with topical applications of curcumin may be due low stability and or its faster elimination [54].

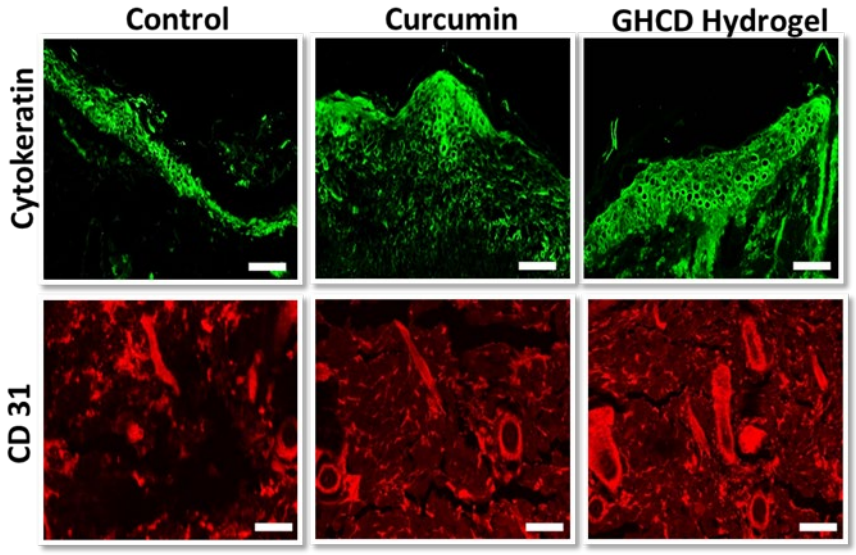

Figure 3.11: Immunohistochemistry of cytokeratin and CD 31 expression. Upper panel represents confocal images of cytokeratin expression; Lower panel reveals CD31 expression. Scale bar represents 100 µm.

3.4 Conclusion: In this study we have established that curcumin carbon dots like curcumin, possess hormetic activity. The carbon dots have superior bioactivity and photo-physical

activity as compared to its source molecule, curcumin. This was evidenced with the response observed in endothelial and fibroblasts cells. Whereas no antibacterial activity was observed with curcumin at concentrations that favour wound healing, the significant bacterial death observed with CurCD, confirmed the latter's potential in preventing wound infections. The delivery of CurCD to the wounds using a protease responsive hydrogel facilitated sustained release of the carbon dots and encouraged wound healing. GHCD2 hydrogel has displayed superior biocompatibility due to lack of chemical cross linker and supported cell proliferation. Improved wound healing observed with GHCD2 hydrogel could be the consequence of CurCD acting on various phases of wound healing such as proliferation, migration and angiogenesis. All these results indicates that GHCD2 hydrogel can be used as an effective wound dressing.

Bibliography

1. E.M. Tottoli, R. Dorati, I. Genta, E. Chiesa, S. Pisani, B. Conti, Skin wound healing process and new emerging technologies for skin wound care and regeneration, Pharmaceutics, 12 (2020), p. 735.
2. H. Sorg, D.J. Tilkorn, S. Hager, J. Hauser, U. Mirastschijski, Skin wound healing: an update on the current knowledge and concepts, Eur. Surg. Res., 58 (2017), pp. 81-94.
3. M. Rodrigues, N. Kosaric, C.A. Bonham, G.C. Gurtner, Wound healing: a cellular perspective, Physiol. Rev., 99 (2019), pp. 665-706.
4. G. FrykbergRober, Challenges in the treatment of chronic wounds, Adv. Wound Care, 4 (2015), pp. 560-582.
5. F.C. Meng, Y.Q. Zhou, D. Ren, R. Wang, C. Wang, L.G. Lin, X.Q. Zhang, W.C. Ye, Q.W. Zhang, Turmeric: a review of its chemical composition, quality control, bioactivity, and pharmaceutical application, Natural and artificial flavoring agents and food dyes (2018), pp. 299-350.
6. A.H. Rahmani, M.A. Al Zohairy, S.M. Aly, M.A. Khan, Curcumin: a potential candidate in prevention of cancer via modulation of molecular pathways, Biomed. Res. Int., 2014 (2014).
7. L.T. Marton, L.M. Pescinini-e-Salzedas, M.E.C. Camargo, S.M. Barbalho, J.F. Haber, R.V. Sinatora, C.R.P. Detregiachi, R.J. Girio, D.V. Buchaim, P. Cincotto dos Santos bueno, the effects of curcumin on diabetes mellitus: a systematic review, Front. Endocrinol., 12 (2021), p. 443.
8. J.W. Daily, M. Yang, S. Park, Efficacy of turmeric extracts and curcumin for alleviating the symptoms of joint arthritis: a systematic review and meta-analysis of randomized clinical trials, J. Med. Food, 19 (2016), pp. 717-729.
9. D. Namgyal, S. Ali, R. Mehta, M. Sarwat, The neuroprotective effect of curcumin against cd-induced neurotoxicity and hippocampal neurogenesis promotion through CREB-BDNF signaling pathway, Toxicology, 442 (2020).
10. S. Tejada, A. Manayi, M. Daglia, S.F. Nabavi, A. Sureda, Z. Hajheydari, O. Gortzi, H. Pazoki-Toroudi, S.M. Nabavi, Wound healing effects of curcumin: a short review, Curr. Pharm. Biotechnol., 17 (2016), pp. 1002-1007.
11. N. Jirofti, M. Golandi, J. Movaffagh, F.S. Ahmadi, F. Kalalinia, Improvement of the wound-healing process by curcumin-loaded Chitosan/Collagen blend electrospun

nanofibers: in vitro and in vivo studies, ACS Biomater. Sci. Eng., 7 (2021), pp. 3886-3897

12. N.S.A. Moghaddam, M.N. Oskouie, A.E. Butler, P.X. Petit, G.E. Barreto, A. Sahebkar, Hormetic effects of curcumin: what is the evidence? J. Cell. Physiol., 234 (2019), pp. 10060-10071.
13. N.E. Rainey, A. Moustapha, P.X. Petit, Curcumin, a multifaceted hormetic agent, mediates an intricate crosstalk between mitochondrial turnover, autophagy, and apoptosis, Oxidative Med. Cell. Longev., 2020 (2020).
14. N. Rainey, L. Motte, B.B. Aggarwal, P. Petit, Curcumin hormesis mediates a cross-talk between autophagy and cell death, Cell Death Dis., 6 (2015).
15. D. Demirovic, S.I. Rattan, Curcumin induces stress response and hormetically modulates wound healing ability of human skin fibroblasts undergoing ageing in vitro, Biogerontology, 12 (2011), pp. 437-444.
16. M. Mahjoob, U. Stochaj, Curcumin nanoformulations to combat aging-related diseases, Ageing Res. Rev., 69 (2021).
17. P. Anand, A.B. Kunnumakkara, R.A. Newman, B.B. Aggarwal, Bioavailability of curcumin: problems and promises, Mol. Pharm., 4 (2007), pp. 807-818.
18. M. Gera, N. Sharma, M. Ghosh, D.L. Huynh, S.J. Lee, T. Min, T. Kwon, D.K. Jeong, Nanoformulations of curcumin: an emerging paradigm for improved remedial application, Oncotarget, 8 (2017), p. 66680.
19. N. Azam, M.Najabat Ali, T.Javaid Khan, Carbon quantum dots for biomedical applications: review and analysis, Front. Mater., 272 (2021).
20. S.U. Kumar, B. Bhushan, P. Gopinath, Bioactive carbon dots lights up microtubules and destabilises cell cytoskeletal framework–a robust imaging agent with therapeutic activity, Colloids Surf. B, 159 (2017), pp. 662-672.
21. A. Sharma, V. Panwar, J. Thomas, V. Chopra, H.S. Roy, D. Ghosh, Actin-binding carbon dots selectively target glioblastoma cells while sparing normal cells, Colloids Surf. B, 200 (2021).
22. C.J. Lin, L. Chang, H.W. Chu, H.J. Lin, P.C. Chang, R.Y. Wang, B. Unnikrishnan, J.Y. Mao, S.Y. Chen, C.C. Huang, High amplification of the antiviral activity of curcumin through transformation into carbon quantum dots, Small, 15 (2019), p. 1902641.
23. R. Madhyastha, H. Madhyastha, Y. Nakajima, S. Omura, M. Maruyama, Curcumin facilitates fibrinolysis and cellular migration during wound healing by modulating

urokinase plasminogen activator expression, Pathophysiol. Haemos. Thromb., 37 (2010), pp. 59-66.

24. S.P. Ndlovu, K. Ngece, S. Alven, B.A. Aderibigbe, Gelatin-based hybrid scaffolds: promising wound dressings, Polymers, 13 (2021), p. 2959.
25. A. Sharma, V. Panwar, V. Chopra, J. Thomas, S. Kaushik, D. Ghosh, Interaction of carbon dots with endothelial cells: implications for biomedical applications, ACS Appl. Nano Mater., 2 (2019), pp. 5483-5491.
26. J. Wondergem, L. Wedekind, C. Bart, A. Chin, A. van der Laarse, H. Beekhuizen, Irradiation of mechanically-injured human arterial endothelial cells leads to increased gene expression and secretion of inflammatory and growth promoting cytokines, Atherosclerosis, 175 (2004), pp. 59-67.
27. V. Chopra, J. Thomas, A. Sharma, V. Panwar, S. Kaushik, D. Ghosh, A bioinspired, ice-templated multifunctional 3D cryogel composite crosslinked through in situ reduction of GO displayed improved mechanical, osteogenic and antimicrobial properties, Mater. Sci. Eng. C., 119 (2021).
28. V. Panwar, A. Babu, A. Sharma, J. Thomas, V. Chopra, P. Malik, S. Rajput, M. Mittal, R. Guha, N. Chattopadhyay, Tunable, conductive, self-healing, adhesive and injectable hydrogels for bioelectronics and tissue regeneration applications, J. Mater. Chem. B, 9 (2021), pp. 6260-6270.
29. J. Thomas, A. Sharma, V. Panwar, V. Chopra, D. Ghosh, Polysaccharide-based hybrid self-healing hydrogel supports the paracrine response of mesenchymal stem cells, ACS Appl. Bio Mater., 2 (2019), pp. 2013-2027
30. V. Kant, A. Gopal, D. Kumar, N.N. Pathak, M. Ram, B.L. Jangir, S.K. Tandan, D. Kumar, Curcumin-induced angiogenesis hastens wound healing in diabetic rats, J. Surg. Res., 193 (2015), pp. 978-988.
31. A.K. Singh, G.S. Sidhu, T. Deepa, R.K. Maheshwari, Curcumin inhibits the proliferation and cell cycle progression of human umbilical vein endothelial cell, Cancer Lett., 107 (1996), pp. 109-115.
32. G. Dhar, D. Chakravarty, J. Hazra, J. Dhar, A. Poddar, M. Pal, P. Chakrabarti, A. Surolia, B. Bhattacharyya, Actin–curcumin interaction: insights into the mechanism of actin polymerization inhibition, Biochemistry, 54 (2015), pp. 1132-1143.
33. S.A. Guo, L.A. DiPietro, Factors affecting wound healing, J. Dent. Res., 89 (2010), pp. 219-229.

34. X.Y. Xu, X. Meng, S. Li, R.Y. Gan, Y. Li, H.B. Li, Bioactivity, health benefits, and related molecular mechanisms of curcumin: current progress, challenges, and perspectives, Nutrients, 10 (2018), p. 1553.
35. P.C. Li, S.C. Chen, Y.J. Hsueh, Y.C. Shen, M.Y. Tsai, L.W. Hsu, C.K. Yeh, H.C. Chen, C.C. Huang, Gelatin scaffold with multifunctional curcumin-loaded lipid-PLGA hybrid microparticles for regenerating corneal endothelium, Mater. Sci. Eng. C, 120 (2021).
36. S. Zorofchian Moghadamtousi, H. Abdul Kadir, P. Hassandarvish, H. Tajik, S. Abubakar, K. Zandi, A review on antibacterial, antiviral, and antifungal activity of curcumin, Biomed. Res. Int. (2014).
37. A.K. Singh, P. Prakash, R. Singh, N. Nandy, Z. Firdaus, M. Bansal, R.K. Singh, A. Srivastava, J.K. Roy, B. Mishra, Curcumin quantum dots mediated degradation of bacterial biofilms, Front. Microbiol., 8 (2017), p. 1517.
38. R.S. Pandit, S.C. Gaikwad, G.A. Agarkar, A.K. Gade, M. Rai, .Curcumin nanoparticles: physico-chemical fabrication and its in vitro efficacy against human pathogens, Biotech, 5 (2015), pp. 991-997.
39. S.K. Bhattacharyya, M. Dule, R. Paul, J. Dash, M. Anas, T.K. Mandal, P. Das, N.C. Das, S. Banerjee, Carbon dot cross-linked gelatin nanocomposite hydrogel for pH-sensing and pH-responsive drug delivery, ACS Biomater. Sci. Eng., 6 (2020), pp. 5662-5674.
40. M. Ågren, Gelatinase activity during wound healing, Br. J. Dermatol., 131 (1994), pp. 634-640.
41. D.M. Correia, J. Padrão, L. Rodrigues, F. Dourado, S. Lanceros-Méndez, V. Sencadas, Thermal and hydrolytic degradation of electrospun fish gelatin membranes, Polym. Test., 32 (2013), pp. 995-1000.
42. G. Yang, Z. Xiao, H. Long, K. Ma, J. Zhang, X. Ren, J. Zhang, Assessment of the characteristics and biocompatibility of gelatin sponge scaffolds prepared by various crosslinking methods, Sci. Rep., 8 (2018), pp. 1-13.
43. Y. Piao, B. Chen, Self-assembled graphene oxide–gelatin nanocomposite hydrogels: characterization, formation mechanisms, and pH-sensitive drug release behaviour, J. Polym. Sci. B Polym. Phys., 53 (2015), pp. 356-367.
44. C. Gong, Q. Wu, Y. Wang, D. Zhang, F. Luo, X. Zhao, Y. Wei, Z. Qian, A biodegradable hydrogel system containing curcumin encapsulated in micelles for cutaneous wound healing, Biomaterials, 34 (2013), pp. 6377-6387.

45. D. Akbik, M. Ghadiri, W. Chrzanowski, R. Rohanizadeh, Curcumin as a wound healing agent, Life Sci., 116 (2014), pp. 1-7.
46. M. Panchatcharam, S. Miriyala, V.S. Gayathri, L. Suguna, Curcumin improves wound healing by modulating collagen and decreasing reactive oxygen species, Mol. Cell. Biochem., 290 (2006), pp. 87-96.
47. C. Mohanty, S.K. Sahoo, Curcumin and its topical formulations for wound healing applications, Drug Discov. Today, 22 (2017), pp. 1582-1592.
48. . Zhao, Z. Li, S. Song, K. Yang, H. Liu, Z. Yang, J. Wang, B. Yang, Q. Lin, Skin-inspired antibacterial conductive hydrogels for epidermal sensors and diabetic foot wound dressings, Adv. Funct. Mater., 29 (2019), p. 1901474.
49. K.A. Bielefeld, S. Amini-Nik, B.A. Alman, Cutaneous wound healing: recruiting developmental pathways for regeneration, Cell. Mol. Life Sci., 70 (2013), pp. 2059-2081.
50. H.H. Bragulla, D.G. Homberger, Structure and functions of keratin proteins in simple, stratified, keratinized and cornified epithelia, J. Anat., 214 (2009), pp. 516-559.
51. S.I. Okizaki, Y. Ito, K. Hosono, K. Oba, H. Ohkubo, K. Kojo, N. Nishizawa, M. Shibuya, M. Shichiri, M. Majima, Vascular endothelial growth factor receptor type 1 signaling prevents delayed wound healing in diabetes by attenuating the production of IL-1β by recruited macrophages, Am. J. Pathol., 186 (2016), pp. 1481-1498.
52. M. Kharat, Z. Du, G. Zhang, D.J. McClements, Physical and chemical stability of curcumin in aqueous solutions and emulsions: impact of pH, temperature, and molecular environment, J. Agric. Food Chem., 65 (2017), pp. 1525-1532.

Chapter 4: Interaction of carbon dots with endothelial cells

4.1 Introduction

Ever since the discovery of carbon dots (CDs) in 2004 [1], CDs have received considerable attention from researchers in view of their high-water solubility [2,3], biocompatibility, low toxicity, unique photoluminescence (PL) properties, and flexibility for surface modification [4]. In addition, these fluorescent quasi-spherical, zero-dimensional nanomaterials with sizes below 10 nm demonstrate high resistance to photobleaching in contrast to established fluorescent organic dyes and semiconductor quantum dots [5]. These properties have driven scientists to explore CDs in several biological applications, including bioimaging [6], drug delivery [7], and theranostics [8].

In several in vivo applications, the CDs are administered through the circulation system [9,10]. Such in vivo administration of the CDs would lead to their exposure to the endothelial cells (ECs) that line the lumen of blood vessels. It is therefore important to understand the response of the ECs to CD exposure because these cells are involved in angiogenesis. Angiogenesis or neovascularization occurs through the development of capillary sprouts from the pre-existing ones following EC migration and the splitting of vessels. The process of angiogenesis is tightly regulated, and any inadequate or excessive angiogenesis is implicated in a number of pathologic conditions [11]. In certain occlusive diseases, such as in chronic wounds [12] or ischemic heart diseases [13], where insufficient angiogenesis is observed, treatment with proangiogenic factors has been proposed to improve blood flow to the damaged area [14]. Conversely, excessive angiogenesis can trigger pathological conditions such as cancer, chronic inflammation, diabetic retinopathy, and arthritis [15]. In such conditions, antiangiogenic therapy is favored. Thus, strategies to inhibit or induce angiogenesis are of considerable therapeutic interest.

Because ECs serve as the first point of contact for the CDs that enter the blood before they reach their targets, it is important to assess the effect of these CDs on ECs. A review of the

literature on the CDs' influence on angiogenesis indicated a single study in which the CDs were prepared from styrene soot [16]. In view of the fact that the angiogenic response observed with nanomaterials is influenced by the nature of the materials tested [17-19], it becomes relevant to study those CDs that are being designed for biomedical applications. Although CDs are synthesized from a plethora of renewable carbon sources [20-22], the most common CDs designed for biomedical applications are synthesized from citric acid and nitrogen-containing dopants like urea, ethylenediamine, poly (ethylenimine), etc [23]. To evaluate the response of ECs upon CD exposure, we used CDs prepared from citric acid and urea on the basis of their reported in vivo applications [24,25]. The CDs, henceforth referred to as CD-urea, were prepared using a facile solvothermal process [26] and characterized by transmission electron microscopy (TEM), X-ray photoelectron spectroscopy (XPS), X-ray diffraction (XRD), etc. The effects of CD-urea on EC proliferation, migration, capillary network formation, and gene expression were evaluated using the appropriate studies. In addition, downstream signaling following CD-urea uptake, including the activation of reactive oxygen species (ROS) and nuclear factor κ-light-chain enhancer of activated B cells (NF-κB), was evaluated to identify a possible mechanism through which CD-urea induced the angiogenic response.

4.2 Material and methods

I Materials: Citric acid, urea and NaOH were procured from Himedia laboratories, India. Solvents like ethanol and Dimethylformamide were from MERCK, USA. DMEM, Medium 200, Trypsin, Foetal bovine Serum (US origin) Penicillin-streptomycin-Amphotericin B, MTT, Hoechst, Rhodamine TRITC and Vybrant® cell-labelling solutions were purchased from Thermo Fisher Scientific, USA. Matrigel and all the plastic ware for tissue culture were procured from Corning. Taqman QPCR kit and primers were obtained from Invitrogen. Both

primary (NFkBp65) and secondary (Alexaflour 488) antibodies were purchased from Invitrogen.

II Experimental

4.2.1 Synthesis of CD-urea: CD-urea was prepared by the solvothermal method [19]. Briefly, citric acid and urea were taken in 1:2 ratio, dissolved in 10ml DMF and reacted at 200 °C for 12 h in a hydrothermal environment. The cooled material was mixed with 20 mL alkali (50mg/ml NaOH) and centrifuged at 16000 r min $^{-1}$ for 30 min. The precipitate was washed with water and centrifuged (16 000 r min $^{-1}$, 30 min) thrice to remove unreacted salts and alkali. The pellet was re-dispersed in water, lyophilised and kept at 4°C.

4.2.2 Characterization of CD-urea: A JEOL JEM-2100 transmission electron microscope operating at 200 kV was utilized to obtain high-resolution transmission electron microscopy (TEM) images. The ultraviolet-visible (UV−Vis) absorption spectra were measured on a Shimadzu Spectrophotometer. The fluorescence spectra were recorded using an F-4600 spectrofluorometer. The ATR spectra were recorded on a VERTEX 80v spectrometer. The X-ray photoelectron spectra were recorded using an ESCALAB 250Xi spectrometer (Thermo Fisher). The crystal structure was characterized by a Bruker D8 Advance X-ray diffractometer (λ= 0.151056 nm). The time-resolved fluorospectroscopy was performed using an FLS 920 spectrometer.

(a) UV absorption and Fluorescence spectroscopy: UV-Vis absorption spectra was measured in the range from 300 to 800 nm with a Shimadzu UV-Vis 2600 spectrophotometer. Fluorescence spectra were recorded with an Edinburg FS 5 spectrofluorometer. All absorbance and fluorescence spectra were measured at room temperature using quartz cuvettes having a volume of 1 ml. All the measurements were repeated 3 times.

(b) X-ray diffraction studies (XRD): X-ray diffraction pattern (XRD) was determined using Bruker Eco D8 setup consisting of Cu Kα radiation (λ = 0.154056 nm). Copper anode was taken as the target material with fine focus filament as the cathode. The freeze-dried samples were drop casted on the coverslips to obtain the measurements.

(c) Transmission electron Microscopy (TEM): The particle size distribution of the synthesized carbon dots was obtained with the help of instrument at an accelerating voltage of 200 kV. The diluted samples were sonicated and placed on copper coated carbon grids. The samples were evaporated at room temperature. To avoid any cross contamination with dust particles, TEM grids were kept in desiccator till use.

(d) Fourier Transform Infrared Spectroscopy (FTIR): FTIR spectra of Citric acid, Urea and carbon dots were measured using a Bruker FTIR spectrophotometer equipped with a horizontal attenuated total reflectance (ATR) accessory containing a zinc selenide crystal.

(e) AFM: The height of CD-urea was measured using Atomic force microscopy (AFM, Nanoscope IIIa, Digital Instrument, USA) in tapping mode. CD-urea were dispersed in mili Q water and 10 μL of dispersion was drop casted on the silicon wafer. X-ray photoelectron spectroscopy (XPS): The X-ray photoelectron spectra were recorded using an ESCALAB 250Xi spectrometer (Thermo Fisher).

4.2.3 Cell Isolation and Propagation: We studied the response of fibroblasts and HUVECs following their exposure to CD-urea. HUVECs were derived from human umbilical cord, while fibroblasts were derived from neonatal foreskin after informed consent was obtained as per the protocol approved by the Institutional Ethics Committee of PGIMER (IEC-08/2017-658), Chandigarh, India. Human dermal fibroblasts (HDFs) were isolated using our previously reported protocol [57]. Briefly, neonatal foreskin was washed with phosphate-

buffered saline (PBS) followed by decontamination with iodine−povidone and incubation with Dispase (Sigma) to separate the dermis from the epidermis. After digestion of the dermis with 0.1% collagenase (Sigma), the fibroblasts were dissociated and cultured in a Dulbecco's modified Eagle's medium (DMEM) containing 10% fetal bovine serum (FBS) and antibiotics. Cells were used for passages 5−8. The HUVECs were isolated as previously described.58 In brief, the decontaminated umbilical cord was washed three times with Hank's buffered salt solution, and the ends of the cord were sealed. Through one end, 15 mL of collagenase type II was injected through the vein. After digestion for 15 min at 37 °C, the detached cells were pooled in a centrifuge tube and centrifuged at 1500 rpm for 5 min. The cell pellet was dispersed in HUVEC media and cultured. The cells in passages 2−5 were used in the studies.

4.2.4 Cell Proliferation Assay: The proliferation potential of CD-urea was assessed using MTT assay [59]. In brief, 1500 cells/well (HUVEC/ HDF) were plated in a 96-well plate and incubated for 24 h at 37 °C in a 5% CO2 incubator. After 24 h, CD-urea (0−200 μg/mL) made in the growth medium was added to each well in triplicate. MTT was added after 24 h/48 h of incubation. The resulting formazan crystals were solubilized in dimethyl sulfoxide, and the absorbance was measured at 570 nm using a microplate reader (Tecan multimode reader).

4.2.5 Hemocompatibility: To check the hemocompatibility of CD-urea, an in vitro hemolysis assay was performed using the standard protocol. Briefly, the goat blood (5 mL) obtained from a local abattoir was centrifuged at 1500 rpm for 5 min to separate the RBCs. The isolated RBCs were suspended in PBS to form a 2% suspension. To 1 mL of the 2% RBC suspension was added 100−1000 μg/mL CDurea. PBS and water were used as the negative and positive controls, respectively. The RBC suspension along with CD-urea was incubated for 3 h at 37 °C and centrifuged at 1500 rpm for 5 min to collect the supernatant. The supernatant was visually checked for the presence/ absence of a red color.

4.2.6 In Vitro Tube Formation Assay: The effect of CD-urea on capillary network formation was studied on a matrigel using HUVECs. Briefly, 50 µL/well of a growth-factor-reduced matrigel (Corning) was added to a 96-well plate and incubated for 30 min at 37 °C in the incubator. Before the cells were harvested, Di0 dye (Vybrant cell-labeling solution, Invitrogen) was added to the flasks at a concentration of 5 µL/mL and incubated for 30 min. The HUVEC cells were trypsinized and seeded at a cell density of 2.5 × 103 cells/well with and without CD-urea (100 µg/mL). The plates were kept for 4 h at 37 °C in the incubator, and network formation was observed by a confocal microscope (Carl Zeiss). The length of the capillary network was obtained from random fields in each well and quantified using ImageJ software.

4.2.7 Scratch Wound-Healing Assay: To investigate the effect of CD urea on endothelial migration, scratch assay was performed according to a published protocol [60]. In brief, HUVECs were seeded in a 24-well plate (Nunc) at a density of 2 × 104 cells/well in complete DMEM. In order to avoid cell proliferation, cells were serum-starved for 12 h and after that maintained in 2% FBS for the entire experiment. Before a scratch was created, a monolayer of cells was allowed to form. A sterile 20-µL pipet tip was used to create a scratch in each well, and the media were removed and rinsed twice with DPBS to remove cell debris. Further, different concentrations of CD were added to the wells and incubated at 37 °C. Wound paths were observed under the microscope at the same location in different periods of time to mark the migration of fibroblasts in the control/sample. Cells in the wound area were counted at 6 and 12 h by three different observers to avoid biases in the results, and the mean was taken. Images were taken at 4× magnification using a digital camera mounted on a microscope.

4.2.8 Cell Uptake Studies: To evaluate CD-urea uptake and distribution, HDFs and HUVECs were seeded in chamber slides and incubated for 24 h at 37 °C in the incubator. After

24 h, the cells were treated with CD-urea at a concentration of 100 µg/mL. At the end of 24 h, the cells were fixed with 4% (w/v) paraformaldehyde. The cells were rinsed and incubated with Hoechst for 5 min in the dark and observed using a confocal microscope. The cell uptake efficiency was estimated by calculating the absorbance of media containing CD-urea at 0 h and after 24 h of incubation with the cells, using the formula (Abs of CDurea at 0 h − Abs of CD-urea at 24 h)/Abs of CD-urea at 0 h × 100 = % cell uptake.

4.2.9 Qualitative polymerase chain reaction: Gene expression studies were conducted on HUVECs treated with/without CD-urea (100 µg/mL) for 24 h. The total RNA was isolated from the cells using the pure-link RNA mini kit (Invitrogen). cDNA was made with the help of a high-capacity RNAto-cDNA kit (Invitrogen). qPCR was done using a TaqMan PCR Master Mix (Applied Biosystems) on a Quant studio 2 (Applied Biosystems). The primers and probes used were TGF-β (Hs00820148), FGF2 (Hs00266645_m1), VEGFA (Hs00900055_m1), MMP-2 assay (Hs01548727), PDGF (Hs00966522_m1), PGF (Hs00182176_m1), and GAPDH (Hs02786624-g1) (Applied Biosystems). The amplification conditions for analysis were 50 °C for 2 min and 95 °C for 10 min, followed by 40 cycles at 95 °C for 15 s and 50 °C for 1 min. The obtained PCR results were normalized to the housekeeping gene, GAPDH (Hs00204173_m1), and ΔCt was calculated. Fold changes between various groups are expressed using ΔΔCt values [61].

4.2.10 In Ovo Angiogenesis Assay: The angiogenic potential of CD-urea was assessed using CEA assay [18]. Briefly, the fertilized chicken eggs procured from a local poultry farm were incubated at 37 °C for 4 days. The eggs were cracked, and the contents were transferred carefully to 90 mm Petri dishes under aseptic conditions. Sterile filter paper disks treated with a media/media-containing CD solution (100 µg/mL) were placed carefully on the egg yolks, and the samples were incubated for a further 12 h. The images were captured on a camera

mounted on a stereomicroscope (Stemi 2000 C with Axio Cam ICc1) and quantitated using Angiotool 64 software. The images were captured at 0 and 12 h after treatment.

4.2.11 Determination of ROS: The intracellular ROS levels were measured using 2′,7′-dichlorofluorescein diacetate (DCFDA) dye-based assay [62]. Upon cellular uptake, the nonfluorescent DCFDA was oxidized by ROS into 2′,7′-dichlorofluorescein (DCF). DCF is a highly fluorescent compound that can be detected by fluorescence spectroscopy with excitation/emission at 485/535 nm. To detect the ROS levels in HUVECs following CD-urea treatment, the cells were seeded in a 24-well plate at a cell density of 1.5 × 104 cells/well and incubated with different concentrations of CD-urea (50−200 μg/mL) for 24 h. The untreated cells were used as controls to investigate the basal level of ROS in cells. After 24 h, the cells were rinsed with PBS and incubated with DCFH-DA dye (working concentration of 25 μM) for 30 min at 37 °C. Fluorescence was measured (Ex/Em = 485/ 535 nm) in a microplate reader.

4.2.12 Determination of p65 Translocation: Immunofluorescence analysis of the translocation of NF-κB p65 was checked on HUVECs. Briefly, HUVEC cells were seeded on a coverslip at a cell density of 104 cells/mL. After 24 h, the cells were incubated with CD-urea (100 μg/mL) and fixed with paraformaldehyde. In order to permeabilize the cells for antibody incubation, the cells were treated with 0.1% Triton X-100 for 15 min and blocking was done with bovine serum albumin (1%) for 60 min at room temperature. To check the translocation of p65, the cells were labeled with a NF-κB p65 antibody (Invitrogen) at 1:300 dilution overnight at 4 °C. p65 was detected using an Alexa Fluor 488-conjugated Superclonal Secondary Antibody (Invitrogen). Hoechst (Invitrogen) was used as the nuclear stain. The cytoskeleton was stained red with Rhodamine TRITC Phalloidin (Invitrogen).

4.2.13 Statistics: The significance level in all statistical observations was set at a probability of $p \leq 0.05$. All of the data are presented as mean ± standard deviation. ANOVA and student's t tests were used to analyze the data and to calculate the significance level.

4.3 Results and discussion:

4.3.1 Characterization of CD-Urea: CD-urea was prepared using an earlier reported process [26] with 1:2 molar mixture of citric acid and urea using a solvo-thermal method at 200°C for 12 h. The morphology was analyzed by transmission electron microscopy (TEM) and high-resolution transmission electron microscopy (HR-TEM) of the as –prepared CD-urea, drop-cast on a gold grid. The images exhibit the spherical structure of CD-urea (Figure. 4.1a) in the range of 2-10 nm with an average size of 6.3 nm (N=100) (Figure. 4.1d). The HR- TEM image also shows visible crystalline lattice fringes with interlattice spacing of 0.21 nm (Figure 4.1c) which correlates to the d-spacing of the graphene planes. Most of the CD-urea exhibited uniform atomic arrangements, indicating a high degree of crystallinity. The bright spots in SAED pattern clearly indicate the crystalline nature of the material (Figure 4.1b).

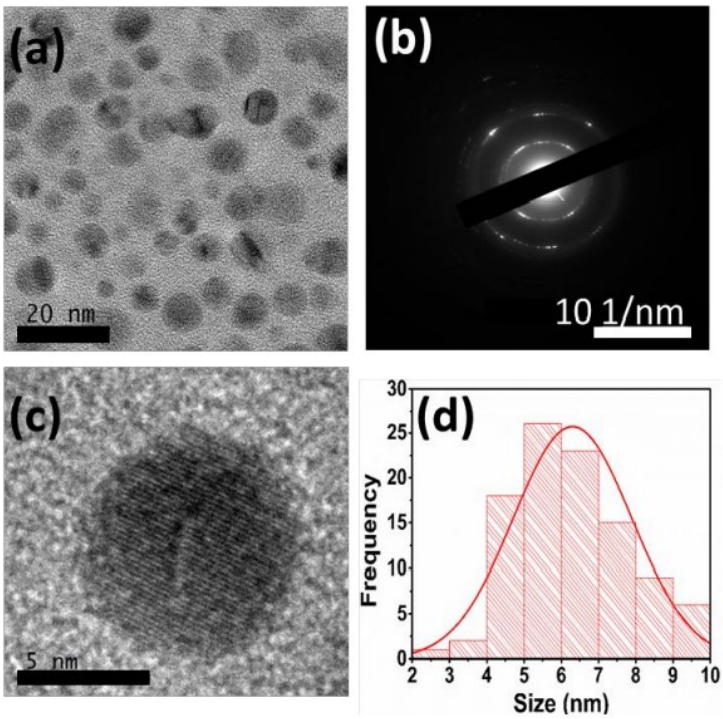

Figure 4.1: Characterization of CD-urea. (a) TEM image (Scale bar 20 nm); (b) SAED pattern; (c) HRTEM image (scale bar 5 nm); (d) Size distribution (n=100).

The optical properties of CD-urea were measured by UV–Vis absorption and photoluminescence (PL) spectra (Figure 4.2a & 4.2b). The quantum yield of CD-urea was 48 % which is comparable to a previous report [26]. As shown in Figure 4.2a, the UV-Vis spectra of CD-urea exhibits two absorption peaks, one at 370 nm due to n-π* transition of C=O bond and the other at 556 nm due to sp2 domain in the particles with a tail extending into the visible range. In the PL spectra of CD-urea (Figure 4.2b) as the excitation wavelength increased from 300 nm to 500 nm, the emission gradually shifted from 510 nm to 620 nm with the strongest emission at 620 nm when excited at 510 nm. The full-spectrum PL behaviour of the CD-urea can be exploited for bioimaging [27].

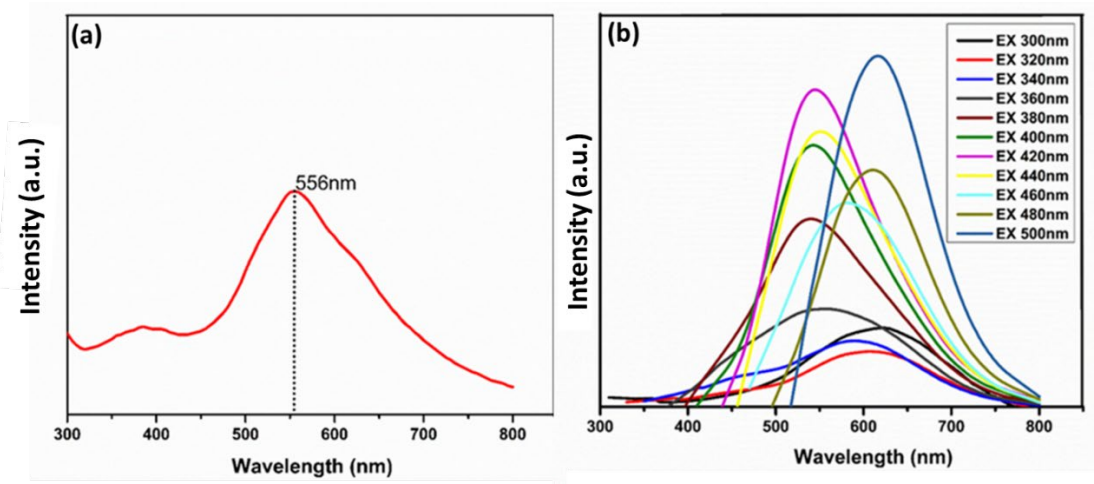

Figure 4.2: Photophysical properties of CD-urea: (a) Uv visible spectra of CD-urea; (b) PL spectra of CD-urea at different wavelengths.

To identify the surface functional groups on CD-urea; Fourier-transform infrared (FT-IR) spectroscopy was performed as shown in Figure 4.3. The IR spectra of citric acid show peaks in the region from 1050-1200, 1720 and 2930 cm-1 due to C-O stretching, C= O stretching and C-H stretching along with a broad peak in the region of 3200-3400 cm−1 which is due to the presence of stretching vibration of O-H in carboxylic acid. In case of urea, the absorption bands in the region from 3428-3360 cm−1 and 1616 are due to stretching and bending mode of N-H along with other peaks for C-N, C=O at 1528 cm-1 and 1685 cm-1. In the case of CD-urea no characteristic peaks similar to pure urea and citric acid was observed. A small shift in the peaks of C=O, OH, N-H and C-N indicated the successful synthesis of CD-urea.

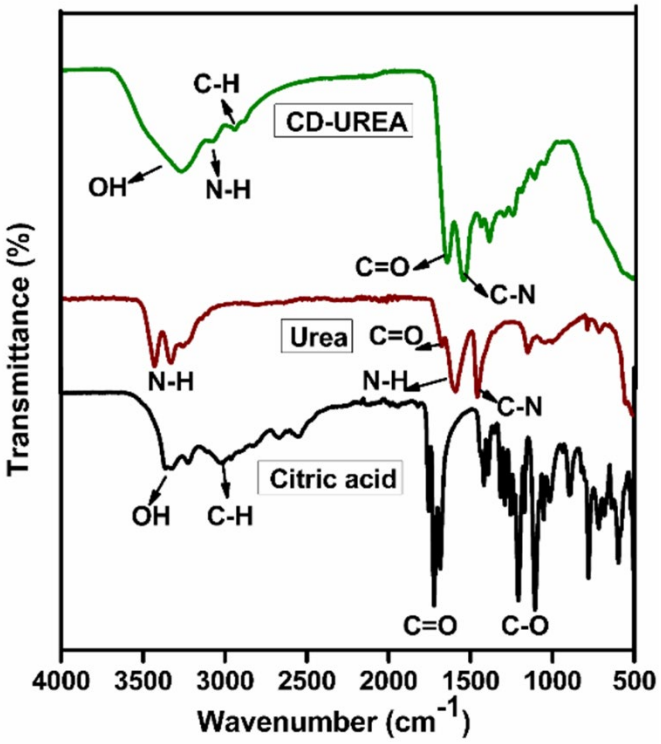

Figure 4.3: FTIR spectra of CD-urea

In accordance with the FTIR results, the X-ray Photoelectron Spectroscopy (XPS) measurements were carried out to prove the composition of as-prepared CD-urea and the full scan spectrum is shown in Figure 4.4. The experimental data revealed the presence of C, N and O element in CD-urea with atomic ratio of 65.48%, 15.43% and 19.09% respectively (Figure. 4.4a). The deconvoluted XPS spectra of C1s (Figure. 4.4b) revealed the presence of several components. The peak at 283.67 eV is due to C=C while the peak at 284.38 eV corresponds to aliphatic C-C. Further the peak at 285.64 eV and 287.23 eV is due to C–N–C, C=O carbonyl indicating amide linkage formation [28]. The partial XPS spectra of N1s was resolved into three components with peaks at 398.44, 399.19 and 401.53 eV indicating that nitrogen exists mostly in the form of C=N-C, C-N-C and C-N as shown in Figure 4.4c. [29] . Similarly, the broad peak of O1s can be deconvolved into three components with binding energy 530.23 eV (CO/N-O), 531.23 eV (C=O/–O–C=O) and 533.3 eV (C–O/C–OH) (Figure.4.4d) [30].

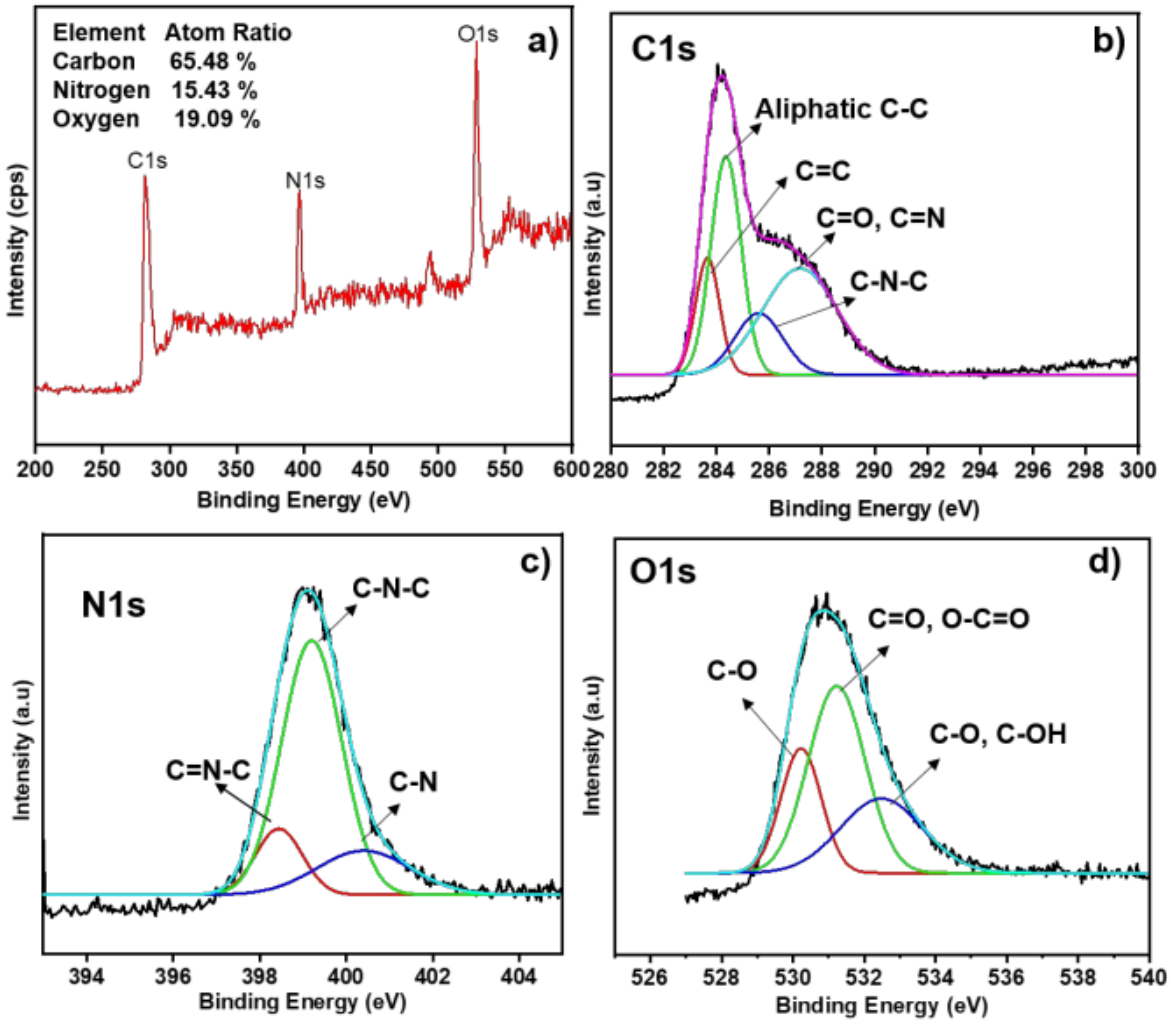

Figure 4.4: XPS survey scan of CD-urea. a) XPS full scan spectrum. XPS high resolution survey scan of (b) C1s, (c) N1s, and (d) O1s region

4.3.2 Compatibility of CD-urea with cells and RBCs: The cytocompatibility of CD-urea was assessed with dermal fibroblasts using the MTT assay. As shown in Figure 4.5a, the proliferation of the cells following 24 h treatment with various concentrations of CD-urea (0-200 µg/ml) was comparable to control. At 48 h after treatment, in comparison with the untreated cells, the treated cells demonstrated a dose-dependent increase in cell proliferation. Treatment with 80-200 µg/ml of CD-urea displayed a notable increase in proliferation as compared to control. These results confirm the earlier reports which demonstrated the

cytocompatibility of CDs prepared with citric acid and urea [31,32]. The confocal images of the cells captured using an argon laser at 500 nm excitation, demonstrated the selective accumulation of CD-urea in the cytoplasm of cells (Figure 4.5b). The hemocompatibility of CD-urea was assessed by incubating CD-urea (100-1000 µg/ml) for 3 h with RBCs isolated from goat blood. As demonstrated in Figure 4.5c, in comparison to the positive control (water), no lysis of the RBCs was observed with CD-urea, indicating its hemocompatibility.

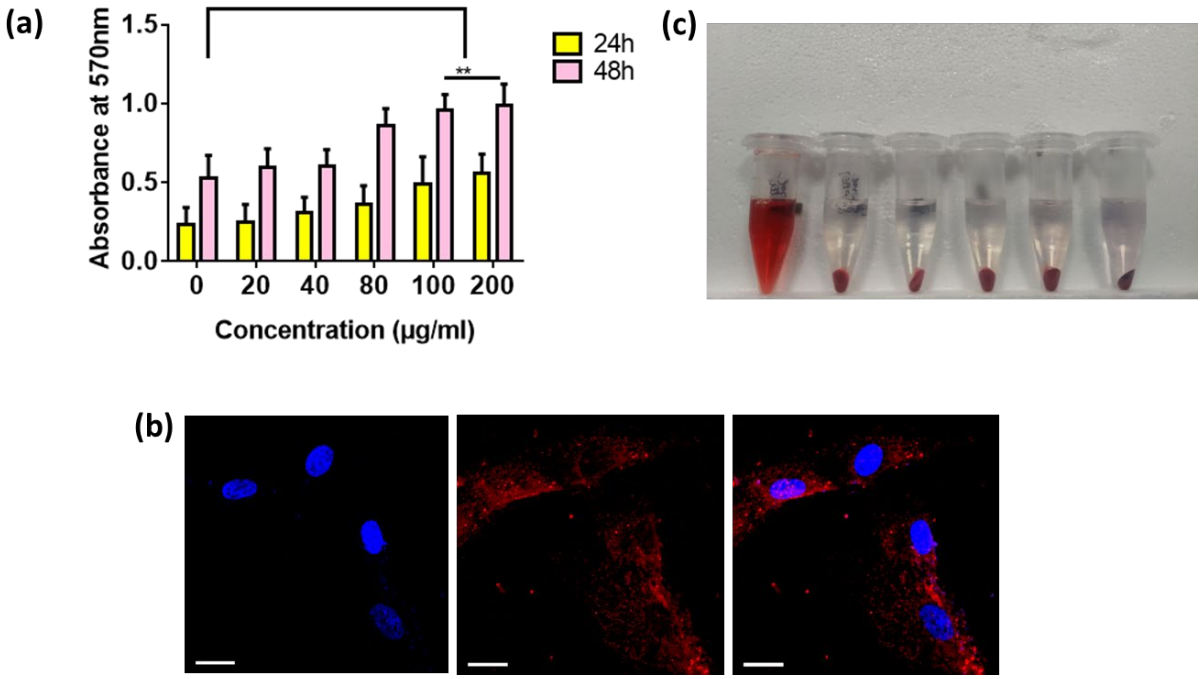

Figure 4.5: Biocompatibility of CD-urea; (a). Fibroblast proliferation assessed by MTT assay ** represents P value < 0.01 (one way. ANOVA, Tukey's multiple comparison test), (b). Fibroblast uptake of CD-urea. Scale bar represents 20 µm. (c). Hemocompatibility of CD-urea

4.3.3 Response of endothelial cells to CD-urea: Human umbilical vein endothelial cells (HUVEC) derived from the umbilical cord are the most favored ECs used in research [27]. The proliferative response of HUVEC on treatment with CD-urea (0-200 µg/ml) was investigated using the MTT assay. Figure 6a demonstrates the viability of HUVEC on treatment with various concentrations of CD-urea at the end of 24 h and 48 h respectively. As

compared to the untreated cells, the number of cells at 48 h post-treatment with CD-urea (100 µg/ml and 200 µg/ml) exhibited a significant increase indicating the proliferative response of endothelial cells to CD-urea. As no significant change was observed at lower concentrations, we chose to further explore the effect of 100 µg/ml of CD-urea on other aspects of angiogenesis. The distribution of CD-urea (100 µg/ml) in HUVEC after 24 h exposure was monitored using a confocal microscope as mentioned above. The efficiency of CD-urea uptake by HUVEC was 13.8% after 24 h exposure. The distribution pattern of CD-urea following its uptake in HUVEC was similar to that of fibroblasts (Figure 4.5b), with the majority of its accumulation observed in the cytoplasm at the end of 24 h (Figure 4.6b). An earlier report indicated the accumulation of similar CDs in the nucleolus of HeLa cells [32]. While HeLa cells are transformed cells, HUVEC and fibroblasts used in this study are of primary origin, indicating its cell specific response.

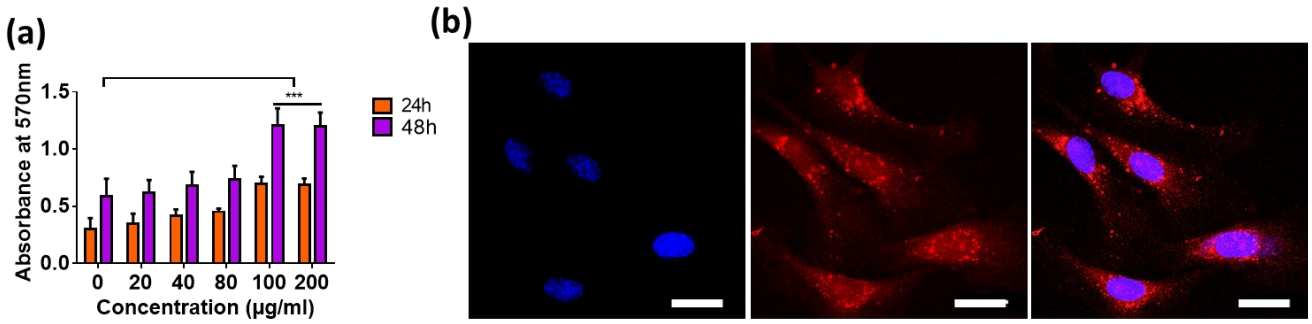

Figure 4.6: HUVEC viability and uptake. (a) MTT assay of HUVEC treated with CD-urea (0-200 µg/ml) for 24 h & 48 h. b) Confocal images of HUVEC incubated with CD-urea (100 µg/ml) for 24 h; Scale bar represents 20 µm.

4.3.4 Effect of CD-urea on HUVEC migration: The migration of endothelial cells is a key aspect of angiogenesis. The migratory response of HUVEC to CD-urea was studied using the scratch assay, a standard wound healing assay widely used for probing cell migration in vitro [33]. To check the effect of CD-urea on HUVEC migration, a wound area was created in

a confluent monolayer of HUVEC by physically removing the cells from the area through physical damage. The migration of cells into the wound area was monitored in untreated cells (which served as control) and cells treated with CD-urea (100 μg/ml) for 12 h. Figure 4.7a shows representative images of the scratch area taken in untreated cells (top panel) and CD-urea treated cells (bottom panel) at various time points. The data demonstrated the initiation of migration at 6 h in both conditions. The presence of a significant number of cells in the scratch area of CD-urea treated cells as compared to control at the end of 12 h following treatment, indicated the stimulation of migration by CD-urea. The percentage wound closure, calculated as the percentage of the initial scratch area covered with cells indicated a significant reduction in the wound area following CD-urea treatment as compared to control (Figure. 4.7b).

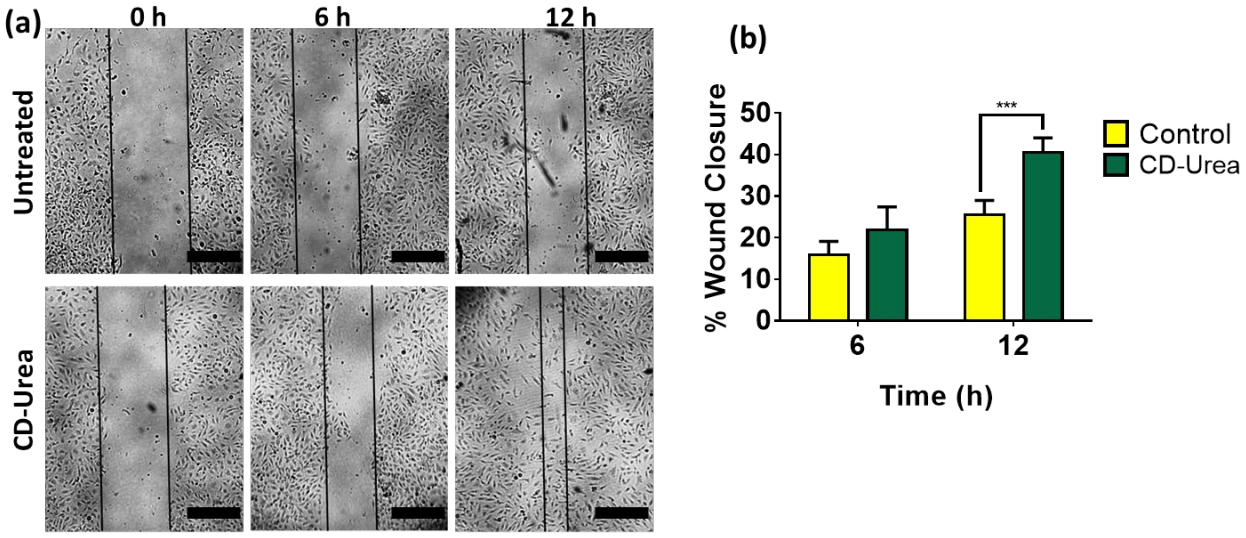

Figure 4.7: Migratory Response of HUVEC to CD-urea. (a) Phase contrast microscopic images of the scratch wound area in HUVEC cells without (upper panel) and 100 μg/ml CD-urea (lower panel) at 0 h, 6 h and 12 h respectively. (b) Graph represents the percentage wound area covered with cells at different time points. Data expressed represents the average of three experiments performed in triplicate. *** indicates P value ≤0.001 (two way ANOVA Bonferroni's multiple comparison test). Scale 250 μm.

4.3.5 Network formation assay: Angiogenesis is marked by the formation of a new network of blood vessels [34]. We used an in vitro matrigel model for the study of angiogenesis, wherein the endothelial cells assemble into capillary-like structures on matrigel made of basement membrane matrix [35]. At the end of 6 h treatment with CD-urea, a significant increase in the capillary network formation by HUVEC was observed as compared to control (Figure 4.8a). A comparative quantitative analysis of the network formation revealed a significant increase in the number of branches (Figure. 4.8b), number of rings (Figure. 4.8c) and tube length (Figure. 4.8d) in CD-urea treated cells as compared to control. This data suggests the pro-angiogenic property of CD-urea.

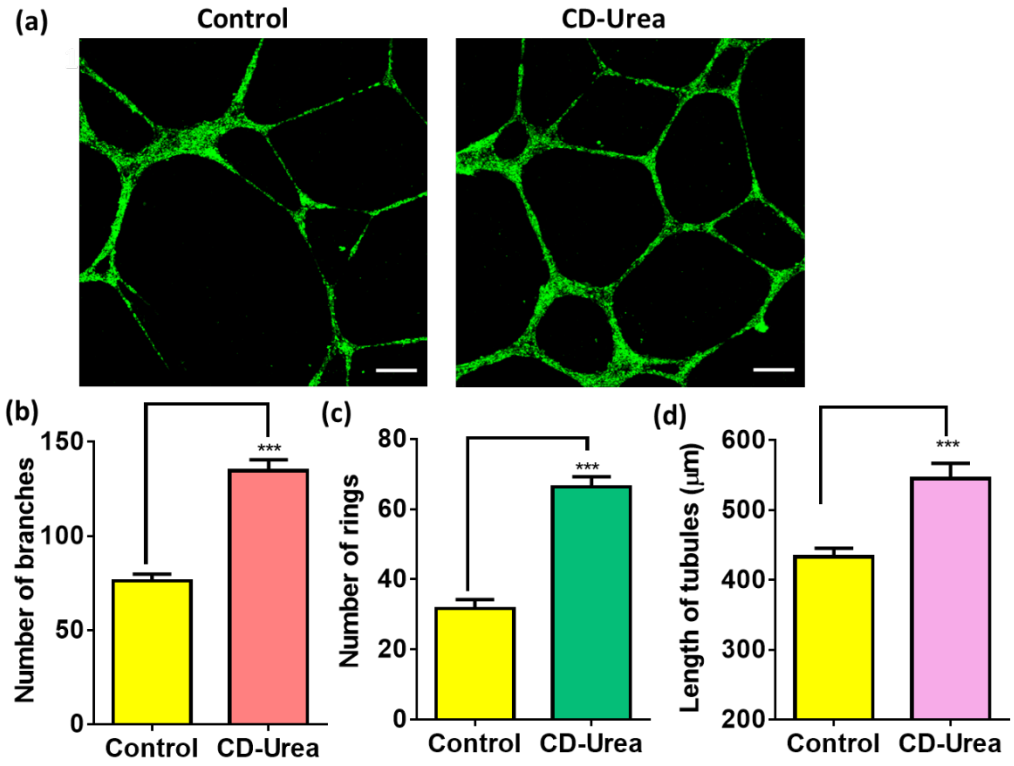

Figure 4.8. Capillary network formation on matrigel. (a) Confocal images of the network formed by untreated control cells and in CD-urea (100 µg/ml) treated cells for 6 h. Quantitative analysis of the network formation with and without CD-urea treatment representing (b) Number of branches; (c) Number of rings and (d) Length of capillary network. The data represents an average of six different

areas captured from each well conducted in triplicate and quantitated using Image J software. *** represents P value ≤0.001 (student t test). Scale represents 200 µm.

4.3.6 Angiogenic gene profiling: The angiogenic process is regulated by a wide array of factors such as growth factors and signaling molecules that regulate gene expression. We evaluated some of the genes that are reported to play an important role in angiogenesis [36-37]. HUVEC were treated with or without CD-urea (100 µg/ml) for 24 h and their expression of pro-angiogenic genes like VEGF (vascular endothelial growth factor), bFGF (basic Fibroblast growth factor), PDGF (Platelet derived growth factor), TGF-β (Transforming growth factor-β), PGF (Placental growth factor), MMP-9 (Matrix metalloproteases-9) were evaluated by qPCR (Figure 4.9). These signaling molecules individually as well as collectively are believed to support endothelial cell survival, influence endothelial migration, chemotaxis and matrix invasion leading to new capillary formation [38-40]. While a two fold increase in the expression levels of VEGF and PGF was observed in the treated cells; the expression of PDGF, TGF-β and bFGF increased by four fold and MMP-9 by three fold respectively. The above pro-angiogenic factors secreted by endothelial cells in response to CD-urea could be responsible for the observed endothelial response. In addition, the probability of involvement of other similar factors need to be further explored.

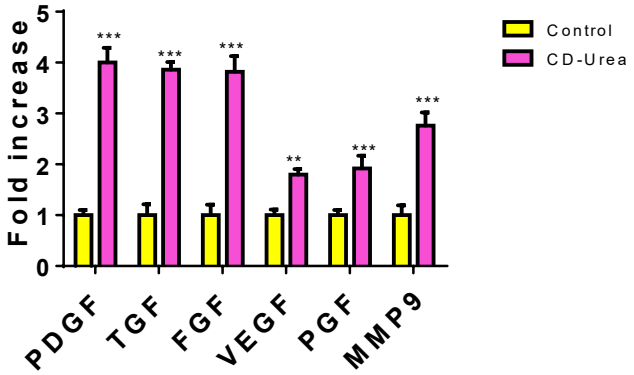

Figure 4.9. Expression of pro-angiogenic genes by CD-urea. Relative expression (fold increase) of pro-angiogenic genes measured by qPCR in HUVEC treated with/without CD-urea (100 μg/ml). Data represents average values obtained from 3 experiments conducted in duplicate. *** represents P value ≤0.001; ** P-value ≤0.01.

4.3.7 Ex-vivo angiogenesis assay: To confirm the pro-angiogenic activity of CD-urea, we assessed the response of nascent blood vessels to CD-urea. The chick embryo angiogenesis (CEA) assay [41] , a standard in-ovo assay was used to study the influence of CD-urea on new blood vessel formation as compared to untreated control. The images were captured at 0 h and 12 h after treatment. Figure. 10a shows the capillary network at 0 h and at 12 h after treatment. As compared to 0 h (Figure. 4.10 i & ii), the capillaries were more pronounced at 12 h (Figure. 4.10 iii & iv). On visual assessment of the capillary network, the embryos treated with CD-urea (Figure. 4.10 iv) showed a significant increase in blood vessel formation as compared to untreated control (Figure. 4.10 iii) in the same time frame. Quantitation of the blood vessels using Angiotool64 software demonstrated a two-fold increase in branch points (Figure. 4.10b), around five fold increase in vessel length (Figure. 4.10c) and a two fold increase in vessel area (Figure. 10d) in CD-urea treated egg yolk as compared to untreated control, thus confirming the angiogenic potential of CD-urea.

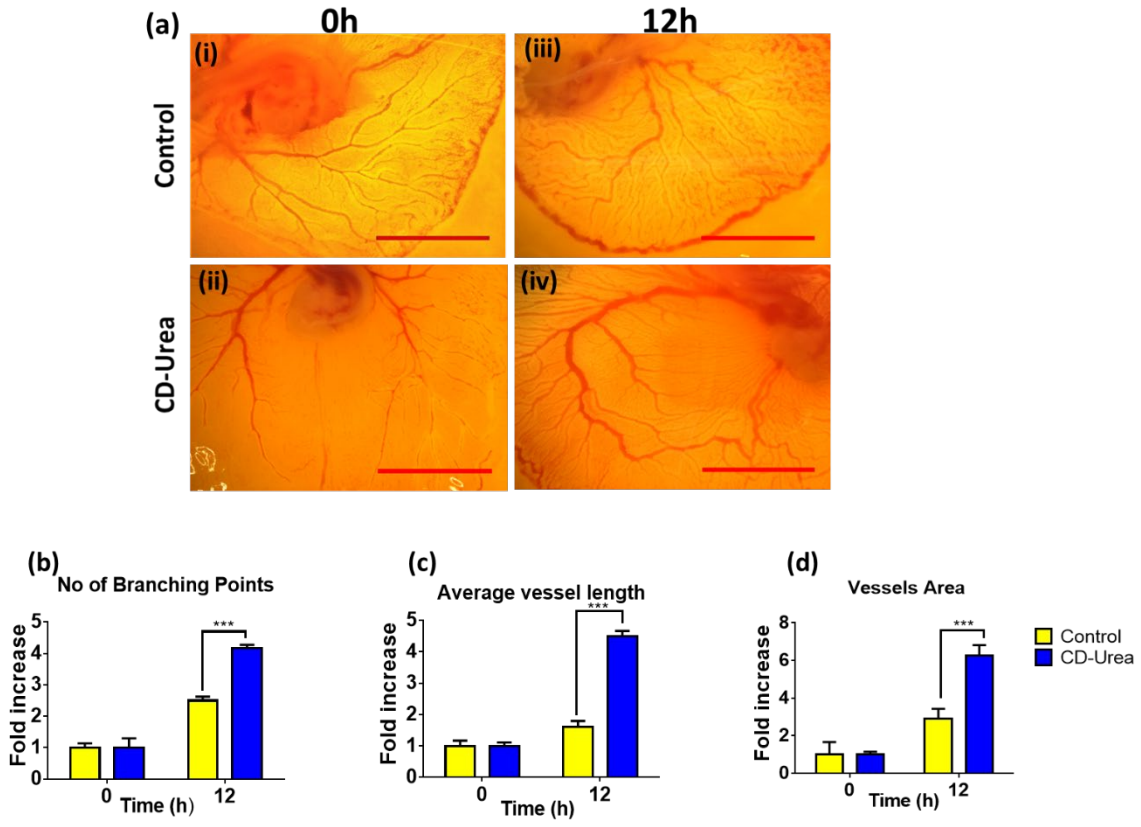

Figure 4.10. Chick embryo angiogenesis assay. a) Stereomicroscope images of capillary network in embryos before (i & ii) and after 12 h treatment (iii & iv). The capillary network in control embryos were treated with buffer only (i & iii) and for treatment, the embryos were exposed to CD-urea suspended in buffer (ii & iv). The quantitative data represents the number of (b) number of branching points (c) average vessels length, (d) vessels area (n=3) in control and CD-Urea treated chick ova's. *** represents P value ≤0.001. Scale bar represents 500 μm.

4.3.8 Mechanism of action behind CD-urea mediated angiogenesis: The in vitro and in-ovo angiogenesis data evidently surmise the pro-angiogenic property of CD-urea. We explored the molecular mechanism of CD-urea mediated angiogenesis in HUVEC. It is reported that endothelial cells exhibit oxidative stress when exposed to carbon nanoparticles [42,43]. The biological response however depends on the level of oxidative stress produced in the cells [44]. According to the proposed three-tier model, at low level of oxidative stress, an antioxidant response mediated by Nrf-2 signalling pathway is observed, while at the

intermediate level, an inflammatory response due to the activation of NF-κB cascade occurs. In contrast, at high levels of oxidative stress, oxidative damage leading to apoptosis and necrosis is observed [45]. Since oxidative stress at low levels play a positive role during angiogenesis, and numerous studies have demonstrated the positive relationship between ROS and angiogenesis [46,47] , we explored the effect of CD-urea on ROS using the DCFH-DA assay, a widely used method to detect ROS generation. Data represented in Figure. 4.11 a & b demonstrates the ROS levels following CD-urea exposure. As compared to the constitutive expression of ROS in HUVEC, CD-urea exposure resulted in a dose dependent increase in ROS expression. The expression although significant as compared to untreated cells, the increase in however moderate. Our data corroborates with an earlier report demonstrating that ROS at low levels function as signalling molecules to mediate angiogenesis by promoting cell growth, migration, differentiation and gene expression [48]. ROS is reported to upregulate several angiogenic factors through nuclear factor NF-κB mediated pathway [49,50]. The NF-κB/Rel family in the form of homo- and heterodimers exist in the cytosol in an inactive form, complexed with proteins of the IκB family. Upon stimulation, the phosphorylation by IκB kinase (IKK) leads to the degradation of IκB and renders NF-κB free to translocate to the nucleus and bind to promoters and enhancers, leading to gene regulation [51]. ROS-induced activation of NF-κB resulted in VEGF and MMP-9 expression in endothelial cells [52]. The expression of genes like VEGF and MMP-9 (Figure 4.9) observed following CD-urea treatment, point towards NF-κB involvement in gene regulation. In addition, activation of NF-κB leads to the release of cytokines/chemokines that subsequently lead to the expression of pro-angiogeneic factors [53-54]. The expression of other proangiogenic factors like PDGF, bFGF and TGFβ observed on EC treatment with CD-urea could be the consequence of NF-κB activation. To verify NF-κB activation on CD-urea treatment, HUVEC were treated with CD-urea and NF-κB activation was analyzed by nuclear p65 immunoreactivity as a marker for NF-

κB activation. Figure. 4.11c demonstrates the presence of p65 immunoreactivity in the cells treated with CD-urea indicating the downstream signaling following CD-urea uptake in endothelial cells. The observed induction of angiogenesis following CD-urea treatment could be the result of ROS-induced NF-κB activation. The distinct change in morphology seen in HUVEC exposed to CD-urea as compared to the untreated cells is due to actin reorganization which is induced by oxidative stress [55]. This change in actin regulation is reported to facilitate endothelial motility [56]. The improved cell migration observed on CD-urea treatment might be the consequence of the actin reorganization.

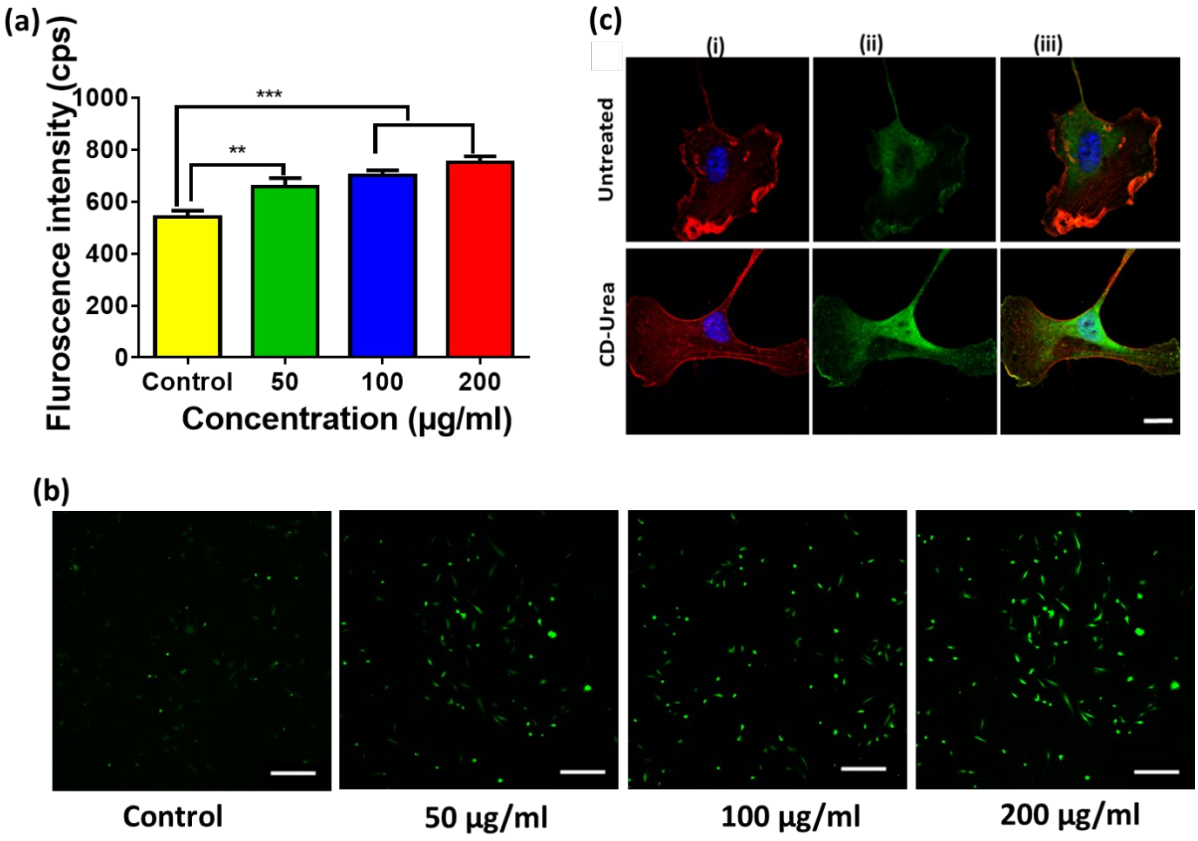

Figure 4.11: ROS activity a). Quantitative analysis of ROS expression using the DCFH-DA assay assessed after 24 h treatment with CD-urea. b) ROS activity with DCFH-DA treatment in CD-urea treated HUVEC Scale bar represents 200 µm. c) Confocal images of HUVEC untreated (upper panel)/ CD-urea (lower panel) stained with p65 antibody. i) Actin filaments stained with phalloidin (red) and

nucleus stained with Hoechst (blue); ii) p65 detection in nucleus and cytoplasm of treated cells iii) Merged images of (i) and (ii). Scale bar represents 10 μm.

4.4. Conclusion:

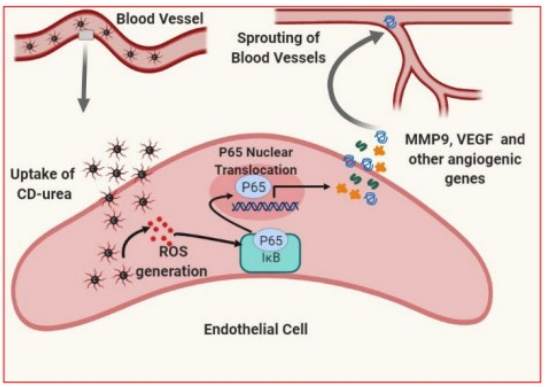

Schematic representation of CD-urea mediated angiogenesis

In summary, we explored the biological response of endothelial cells on exposure to carbon dots (CD-urea) prepared from citric acid and urea. HUVEC on treatment with the cytocompatible and hemocompatible CD-urea, demonstrated a dose-dependent increase in proliferative and improved pro-angiogenic response which was subsequently confirmed in the in-ovo studies using chick embryo. Based on ROS induction and NF-κB activation in CD-urea treated cells, we propose the angiogenic response observed with CD-urea could be the result of downstream signaling of NF- κB. This has been supported by the increase in the expression of pro-angiogenic factors that are known to play a major role in improving angiogenesis. This study becomes highly relevant especially when CDs are being widely developed for biological applications like imaging, drug delivery etc. In addition, given the favourable role played by pro-angiogenic factors in the treatment of conditions like ischemic limb disease, wound healing, cardiovascular disease etc., the CD-urea, can be explored further to address the angiogenic insufficiency in the above-mentioned conditions.

Bibliography

1. Xu, X.; Ray, R.; Gu, Y.; Ploehn, H. J.; Gearheart, L.; Raker, K.; Scrivens, W. A. Electrophoretic analysis and purification of fluorescent single-walled carbon nanotube fragments. J. Am. Chem. Soc. 2004, 126 (40), 12736−12737.
2. Lu, W.; Gong, X.; Yang, Z.; Zhang, Y.; Hu, Q.; Shuang, S.; Dong, C.; Choi, M. M. High-quality water-soluble luminescent carbon dots for multicolor patterning, sensors, and bioimaging. RSC Adv. 2015, 5 (22), 16972−16979.
3. Li, H.; He, X.; Kang, Z.; Huang, H.; Liu, Y.; Liu, J.; Lian, S.; Tsang, C. H. A.; Yang, X.; Lee, S. T. Water-soluble fluorescent carbon quantum dots and photocatalyst design. Angew. Chem., Int. Ed. 2010, 49 (26), 4430−4434.
4. Li, L.; Dong, T. Photoluminescence tuning in carbon dots: surface passivation or/and functionalization, heteroatom doping. J. Mater. Chem. C 2018, 6 (30), 7944−7970.
5. Fan, Z.; Li, S.; Yuan, F.; Fan, L. Fluorescent graphene quantum dots for biosensing and bioimaging. RSC Adv. 2015, 5 (25), 19773− 19789.
6. Ding, H.; Wei, J.-S.; Zhong, N.; Gao, Q.-Y.; Xiong, H.-M. Highly efficient red-emitting carbon dots with gram-scale yield for bioimaging. Langmuir 2017, 33 (44), 12635−12642.
7. Kong, T.; Hao, L.; Wei, Y.; Cai, X.; Zhu, B. Doxorubicin conjugated carbon dots as a drug delivery system for human breast cancer therapy. Cell Proliferation 2018, 51 (5), No. e12488.
8. Wu, Y.-F.; Wu, H.-C.; Kuan, C.-H.; Lin, C.-J.; Wang, L.-W.; Chang, C.-W.; Wang, T.-W. Multi-functionalized carbon dots as theranostic nanoagent for gene delivery in lung cancer therapy. Sci. Rep. 2016, 6, 21170.
9. Yang, S.-T.; Cao, L.; Luo, P. G.; Lu, F.; Wang, X.; Wang, H.; Meziani, M. J.; Liu, Y.; Qi, G.; Sun, Y.-P. Carbon dots for optical imaging in vivo. J. Am. Chem. Soc. 2009, 131 (32), 11308−11309.
10. Huang, X.; Zhang, F.; Zhu, L.; Choi, K. Y.; Guo, N.; Guo, J.; Tackett, K.; Anilkumar, P.; Liu, G.; Quan, Q.; Choi, H. S.; Niu, G.; Sun, Y.-P.; Lee, S.; Chen, X. Effect of injection routes on the biodistribution, clearance, and tumor uptake of carbon dots. ACS Nano 2013, 7 (7), 5684−5693.
11. Carmeliet, P.; Jain, R. K. Molecular mechanisms and clinical applications of angiogenesis. Nature 2011, 473 (7347), 298.

12. Demidova-Rice, T. N.; Durham, J. T.; Herman, I. M. Wound healing angiogenesis: innovations and challenges in acute and chronic wound healing. Advances in wound care 2012, 1 (1), 17−22.
13. Kobayashi, K.; Maeda, K.; Takefuji, M.; Kikuchi, R.; Morishita, Y.; Hirashima, M.; Murohara, T. Dynamics of angiogenesis in ischemic areas of the infarcted heart. Sci. Rep. 2017, 7 (1), 7156.
14. Mac Gabhann, F.; Qutub, A. A.; Annex, B. H.; Popel, A. S. Systems biology of pro-angiogenic therapies targeting the VEGF system. Wiley Interdisciplinary Reviews: Systems Biology and Medicine 2010, 2 (6), 694−707.
15. Chung, A. S.; Lee, J.; Ferrara, N. Targeting the tumour vasculature: insights from physiological angiogenesis. Nat. Rev. Cancer 2010, 10 (7), 505.
16. Shereema, R.; Sruthi, T.; Kumar, V. S.; Rao, T.; Shankar, S. S. Angiogenic profiling of synthesized carbon quantum dots. Biochemistry 2015, 54 (41), 6352−6356.
17. Bartczak, D.; Muskens, O. L.; Sanchez-Elsner, T.; Kanaras, A. G.; Millar, T. M. Manipulation of in vitro angiogenesis using peptidecoated gold nanoparticles. ACS Nano 2013, 7 (6), 5628−5636.
18. Barui, A. K.; Veeriah, V.; Mukherjee, S.; Manna, J.; Patel, A. K.; Patra, S.; Pal, K.; Murali, S.; Rana, R. K.; Chatterjee, S.; Patra, C. R. Zinc oxide nanoflowers make new blood vessels. Nanoscale 2012, 4 (24), 7861−7869.
19. Spigoni, V.; Cito, M.; Alinovi, R.; Pinelli, S.; Passeri, G.; Zavaroni, I.; Goldoni, M.; Campanini, M.; Aliatis, I.; Mutti, A.; Bonadonna, R. C.; Dei Cas, A. Effects of TiO2 and Co3O4 nanoparticles on circulating angiogenic cells. PLoS One 2015, 10 (3), No. e0119310.
20. Bayda, S.; Hadla, M.; Palazzolo, S.; Kumar, V.; Caligiuri, I.; Ambrosi, E.; Pontoglio, E.; Agostini, M.; Tuccinardi, T.; Benedetti, A.; Riello, P.; Canzonieri, V.; Corona, G.; Toffoli, G.; Rizzolio, F. Bottom-up synthesis of carbon nanoparticles with higher doxorubicin efficacy. J. Controlled Release 2017, 248, 144−152.
21. Asghar, K.; Qasim, M.; Das, D. One-pot green synthesis of carbon quantum dot for biological application. AIP Conference Proceedings; AIP Publishing, 2017; p 50117.
22. Chen, W.; Hu, C.; Yang, Y.; Cui, J.; Liu, Y. Rapid synthesis of carbon dots by hydrothermal treatment of lignin. Materials 2016, 9 (3), 184.
23. Wang, C.; Xu, Z.; Zhang, C. Polyethyleneimine-functionalized fluorescent carbon dots: water stability, pH sensing, and cellular imaging. Chem. Nano Mat 2015, 1 (2), 122−127.

24. Yang, W.; Zhang, H.; Lai, J.; Peng, X.; Hu, Y.; Gu, W.; Ye, L. Carbon dots with red-shifted photoluminescence by fluorine doping for optical bio-imaging. Carbon 2018, 128, 78−85.
25.) Bao, X.; Yuan, Y.; Chen, J.; Zhang, B.; Li, D.; Zhou, D.; Jing, P.; Xu, G.; Wang, Y.; Hola, K.; Shen, D.; Wu, C.; Song, L.; Liu, C.;́ Zboril, R.; Qu, S. In vivo theranostics with near-infrared-emitting˜ carbon dots□highly efficient photothermal therapy based on passive targeting after intravenous administration. Light: Sci. Appl. 2018, 7 (1), 91.
26. Qu, S.; Zhou, D.; Li, D.; Ji, W.; Jing, P.; Han, D.; Liu, L.; Zeng, H.; Shen, D. Toward Efficient Orange Emissive Carbon Nanodots through Conjugated sp2-Domain Controlling and Surface Charges Engineering. Adv. Mater. 2016, 28 (18), 3516−3521.
27.) Zheng, M.; Ruan, S.; Liu, S.; Sun, T.; Qu, D.; Zhao, H.; Xie, Z.; Gao, H.; Jing, X.; Sun, Z. Self-targeting fluorescent carbon dots for diagnosis of brain cancer cells. ACS Nano 2015, 9 (11), 11455− 11461.
28. Stefanakis, D.; Philippidis, A.; Sygellou, L.; Filippidis, G.; Ghanotakis, D.; Anglos, D. Synthesis of fluorescent carbon dots by a microwave heating process: structural characterization and cell imaging applications. J. Nanopart. Res. 2014, 16 (10), 2646.
29. Choi, H. C.; Park, J.; Kim, B. Distribution and structure of N atoms in multiwalled carbon nanotubes using variable-energy X-ray photoelectron spectroscopy. J. Phys. Chem. B 2005, 109 (10), 4333− 4340.
30. Ogi, T.; Aishima, K.; Permatasari, F. A.; Iskandar, F.; Tanabe, E.; Okuyama, K. Kinetics of nitrogen-doped carbon dot formation via hydrothermal synthesis. New J. Chem. 2016, 40 (6), 5555−5561.
31. Zholobak, N. M.; Popov, A. L.; Shcherbakov, A. B.; Popova, N. R.; Guzyk, M. M.; Antonovich, V. P.; Yegorova, A. V.; Scrypynets, Y. V.; Leonenko, I. I.; Baranchikov, A. Y.; Ivanov, V. K. Facile fabrication of luminescent organic dots by thermolysis of citric acid in urea melt, and their use for cell staining and polyelectrolyte microcapsule labelling. Beilstein J. Nanotechnol. 2016, 7 (1), 1905−1917.
32. Khan, S.; Verma, N. C.; Nandi, C. K.; Chethana. Carbon Dots for Single-Molecule Imaging of the Nucleolus. ACS Applied Nano Materials 2018, 1 (2), 483−487.
33. Ilina, O.; Friedl, P. Mechanisms of collective cell migration at a glance. J. Cell Sci. 2009, 122 (18), 3203−3208.

34. Malinda, K. M.; Sidhu, G. S.; Banaudha, K. K.; Gaddipati, J. P.; Maheshwari, R. K.; Goldstein, A. L.; Kleinman, H. K. Thymosin α1 stimulates endothelial cell migration, angiogenesis, and wound healing. J. Immunol. 1998, 160 (2), 1001−1006.
35. Kuchroo, P.; Dave, V.; Vijayan, A.; Viswanathan, C.; Ghosh, D. Paracrine factors secreted by umbilical cord-derived mesenchymal stem cells induce angiogenesis in vitro by a VEGF-independent pathway. Stem Cells Dev. 2015, 24 (4), 437−450.
36. Dunn, I. F.; Heese, O.; Black, P. M. Growth factors in glioma angiogenesis: FGFs, PDGF, EGF, and TGFs. J. Neuro-Oncol. 2000, 50 (1−2), 121−137.
37. Tan, A. W.; Liau, L. L.; Chua, K. H.; Ahmad, R.; Akbar, S. A.; Pingguan-Murphy, B. Enhanced in vitro angiogenic behaviour of human umbilical vein endothelial cells on thermally oxidized TiO2 nanofibrous surfaces. Sci. Rep. 2016, 6, 21828.
38. Viñals, F.; Pouyssegur, J. Transforming growth factoŕ β1 (TGF-β1) promotes endothelial cell survival during in vitro angiogenesis via an autocrine mechanism implicating TGF-α signaling. Mol. Cell. Biol. 2001, 21 (21), 7218−7230. (b) Carmeliet, P. VEGF as a key mediator of angiogenesis in cancer. Oncology 2005, 69, 4−10.
39. Murakami, M. Signaling required for blood vessel maintenance: molecular basis and pathological manifestations. Int. J. Vasc. Med. 2012, 2012, 1.
40. Rafii, S.; Avecilla, S.; Shmelkov, S.; Shido, K.; Tejada, R.; Moore, M. A.; Heissig, B.; Hattori, K. Angiogenic factors reconstitute hematopoiesis by recruiting stem cells from bone marrow microenvironment. Ann. N. Y. Acad. Sci. 2003, 996 (1), 49−60.
41. Nethi, S. K.; Mukherjee, S.; Veeriah, V.; Barui, A. K.; Chatterjee, S.; Patra, C. R. Bioconjugated gold nanoparticles accelerate the growth of new blood vessels through redox signaling. Chem. Commun. 2014, 50 (92), 14367−14370.
42. Cao, Y.; Roursgaard, M.; Danielsen, P. H.; Møller, P.; Loft, S. Carbon black nanoparticles promote endothelial activation and lipid accumulation in macrophages independently of intracellular ROS production. PLoS One 2014, 9 (9), No. e106711.
43. Long, J.; Xiao, Y.; Liu, L.; Cao, Y. The adverse vascular effects of multi-walled carbon nanotubes (MWCNTs) to human vein endothelial cells (HUVECs) in vitro: role of length of MWCNTs. J. Nanobiotechnol. 2017, 15 (1), 80.
44. Cao, Y. The toxicity of nanoparticles to human endothelial cells. Cellular and Molecular Toxicology of Nanoparticles; Springer, 2018; pp 59−69.
45. Nel, A.; Xia, T.; Meng, H.; Wang, X.; Lin, S.; Ji, Z.; Zhang, H. Nanomaterial toxicity testing in the 21st century: use of a predictive toxicological approach and high-throughput screening. Acc. Chem. Res. 2013, 46 (3), 607−621.

46. Hopf, H. W.; Gibson, J. J.; Angeles, A. P.; Constant, J. S.; Feng, J. J.; Rollins, M. D.; Zamirul Hussain, M.; Hunt, T. K. Hyperoxia and angiogenesis. Wound repair and regeneration 2005, 13 (6), 558−564.
47. Wang, Y.; Zang, Q. S.; Liu, Z.; Wu, Q.; Maass, D.; Dulan, G.; Shaul, P. W.; Melito, L.; Frantz, D. E.; Kilgore, J. A.; Williams, N. S.; Terada, L. S.; Nwariaku, F. E. Regulation of VEGF-induced endothelial cell migration by mitochondrial reactive oxygen species. American Journal of Physiology-Cell Physiology 2011, 301 (3), C695− C704.
48. Yasuda, M.; Ohzeki, Y.; Shimizu, S.; Naito, S.; Ohtsuru, A.; Yamamoto, T.; Kuroiwa, Y. Stimulation of in vitro angiogenesis by hydrogen peroxide and the relation with ETS-1 in endothelial cells. Life Sci. 1998, 64 (4), 249−258.
49. Gloire, G.; Legrand-Poels, S.; Piette, J. NF-κB activation by reactive oxygen species: fifteen years later. Biochem. Pharmacol. 2006, 72 (11), 1493−1505
50. Denk, A.; Goebeler, M.; Schmid, S.; Berberich, I.; Ritz, O.; Lindemann, D.; Ludwig, S.; Wirth, T. Activation of NF-κB via the IκB kinase complex is both essential and sufficient for proinflammatory gene expression in primary endothelial cells. J. Biol. Chem. 2001, 276 (30), 28451−28458.
51. Kinose, Y.; Sawada, K.; Makino, H.; Ogura, T.; Mizuno, T.; Suzuki, N.; Fujikawa, T.; Morii, E.; Nakamura, K.; Sawada, I.; et al. IKKβ regulates VEGF expression and is a potential therapeutic target for ovarian cancer as an antiangiogenic treatment. Mol. Cancer Ther. 2015, 14 (4), 909−919.
52. DeNiro, M.; Al-Mohanna, F. H.; Alsmadi, O.; Al-Mohanna, F. A. The nexus between VEGF and NFκB orchestrates a hypoxiaindependent neovasculogenesis. PLoS One 2013, 8 (3), No. e59021.
53. Kitahata, K.; Matsuo, K.; Hara, Y.; Naganuma, T.; Oiso, N.; Kawada, A.; Nakayama, T. Ascorbic acid derivative DDH-1 ameliorates psoriasis-like skin lesions in mice by suppressing inflammatory cytokine expression. J. Pharmacol. Sci. 2018, 138 (4), 284−288.
54.) Bond, M.; Fabunmi, R. P.; Baker, A. H.; Newby, A. C. Synergistic upregulation of metalloproteinase-9 by growth factors and inflammatory cytokines: an absolute requirement for transcription factor NF-κB. FEBS Lett. 1998, 435 (1), 29−34.
55. Huot, J.; Houle, F.; Marceau, F.; Landry, J. Oxidative stressinduced actin reorganization mediated by the p38 mitogen-activated protein kinase/heat shock protein 27 pathway in vascular endothelial cells. Circ. Res. 1997, 80 (3), 383−392.

56. Qu, M.-J.; Liu, B.; Qi, Y.-X.; Jiang, Z.-L. Role of Rac and RhoGDI alpha in the frequency-dependent expression of h1-calponin in vascular smooth muscle cells under cyclic mechanical strain. Ann. Biomed. Eng. 2008, 36 (9), 1481−1488.
57. Thomas, J.; Sharma, A.; Panwar, V.; Chopra, V.; Ghosh, D. Polysaccharide-based Hybrid Self-healing Hydrogel Supports Paracrine Response of Mesenchymal Stem Cells. ACS Applied Bio Materials 2019, 2, 2013.
58.) Baudin, B.; Bruneel, A.; Bosselut, N.; Vaubourdolle, M. A protocol for isolation and culture of human umbilical vein endothelial cells. Nat. Protoc. 2007, 2 (3), 481.
59. Mosmann, T. Rapid colorimetric assay for cellular growth and survival: application to proliferation and cytotoxicity assays. J. Immunol. Methods 1983, 65 (1−2), 55−63.
60. Goodwin, A. M. In vitro assays of angiogenesis for assessment of angiogenic and anti-angiogenic agents. Microvasc. Res. 2007, 74 (2−3), 172−183.
61. Hoch, A. I.; Binder, B. Y.; Genetos, D. C.; Leach, J. K. Differentiation-dependent secretion of proangiogenic factors by mesenchymal stem cells. PLoS One 2012, 7 (4), No. e35579.
62. Eruslanov, E.; Kusmartsev, S. Identification of ROS using oxidized DCFDA and flow cytometry. Advanced protocols in oxidative stress II; Springer, 2010; pp 57−72.

Chapter 5: Development of piezo-driven triboelectric nanogenerator and electroactive hydrogel composite for wound healing.

5.1 Introduction: Diabetic foot ulcer (DFU) is a major complication in people suffering from diabetes mellitus (DM). It is estimated that about 15% diabetics develop foot ulcers and is identified as the single most common cause of morbidity among diabetic patients [1]. DFU manifests as deep lesions on the foot soles and is associated with peripheral vascular disease and neuropathy. The commonly employed treatment methods like pressure off-loading, wound debridement, skin grafting, anti-bacterial dressings, negative pressure wound Therapy (NPWT), hyper-baric oxygen therapy (HBOT) are not consistently effective in all patients [2]. Cell-to-cell communication in biological systems is regulated by ion movement across cell membranes and electrical signals through the tissue spaces. Hence, bioelectricity serves as a critical communication mode in the body [3]. Recent studies have demonstrated the significance of using bioelectric therapy in a variety of diseases, such as tissue repair, infection control, bone fracture healing, nerve regeneration etc. [4]. Upon electrical stimulation (ES), wounds are reported to show improved healing as a result of increased protein synthesis, cell migration and increased blood flow [5,6]. While ES has been used for the treatment of DFU, however the application is not well defined. The ES treatment conditions vary from 10 to 60 min per day at different frequencies and the treatment lasts from four to twelve weeks [2]. Despite the dissimilarities, a recent meta-analysis of 114 randomized clinical trials confirmed that ES was an effective adjunct therapy for accelerating DFU healing. Although ES is proven to enhance wound repair, it is not regularly used in the clinics due to patient non-compliance. To improve patient compliance, a wireless micro current stimulation (MCS) method was used, in which the charged gases present in the wound served as electron acceptor/donor [5]. Few battery-operated wearable technologies like PosiFect RD® and Procellera® are approved by the regulatory bodies for ES [6]. In recent years, the development of portable, human-friendly, wearable electronic devices such as triboelectric and piezoelectric nanogenerators (TENG and PENG) is attracting tremendous attention [7] due to their self-powered functionality. In

particular, the electrical energy in TENG is obtained from friction between two triboelectric layers [8], whereas the energy in PENG is based on the deformation of crystalline symmetry due to mechanical stimuli [9]. Due to inherent surface charge density available in the polymer based piezoelectric materials, it is possible to use such material as TENG and/or hybrid TENG/PENG by simply monitoring the device architecture. For example, a TENG/PENG-based device was used for the electrical stimulation of wounds, in which a bandage prepared with Cu/PTFE layers was used on either side of a polyethylene terephthalate [10]. A recent study has reported a wearable TENG composed of an organogel to harvest biophysical energy and provide electric stimulation to the impaired tissue [11]. Whereas, such dressings might provide optimal ES, however its use in wounds of DFU would be restricted due to its inability to regulate the high exudate and infection. In addition the complexity of its construction and application might serve as a deterrent for patient compliance. The use of hydrogels as wound dressing is well established [12]. The high water content in the hydrogel and its ability to absorb excess exudate, ensures a moist wound environment that facilitates debridement and faster epithelialization [13]. Conductivity in hydrogels is obtained by the incorporation of conductive materials, e.g., metals, carbon nanomaterials [14] or polymeric materials, such as polypyrrole [15], polyaniline [16] and poly(3,4-ethylenedioxythiophene) [17]. Few conducting hydrogels have shown promise in promoting wound healing [18]. The conductive hydrogels have electronic characteristic which is similar to the human skin and can be assembled into flexible electrodes in the human body [17]. With an intention to develop a patient-friendly, advanced interactive dressing for DFU, we proposed to develop a dressing having the following attributes: a) able to deliver ES; b) easy to use; c) wearable; d) non-invasive; e) provide a moist wound environment and f) having electronic skin-like characteristics. To achieve this, we conceptualized a dressing having a piezoelectric driven triboelectric nanogenerator (PTENG) with a conducting hydrogel as an electrode. The PTENG was made with electrospun fibers of

PVDF, as it is proven that the piezoelectric PVDF material can be directly used as the triboelectric layer aided by the intrinsic dipole moment which allows the surface charges to transfer during the contact and release process [19]. In order to provide a moist wound environment, a biocompatible hydrogel was prepared using polyacrylamide and polydopamine (PDA). As the structure of carbonized PDA (CPDA) is similar to nitrogen-doped graphite [20], and exhibits electrical conductivity equal or much superior than reduced graphene oxides [21], we introduced CPDA in the hydrogel for conductivity. The conductivity, rheological and mechanical properties, antibacterial activity, tissue adhesiveness and biocompatibility of the hydrogel was evaluated in vitro. The electrical output of the device was studied using appropriate models. Finally, the efficacy of the dressing to promote wound healing was demonstrated using an excision rat model.

5.2 Materials and methods

Materials: All chemicals used were of high purity and purchased from Sigma and Merck. Dopamine hydrochloride (DA), Acrylamide, N, N-methylenebis (acrylamide) (MBA), *N*, *N*, *N*′, *N*′-Tetramethyl ethylenediamine (TEMED) and Tris buffer were purchased from Sigma Aldrich. Phosphate buffered saline (PBS) was purchased from Himedia Laboratories. 3-(4,5-dimethylthiazol-2-yl)-2,5-diphenyl tetrazolium bromide (MTT) was from Invitrogen. All other chemicals and solvents were of analytical grade (commercially available) and used as received. Ethanol was purchased from Merck (India) and used without further purification. Distilled water was used throughout the synthesis.

5.2.1 Characterization techniques used:

Transmission electron microscopy (TEM) studies were carried out on a JEM2100 instrument, equipped with digital micrograph software for investigating the selected area electron diffraction (SAED) pattern of the graphene sheets. The FTIR spectra was recorded on Bruker spectrophotometer equipped with a horizontal attenuated total reflectance (ATR) accessory

containing a zinc selenide crystal. FE-SEM images were obtained on JSM-IT300 scanning electron microscope (JEOL Ltd, Japan) at an operating voltage of 15 kV. For this, the hydrogels were freeze-dried using a freeze-drier (FDUT-12003, Operon, Republic of Korea) for 24 h. The samples were then sectioned, sputter coated with gold and visualised using JSM-IT300 scanning electron microscope (JEOL Ltd, Japan). The FT-IR spectra of pure PAM, pure PDA and the PDA–PAM hydrogel (5 wt% DA/AM) were also analyzed to search for possible interactions between PAM and PDA using an FT-IR spectrometer (Nicolet 5700, Thermo, Waltham, MA, USA), and the spectra were recorded between 4000 and 500 cm^{-1}. The surface chemical compositions of the PDA, PAM and PDA–PAM hydrogels were measured using XPS (Kratos, Axis Ultra DLD, Manchester, UK). A monochromatic Al Kα X-ray was used as an excitation source (hν=1486.6 eV) running at 15 kV and 150 W. The neutral C1s peak (C–C (H), set at 285.0 eV) was used as a reference for charge correction. Before each measurement, the sample was washed three times in deionized water and ethanol to eliminate reactant residue from the sample and dried in a vacuum chamber at 40 °C for 2 days. Atomic force microscopy (AFM, Bruker Multimode 8) was used to investigate the surface topologies of the synthesized material. Raman analysis was carried out with a 532 nm laser line using a WITEC alpha 300 R Raman spectrometer, having a 600-line mm^{-1} grating. XRD analysis was performed on Bruker D8 Advance diffractometer at 40 kV and 40 mA with Cu Kα radiation (λ= 0.15418 nm) in the range 2-80º. Rheological properties of the hydrogels were studied with Modular Rheometer MCR302 (Anton Paar, Austria) using plate geometry (PP-25). The contact angle measurements were performed with a drop shape analyzer, KRUSS, DSA 100E at Operating temperature 10-40 °C. Conductivity measurement was done using a source meter, Keysight B2902A. Lap shear measurement was carried out to evaluate the adhesive strength of the hydrogel. Mechanical testing was done on BISS Tissue Compression Bioreactor. Cells in the hydrogel were visualized using a confocal laser scanning microscope (Zeiss LSM880 confocal

microscope, Carl Zeiss) and the images captured using Z-stacking mode under 10x magnification.

5.2.2 Synthesis of PDA

PDA and CPDA were synthesized according to reported method with slight modification [1]. Briefly, 0.5 g of dopamine was homogeneously stirred in 100 mL tris base having pH 8.5. The reaction mixture was kept for stirring for 24 h at room temperature. With the polymerization of PDA, the solution underwent a colour change from colourless to pale brown and finally turned to deep brown black over time, which is the typical colour of PDA. The material obtained is centrifuged and dried overnight in an oven.

5.2.3 Synthesis of CPDA sheets

Carbonization of PDA was done at 800 ºC for 2h at the heating rate of 10 ºC/min, to form the CPDA sheets.

5.2.4 Preparation of hydrogel

Series of hydrogels were synthesized by mixing PDA solution with CPDA nanosheets to make different combination of PDA: CPDA (1:1, 1:2, 2:1). Thereafter, acrylamide (AM), APS and BIS were mixed with the above solution and after mixing for 10 min, TEMED was added to initiate the polymerization of acrylamide to form CPDA hydrogels. The control gel was prepared in a similar manner without the addition of PDA and CPDA.

5.2.5 Self-healing and conducting property: The self- healing property of CPDA hydrogel was determined using two methods [2]. While the cut & heal test was performed according to our previous study, a similar test was done to monitor the flow of current during healing process. For this, the hydrogel discs were cut into 2 halves and kept in close proximity at 37°C and the time taken for the LED bulb to glow was noted. The conductivity of the CPDA hydrogel was measured using four probe method with Keithely 2635B as source meter.

5.2.6 Rheology: The strength of the hydrogels was studied with Modular Rheometer MCR302 (AntonPaar, Austria) using plate geometry (PP-25) according to our previous report [3]. For this the hydrogels were prepared in a disc shape mold and transferred to the plate. The spindle was lowered to the measurement position with a gap of 0.21 mm and the storage and loss moduli were recorded under time sweep with changing strain.

5.2.7 Adhesiveness: Texture analyzer was used to determine the adhesiveness of CPDA hydrogel according to our previous reported method [3]. The following substrates were chosen for the investigation: glass, steel, plastic, rubber, skin, kidney, liver and heart and all the measurements were performed in triplicate.

5.2.8 Mechanical Testing: The compression test of the hydrogel was carried out using BISS Tissue Compression Bioreactor (India). Using a hydrogel of 2 mm in height and 22 mm in diameter, the compression test was performed using speed of the crosshead 1 mm/s and the load cell was 200 N. The compression strength was determined when compressive strain reached 60%.

5.2.9 Fluid handling capacity: The ability of the hydrogel to retain moisture and provide a moist environment, was evaluated using the modified SMTL test method TM-238 as mentioned by Das *et al*. [4] . The swelling index of the hydrogel was determined in PBS (phosphate buffered saline) at 37 ^{o}C as reported [3]. For donation study,20% gelatin solution was prepared and transferred to a petri dish. Pre-weighed CPDA hydrogel was placed on the surface of the simulated wound for various time durations to allow the underlying gelatin gel to absorb the moisture donated by the CPDA hydrogel. The fluid retention (FR) ability of the hydrogel was calculated by using the following equation.

$$\boldsymbol{Fluid\ retention}\ (\%) = \frac{\boldsymbol{Wf - Wi}}{\boldsymbol{Wg}} * \mathbf{100} \quad \textbf{(Equation 1)}$$

where Wi = initial weight of the plate along with the gelatin before hydrogel

Wf = final weight of the Plate along with the gelatin after removing hydrogel

Wg = weight of hydrogel used

The study was carried out for 24, 48, 72 and 96 h using four different set of samples, each in triplicate.

5.2.10 Preparation of PVDF membrane: PVDF membrane was made with slight modification to the reported protocol [5]. Briefly 12 wt % solution was made by dissolving PVDF pellets in a mixture of DMF and acetone (mass ratio of 6:4) at 60 ^{o}C. The homogeneous solution was transferred to a syringe (10 mL) fitted with a stainless-steel needle for electrospinning. The electrospinning process was carried out at a high-voltage power supply of 12 kV, and the distance between the needle and the roller collector was 13 cm. The speed of the drum was 1200 rpm. The syringe pump was used to feed the polymer solution into the needle tip at a rate of 0.4 mL h^{-1} and the electro spun fibres were collected on a rotating collector. The electro spun PVDF membrane was dried at 60 ^{o}C for 12 h to eliminate the remaining solvents for further characterization and dressing fabrication.

5.2.11 PTENG Evaluation: To evaluate the electrical output of the nano generator, 3.5 cm × 3.5 cm of PVDF membrane was sandwiched between two preformed rectangular conducting CPDA hydrogels of same size as that of PVDF membrane. While PVDF served as the source for voltage generation, the conducting hydrogels served as electrodes. On application of mechanical pressure, the triboelectric voltage that was generated was evaluated.

5.2.12 Dressing fabrication: The wound dressing for addressing impaired wound healing was fabricated with a surface of the hydrogel laminated with PVDF membrane. For application, the conducting hydrogel would be in close proximity to the wound, and the PVDF membrane would face the opposite side. The dressing was designed for providing electrical stimulation to the wound during physical movements like walking/stretching etc.

5.2.13 Biocompatibility assay: The biocompatibility of the CPDA hydrogel was tested using a standard protocol as reported earlier [3]. Briefly, the hydrogels were incubated in cell culture media for 72 h at 37 ^{0}C. The fibroblasts seeded in multi-well plate were treated with the contact media from the hydrogel and incubated for 24 h at 37 ^{0}C. The morphology was monitored using microscope, and the MTT assay was performed to evaluate the viability.

5.2.14 Viability of encapsulated cells in CPDA hydrogel: To evaluate the potential of the hydrogel to support cell growth, two primary cells i.e. human dermal fibroblasts (HDF) and human endothelial cells (HUVEC) were used. The cells were isolated from human tissues after receiving the donor consent, as per the ethics committee approval of PGIMER, Chandigarh, India. For the study, HUVEC/HDF cells were seeded on the pre-cast sterile CPDA hydrogels. After seeding, the hydrogels were incubated in a CO_2 incubator with regular medium change every alternate day. On day 3, 5 and 7 after seeding, the viability of the cells was checked using live/dead staining with FDA (Fluorescein-di acetate) and PI (propidium iodide. After staining, the respective hydrogels were visualised using confocal microscope (Zeiss LSM880 confocal microscope, Carl Zeiss) [3].

5.2.15 Migration of HUVEC in the hydrogel: The response of the endothelial cells cultured in the CPDA hydrogel under the influence of an electric field was evaluated using a customized electric stimulation device. Briefly, CPDA hydrogels were taken and sterilized with the help of 70 % ethanol. HUVEC cells were then seeded on top of the hydrogel at a cell density of 50000 cells /hydrogel and incubated for 24 h in media. Following the renewal of the culture medium at 24 h, the seeded hydrogels were connected to a DC constant potential source through external electrodes placed in a 35 mm petri plate. A potential difference of 100 mV/mm was applied for 6 h on 3 consecutive days. After 3 d, the hydrogel was subjected to live dead assay using FDA and PI and the cells visualized using confocal laser microscopy [5].

5.2.16 Bacterial viability Studies: To check bacterial viability on contact with the synthesized hydrogel, E. coli was seeded on top of both the control and CPDA hydrogels and incubated at optimum conditions for 24 h. At the end of exposure, the hydrogels were stained using FDA and PI for 30 min in the dark. The stained bacterial cells were captured using a laser scanning confocal microscope [6]. For FESEM gels seeded with bacteria were collected and fixed with 2.5% glutaraldehyde solution for 30 min. The fixed samples were dehydrated using alcohol gradient method. The samples were then air dried and sputter coated with gold palladium before analysis. FE-SEM images were obtained on JSM-IT300 scanning electron microscope (JEOL Ltd, Japan) at an operating voltage of 2 kV.

5.2.17 *In vivo* wound healing studies: The wound healing potential of CPDA hydrogels was studied using the excision wound model in Sprague Dawley (SD) rats after receiving ethic approval from the Institutional Animal Ethics Committee of Maharishi Markandeshwar university (deemed to be), Mullana (Ambala), India. The rats were anaesthetized using an intra-peritoneal injection of a mixture of xylazine and ketamine. The dorsal surface of the rat skin was shaved with the help of trimmer and a full thickness wound of diameter 8 mm was created using a biopsy punch. After creating the wound, the animals were divided into 3 groups namely control, hydrogel and Dressing. The wounds were covered with either CPDA hydrogels or the fabricated dressing. The wounds in the control group animals were covered with adhesive film dressing (Tegaderm). The wound site of every animal was photographed on d 1, 3, 7 and 14 and the wound diameter was measured. At the end of 14 d, the animals were sacrificed and the implanted skin tissues were harvested to process for immunohistological and H&E staining [7]. For immunostaining, the excised wound area was processed and sectioned using cryo-microtome. For immune histological staining, the sections were incubated with 10 mm sodium citrate buffer for 1 h. To prevent non-specific binding, the sections were blocked with 5 % BSA solution for 2 h. To identify the blood vessels, the tissue sections were labelled with an

endothelial marker, CD 31 (Invitrogen) at a dilution of 1:300 O/N at 4 ^{0}C. CD31 positive samples were identified using an Alexa Fluor 568-conjugated secondary antibody (Invitrogen). Hoechst (Invitrogen) was used as the nuclear stain. Sections were assessed under confocal laser microscope (Zeiss LSM 880) [8].

5.2.18 Statistical Analysis: The significance level in all statistical observations was set at a probability of $p < 0.05$. All the data is presented as mean ± SD. ANOVA and Bonferroni test were used to analyse the data and to calculate the level of significance.

5.3 Results and discussion: Taking into consideration the unique challenges facing DFU dressings, we developed a simple bi-component dressing made with PVDF membrane and a conducting CPDA hydrogel respectively.

5.3.1 Synthesis and characterization of CPDA: PDA and CPDA were synthesized using a facile two-step method as shown in Figure 5.1. The first step was an alkali-induced PDA polymerization, in which DA molecules were oxidized to form PDA chains through reaction of the catechol and quinone groups. In the second step, carbonization of PDA was done at 800 ºC for 2 h at the heating rate of 10 ºC/min, to form the CPDA particles. Pyrolysis at high temperatures (800 ºC) of PDA particles resulted in N-doped carbon materials with graphene-like structures. Conclusions drawn from the structure of the carbonized films revealed layered-stacking supramolecular arrangements.

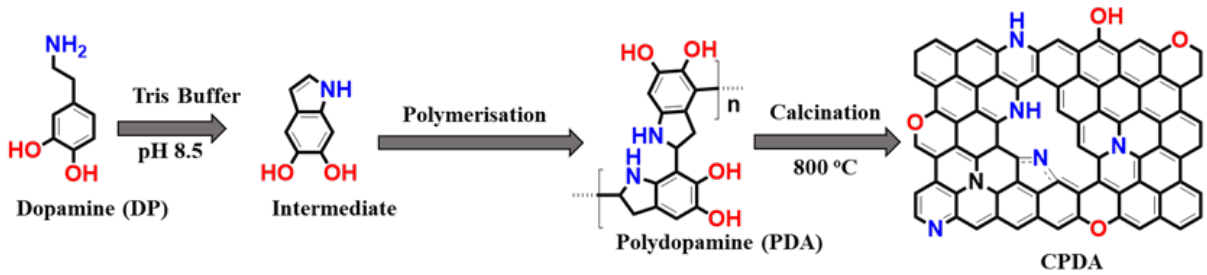

Figure 5.1: Schematic representation for the synthesis of PDA and CPDA sheets.

5.3.2 Morphological studies: The morphology of the synthesized CPDA material was investigated by TEM and AFM microscopy. The images shown in Figure 5.2 (A-C) confirm the sheet like pattern of CPDA similar to graphitic sheets [1]. High resolution TEM images of selected region shown in Figure 5.2C, revealed the interplanar distance of 0.341 nm corresponding to 002 plane of graphitic nanosheet. Additionally, we carefully measured the layer distance of these thin films using image J software and found to be approximately 0.34 nm, which was similar to the data obtained from FFT. The value indicated its similarity to the typical distance observed between graphite stacking layers, Figure 5.2 C. Besides, we also found several dark domains indicating few ordered stacking layers of graphitic sheets and its corresponding FFT images confirmed the interplanar spacing of 0.215 nm, 0.341nm and 0.556 nm corresponding to 100, 002 and 001 planes of graphitic sheets (Figure 5.2B). The real-space image and its fast fourier transform (FFT) pattern (inset in Fig. 5.2C) further confirmed that the material was layered graphene with a spacing of 0.34 nm. The SAED pattern shown in Figure 5.2D reveals the presence of a hexagonal lattice of crystalline graphitic like sheets with long-range order. The observed diffraction pattern revealed both diffraction rings and ordered hexagonal diffraction patterns. On the basis of these results, CPDA may be regarded as a multi-layered graphitic film. Kong *et al.* had reported that highly electrically conductive layered carbon can be derived from PDA after its carbonization [9]. The active crystal planes of the nanosheets calculated to be (002) and (100) planes of the reciprocal lattice (Figure 5.2D), which is in line with the data obtained from XRD measurements (Figure 3F1). The AFM analyses, Figure 5.2 (E-F) indicated an average thickness of 9.5 nm which corresponds ≈28 layers of graphene. From the morphological characterization, it is predicted that the layered structure of graphitic carbon can have high conductivity. This coincides with the graphitic nature of the material deduced from the Raman and X-ray photoelectron spectra. The smooth and continuous morphology, together with the graphitic nature, might bestow high conductivity to CPDA.

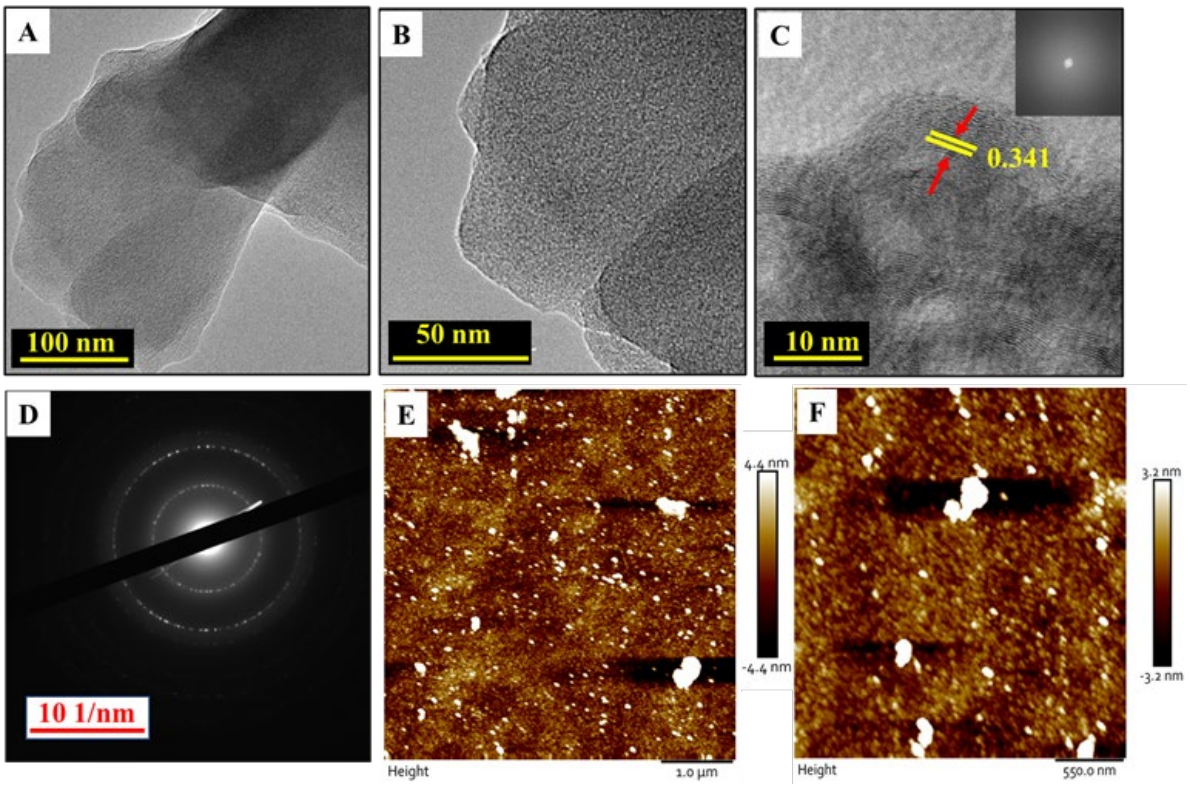

Figure 5.2: Characterization of CPDA. A, B) TEM image; (C) HR-TEM image, inset in (c) shows the FFT pattern of CPDA and (C) SAED pattern. (E, F) tapping-mode atomic force microscopy (AFM).

5.3.3 Raman, XRD and XPS: The Raman spectra of both PDA and CPDA particles showed two distinct peaks, a D band at ~1350 cm^{-1} and a G band at ~1580 cm^{-1} respectively (Figure 5.3 (D1, D2)). The D band is due to the distorted carbon, and the G band corresponded to graphitic carbon. The area integral intensity ratio of the two peaks (I_D/I_G ratio) was increased, and the peak position of the G band tended to shift to a higher Raman shift with carbonization (Figure 5.3 D1). The increased Id/Ig ratio and gradual blue shift indicated that the PDA layer, which consists of amorphous carbon, was converted to a nanocrystalline graphite-like structure. In addition, this increase in the intensity ratio indicated a generation of defects and doping by heteroatoms (nitrogen and oxygen) in the graphitic planes during the calcination of PDA [1]. This Raman spectrum showed typical feature of a mixture of amorphous carbon and nanocrystalline graphite, which is in agreement with our HRTEM observation.

Wide angle X-ray powder diffraction analysis was conducted under monochromatized Cu-K_α. To confirm the crystallinity and phase structure of the material as shown in Figure 5.3 (F1, F2). In PDA, an intense crystalline peak observed at $2\theta = 26.4°$ (d=0.34 nm) corresponds to the (002) diffraction peak of PDA. In CPDA, the intensity of the peak reduced and the peak appeared broader due to the partial breakdown of the long-range order of the graphitic like sheet. Moreover, the peak position remained almost the same. Meanwhile, a relatively weak and broad shoulder was observed at $2\theta=22.8°$, yielding an interlayer separation of 0.39 nm. The interlayer spacing was calculated to be the (002) graphite peak of 0.35 nm. The prominent diffraction peak at $2\theta = 30.1°$ originated because of the characteristic reflection from the (002) graphitic plane. This peak is much sharper than the small peak at $2\theta = 43.5°$ assigned to the (100) plane of distorted graphitic sheets, confirming the high degree of crystallinity (Figure 5.3 F2).

The chemical structural analysis of PDA and CPDA was evaluated by the X-ray photoelectron spectroscopy (XPS) spectrum. Figure 5.3 (A1, A2, B1, B2, C1, C2) displays the wide survey spectra of PDA and CPDA, indicating the presence of oxygen, carbon and nitrogen. Deconvoluted spectrum of C1s shows five characteristics peaks at 284.7, 286.3, 287.8, 288.9, and 290.5 eV that correspond to the C-C, C-O/ C-N, C=O/C=N, O-C=O and π-π^* transitions respectively (Figure 5.3 (B1, B2)) [1].The high-resolution N1s spectra can be deconvoluted into three peaks located at 397.8, 399.6, and 402.1 eV, which can be assigned to the pyridinic N, pyrrolic N, and graphitic N respectively Figure 5.3 (C1, C2). In PDA, the N1s spectrum is solely dominated by pyrrolic nitrogen Figure 5.3 (C2). Meanwhile, the XPS survey of CPDA exhibited a significant peak area of pyridinic nitrogen, which is comparable with that of pyrrolic nitrogen, thus indicating the appearance of nitrogen at the edge of the graphitic layer Figure 5.3 C1. Similarly, the peaks of O1s can be deconvolved into three components with binding energies of 530.01 eV, 531.65 eV and 534.02 eV which correspond to C-O, C=O and

C-OH/C-O-C groups both in PDA and CPDA (Figure 5.3 (A1, A2)). Moreover, the peak intensity in CPDA for C=O has been increased w. r. t. PDA confirming its carbonization. The survey scan illustrates the existence of C1s, N1s, and O1s peaks at approx. 284.5, 400.9, and 533.5 eV. With carbonization, while the percentage of carbon was increased significantly, nitrogen and oxygen decreased. In CPDA, the percentage of N and O was found to be 4.3% and 16.1% while in PDA it was 3.3% N and 33.3% O respectively (Figure 5.3 (E1, E2).

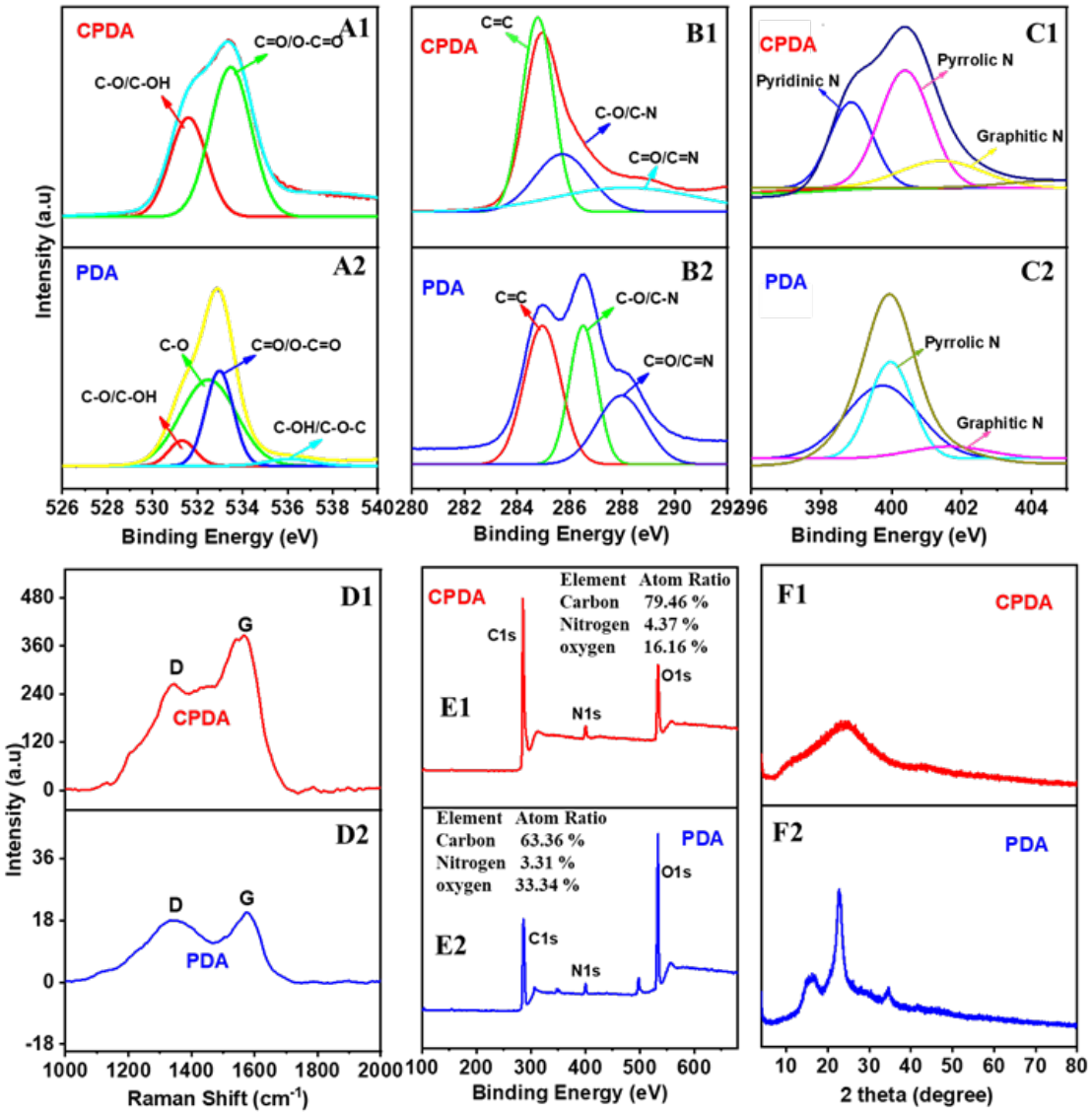

Figure 5.3: X-ray photoelectron spectroscopy survey of PDA and CPDA. XPS high resolution spectrum. B1, B2) O1 region; (C1, C2) C1s region; (D1, D2) N1s region; (D1, D2) XPS full scan spectrum. Raman spectra. E1) CPDA; E2) PDA. XRD diffractogram. F1) CPDA; F2) PDA.

5.3.4 Synthesis and characterization of the CPDA hydrogel: The CPDA hydrogels were synthesized using a facile two-step method as shown in the Figure 5.4.

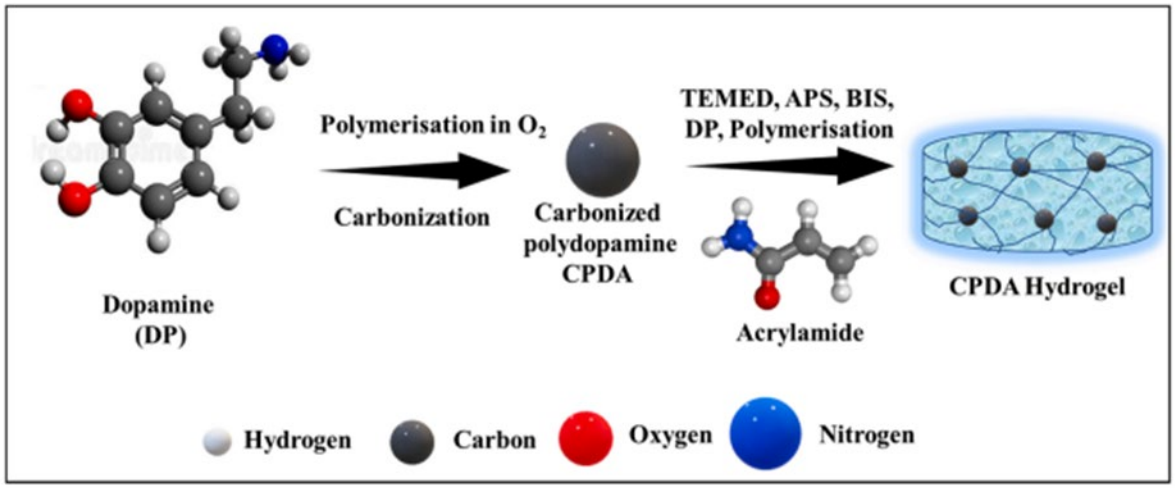

Figure 5.4. Schematic representation for the synthesis of CPDA hydrogel

A series of hydrogels were made by varying the ratios of PDA and CPDA i.e., 1:1, 1:2 and 2:1 of PDA: CPDA respectively, while keeping the other components constant as discussed in experimental section. For DFU application, a hydrogel was chosen on the basis of its conductivity, adhesiveness and storage modulus. The conductivity studies confirmed the positive influence of the CPDA content in the hydrogel formation (Figure. 5.5 A). PDA content had an influence on the adhesiveness of the hydrogel (Figure. 5.5 B) [23]. The mechanical strength, evaluated using rheological tests indicated that respective hydrogels followed the order: PDA: CPDA (1:1) < PDA: CPDA (2:1)> PDA: CPDA (1:2) (Figure. 5.5 C). The increase in mechanical strength observed with increasing content of PDA may be facilitated by the higher entanglement of the polymer chains that act as a reinforcement for the hydrogel [24]. Considering its application in DFU, we selected the hydrogel with 2:1 ratio of PDA: CPDA, on the basis of its favourable conductivity (0.02 S/ cm), strength (~100 kPa) and adhesiveness (~75 kPa). Henceforth this hydrogel would be referred to as CPDA hydrogel and further studies were pursued in comparison with the control gel (plain acrylamide gel). During the hydrogel

formation, the CPDA sheets interlink with the PDA chains through covalent and non-covalent interactions. Additionally, the catechol groups present on PDA interact with the amino groups of the polyacrylamide to form covalent and recoverable non-covalent bonds, including π–π stacking and hydrogen bonds through intertwining in the polyacrylamide network [24]. A vibrational band at around 1260 cm^{-1} corresponds to C-N stretching in phenyl amines as confirmed from the FTIR spectra (Figure. 5.5 D). This peak also indicated the interactions between the -NH2 groups of polyacrylamides and the catechol groups of polydopamine. The broad band from 3700 to 3300 cm^{-1} is assigned to N-H and O-H stretching modes, and peaks at 2936 to 2881 cm^{-1} are due to the C-H stretching mode. The strong absorption peaks at around 1720 cm^{-1} is due to the C– –O stretching and another sharp peak at around 1640 cm^{-1} is attributed to the vibrations of sp2 domains which confirms π–π stacking.

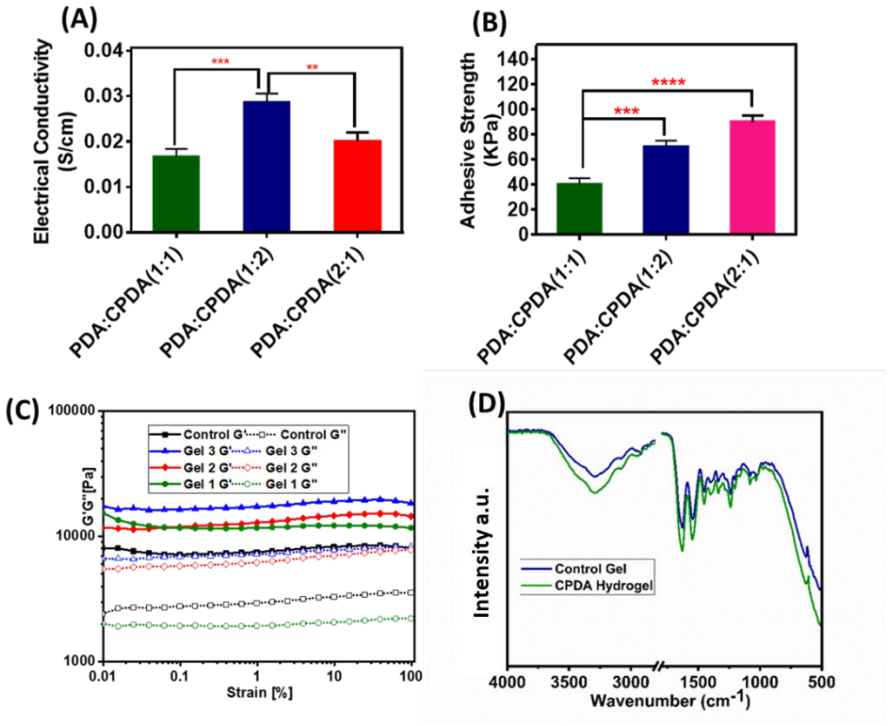

Figure 5.5: Physical characteristics of CPDA hydrogel. (A) Electrical conductivity of series of CPDA hydrogels, (B) Adhesive strength of CPDA hydrogels, (C) rheological studies, (D) FTIR spectrum

5.3.5 Morphology, fluid handling capacity and rheological properties:

Hydrogels can serve as scaffolds for the regenerating tissue and the cellular response is dependent on the structural properties of the hydrogels. Hydrogels having pore size in the range of 50–300 μm are known to facilitate the transport of nutrients and support cell growth [25]. The FESEM images of freeze-dried CPDA hydrogel revealed interconnected network of pores in the range of 50–100 μm (Figure. 5.6 A), suggesting it can provide optimal condition for favouring tissue growth. Hydrogels with good fluid handling capacity are known to enhance the rate of wound healing by providing a moist environment to the wound [26] to encourage autolytic debridement and facilitate epithelial migration [27]. Therefore, a hydrogel that combines both fluid absorption and moisture donating properties can provide an optimal environment for healing. Non-healing ulcers generally produce high levels of exudate that must be promptly removed, to prevent wound infection/maceration [28]. Upon evaluation of fluid uptake, both control and CPDA hydrogels absorbed a significant amount of fluid and exhibited swelling of around 280% and 260% respectively (Figure. 5.6 B). As hydrogel dressings are replaced every 2–3 d, the swelling ability of the CPDA hydrogel suggested that it can absorb a significant amount of wound exudate. In cases where the wound may be desiccated, the hydrogel with its high-water content can provide a moist wound environment by fluid donation [26]. The ability of the CPDA hydrogel to donate moisture is shown in Figure. 5.6 C. It was observed that the gel could donate ~ 30 ± 2% of its moisture by 96 h, suggesting that the hydrogel can provide a moist environment even to desiccated wounds [13]. Apart from fluid handling, the hydrophilicity of the hydrogel was assessed using contact angle [29]. As the DFU is located on the foot, it is subjected to frequent mechanical stretching and compression. Hence, the dressings meant for such areas demand higher mechanical properties. Rheological studies were performed to assess the mechanical properties of the respective hydrogels. Data from the amplitude sweep study revealed that both the control and CPDA hydrogel showed higher

elastic modulus than the viscous modulus, thereby confirming its gel property [24] (Figure. 5.6 D). The frequency sweep data revealed little change in storage modulus with less variations in the loss moduli indicating no sign of breakage (Figure. 5.6 E). These results confirmed that the hydrogels were mechanically robust and had higher strength than the conducting hydrogels reported for tissue regeneration and wound healing [30]. Since the storage modulus of soft tissues, like the dermis is in the range of 10^2 ~10^3 Pa [31], the CPDA hydrogel with adequate mechanical properties has the potential to meet the mechanical requirements matching that of soft tissues [32]. As shown in Figure. 5.6 F, the incorporation of CPDA had resulted in an increase in the storage modulus of the hydrogel (~1 ×10^5 Pa) in comparison to the control gel (~1 ×10^4 Pa). These results are in good agreement with the storage modulus of hydrogels reported for wound healing.

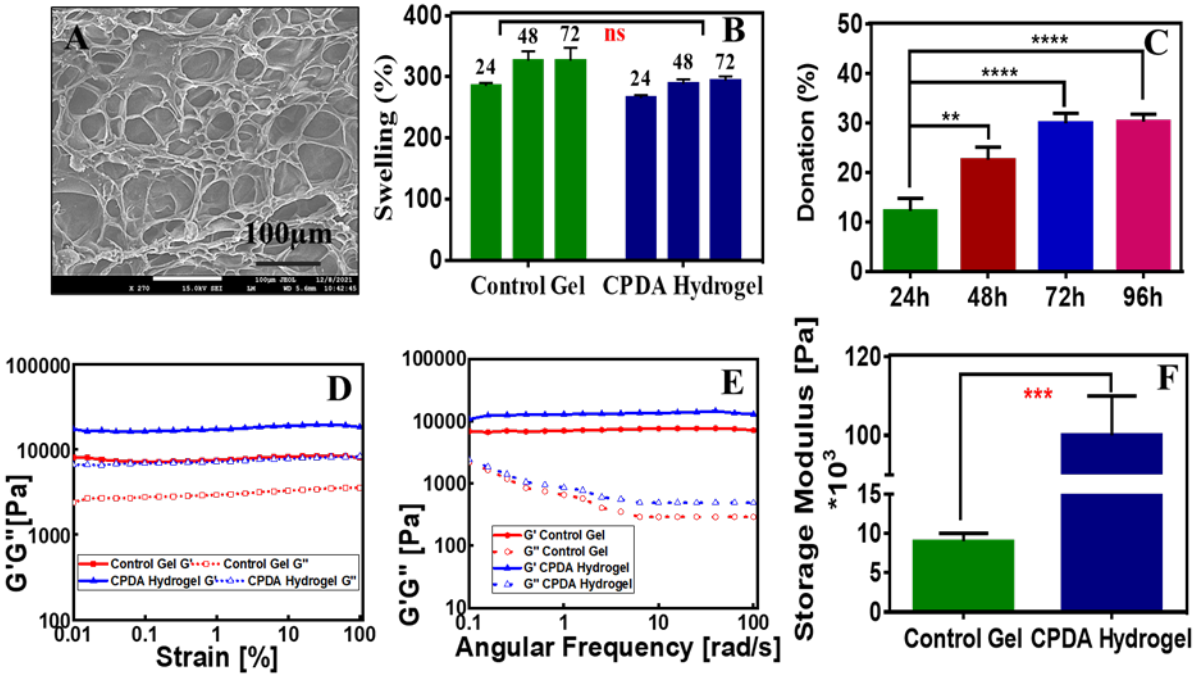

Figure 5.6: Characterization of CPDA hydrogel (A) FESEM images of freeze-dried CPDA hydrogel; (B) Swelling index; (C) Fluid donation by CPDA hydrogel. **Rheological properties** (D) Amplitude sweep of CPDA hydrogel showing the elastic modulus (solid lines) and viscous modulus (dotted lines) at different shear strain; (E) Frequency sweep measurements demonstrating their viscoelastic behaviour (G' > G''); (F) Storage modulus; Data represents an average of 3 experiments. **** represents P-value

≤0.0001, *** P-value ≤ 0.001 and ** P-value ≤0.01 respectively (One-way ANOVA, Tukey's multiple comparisons test).

5.3.6 Self-healing and conductivity of the CPDA hydrogel

Self-healing ability is recommended in hydrogels, especially for application on surfaces that are subjected to mechanical stress. The self-healing ability of the CPDA hydrogel was investigated using the brake–heal test (Figure. 5.7(A1-A3). The time required for self-healing without any external stimulus was 12 ± 3 min and 8 ± 2 min for control and CPDA hydrogel respectively (Figure. 5.7 C). The time for self-healing in these hydrogels is considerably shorter than that reported in self-healing hydrogels for wound repair applications [24]. The faster recovery can be ascribed to catechol-mediated interfacial hydrogen bonds and π–π stacking in the hydrogel network. The good self-healing performance of the hydrogel would ensure that it can prevent the potential risk of infection as a result of dressing rupture, apart from protecting the underlying wound. While few conducting hydrogels per se have been tested in wound healing [33], there are no reports on its use as an electrode for ES. Since CPDA is conducting in nature [22], we postulated that the CPDA hydrogel can serve as an electrode in our application. Using the four-probe method, the conductivity of the control gel and CPDA hydrogel was observed to be 2 × 10− 6 S/cm and 2 × 10− 2 S/cm respectively (Figure. 5.7 D). The results confirmed the conductivity of CPDA matched the dermal tissue (0.01–0.07 S/cm) [34] and the electroactive hydrogel could serve as an electrode for ES. The illumination of LED light in the hydrogel on post-healing, confirmed that current flow was re-established post its distortion (Figure. 5.7 (B1-B3)). The relative change in resistance at different strains following its stretching is shown in Figure. 5.7 E. The conductivity of CPDA hydrogel was also assessed in response to various human gesticulations like elbow and finger bending and finger flapping by using it as a wearable strain sensor. As shown in Figure. 5.7(F1-F3), the hydrogel applied on the various joints displayed a change in current during movement, indicating its potential as

a motion sensor. These results are in agreement with the reported values of current for wearable strain sensors and tissue repair [35].

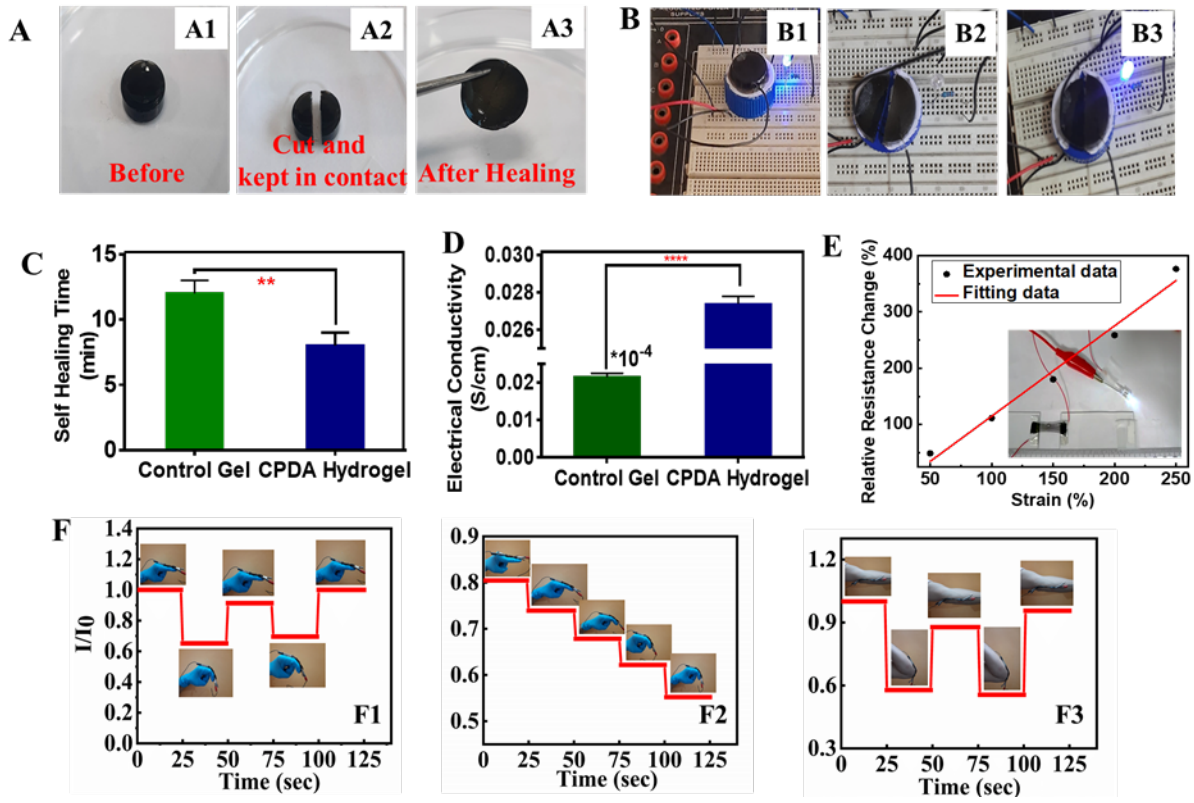

Figure 5.7: Self-healing and conductivity tests. (A1-A3) Self-heal test; (B1-B3) LED illumination post self-healing; (C) Time for self-healing; (D) Conductivity measurement; (E) Relative change in resistance in CPDA hydrogel at different strains; Change in current on: (F1) Finger bending; (F2) Finger flapping (F3) Elbow bending. Data represents an average of 3 experiments. **** represents P-value ≤0.0001 and ** P-value ≤0.01 respectively (One-way ANOVA, Tukey's multiple comparisons test).

5.3.7 Adhesiveness, stretchability and compressive properties

The foot wounds are subjected to various degrees of pressure during movement and good adhesion of the dressing to the tissue can avoid potential exposure of the wounds to the external environment. The hydrogels in the dressing should therefore have good adhesive property to enable it to attach to the underlying wound. PDA based hydrogels have good tissue adhesiveness in view of its structural similarity to an adhesive protein secreted by mussels [36]. The ability of the CPDA hydrogel to adhere to various substrates was tested Figure. 5.8 (A1-

A8). The adhesiveness of the CPDA hydrogel with skin (70 ± 10 kPa) was significantly higher than the control gel (40 ± 5 kPa) (Figure. 5.8 A9). This data matches with the recommendations of Hao et.al. for tissue repair applications [35]. Its excellent adhesive strength is displayed by its ability to support a tube containing 50 mL of water (63.9 g) (Figure. 5.8 A10). Wound healing is a well-orchestrated process with multiple overlapping stages including hemostasis, inflammation, proliferation, reepithelization and remodeling. Delay at any stage can affect the healing process. In DFU, repeated injury to the wound site as a result of physical movement is a major factor affecting healing [37]. The existing DFU dressings are unable to provide protection to the underlying wounds and hence off-loading is recommended [38]. Only few studies have paid attention to wounds in areas frequently subjected to motion. [33]. We evaluated the ability of the hydrogel to accommodate physical movement. As revealed in Figure. 5.8 C, the CPDA hydrogel could withstand stretching and was able to sustain large deformations while retaining the elasticity of the hydrogel [24]. The compressibility of the hydrogel is another important aspect for application in weight-bearing areas, such as the foot. The potential of the hydrogel to withstand compressibility was confirmed using a tissue compression bioreactor (Figure. 5.8 (B1-B3)). Figure. 5.8 (B4) shows the typical stress–strain curve of the CPDA hydrogel. The maximum compressive strength of the hydrogel determined at 60% of compressive strain was found to be 0.18 MPa, suggesting the ability of the hydrogel to sustain mechanical deformation caused by movements. The changes in strain and stress w.r.t time is shown in Figure. 5.8 (D-F) and the data revealed that the CPDA hydrogel maintained its integrity even after multiple cycles of compression and relaxation.

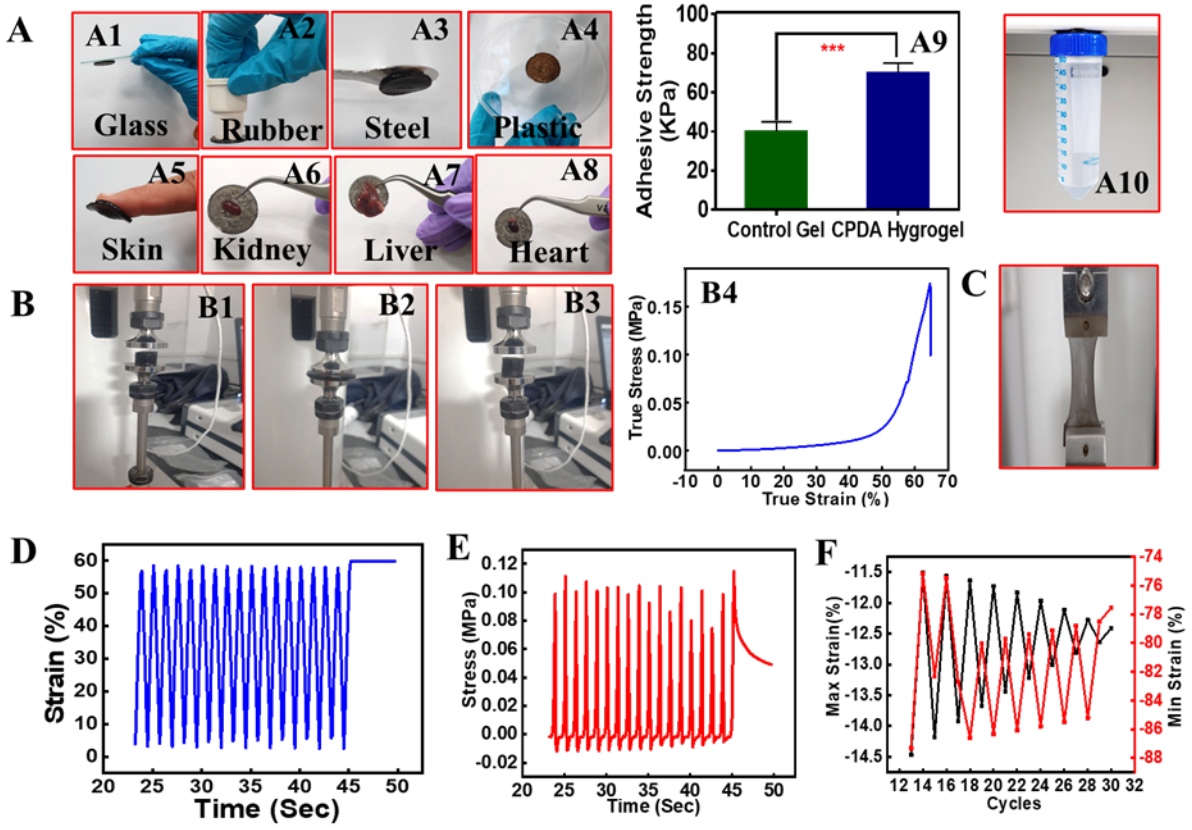

Figure 5.8: Adhesiveness, stretchability and compressibility of CPDA hydrogel. Photographs of the hydrogels adhered to various substrates. (A1) Glass; (A2) Rubber; (A3) Steel; (A4) Plastic; (A5) Skin; (A6) Kidney; (A7) Liver and (A8) Heart; (A9) Adhesive strength of the hydrogel with skin. *** represents P-value ≤ 0.001 respectively (One-way ANOVA, Tukey's multiple comparisons test). (A10) Hydrogel supporting tube containing water [50 mL]. Response to compression. Shape of the hydrogel (B1) Pre-compression; (B2) Upon compression; (B3) Post-compression; (B4) Typical compression stress–strain curve of for CPDA hydrogel. (C) Stretching potential. (D) Change in strain on continuous compression and relaxation process. (E) Change in stress on continuous compression and relaxation process. (F) Curve showing maximum strain and minimal stress during the compression and relaxation process.

5.3.8 Fabrication of the PTENG wound dressing and Electrical output evaluation

To provide ES to the underlying wound, we fabricated a composite PTENG wound dressing by pairing a PVDF membrane (prepared by electrospinning technique as illustrated in Figure. 5.9 A) along with the CPDA hydrogel. The adhesive property of the CPDA hydrogel enabled

its firm fixation to the PVDF membrane and assist in the collection of the piezoelectric driven triboelectric charges from the surface of the PVDF membrane. To investigate the surface morphology of the PVDF membrane, FE-SEM images of the nanofibers was recorded (Figure. 5.9 B1). The images revealed the surface of the nanofibers to be smooth and bead-free, and the average fiber diameter was ~78 nm. Furthermore, in order to understand the chemical composition of the PVDF membrane, XPS spectra was measured using monochromatic Al K alpha X-ray source. The survey scan of the membrane revealed the presence of carbon (C) and fluorine (F) elements in the PVDF membrane with atomic percentage ratio~ 1:1 (Figure. 5.9 B2), indicating that the high voltage assisted electrospinning had not caused its degradation. From the curve fitting analysis, the presence of some adventitious carbon observed may be due to environmental contaminants which is hard to avoid [39]. Next, the electroactive phases of the electrospun PVDF membrane was confirmed from the FTIR spectra. The vibrational bands at 1275, 840 and 509 cm− 1 are attributed to the electroactive β-phase, and the characteristic peak at 762 cm− 1 correspond to the non-polar α-phase (Figure. 5.9 B3) [40]. The transformation from α to β phase in PVDF is attributed to the fact that the high electric field during the electrospinning process can facilitate the growth of the β-phase by producing a completely different arrangement of polarity in the PVDF fibers [41]. The β phase is expected to play a vital role in the PTENG device performance. Electrical output of the PVDF/CPDA hydrogel was determined using the construct shown in Figure. 5.9 C. Here, the PVDF membrane served as the active layer and the conducting hydrogel served as electrodes. When pressure was applied on the above assembly, piezoelectric voltage was generated between the two conducting hydrogels. In the absence of pressure, no piezo response was observed. On application of force/pressure, a flow of electrons between the two electrodes was generated, leading to a potential difference between the two electrodes. The output voltage and short circuit current of the dressing was assessed by repetitive human finger tapping on the PVDF

membrane, using mechanical pressure of ~13 kPa, with a frequency of ~5 Hz. The dressing generated an open circuit output voltage (Voc) and short circuit current (Isc) of ~42 mV and ~ 60 nA respectively (Figure. 5.9 D, E). The results indicated that the open-circuit voltage increased with increasing input pressure (Figure. 5.9 F). The influence of impact frequency on output voltage, was measured through repeated finger compression and release at different frequencies (1–5 Hz), while keeping the mechanical pressure constant (Figure. 5.9 G). The almost constant output voltage observed in the frequency range of 1–5 Hz, suggested that the output voltage was independent on the rate at which the mechanical deformation was imposed, which is favorable for our desired application. With no major adverse events being reported with current between 50 and 1000 μA [42], it might be assumed that the electrical output observed in the dressing would be relatively safe.

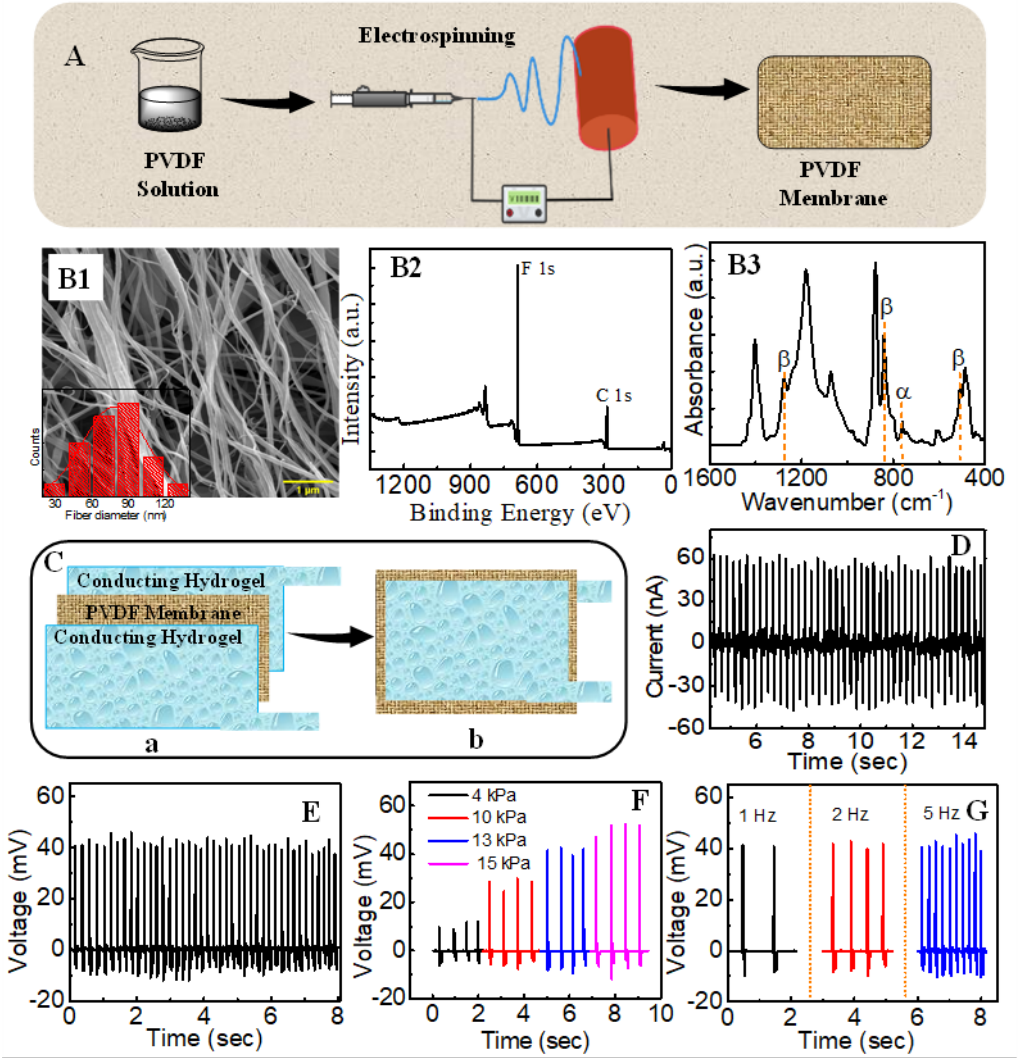

Figure 5.9: Characterization of PTENG dressing (A) Schematic representation of PVDF membrane fabrication using electrospinning. Characterization of PVDF membrane. (B1) SEM image; (B2) XPS survey spectra; (B3) FTIR Spectra in the wavenumber region 1600-400 cm^{-1}; (C) Schematic representation of dressing; (D) Short circuit current (I_{SC}); (E) Open circuit voltage (V_{OC}) under repetitive imparting pressure of 13 kPa; (F, G) Variation of open circuit voltages (V_{OC}) under different conditions.

The piezoelectric β-phase of PVDF membrane prepared during the layer-by-layer stacking of nanofibers using the electrospinning process results in void formation throughout the membrane [43,44]. These void structures are modulated upon the application of external mechanical load/impact. As illustrated, Figure. 5.10 a indicates the distribution of electroactive dipoles attributed to the β-phase of PVDF in initial wound dressing where no mechanical load is applied. Upon application of mechanical load, available dipoles try to align in particular

direction to give rise to the generation of effective electrical potential difference between the top (designated by negative signs) and bottom surface (designated by positive signs) of the nanofiber membrane. In addition, the structural change of voids due the compressive stress leads to induction of resulting potential difference between the top and bottom edges of membrane [45]. Hence, the effective potential difference generated in Figure. 5.10 b is due to aligned dipoles of fibers and induced charges generated due to change in void structure under mechanical load. This distribution of charges changes on removal of mechanical load that leads to relaxation of dipoles of fibers and corresponding induced charges (Figure. 5.10 c). The charge compensation takes place via conducting hydrogel placed between wound and nanofiber membrane. In addition, we have performed finite element analysis of wound dressing structure to evaluate the effective distribution of electric potential, stress and displacement under mechanical load (Figure. 5.10 d (i~iii)). It is observed that the maximum electric potential (Figure. 5.10 d (i)) lies around the interface of nanofiber membrane and conducting hydrogel due to induction of charges as described in Figure. 5.10 b. On the other hand, the distribution of stress (Figure. 5.10 d (ii)) around each nanofiber leads to compressive displacement (Figure. 5.10 d (iii)) that give rise to change in void structure which induce charges between the edges of membrane. The data reveals that the piezo-driven triboelectric nanogenerator would provide continuous electrical impulses to the wound bed from the PTENG dressing.

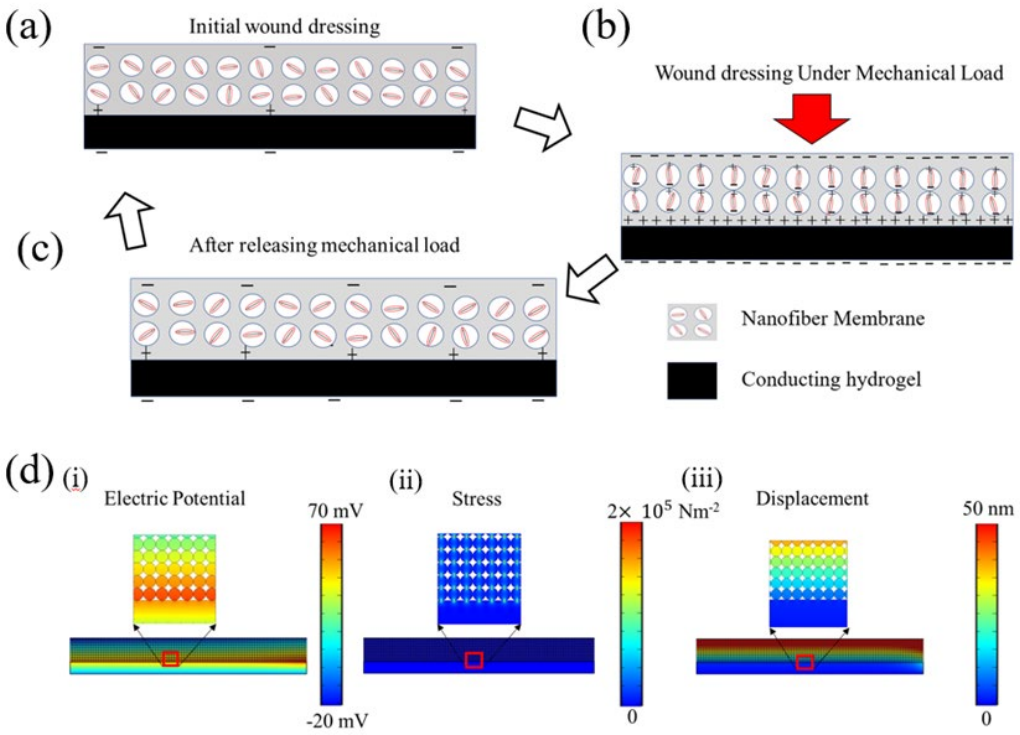

Figure 5.10. Mechanism of the charge generation in piezo-driven triboelectric nanogenerator of wound dressing with (a) the initial distribution of dipoles of nanofiber membrane where induced charges generated at the surface due to effective polarization of randomly oriented dipoles of the nanofiber membrane, (b) the alignment of dipoles of nanofiber membrane under mechanical load and effective distribution of induced potential difference between top and bottom edge of nanofiber membrane and (c) relaxation of dipoles after removal of mechanical load leads to redistribution of dipoles and corresponding induced charges. (d) Finite element analysis of distribution of (i) electric potential, (ii) stress and (iii) displacement in the wound dressing under application of mechanical load of 13 kPa.

5.3.9 Cell response to the wound dressing: As the wound dressing would be in close contact with the wound, it should be biocompatible. We evaluated the biocompatibility of the CPDA hydrogel as per ISO 10993 [46]. Exogenous electric field is known to control cellular activities such as fibroblast proliferation and migration [47]. As fibroblast proliferation play an important role in wound healing, we evaluated the proliferative response of dermal fibroblasts in hydrogels with or without electrical stimulation. Analysis of the cells seeded in the hydrogels revealed a considerable increase in the number of viable fibroblasts with time, suggesting the hydrogels supported fibroblasts proliferation (Figure 5.11 A). The significant

increase in the number of fibroblasts in ES hydrogel, over un-stimulated hydrogel further confirmed the positive influence of ES on fibroblasts proliferation. Vascular deficiency is an underlying factor responsible for delayed healing in DFU [48]. Application of an electric field is reported to provide endothelial cells with significant directional cues which influence its migration and alignment [49]. The response of HUVEC was similarly evaluated in the electrically stimulated hydrogel in comparison to the unstimulated hydrogel. Confocal images of endothelial cells on day 3 revealed the alignment of endothelial cells to form a capillary-like network (Figure 5.11 B)in the ES hydrogels. In contrast, the cells that were not exposed to ES were randomly distributed in the hydrogel. The data suggests that the hydrogel supported endothelial cell viability and encouraged its migration in response to an electrical field to form a capillary network thus confirming its potential to support angiogenesis. The ability to support cellular activity confirmed the hydrogel can serve as a scaffold to encourage skin regeneration.

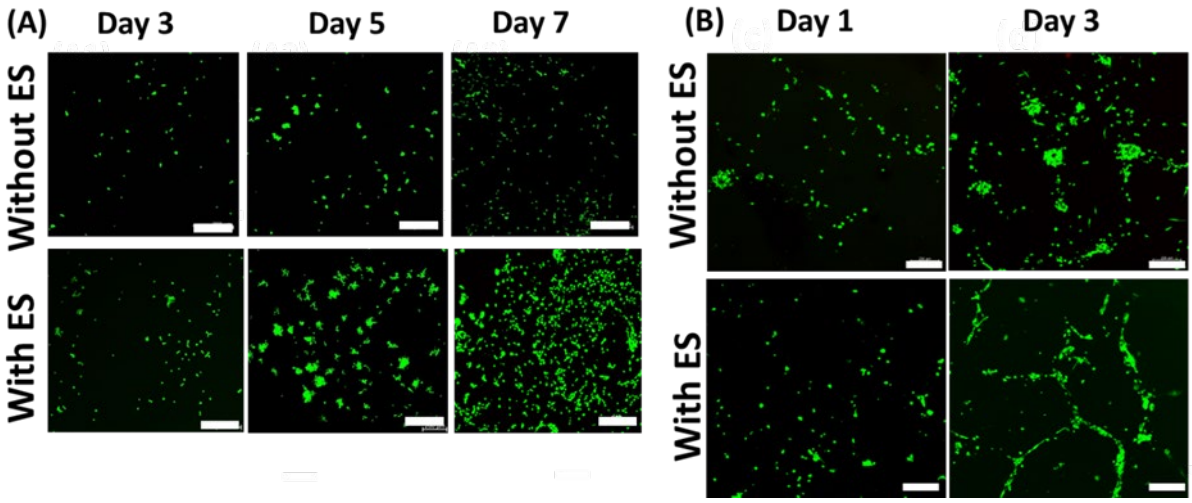

Figure 5.11: Response of fibroblasts and endothelial cells to ES. A. Fibroblast response in hydrogels with or without ES. B. Endothelial cell alignment in the hydrogel with or without ES. Yellow arrow indicates network formation. Scale bar represents 200 µm.

5.3.10 Antibacterial studies: Minor foot lesions in diabetic patients may lead to chronic ulcers, which subsequently are susceptible to infection resulting in gangrene and even

amputation. Infection, if not addressed early can lead to septicemia. As DFUs are chronic and the exudate of DFU provide a rich environment for bacterial growth, appropriate anti-infective treatment is important. However, as most clinically evident bacteria have developed resistance to multiple antibiotics, wound dressings having inherent antimicrobial activity would be preferred. Contact-induced anti-bacterial activity of polydopamine is established [50,51]. Whereas several anti-bacterial mechanisms have been proposed, nonetheless, the destruction of cell membrane has been observed in all such bacteria. We evaluated the antibacterial activity of the CPDA-hydrogels using E. coli as a representative bacterium. A suspension of E. coli was exposed to either CPDA-hydrogel or control hydrogel for 24 h, and then stained with FDA/PI to differentiate between live and dead cells. In the CPDA hydrogel, a significant cell death (stained red) was observed, as compared to the viable cells (green) (Figure. 5.12A). The viability of the bacteria confirmed by checking the optical density drastically reduced after being exposed to the CPDA hydrogel for 24 h as compared to control as shown in (Figure. 5.12B).

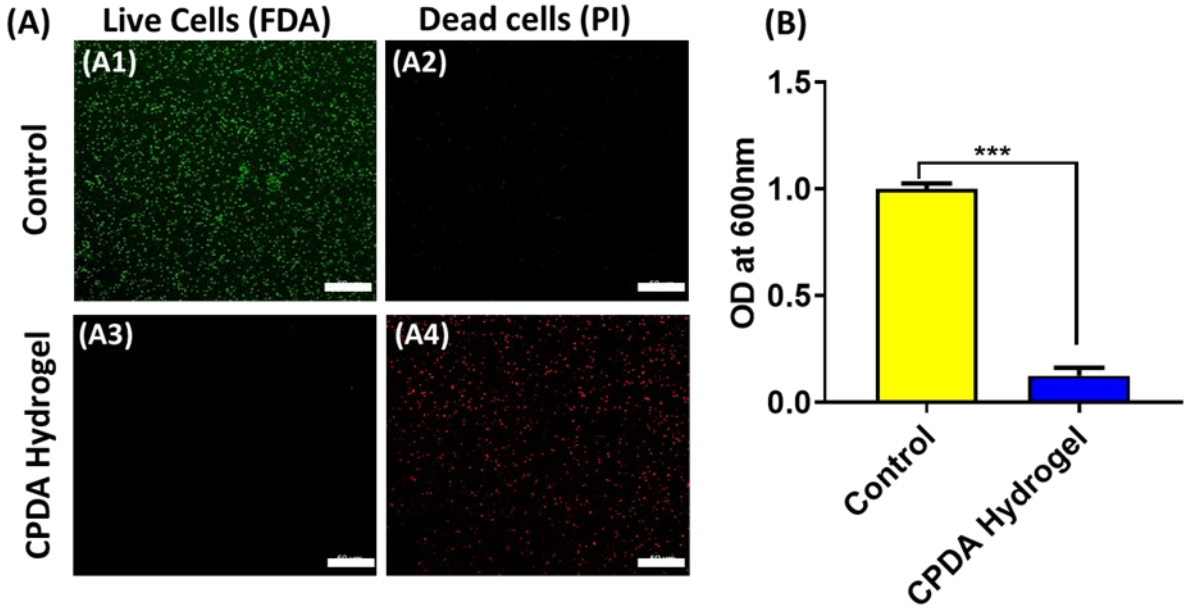

Figure 5.12: Antimicrobial activity of CPDA hydrogel; (A) Live/dead assay of the bacteria seeded on the control hydrogels (A1-A2) and CPDA-hydrogel (A3-A4). Scale bar represents 50 μm; (B)

Optical density at 600 nm (post 24 h exposure to respective hydrogels). Data is represented as mean ± SD (n = 3). ***P < 0.001

The morphology of the bacteria in contact with the control and CPDA hydrogel was assessed using FE-SEM (Figure. 5.13). In comparison to the bacteria in contact with the control gel, the bacteria in contact with the CPDA-hydrogel displayed cell wall destruction. As the results are similar to the reported observation [50, 51], it can be concluded that the anti-bacterial activity observed in the CPDA-hydrogel is on account of PDA.

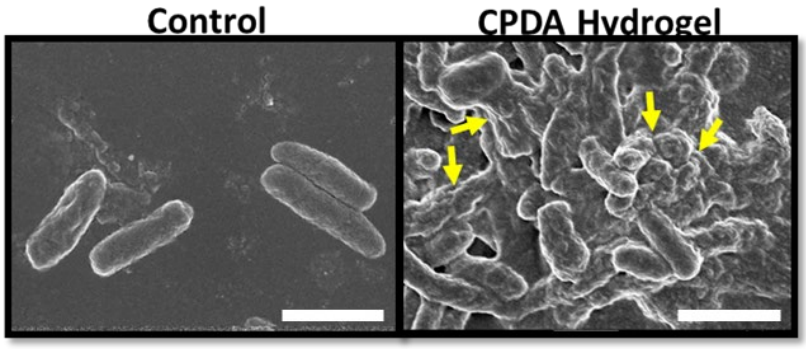

Figure 5.13: SEM analysis of bacterial morphology: FESEM images of bacteria seeded on the Control hydrogel and CPDA hydrogel. Yellow arrows indicate the bacterial wall disruption. Scale bar represents 1μm.

5.3.11 Effect of the dressing on wound healing: Although ES and hydrogels per se have been reported to aid wound healing, however their combined response in wounds is not known. Whereas the mechanism involved in both the modes of treatment are different [52], it can be proposed that the outcome would be further improved if both such approaches are combined. The efficacy of the developed PTENG wound dressing was evaluated using a full thickness skin excisional wound model as such wounds are difficult to heal. The excised wounds were covered either with a commercially available standard wound dressing (Tegaderm), CPDA hydrogel or the PTENG dressing respectively and visualized on regular basis. It can be seen from Figure. 5.14 A that the wound area in all the three groups decreased

gradually with time, with the rate of wound closure being the fastest in the wounds covered with the PTENG dressing. The improved healing observed in the hydrogel-treated wounds, as compared to Tegaderm reiterated the potential of the CPDA hydrogel to aid tissue repair [16]. Quantitative analysis of the wounds, revealed a significant increase in the rate of closure of wounds covered with the PTENG dressing as compared to the CPDA hydrogel alone. The results confirmed that the electrical activity induced through the activation of PTENG during physical activity facilitated faster healing (Figure. 5.14 B).

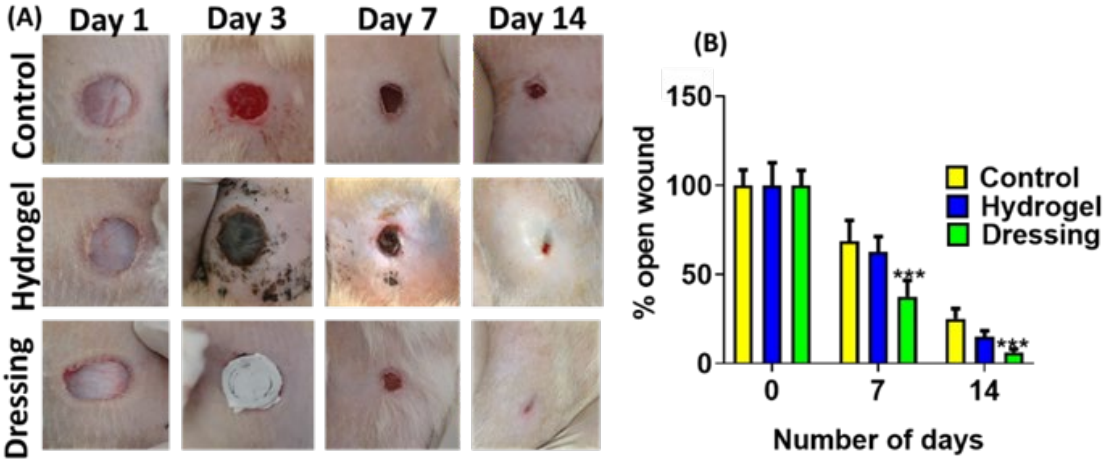

Figure 5.14: In vivo wound healing studies (A) Representative images of the wounds at day 1, 3, 7 and 14. (B) Estimation of wound area. Data is represented as mean ± SD (n = 6). **P < 0.01, and ***P < 0.001.

H&E sections obtained from the respective wound area on day 14 revealed the internal organization of the cells (Figure 5.15 A&B). The control group revealed extensive cellular activity suggesting the formation of granulation tissue. In contrast, the wounds treated with both the CPDA hydrogel and the PTENG dressing, displayed minimal cellular activity, suggesting completion of the granulation tissue formation and the initiation of tissue remodeling [53]. In comparison to the hydrogel treatment, the wounds treated with the PTENG dressing revealed a dense connective tissue and multi-layered epithelium (marked by arrow).

In addition, the presence of hair follicles in the dermis of the wounds covered with PTENG dressing indicated advanced healing. Further CD-31, a marker of endothelial cells was used to analyse the regeneration of blood vessels (Figure. 5.15 C). In comparison to control and hydrogel treated wounds, the number of CD-31 positive cells was remarkably higher in the wounds covered with PTENG dressing, implying the improved vascularization was a consequence of ES. In addition to the regeneration of blood vessels, epithelialization of the wounds was confirmed using cytokeratin antibody Figure. 5.15 D). Whereas epithelization was complete in both the hydrogel and PTENG dressing treated wounds, the presence of a well-defined multilayer epithelium in the wounds covered with PTENG dressing, confirmed the completion of the epidermal construction, while it was progressing in the case of hydrogel covered wounds. The above results suggest that PTENG promoted wound healing through the combined beneficial effects of moist wound healing along with ES.

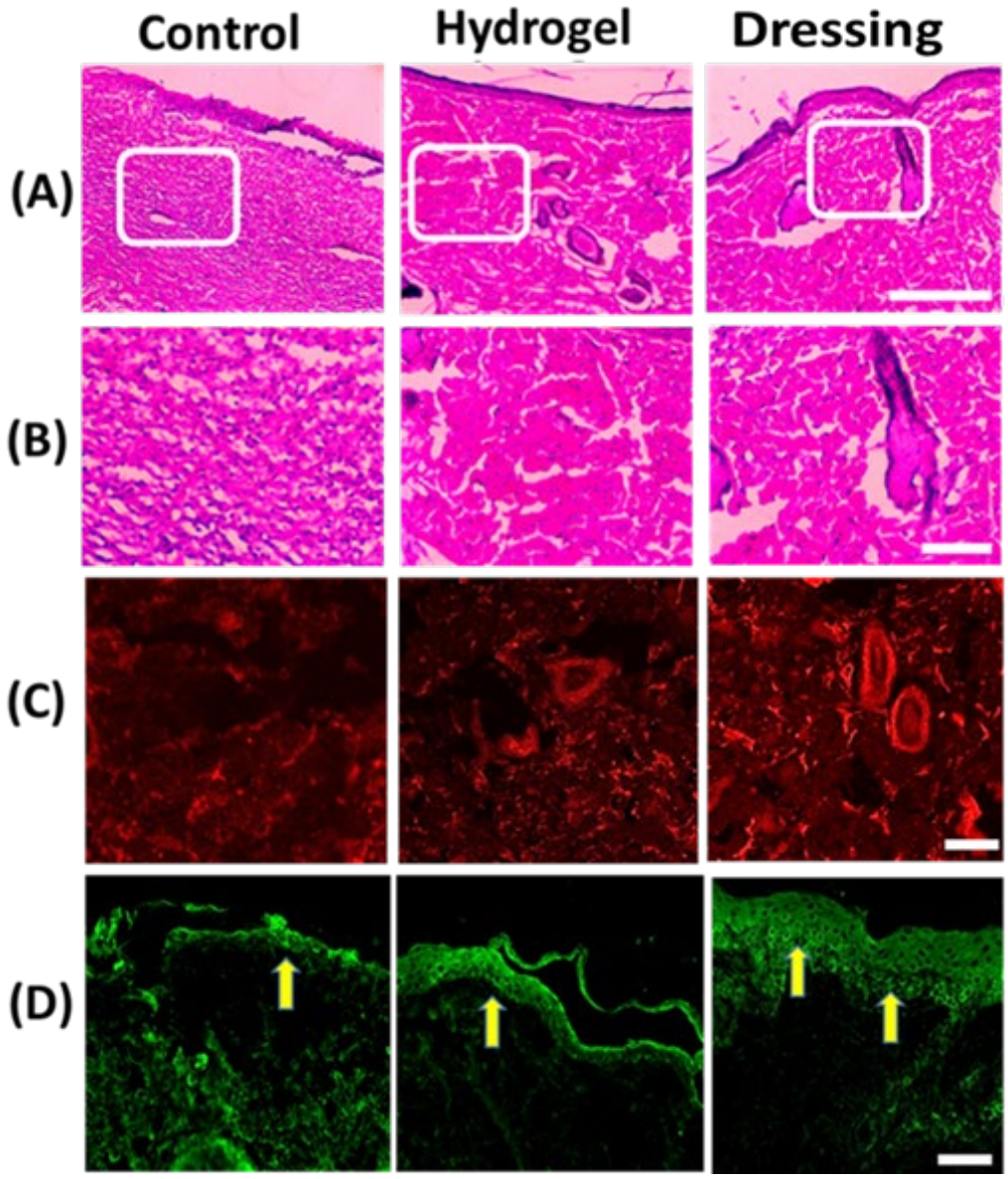

Figure 5.15 H&E and Immuno-histological analysis. A&B. H&E-stained sections of respective wounds. A Images of the wound area (10X), Scale bar represents 400 µm; B. Magnified images of the respective boxed area (20X). Scale bar indicates 200 µm; C. Endothelial cells identified red with CD-31 antibody; D. Epithelial cells identified with cytokeratin staining. Yellow arrows indicate epithelial cells. Scale bar represents 100 µm.

5.4 Conclusion:

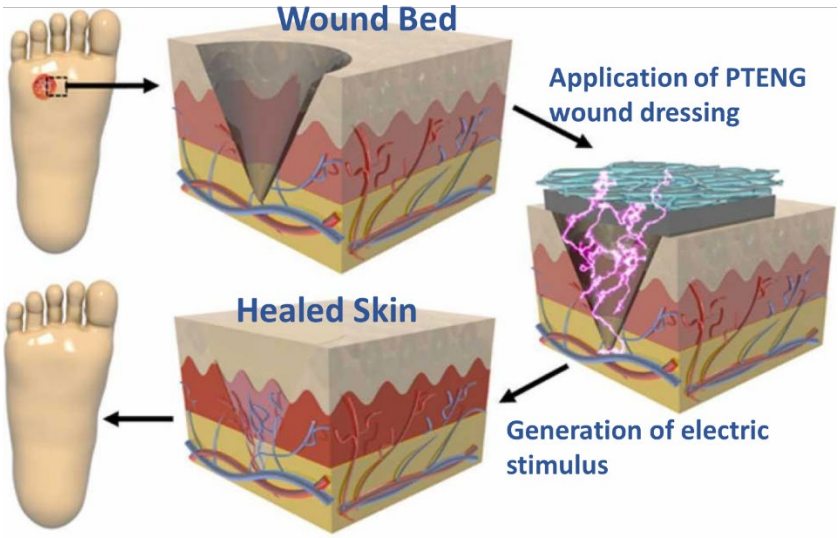

Schematic representation of wound healing mechanism by PTENG wound dressing

In summary, we have developed a self-powered, wearable, multifunctional, adhesive, antibacterial dressing for encouraging the repair of wounds with healing deficiency. The rheological and good mechanical properties of the hydrogel will enable it to provide protection to the underlying wound and withstand the mobility challenges that face existing diabetic foot ulcer dressings. The optimal fluid handling property of the hydrogel component of the PTENG dressing can provide a moist wound environment to facilitate autolytic debridement. Its application as an epidermal sensor and electrode is facilitated by the high conductivity enabled by the presence of carbonized PDA nano sheets in the hydrogel. The biocompatible PTENG dressing promoted fibroblasts proliferation and endothelial network formation. Evidence of accelerated wound healing through faster wound closure, reepithelialization, regeneration of blood vessels and follicles proved that the PTENG dressing promoted healing using a combination of moist wound dressing and ES. Our approach thus provides a user friendly, patient compliant wound dressing to encourage the healing of chronic wounds like the diabetic foot ulcers.

Bibliography

1. A.J. Boulton, The diabetic foot: a global view, Diabetes/Metab. Res. Rev., 16 (Suppl. 1) (2000), pp. S2-S5.
2. Z. Chen, Z.-Y. Chen, W.-H. Liu, G.-S. Li, Electric stimulation as an effective adjunctive therapy for diabetic foot ulcer: a meta-analysis of randomized controlled trials, Adv. Ski. Wound Care, 33 (11) (2020), pp. 608-612.
3. S.E. Tyler, Nature's electric potential: A systematic review of the role of bioelectricity in wound healing and regenerative processes in animals, humans, and plants, 627, Front. Physiol., 8 (2017), pp. 1-18.
4. J.L. Whited, M. Levin, Bioelectrical controls of morphogenesis: from ancient mechanisms of cell coordination to biomedical opportunities, Curr. Opin. Genet. Dev., 57 (2019), pp. 61-69.
5. G. Lagoumintzis, Z. Zagoriti, M.S. Jensen, T. Argyrakos, C. Koutsojannis, K. Poulas, Wireless direct microampere current in wound healing: clinical and immunohistological data from two single case reports, 107, Biosensors, 9 (3) (2019), pp. 1-13.
6. S. Zhao, A. Mehta, M. Zhao, Biomedical applications of electrical stimulation, Cell. Mol. Life Sci., 77 (14) (2020), pp. 2681-2699.
7. R. Fu, L. Tu, Y. Zhou, L. Fan, F. Zhang, Z. Wang, J. Xing, D. Chen, C. Deng, G. Tan, A tough and self-powered hydrogel for artificial skin, Chem. Mater., 31 (23) (2019), pp. 9850-9860.
8. H. Wang, M. Han, Y. Song, H. Zhang, Design, manufacturing and applications of wearable triboelectric nanogenerators, Nano Energy, 81 (2021).
9. C. Ghosal, S.K. Ghosh, K. Roy, B. Chattopadhyay, D. Mandal, Environmental bacteria engineered piezoelectric bio-organic energy harvester towards clinical applications, Nano Energy, 93 (2022).
10. F.C. Kao, H.H. Ho, P.Y. Chiu, M.K. Hsieh, J.C. Liao, P.L. Lai, Y.F. Huang, M.Y. Dong, T.T. Tsai, Z.H. Lin, Self-assisted wound healing using piezoelectric and triboelectric nanogenerators, Sci. Technol. Adv. Mater., 23 (1) (2022), pp. 1-16.
11. S.-H. Jeong, Y. Lee, M.-G. Lee, W.J. Song, J.-U. Park, J.-Y. Sun, Accelerated wound healing with an ionic patch assisted by a triboelectric nanogenerator, Nano Energy, 79 (2021).

12. H. Hu, F.-J. Xu, Rational design and latest advances of polysaccharide-based hydrogels for wound healing, Biomater. Sci., 8 (2020), pp. 2084-2101.
13. A. Das, A. Kumar, N.B. Patil, C. Viswanathan, D. Ghosh, Preparation and characterization of silver nanoparticle loaded amorphous hydrogel of carboxymethylcellulose for infected wounds, Carbohydr. Polym., 130 (2015), pp. 254-261.
14. L.-Y. Hsiao, L. Jing, K. Li, H. Yang, Y. Li, P.-Y. Chen, Carbon nanotube-integrated conductive hydrogels as multifunctional robotic skin, Carbon, 161 (2020), pp. 784-793.
15. E. Chalmers, H. Lee, C. Zhu, X. Liu, Increasing the conductivity and adhesion of polypyrrole hydrogels with electropolymerized polydopamine, Chem. Mater., 32 (2020), pp. 234-244.
16. C. Wu, L. Shen, Y. Lu, C. Hu, Z. Liang, L. Long, N. Ning, J. Chen, Y. Guo, Z. Yang, Intrinsic antibacterial and conductive hydrogels based on the distinct bactericidal effect of polyaniline for infected chronic wound healing, ACS Appl. Mater. Interfaces, 13 (44) (2021), pp. 52308-52320.
17. M. Talikowska, X. Fu, G. Lisak, Application of conducting polymers to wound care and skin tissue engineering: a review, Biosens. Bioelectron., 135 (2019), pp. 50-63.
18. Y. Liang, B. Chen, M. Li, J. He, Z. Yin, B. Guo, Injectable antimicrobial conductive hydrogels for wound disinfection and infectious wound healing, Biomacromolecules, 21 (2020), pp. 1841-1852.
19. S. Cheon, H. Kang, H. Kim, Y. Son, J.Y. Lee, H.J. Shin, S.W. Kim, J.H. Cho, High-performance triboelectric nanogenerators based on electrospun polyvinylidene fluoride–silver nanowire composite nanofibers, Adv. Funct. Mater., 1703778 (2017), pp. 1-7.
20. K. Ai, Y. Liu, C. Ruan, L. Lu, G. Lu, Sp2 C-dominant N-doped carbon sub-micrometer spheres with a tunable size: a versatile platform for highly efficient oxygen-reduction catalysts, Adv. Mater., 25 (2013), pp. 998-1003.
21. R. Li, K. Parvez, F. Hinkel, X. Feng, K. Müllen, Bioinspired wafer-scale production of highly stretchable carbon films for transparent conductive electrodes, Angew. Chem. Int. Ed., 52 (2013), pp. 1-5.
22. D.N. Nguyen, U. Sim, J.K. Kim, Biopolymer-inspired N-doped nanocarbon using carbonized polydopamine: a high-performance electrocatalyst for hydrogen-evolution reaction, 912 Polymers, 12 (2020), pp. 1-12.

23. V. Panwar, A. Babu, A. Sharma, J. Thomas, V. Chopra, P. Malik, S. Rajput, M. Mittal, R. Guha, N. Chattopadhyay, Tunable, conductive, self-healing, adhesive and injectable hydrogels for bioelectronics and tissue regeneration applications, J. Mater. Chem. B., 9 (2021), pp. 6260-6270.
24. L. Han, L. Yan, K. Wang, L. Fang, H. Zhang, Y. Tang, Y. Ding, L.-T. Weng, J. Xu, J. Weng, Tough, self-healable and tissue-adhesive hydrogel with tunable multifunctionality, NPG Asia Mater., 9 (2017), pp. 1-12.
25. J. Thomas, A. Sharma, V. Panwar, V. Chopra, D. Ghosh, Polysaccharide-based hybrid self-healing hydrogel supports the paracrine response of mesenchymal stem cells, ACS Appl. Bio Mater., 2 (5) (2019), pp. 2013-2027.
26. E. Grip, R.E. Steene, J. Engstad, A. Hart, I. Bell, P. Skjæveland, N. Basnet, A.M. Škalko-Basnet, Holsæter, Development of a novel beta-glucan supplemented hydrogel spray formulation and wound healing efficacy in a db/db diabetic mouse model, Eur. J. Pharm. Biopharm., 169 (2021), pp. 280-291.
27. F. Fan, S. Saha, D.H. Putra, Biomimetic hydrogels to promote wound healing, 718377 Front. Bioeng. Biotechnol., 9 (2021), pp. 1-24.
28. E. Brooks, M. Burns, R. Ma, H.J. Scholten, S. Becker, Remote diabetic foot temperature monitoring for early detection of diabetic foot ulcers: a cost-effectiveness analysis, Clin. Outcomes Res., 13 (2021), pp. 873-881.
29. K.L. Menzies, L. Jones, The impact of contact angle on the biocompatibility of biomaterials, Optom. Vis. Sci., 87 (6) (2010), pp. 387-399.
30. L. Han, M. Wang, P. Li, D. Gan, L. Yan, J. Xu, K. Wang, L. Fang, C.W. Chan, H. Zhang, Mussel-inspired tissue-adhesive hydrogel based on the polydopamine–chondroitin sulfate complex for growth-factor-free cartilage regeneration, ACS Appl. Mater. Interfaces, 10 (2018), pp. 28015-28026.
31. I. Levental, P.C. Georges, P.A. Janmey, Soft biological materials and their impact on cell function, Soft Matter, 3 (2007), pp. 299-306.
32. C.F. Guimarães, L. Gasperini, A.P. Marques, R.L. Reis, The stiffness of living tissues and its implications for tissue engineering, Nat. Rev. Mater., 5 (2020), pp. 351-370.
33. S. Li, L. Wang, W. Zheng, G. Yang, X. Jiang, Rapid fabrication of self-healing, conductive, and injectable gel as dressings for healing wounds in stretchable parts of the body, Adv. Funct. Mater., 2002370 (2020), pp. 1-12.
34. V. De Santis, X.L. Chen, I. Laakso, A. Hirata, An equivalent skin conductivity model for low-frequency magnetic field dosimetry, Biomed. Phys. Eng. Express, 1 (2015).

35. C. Chai, Y. Guo, Z. Huang, Z. Zhang, S. Yang, W. Li, Y. Zhao, J. Hao, Antiswelling and durable adhesion biodegradable hydrogels for tissue repairs and strain sensors, Langmuir, 36 (2020), pp. 10448-10459.
36. L. Han, L. Yan, M. Wang, K. Wang, L. Fang, J. Zhou, J. Fang, F. Ren, X. Lu, Transparent, adhesive, and conductive hydrogel for soft bioelectronics based on light-transmitting polydopamine-doped polypyrrole nanofibrils, Chem. Mater., 30 (2018), pp. 5561-5572.
37. S.A. Eming, P. Martin, M. Tomic-Canic, Wound repair and regeneration: mechanisms, signaling and translation, Sci. Transl. Med., 6 (265sr6) (2014), pp. 1-36.
38. Z. Qiao, J. Parks, P. Choi, H.-F. Ji, Applications of highly stretchable and tough hydrogels, 1773 Polymers, 11 (2019), pp. 1-15.
39. D. Mandal, K.J. Kim, J.S. Lee, Simple synthesis of palladium nanoparticles, β-phase formation, and the control of chain and dipole orientations in palladium-doped poly (vinylidene fluoride) thin films, Langmuir, 28 (28) (2012), pp. 10310-10317.
40. K. Maity, U. Pal, H.K. Mishra, P. Maji, P. Sadhukhan, Z. Mallick, S. Das, B. Mondal, D. Mandal, Piezo-phototronic effect in highly stable CsPbI3-PVDF composite for self-powered nanogenerator and photodetector, Nano Energy, 92 (2022).
41. W. Guo, C. Tan, K. Shi, J. Li, X.-X. Wang, B. Sun, X. Huang, Y.-Z. Long, P. Jiang, Wireless piezoelectric devices based on electrospun PVDF/BaTiO 3 NW nanocomposite fibers for human motion monitoring, Nanoscale, 10 (2018), pp. 17751-17760.
42. P.G. Wirsing, A.D. Habrom, T.M. Zehnder, S. Friedli, M. Blatti, Wireless micro current stimulation–an innovative electrical stimulation method for the treatment of patients with leg and diabetic foot ulcers, Int. Wound J., 12 (2015), pp. 693-698.
43. Z. Ren, Q. Zheng, H. Wang, H. Guo, L. Miao, J. Wan, C. Xu, S. Cheng, H. Zhang, Wearable and self-cleaning hybrid energy harvesting system based on micro/nanostructured haze film, Nano Energy, 67 (2020).
44. C. Jiang, C. Wu, X. Li, Y. Yao, L. Lan, F. Zhao, Z. Ye, Y. Ying, J. Ping, All-electrospun flexible triboelectric nanogenerator based on metallic Mxene nanosheets, Nano Energy, 59 (2019), pp. 268-276.
45. F.-R. Fan, Z.-Q. Tian, Z.L. Wang, Flexible triboelectric generator, Nano Energy, 1 (2012), pp. 328-334.

46. A.V. Thanusha, V. Koul, Biocompatibility evaluation for the developed hydrogel wound dressing–ISO-10993-11 standards–in vitro and in vivo study, Biomed. Phys. Eng. Express, 8 (1) (2021).
47. S. Naskar, V. Kumaran, Y.S. Markandeya, B. Mehta, B. Basu, Neurogenesis-on-chip: electric field modulated transdifferentiation of human mesenchymal stem cell and mouse muscle precursor cell coculture, Biomaterials, 226 (2020).
48. U.A. Okonkwo, L. Chen, D. Ma, V.A. Haywood, M. Barakat, N. Urao, L.A. DiPietro, Compromised angiogenesis and vascular Integrity in impaired diabetic wound healing, e0231962, PLoS One, 15 (4) (2020), pp. 1-17.
49. F. Cunha, A.M. Rajnicek, C.D. McCaig, Electrical stimulation directs migration, enhances and orients cell division and upregulates the chemokine receptors CXCR4 and CXCR2 in endothelial cells, J. Vasc. Res., 56 (1) (2019), pp. 39-53.
50. Z. Iqbal, E.P. Lai, T.J. Avis, Antimicrobial effect of polydopamine coating on Escherichia coli, J. Mater. Chem., 22 (2012), pp. 21608-21612.
51. Y. Fu, J. Zhang, Y. Wang, J. Li, J. Bao, X. Xu, C. Zhang, Y. Li, H. Wu, Z. Gu, Reduced polydopamine nanoparticles incorporated oxidized dextran/chitosan hybrid hydrogels with enhanced antioxidative and antibacterial properties for accelerated wound healing, 117598, Carbohydr. Polym., 257 (2021), pp. 1-10.
52. W. Hu, X. Wei, L. Zhu, D. Yin, A. Wei, X. Bi, T. Liu, G. Zhou, Y. Qiang, X. Sun, Enhancing proliferation and migration of fibroblast cells by electric stimulation based on triboelectric nanogenerator, Nano Energy, 57 (2019), pp. 600-607.
53. C. Yu, Z.-X. Xu, Y.-H. Hao, Y.-B. Gao, B.-W. Yao, J. Zhang, B. Wang, Z.-Q. Hu, R.-Y. Peng, A novel microcurrent dressing for wound healing in a rat skin defect model, Mil. Med. Res., 6 (22) (2019), pp. 1-9.

Chapter 6: Conclusion and Future Prospective

6.1 Conclusion

Over the last couple of decades, elaborative studies have been performed on CBNs as one of the most popular and useful class of smart nanomaterials. Carbon nanomaterials serve as an excellent candidate in the field of material sciences because of their inherent optical, electrical, mechanical and electrochemical properties. Moreover, these materials have high surface area, versatile size and shapes which is responsible for their widespread usage in biomedical applications.

The surface of carbon based nanomaterials can be easily functionalised with different molecules (inorganic/organic) to obtain modified carbon nanostructures with improved physicochemical properties, excellent biocompatibility and enhanced biological activity. Owing to its nano dimensions, these materials can easily penetrate biological membranes to exert the desired biological effect. In this thesis, I have tried to develop carbon based bioactive nanomaterials and explored their applications in anti-cancer and wound healing.

In my first study, I had explored the biological activity of carbon dots derived from curcumin (CurCD). Curcumin is a well-known therapeutic molecule obtained from *Curcuma longa*. Its pleiotropic activity is reported to be effective against multiple disorders. Despite its promising effect, curcumin had failed in clinical trials due to its low solubility, stability and poor bioavailability. The as-synthesised CurCD had shown improved aqueous solubility, high biocompatibility and enhanced fluorescence as compared to the parent compound curcumin. In addition to this, CurCD had displayed selective actin binding phenomenon which can be exploited for bioimaging or actin specific drug delivery applications. In order to check the inherent therapeutic response retained by CurCD, its anti-cancer activity was checked using glioblastoma cells and compared with curcumin. CurCD exhibited comparable/enhanced anticancer activity in the in vitro cancer models.

After confirming the inherent or retained biological response of CurCD was similar to curcumin even after carbonization, I explored the hormetic activity of CurCD by taking wound healing, as a model. Curcumin is known to show wound healing effect at lower concentrations and anti-proliferative activity at higher concentrations. In the previous study, higher concentration of CurCD was used for anti-cancer activity against glioma cells. When CurCD was used at lower concentrations, it had superior proliferative, pro-angiogenic and anti-bacterial activity. Due to its small size and faster excretion from the biological system, a delivery system was needed for the topical application of carbon dots for wound healing activity. To overcome this limitation, I designed a protease responsive hydrogel for the sustained delivery of CurCD at the site of wound. A comparative study using a skin excision model revealed that CurCD-crosslinked hydrogel supported faster healing with improved angiogenesis and epidermal restoration, as compared to curcumin alone.

Carbon dots are being used for various healthcare applications like bioimaging, tissue regeneration, drug delivery, anticancer therapies and as theranostics. In such applications, the carbon dots are administered to the biological system via intravenous route. Such in-vivo administration of the CD would lead to its exposure to the endothelial cells (ECs) that line the lumen of blood vessels. There are no reports of the response of endothelial cells to the CD. To evaluate the response, I had used an extensively reported carbon dot synthesised from citric acid and urea (CD-urea) for exploring its interaction with the endothelial system. CD-urea had shown an increase in angiogenesis both in the *in vitro* and *ex vivo* models, suggesting the importance of evaluating the response of carbon nanomaterials with the endothelial cells prior to in vivo applications as angiogenic response is beneficial in some conditions (wound healing, ischemia etc) while such a response would be detrimental in conditions such as cancers.

In my last part of the thesis, I developed a wearable bioelectronics device for the healing of chronic wounds like diabetic foot ulcers. For this, carbon-based nanomaterial (carbonised

polydopamine) was utilized in the making of a conductive hydrogel and a nanocomposite was developed by coupling the conductive hydrogel with an electroactive PVDF membrane. In this composite, CPDA hydrogel act as an electrode whereas the PVDF membrane provided the piezo-response. The PVDF in combination with the hydrogel was capable of providing the electrical stimulus to the underlying wound by serving as a piezoelectric driven triboelectric nanogenerator (PTENG). In vitro studies revealed that PTENG dressing was able to support the proliferation of fibroblasts cells and also provided directional cues to the endothelial cells which aids in the process of network formation known as angiogenesis. The in vivo wound healing efficiency of the dressing was confirmed by using an excisional skin wound model. The electrical stimulation and moist wound environment provided by the PTENG dressing resulted in complete restoration of epithelium, improved neovascularisation and remodelling of wounds.

To summarise

1. I have been able to synthesise and explore the bioactivity of carbon based nanomaterials for antitumor and wound healing therapies. The economical synthetic process, as well as the bioactivity of these materials make them as promising candidates in the field of medicine.
2. It is evident from the above studies that these materials possess excellent mechanical strength, bioactive nature and exceptional optical properties which makes them useful in versatile applications like drug delivery agents, bioimaging probes or scaffolds for tissue regeneration.
3. While the first part of work represents a promising approach to generate molecules with improved biophysical properties from plats derived molecules, which otherwise have limitations, the later part of my work demonstrates a potential device developed with nanomaterials for addressing chronic wounds.

6.2 Future prospective

Carbon based nanomaterials are developing as a new generation of smart structures which are versatile, biocompatible and possess excellent mechanical strength. In the last two decades, intensive research on carbon nanomaterials has shown the selectivity, specificity of these nanostructures for healthcare applications. As a result, they are extensively applied in drug delivery systems, cell-based sensors and in scaffolds for tissue regeneration. Despite their usefulness, there are muiltiple challenges that must be resolved before their translation into clinical applications.

Challenges that need to be addressed

i. Consistency and scalability of the carbonised materials should be achieved for the development of technology.

ii. Extensive evaluation of the materials in the *in vivo* models to check their long-term effect on the biological system.

Annexure I: List of manuscripts authored during PhD tenure

Publications part of the thesis:

1. **Sharma, A.,** Panwar, V., Chopra, V., Thomas, J., Kaushik, S. and Ghosh D., 2019. Interaction of carbon dots with endothelial cells: implications for biomedical applications. *ACS Applied Nano Materials*, *2*(9), pp.5483-5491.
2. **Sharma, A.,** Panwar, V., Thomas, J., Chopra, V., Roy, H.S. and Ghosh, D., 2021. Actin-binding carbon dots selectively target glioblastoma cells while sparing normal cells. *Colloids and Surfaces B: Biointerfaces*, *200*, p.111572.
3. **Sharma, A.,** Panwar, V., Salaria, N., & Ghosh, D. (2022). Protease-responsive hydrogel, cross-linked with bioactive curcumin-derived carbon dots, encourage faster wound closure. *Biomaterials Advances*, 212978.
4. **Sharma, A.,** Panwar, V., Mondal, B., Prasher, D., Bera, M.K., Thomas, J., Kumar, A., Kamboj, N., Mandal, D. and Ghosh, D., 2022. Electrical Stimulation Induced by a Piezo-driven Triboelectric Nanogenerator and Electroactive Hydrogel Composite, Accelerate Wound Repair. *Nano Energy*, p.107419.

Publications other than the thesis

1. **Sharma, A.,** Yerra, V.G. and Kumar, A., 2017. Emerging role of Hippo signalling in pancreatic biology: YAP re-expression and plausible link to islet cell apoptosis and replication. *Biochimie*, *133*, pp.56-65.
2. Thomas, J., **Sharma, A.,** Panwar, V., Chopra, V. and Ghosh, D., 2019. Polysaccharide-based hybrid self-healing hydrogel supports the paracrine response of mesenchymal stem cells. *ACS Applied Bio Materials*, *2*(5), pp.2013-2027.
3. Panwar, V., **Sharma, A**., Thomas, J., Chopra, V., Kaushik, S., Kumar, A. and Ghosh, D., 2019. In-vitro and In-vivo evaluation of biocompatible and biodegradable calcium-modified carboxymethyl starch as a topical hemostat. *Materialia*, *7*, p.100373.
4. Panwar, V., Thomas, J., **Sharma, A.,** Chopra, V., Kaushik, S., Kumar, A. and Ghosh, D., 2020. In-vitro and in-vivo evaluation of modified sodium starch glycolate for exploring its haemostatic potential. *Carbohydrate Polymers*, *235*, p.115975.
5. Chopra, V., Thomas, J., **Sharma, A.,** Panwar, V., Kaushik, S., Sharma, S., Porwal, K., Kulkarni, C., Rajput, S., Singh, H. and Jagavelu, K., 2020. Synthesis and evaluation of a zinc eluting rGO/hydroxyapatite nanocomposite optimized for bone augmentation. *ACS*

Biomaterials Science & Engineering, *6*(12), pp.6710-6725.

6. Kaushik, S., Thomas, J., Panwar, V., Ali, H., Chopra, V., **Sharma, A.,** Tomar, R. and Ghosh, D., 2020. In situ biosynthesized superparamagnetic iron oxide nanoparticles (SPIONS) induce efficient hyperthermia in cancer cells. *ACS Applied Bio Materials*, *3*(2), pp.779-788.
7. Chopra, V., Thomas, J., **Sharma, A.,** Panwar, V., Kaushik, S. and Ghosh, D., 2021. A bioinspired, ice-templated multifunctional 3D cryogel composite crosslinked through in situ reduction of GO displayed improved mechanical, osteogenic and antimicrobial properties. *Materials Science and Engineering: C*, *119*, p.111584.
8. Panwar, V., Babu, A., **Sharma, A.,** Thomas, J., Chopra, V., Malik, P., Rajput, S., Mittal, M., Guha, R., Chattopadhyay, N. and Mandal, D., 2021. Tunable, conductive, self-healing, adhesive and injectable hydrogels for bioelectronics and tissue regeneration applications. *Journal of Materials Chemistry B*, *9*(31), pp.6260-6270.
9. Thomas, J., Chopra, V., **Sharma, A.,** Panwar, V., Kaushik, S., Rajput, S., Mittal, M., Guha, R., Chattopadhyay, N. and Ghosh, D., 2021. An injectable hydrogel having proteoglycan-like hierarchical structure supports chondrocytes delivery and chondrogenesis. *International Journal of Biological Macromolecules*, *190*, pp.474-486.

Patents

1. “In situ synthesis of magnetic nanoparticles”. Deepa Ghosh, Swati Kaushik, Vineeta Panwar, Jijo Thomas, **Anjana Sharma**, Vianni Chopra, Rupali Singh. (Indian Patent Filed: 201911021448).

2. "Modified polysaccharide material having haemostatic properties". Deepa Ghosh, Vineeta Panwar, Jijo Thomas, **Anjana Sharma**, Swati Kaushik (Indian Patent Filed: 201911010706)

Annexure II: Permissions & Rights

Permissions from the journal to reuse the content in the thesis

Actin-binding carbon dots selectively target glioblastoma cells while sparing normal cells

Author: Anjana Sharma,Vineeta Panwar,Jijo Thomas,Vianni Chopra,Himadri Shekhar Roy,Deepa Ghosh
Publication: Colloids and Surfaces B: Biointerfaces
Publisher: Elsevier
Date: April 2021

Journal Author Rights

Please note that, as the author of this Elsevier article, you retain the right to include it in a thesis or dissertation, provided it is not published commercially. Permission is not required, but please ensure that you reference the journal as the original source. For more information on this and on your other retained rights, please visit: https://www.elsevier.com/about/our-business/policies/copyright#Author-rights

BACK CLOSE WINDOW

ACS Publications
Most Trusted. Most Cited. Most Read.

Interaction of Carbon Dots with Endothelial Cells: Implications for Biomedical Applications

Author: Anjana Sharma, Vineeta Panwar, Vianni Chopra, et al
Publication: ACS Applied Nano Materials
Publisher: American Chemical Society
Date: Sep 1, 2019

PERMISSION/LICENSE IS GRANTED FOR YOUR ORDER AT NO CHARGE

This type of permission/license, instead of the standard Terms and Conditions, is sent to you because no fee is being charged for your order. Please note the following:

- Permission is granted for your request in both print and electronic formats, and translations.
- If figures and/or tables were requested, they may be adapted or used in part.
- Please print this page for your records and send a copy of it to your publisher/graduate school.
- Appropriate credit for the requested material should be given as follows: "Reprinted (adapted) with permission from {COMPLETE REFERENCE CITATION}. Copyright {YEAR} American Chemical Society." Insert appropriate information in place of the capitalized words.
- One-time permission is granted only for the use specified in your RightsLink request. No additional uses are granted (such as derivative works or other editions). For any uses, please submit a new request.

If credit is given to another source for the material you requested from RightsLink, permission must be obtained from that source.

BACK CLOSE WINDOW

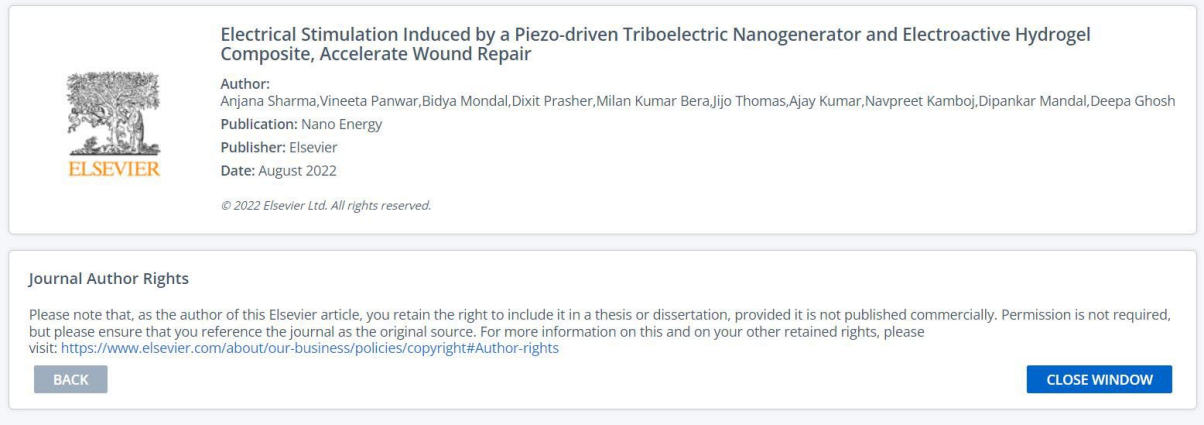

Electrical Stimulation Induced by a Piezo-driven Triboelectric Nanogenerator and Electroactive Hydrogel Composite, Accelerate Wound Repair

Author:
Anjana Sharma,Vineeta Panwar,Bidya Mondal,Dixit Prasher,Milan Kumar Bera,Jijo Thomas,Ajay Kumar,Navpreet Kamboj,Dipankar Mandal,Deepa Ghosh

Publication: Nano Energy

Publisher: Elsevier

Date: August 2022

Journal Author Rights

Please note that, as the author of this Elsevier article, you retain the right to include it in a thesis or dissertation, provided it is not published commercially. Permission is not required, but please ensure that you reference the journal as the original source. For more information on this and on your other retained rights, please visit: https://www.elsevier.com/about/our-business/policies/copyright#Author-rights

BACK CLOSE WINDOW

Type of Publication: Journal

Title: Protease-responsive hydrogel, cross-linked with bioactive curcumin-derived carbon dots, encourage faster wound closure2772-9508
Auhtors: Anjana Sharma
Year: 2022
From page: 212978
To page: 212990
ISSN: 2772-9508
Volume: 139
Article title: Protease-responsive hydrogel, cross-linked with bioactive curcumin-derived carbon dots, encourage faster wound closure

I would like to use: Full article / chapter

I am the author of the Elsevier material: Yes
Involvement: Anjana sharma has ivestigated and written the manuscript

In what format will you use the material: Print and Electronic

Dear Ms. Anjana Sharma,

Thank you for your email.

Please note that, as one of the authors of this article, you retain the right to reuse it in your thesis/dissertation. You do not require formal permission to do so. You are permitted to post this Elsevier article online if it is embedded within your thesis. You are also permitted to post your Author Accepted Manuscript online.

However posting of the final published article is prohibited.

*"As per our Sharing Policy, authors are permitted to post the Accepted version of their article on their institutional repository – as long as it is for **internal institutional use only.***